Shock-Induced Failure of Protection Materials using Laser-Driven Micro-Flyers

by

Debjoy Mallick

A dissertation submitted to The Johns Hopkins University in conformity
with the requirements for the degree of
Doctor of Philosophy

Baltimore, Maryland
May, 2019

Abstract

Protection materials in defense applications must withstand impacts that produce incredible forces and high strain rate deformations, yet remain light enough for use in personal or vehicle armor applications. Understanding the failure processes of these materials is crucial to improving their protection capacity, but experiments to probe these processes are complex. The conventional methods using explosive, gas or gunpowder-driven experiments are dangerous, expensive, and difficult, requiring large-scale facilities where experimental throughput is low. In this thesis, we attempt to achieve similar loading conditions (e.g. strain rates, shock stresses, energy density, etc.) with a high throughput apparatus: a laser-driven micro-flyer plate launcher.

Laser-driven micro-flyer plate (LDMFP) facilities use a short duration pulsed laser with high peak power to launch small metal foil flyers at velocities of several km/s by generating an ablation pressure behind the flyer. Here we describe the Hopkins Extreme Materials Institute LDMFP facility, including the launcher configuration, expected velocity envelope, and photon Doppler velocimetry (PDV) diagnostics. We interrogate the failure of magnesium alloys and boron carbide using the facility.

The widely available AZ31B Mg alloy has a potential application as a low-weight vehicle protection material. We use the LDMFP facility to drive incipient spall failure in AZ31B foils. In spall, shockwave interactions from the impact loading generate high tensile stresses within the target specimen, leading to failure through void growth, coalescence and fracture. Our experiments show an increase in spall strength when compared to lower strain rate spall experiments on the same alloy, and also show differences in strength based on the level of deformation in the as-received microstructure. The LDMFP apparatus facilitates specimen recovery by imparting little kinetic energy, so we perform micro-computed tomography scans of the preserved shocked specimens to learn the void distribution within.

Next, we demonstrate the LDMFP facility capability for high experimental throughput to learn the orientation dependent strength of a Mg-9 wt.%Al binary alloy. The binary alloy is prepared without second phase particles when fully solutionized, and with lath precipitates when warm-aged. The large number of experiments, coupled with numerical simulations, indicate a lack of orientation dependent strength in the solutionized sample, and significant orientation dependent strength in the precipitate-laden microstructure.

Finally, we use the LDMFP facility to examine brittle fragmentation of boron carbide, a lightweight ceramic used in personal body armor. We design the micro-flyer experiment to have a similar energy density as conventional ballistic experiments, and compare the resulting fragmentation statistics. The results suggest that fragment sizes from projectile impact are related to microstructural length scales for both ballistic and laser-driven loading conditions.

Dissertation Committee

Primary Readers

KT Ramesh (Primary Advisor)
Professor
Department of Mechanical Engineering
Johns Hopkins University, Whiting School Engineering

Mark Foster
Associate Professor
Department of Electrical and Computer Engineering
Johns Hopkins University, Whiting School Engineering

Mukul Kumar
Staff Scientist
Materials Engineering Division
Lawrence Livermore National Laboratory

Acknowledgments

"Q: This whole snake thing is just a metaphor, right?

A: I assure you, the snakes are very real."

-"FAQ: The "Snake Fight" Portion of Your Thesis Defense", Luke Burns, *McSweeney's Internet Tendency*

The time is 9 AM on Saturday, February 2, 2019. I have been polishing samples for nearly 60 hours straight without sleep and with little food, and am wondering if the time has come to quit this Ph.D program. I wonder to myself exactly how I came to this point, but to fully understand that, we have to go back to the beginning...

I have to start by thanking Mom and Dad for always putting the strongest emphasis on education. I can't imagine raising children as graduate students, post-docs, and early-career professionals, especially rambunctious kids like Mickey and I, but somehow you pulled it off. With this caliber of a heavily academic background in my parents, scientific curiosity came to my sister and I naturally from an early age. I was blessed to have a sister of similar age to grow up alongside, though we have always had the most epic fights, probably as a result. She is one of the most out-going people I know, and it goes without saying that she is incredibly smart- I am very proud of her accomplishments and am excited to see how her new career unfolds.

The extended family also held a strong academic background. All of my grandparents, uncles, aunts, and cousins have shown a love for education. Chandan Kaku and Nandini Kakimoni have been especially supportive throughout my life. Their love for their children, Paroma and Chandrima is inspiring by itself. I am especially excited to see how Paroma's career unfolds because she has often come to me for advice- hopefully some of it is useful. My parents also kept the company of families of similar backgrounds that had an indelible impact on my childhood. To the Mashis and Kakus of the Chaudhury family, the Ali family, the Banerjee family, and the Sengupta family, I thank you all for the countless hours of baby-sitting and for the role modeling you did for me in my early life. To the kids of these same families (Fariha and Naomi, Pia and Shayan, Sandip, Priyanka, Sonali and Milan), we are not of the same blood but it sure does feel like it sometimes, and I think we have seen that especially during the tough times. Here is to the good times just around the corner! I need to thank my de-facto older brother Sid Chaudhury (also Monisha and Soraya) for being an excellent role model through my life as a brother, scientist, husband, and now a father. I am glad to have had you nearby for all these years. Along those same lines, it is great that we have Dr. Rupsa Boelig (also Dr. Matt Boelig, Simon and Maya) and Aurelia Chaudhury (also Prof. Kunjapur) in such close proximity- maybe we can convince some of the other ones to join us nearby.

Sid encouraged my application to the Johns Hopkins University, which brought about my transition from adolescence to adulthood. In the Lazear-Jennings dorm, I met Lawrence Wei (and Sandra), Paul Park, and Antonio Petrozzino (and Christine), some of my closest friends to this day. In the Beta Theta Pi fraternity, I found brothers in Dr. Ian McCue (and Jessica), Dr. Neil Neumann (and Jackie), Steve Matsumoto (and Jen), Paul Nunley (and Caitlin), John Clarke, Dan Saragnese (and Leyla), Dan D'Orlando (and Sarah), Nate Bates (and Bronwyn), David Bobart, and Terry Casey (I know I am missing a few of you). Many of them went on to pursue higher education at the same time I worked through my Ph.D., and their companionship was very important to me. __Kai__. I am lucky to still be in touch with others I met while at Hopkins along the way- Sonia Sarkar, Chris Pae, David Lu, Dr. Vikram Rajpurohit, Muksit Jamil, Chris Belkas, Dr. Tegan Feehery, Dr. Monica Berrondo, David Dolgin, and Kamini Balaji, among others. I look forward to our next exotic travel destination!

At some point during my time at Johns Hopkins, I became disillusioned with the coursework and research opportunities in the biomedical engineering program. I sought out research in the defense world instead, where I had always maintained a keen interest. I found myself in Prof. Ramesh's office asking for a job during the spring semester of 2007 as an undergraduate research assistant. I had cold-emailed him to set up the meeting and sat in front of him, telling him about my interest in material failure for defense applications. He was surely perplexed as I was pursuing a degree in biomedical instrumentation, but he probably had better things to do with his time than to scrutinize an undergraduate too carefully and instead allowed me work in the lab. It was there that the seed of this educative endeavor was planted.

In the lab, I worked with Prof. Reuben Kraft, Prof. Shailendra Joshi, Dr. Brian Schuster, Prof. Rika Wright, Prof. Jamie Kimberly, Prof. Emily Huskins, Dr. Cyril Williams, Dr. Cindy Byer, Dr. Nitin Daphalapurkar, and Prof. Jessica Muelbroek-Fick. These post-docs, graduate students, and engineers inspired me with their dedication and elbow-grease, but also demonstrated the power of bonding over sports and social events. They showed me that the Ramesh lab is a family where we always look after each other. Upon graduating, I moved to the US Army Research lab with a good portion of this family, and later rejoined the Ramesh lab to pursue this doctorate. At this point, I must thank Prof. Ramesh for his guidance throughout the past decade-plus. His love for science and attention to detail was and is always inspiring to me. To this day I am still captivated when I hear you speak, and I'm sure I will continue to learn from you going forward. You taught me a lot professionally and personally since 2007. That is a very long time.

Between undergrad and graduate school, I had the opportunity to delve deep into defense work at the US Army Research Lab. I'm very grateful to Dr. Brian Schuster, Dr. Jim Newill, Dr. Lee Magness, Dr. Reuben Kraft, and Tyler Ehlers for their guidance and mentorship there. I'm very appreciative of my connection through Army Research Lab and through the Ramesh Lab to Dr. Jim McCauley and Dr. Tim Wright- these two gentlemen are one heck of a scientific one-two punch, and both serve as career role-models to me. Thank you, Jim for going to bat for me a few times during the SMART scholarship application process, without which this work would not have been possible. I had the pleasure of meeting Prof. Rebecca Brannon around this time, and her quirky obsession with accuracy of definitions has stuck with me. I thank her for her help with the scholarship application as well. Dr. Rich Becker and Dr. Jeff Lloyd have served as excellent collaborators since that time, and I look forward to working together in the future.

During this time I got married and gained amazing in-laws in Maria, Doug, and Mark as a result. I am always impressed by Maria's resilience regardless of the situations she faces, and am grateful for the unconditional love she has shown me over the past decade. I'm especially thankful to my brother-in-law James for keeping me young. We'll break open one of those board games one day.

Once I returned to the Ramesh lab for my Ph.D, I was again a part of the Ramesh lab family. To the lab members I had the pleasure of working alongside, the honor was truly mine. Postdocs Dr. Lukasz Farbaniec, Prof. Sarah Bentil, and Prof. Kavan Hazeli have proven to be excellent collaborators and researchers in their own right. I am happy to still be in touch with graduated students: Kimmie Andes, Dr. Andy Tonge, Dr. Adam Fournier, Dr. Charles El-Mir, and Prof. Fatma Madouh. Dr. Vignesh Kannan, Dr. Meng Zhao, and Dr. Andrew Leong deserve special mentions for the co-authoring, the sports, the eating, the climbing, the proofreading, and of course the heavy workouts. The nightly debauchery with Prof. Justin Wilkerson, Dr. Neha Dixit, Prof. Jamie Hogan, Matt Shaeffer, and Andrew Robinson certainly hold the honor of being some the best years of my life- here is to many more!

To the current lab members- Jason Parker, Gary Simpson, Adyota Gupta, Sakshi Braroo, Dr. Qinglei Zeng, Dr. Weixin Lee, Connor Bradfield, and Alex Sun, I have loved all the time we have spent together and look forward to seeing your accomplishments as you continue your careers. Dr. Minju Kang has proven to be particularly trustworthy; I entrust her with keeping me from falling from great heights on a nightly basis, and she has not disappointed yet! You have all exposed me to such a wide variety of scientific topics, for which I am thankful.

The HEMI support staff has been crucial to my efforts here, particularly Matt Shaeffer, Katie Vaught, Bess Bieluczyk, Victor Nakano, and Scott McGhee. I know we sometimes butted heads on resources and cleanliness, but this is a symptom of your excellence! The collaborations with Milad Alemohammad, Prof. Mark Foster, and Dr. Bryan bosworth have been most fruitful. Bryan and Mark have been exceptional teachers and collaborators- we're not done yet! Thank you to Dr. Nick Krywopusk, Suhas Eswarappa Prameela, Prof. Tim Weihs, Dr. Ravi Shivaraman, and Hao Sheng for providing me with processing and materials science assistance throughout this journey, I look forward to future collaborations. Outside of Johns Hopkins, I have to thank Dr. Will Bassett, Dr. Will Shaw, and Erin Nissen from the Dlott lab at University of Illinois, Urbana-Champaign for their assistance in developing the facility described in this work. At the department of energy, I must thank Dr. Joe Zaug and Dr. Dan Dolan for always going out of their way to answer my questions. At Marquette University, I have to thank Dr. Peter Sable and Chris Johnson from the Borg lab for keeping conference attendance fun.

The lessons from Ramesh Lab students and post-docs of old about taking a break from time-to-time did not fall on deaf ears, and the people who joined me from the department (perhaps too frequently) deserve mention. I am grateful to the students from the Ghosh, Hemker, El-Awady, Nguyen, Wang, Graham-Brady, and Kang labs. From sports, to movies, to sharing meals, to traveling, to crawling through bars, I must thank Matt Vaughn, Morgan Kuczler, David Eastman, Gary Lin, Nicolas Venkovic, Koroush Shaba, and Steve Lavenstein. I have had a great time exploring the world alongside Gianna Valentino, Tracy Ling, Anu Kaushik, and Harsh Singh. Here's to the group that doesn't exist: George Weber (and Laura), Mattia Almansi, Mohamad Mohamad, Deniz Ozturk, and not Max Pinz.

I am very grateful to my thesis committee for taking their time to review my work and provide feedback. Professor Mark Foster has been invaluable to conducting the work in this thesis, and I look forward to developing and employing further novel diagnostics for shock and impact physics investigations with his help. Dr. Mukul Kumar generously agreed to sit on my committee with short notice. His body of work is very impressive and his current research directions into laser shock at the Dynamic Compression Sector stand at the forefront of shock physics research. I thank them both for agreeing to be on my committee, and look forward to any opportunities we have to collaborate going forward.

I have saved the best for last- Amy made it all possible. Life so far has been easy because I have you at my side, and I look forward to more fruitful collaborations. I could not undertake this journey without you- well it was your idea to do all this anyway...

Thinking back on all of these life experiences that led to this multi-day polishing nightmare, clearly the people who supported me and mentored me were the most important aspect of this entire endeavor. The journey with these people is much more valuable than the end. Their efforts should not have been made in vain. I will press on.

Table of Contents

List of Tables

List of Figures

Chapter 1

Introduction

1.1 Motivation

"Unleash us from the tether of fuel."

– Gen. James Mattis, 1st Marine Division, the drive to Baghdad, March 2003[1]

Protection materials must withstand rapid and intense loading conditions to preserve life, yet be cost effective to produce and field. They must perform at strain rates between 10^4 to 10^7 s^{-1} in military applications (these rates are getting higher as directed energy weapons and hypervelocity projectile launchers are entering service [1]). In-situ observations of the deformation and failure events are extremely difficult at these rates. This design envelope necessitates the development of research techniques at the forefront of multiple disciplines in order to develop materials with improved dynamic performance.

Vehicle armor applications always benefit from lighter structural materials to reduce fuel costs. Here magnesium and its alloys present a material system ripe for exploitation owing to their high specific strength. Magnesium is interesting because it features deformation mechanisms with widely varying activation thresholds and preferential directions with respect to the material crystal structure. The drawbacks come when considering manufacturing costs. Though Mg is a metal with high abundance, it has low formability and ductility owing to deformation asymmetries. Different strategies are being developed to control these effects through alloying and control of material texture [2]. During spall failure, an armor that might initially stop an incident penetration event may develop a region of high tensile stress within the armor after the impact event, generating and launching fragments with significant velocity into whatever the armor is protecting. We explore the dynamic tensile failure of Mg alloys under spall in this work.

In the field of personnel body armor, advanced ceramics have overtaken metals owing to their high hardnesses that can blunt and erode incoming projectiles, and observed rate-dependence (faster-is-stronger) [3]. Alumina, silicon carbide, boron carbide, and other systems are at the forefront of hard personnel armor, but boron carbide offers the highest specific strength (strength-to-density ratio), a useful feature when armor weight directly correlates to person's willingness to wear the armor itself [4]. Krell and Strassburger [5] have reported on the difficulty of correlating material properties, such as strength, stiffness, or fracture toughness, to the protection capacity of various advanced ceramics. Links between performance and properties are often contradictory, making material design very challenging. Beyond material properties, past investigations rarely consider the effect of the microstructure on the performance of the ceramic, so we examine that link in this work.

Direct explosive loading and light gas or powder-driven gun experiments are the conventional methods employed in high rate failure studies for protection materials like those mentioned above, and have the benefit of decades of research in controlling the impact conditions and improving data collection methods. These methods can achieve peak pressures up to several tens of gigapascals while maintaining good planarity and under a milliradian of impact tilt angle [6]. These traditional approaches do have some drawbacks: they require dedicated explosive or gun facilities and are risky to perform. The experiments tend to be expensive and time consuming, so experimental throughput is usually low. Finally, specimen recovery for post-mortem analysis requires special care because of the high amount of kinetic energy in each experiment [7]. The development of an alternative loading technique with lower kinetic energy but similar energy densities, impact velocities and strain rates presents an opportunity to improve experimental throughput relative to the standard methods.

Laser driven approaches have become an important tool to access similar or higher strain rate regimes in the past several decades. As early as the 1970s, researchers used facility lasers to generate stress and shockwaves in matter through direct tamped ablation to develop high pressures and strain rates for fissile material initiation studies [8]. When using pulsed lasers, these approaches offer high power, short duration loading that can achieve the requisite ultra-high strain rates without excessive kinetic energy. The laser ablates a region of material, causing plasma driven pressurization or acceleration depending on the experiment configuration, and can do so with limited set-up time between experiments, improving experimental throughput. We leverage such an approach in this work, and consider two material systems to study.

In this thesis, we first describe the development and validation of a laser-driven impact facility that can achieve the velocities and strain rates in the "lower-hypervelocity" regime yet has high experimental throughput. Next, we use the laser-driven shock facility to interrogate the spall failure of AZ31B and Mg-9Al Mg alloys and the brittle fragmentation of boron carbide. The implications of the work can be extended to other high rate failure situations such as automobile and aircraft strikes, micro-meteoroid impacts, and explosive loading, though we undertake these studies with a particular emphasis on protection materials in the defense sphere.

1.2 Protection Materials

In this section we describe two interesting protection material systems that we examine using the laser driven apparatus, magnesium alloys and boron carbide.

1.2.1 Magnesium Alloys

The attractiveness of magnesium and its alloys as a structural material lies in its high specific strength and low density (1.74 g/cm^3), with Mg being nearly a third less dense than aluminum. Mg is thus an ideal choice for lightweight vehicle applications but has also found applications as a structural material in tooling and electronics [9]. As a potential material for protection applications, Mg must also be easily formed and resistant to ballistic penetration. There are significant challenges along the formability and penetration resistance fronts where Mg often exhibits brittle failure under low forming strains [2], and shows half the penetration resistance [10] in comparison to Al alloys, respectively in examples of the common AZ31B Mg alloy.

Dislocation slip, the movement of a line defect in the crystal structure of a material, is the primary mechanism for irrecoverable (plastic) deformation in metals with body-centered and face-centered crystal structures. In order for dislocation slip to occur, the metal must be subjected to a shear stress on the slip plane in the slip direction (the combination of which comprises a slip system) that is greater than the critically resolved shear stress (CRSS). Hexagonal-close-packed materials such as Mg and Ti feature low-symmetry crystal structures, which have an effect on the CRSS for each slip system in the material. The ratio between the longest axis and the two shorter axes, the c/a ratio, can introduce a wide variance in CRSS for slip systems with different directions. At least 5 independent slip systems are necessary for general uniform non-brittle deformation [11], but the primary slip system (basal $\langle a \rangle$, $(0001)\langle 11\bar{2}0 \rangle$, shown in Fig. 1.1a) in Mg with the lowest CRSS has only two independent modes, so other systems need to be activated.

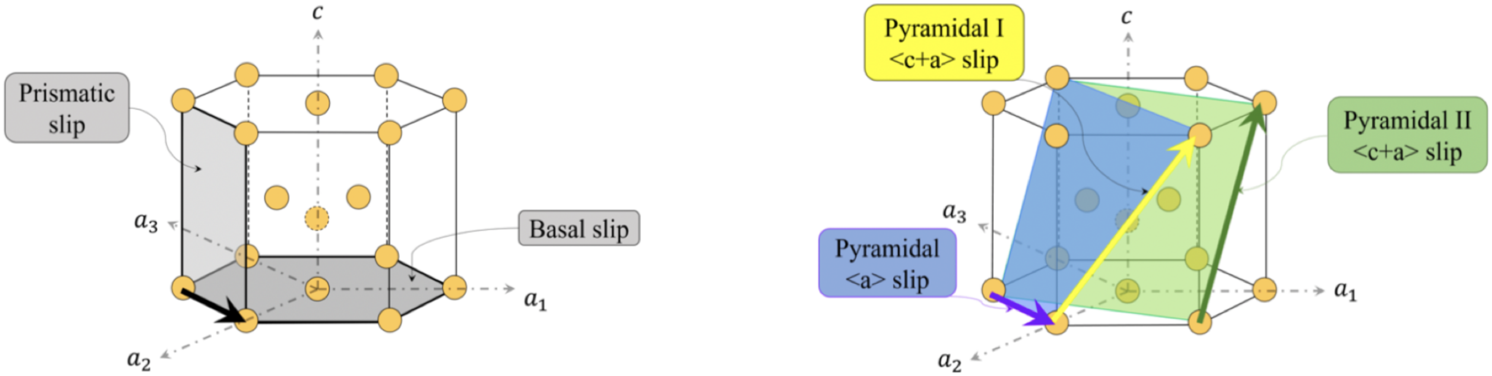

(a) Basal and prismatic slip systems.

(b) Pyramidal slip systems.

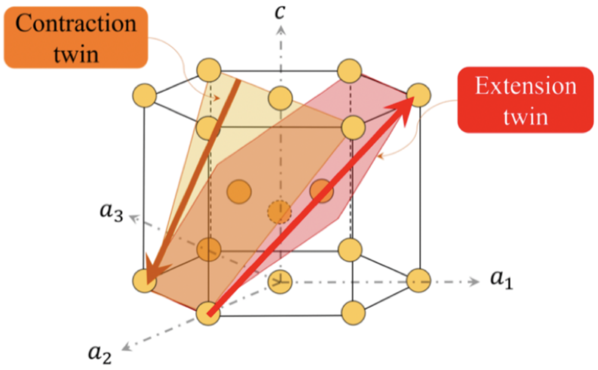

(c) Deformation twinning systems.

Figure 1.1: Mg dislocation slip and deformation twinning direction schematic. (a) Low CRSS basal and prismatic slip systems. (b) Pyramidal slip systems. (c) Extension and contraction twinning modes. Reprinted from Kannan [12].

The next lowest CRSS is an order of magnitude higher for shear on the basal plane [13] and provides two further modes (prismatic $\langle a \rangle$, $\langle 11\bar{2}0 \rangle \{1\bar{1}00\}$ shown in Fig. 1.1a). Pyramidal $\langle a \rangle$ slip offers four independent slip systems equivalent to the four from basal $\langle a \rangle$ and prismatic $\langle a \rangle$ slip ($\langle 11\bar{2}0 \rangle \{10\bar{1}1\}$ shown in Fig. 1.1b). Pyramidal I and II $\langle c + a \rangle$ slip systems allow for shear on non-basal planes and feature a nominally 30 percent higher CRSS than prismatic $\langle a \rangle$ slip ($\langle 11\bar{2}3 \rangle \{10\bar{1}1\}$ for I and $\langle 11\bar{2}3 \rangle \{11\bar{2}2\}$ for II, shown in Fig. 1.1b). Pyramidal slip should provide the five requisite systems, but is the most difficult to activate, so deformation twinning is typically required to accommodate general plasticity.

In deformation twinning, the parent crystal lattice is reoriented by shear to develop a mirror plane between the parent and twinned lattice [14]. Unlike in the case of dislocation slip, deformation twinning is directional, or polar, and can only operate in the one direction. Tension along the $\langle c \rangle$ axis of the lattice activates extension twinning ($\langle 10\bar{1}1 \rangle \{10\bar{1}2\}$ shown in Fig. 1.1c) while compression along the $\langle c \rangle$ activates contraction twins ($\langle 10\bar{1}\bar{2} \rangle \{10\bar{1}1\}$ shown in Fig. 1.1c). Extension twins have a much lower critical stress and are more prevalent in experimental observations [13]. The polarity of both mechanisms introduces what is called a tension-compression asymmetry. The variance in critical stress required to activate different twinning and dislocation slip systems imposes strong plastic anisotropy in the system, making the material system quite intriguing to study.

The anisotropy in deformation mechanisms has been fairly well characterized in Mg single crystals, but single crystal metals are not feasible for mass production. Instead, typical processing of Mg first consists of alloying with other elements for corrosion resistance and solution strengthening, and then rolling and/or extruding the material to form sheets for structural use. The resulting microstructures are polycrystalline to exploit strengthening from introducing grain boundaries (e.g. Hall-Petch strengthening). Rolling tends to introduce strong basal texture where the majority of grains in the material have their $\langle c \rangle$ axis aligned along or near the sheet normal direction [15]. Solid solution strengthening of Mg alloys sometimes also introduces second phase particles into the alloy matrix that might increase strength but also may introduce failure nucleation sites in the material.

The consequence of the strong texture in polycrystalline Mg is a continuation of plastic anisotropy. Under tension in the direction of the sheet normal, in the direction parallel to the $\langle c \rangle$ axis (or equivalent compression in the direction transverse to the sheet normal by Poisson effect), extension twinning is activated with a very low CRSS in the majority of grains, contributing to a low yield strength. Under compressive loading along the sheet normal, most grains in the material can only contraction twin or can undergo pyramidal $\langle c + a \rangle$ slip, both mechanisms with high CRSS, so yield strength is high in this case. The texture induced anisotropy extends into failure of Mg and alloys, where ductility depends similarly on loading orientation [16]. To this end, mitigating the strong texture through various processing methods is one of the primary methods to diminish the plastic anisotropy.

In the case of low rate loading (less than 10^0 s^{-1}), the failure of magnesium and alloys typically occurs as brittle fracture in shear modes [17]. Though there is some evidence of slight differences in peak stresses at failure owing to anisotropic work hardening from increased extension twinning in certain orientations, failure strains are largely not orientation dependent [18]. Dynamic failure (more than 10^3 s^{-1}) of Mg and Mg alloys tends to depend more on the the microstructure in the presence of large second phase particles [19]. For Mg single crystals in the absence of such defects, the dynamic tensile strength at ultra-high rates (10^5 s^{-1}) is controlled by cracking at twin boundaries and shear bands in the material or through void growth and coalescence at regions of high tension [20]. Localized failure from shear banding is associated with the regions just surrounding the primary interaction zone between a target and the impactor [10], and void mediated failure modes (associated with spall failure) are of critical importance in designing for protection against ballistic threats [21].

Gas gun driven plate impact is the conventional method for studying dynamic tensile strength and failure of Mg and Mg alloys [22, 23, 24, 20], though recent studies have employed laser driven compression approaches [25, 26]. We demonstrate the laser-driven compression approach for high throughput spall strength testing in Mg alloys to achieve higher strain rates than commonly found in the literature, but to also impart less kinetic energy in the specimens to aid in recovery analysis.

1.2.2 Boron Carbide

The strength of brittle solids is dominated by the behavior of cracks. Under low rate conditions, global failure initiates at the weakest point of the material, i.e. at the defects or flaws (e.g. inclusions, grain boundaries, pre-existing micro-cracks or porosity, and surface flaws) in the material that are the largest (and so most likely to be activated during loading). When the loading rate is increased past the speed of growing cracks in the material, more defects can initiate failure concurrently, necessitating an understanding of the entire defect distribution to better grasp the failure threshold. Under impact conditions of increasing velocity, experimental measurements have generally shown an increase in strength with increasing strain rate, with some studies relating the compressive strength of the material to the defect distribution of the material with excellent correlation [27].

Boron carbide is an interesting advanced ceramic due to its very high specific strength and low density (2.52 kg/m^3 with strength in the tens of gigaspascals as shown in Fig. 1.2). The high hardness of boron carbide makes it ideal for use in abrasive powders and coatings as well as for ballistic protection, while the low density of the material makes it ideal for nuclear applications [28]. The material is also seeing use as a semiconductor in extreme environments. In addition to the unique light weight of the material, there is an interesting drop in impact resistance beyond some critical loading condition [29](some authors suggest an unloading shearing threshold [30]). This drop in ballistic performance and post yield softening is attributed to a process called “amorphization” and has been explored extensively in the literature with both experiments (Kolsky bar [31, 32, 33], indentation [34], ballistic impact [29], and direct laser shock [35] among others) and numerical simulations (density functional theory [30, 36], and finite elements [37]).

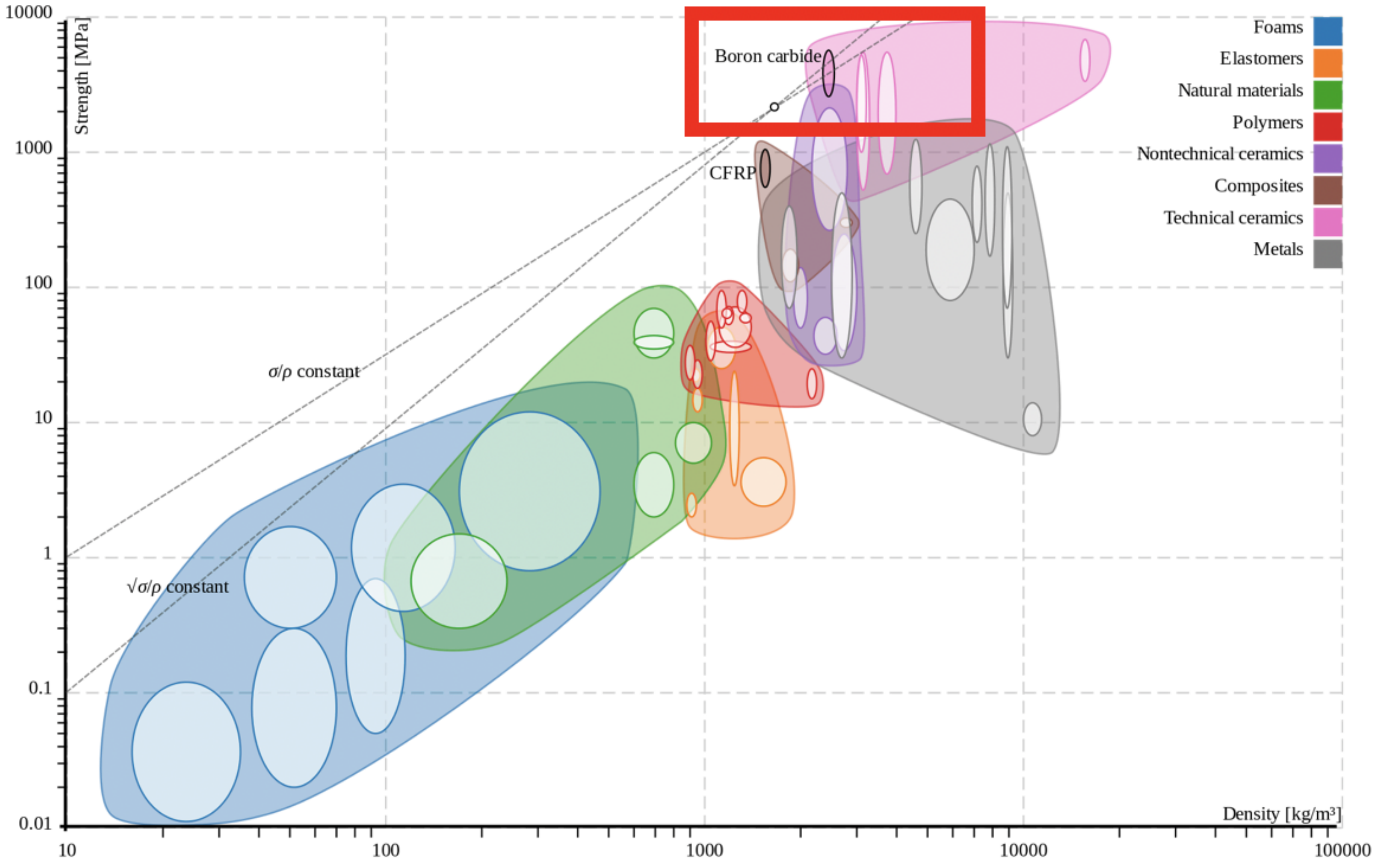

Figure 1.2: Ashby chart comparing yield strength and density of various materials, with boron carbide highlighted. Boron carbide exhibits extremely low density with respect to its very high hardness. Reprinted from wikimedia commons.

Two processing routes are commonly employed to produce boron carbide while achieving adequate densification- (1) hot pressing, and (2) pressureless sintering. Oftentimes additives, such as silicon carbide, alumina, other ceramic powders and graphite, are introduced to improve densification [38]. The chemical reactions from mixing the additives with the bulk powder during processing can produce precipitates and other second phase particles throughout the microstructure. These material defects, in tandem with pores from lack of densification, can act as failure initiation sites during fracture. There is then a competition between densification to improve performance and introduction of second phase inhomogeneities that can potentially detract from performance.

In this thesis we explore the fragmentation of boron carbide. The fragmentation of advanced ceramics is typically studied by employing a dynamic loading device such as a Kolsky bar for 10^3 to 10^4 s^{-1} strain rates [39, 32, 33], or through ballistic impact methods for higher rates [5, 40, 41, 42, 43]. In both cases, the kinetic energies imparted to the specimens are high enough that recovery of fragments after the experiment can be difficult. Thus laser driven methods present an opportunity to design an experiment with complete fragment recovery.

1.3 Laser-Driven Shock Compression

Laser driven approaches offer better throughput by way of safety and ease of specimen recovery via reduced kinetic energy and short loading duration when compared to the conventional explosive or gun driven techniques. Although investigators used facility lasers to generate stress and shockwaves in matter through direct tamped ablation in the 1970s [8], shock studies were not explored in earnest until the 1980s as the energy density of laser systems advanced [44]. These approaches typically used pulsed lasers with high peak power and short pulse durations to produce waves with time durations between several nano-seconds to femto-seconds to generate the desired loading directly on a specimen of interest (Fig. 1.3a), in contrast to the microsecond durations from gun and explosive driven experiments [45, 46, 47]. Direct ablation has continued to see use in generating extreme conditions for equation-of-state characterization [48], spall studies [49], and materials science investigations in extreme environments [35].

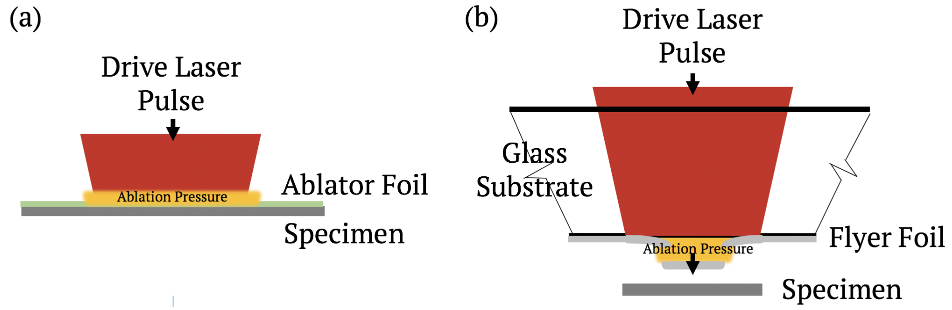

Figure 1.3: (a) Schematic of direct ablation shock compression experiment. (b) Schematic of laser driven flyer launch. Both laser-driven shock compression techniques rely on ablation pressures to impart momentum on the specimen.

In contrast to direct ablation, laser-driven micro-flyer launchers (the approach in this work, often denoted as mini-flyers, LDMFP or LDMF for laser-driven miniature flyer plates, see Fig. 1.3b) have featured a variety of apparatus configurations throughout the decades, but all rely on pulsed laser ablation of a confined flyer. The ablated region expands rapidly, generating a pressure between the flyer and its confinement that accelerates the flyer towards a target specimen. Differences in laser characteristics such as duration and peak power will affect the geometries of the launched flyer, but the operating principle remains the same in each case. The method was pioneered by Ripin et al. [50] and Obenschain et al. [51] in the 1980s as a possible method for fissile material implosion nucleation using a 3 ns 3-4 kJ 1064 nm laser pulse to accelerate a 10 micron thick flyer to 10 km/s. Later studies brought the concept to the lab-bench by using smaller pulsed lasers but with improved coupling to the flyer, either through interfacing with the flyer with fiber-optics, or through adhering the flyer to a confining or tamping window [52, 53, 54]. Flyer velocities and thicknesses with these bench-scale systems tended to be lower due to the decrease in available laser energy to drive the flyer [55].

Shock experiments require reasonably planar waves to impart uniform loading. It quickly became apparent, as LDMFP systems were developed, that flyer planarity was directly correlated to spatial uniformity of the driving laser. Initial attempts to spatially homogenize the driving laser included coupling to fiber-optics and manipulating the fiber to reduce intensity hot-spots[53]. Most recently, Dlott and coworkers have developed a lab bench scale flyer launcher that achieves lower hypervelocity planar launches (1 to 4km/sec) with fairly thick flyers (25 to 100 μm). Their system was developed for Hugoniot characterization and initiation of reactive materials and utilizes diffractive homogenizers to generate a “flat-top” driving beam. Our approach is heavily inspired by their efforts [56, 57, 58, 59, 60, 61]. There are also current efforts to launch spherical projectiles to mimic ballistic experiments at the micro-scale [62, 63, 64].

Advances in LDMFP, by way of improved flyer planarity and more granular diagnostics, have encouraged use of the technique for spall studies where the shock loading can test the dynamic tensile strength of a specimen, but the open literature does not suggest strong adoption of the method in comparison to conventional gun usage. The first LDMFP spall studies were conducted by Paisley et al. in the early 1990s. They conducted spall experiments on 25 μm thick Al, Cu, Mg, and Stainless Steel foils with 10 μm Al flyers propelled up to 5 km/s by a fiber coupled 3.1 J bench-top pulsed laser [65]. With VISAR (Velocity Interferometer System for Any Reflector) velocimetry at their disposal, it was straightforward to obtain the nanosecond time resolution necessary for experiments on such thin samples with the short shock durations from the thin flyer [66, 67, 68]. They later lens-coupled their drive laser to propel thicker flyers (up to 50 μm) and performed limited modeling to compare between the LDMFP and gas gun experiments, showcasing the higher achievable strain rates with the technique [69]. In 1999, Robbins et al. [70] performed spall experiments with a lens-coupled system to propel 50 μm thick Cu foils to impact 100 to 250 μm thick Au foils. They used VISAR to capture the longer spall pulse durations from the thicker flyer, and were able to perform a large number (15) of experiments, illustrating a boon of the method. They followed this up with a 65 experiment study comparing annealed and cold-rolled Cu films thereafter [71]. Paisley et al. brought the method to the powerful Trident laser facility (Los Alamos National Laboratory, New Mexico, USA) to propel much thicker flyers at higher velocities, but many results of their spall experiments are not in the open literature [72, 73, 74]. deResseguier, He, and Berterretche [75] bridged the gap between the large laser facility and common bench-top lasers by using a bench-top 20 J laser to launch up to 250 µm thick Al foils for spall experiments on 500 µm thick Al specimens. They also utilized VISAR to obtain the necessary time resolution for capturing spall data, and found that hydrocode simulations without an inertia driven damage model may not account for stress relaxation owing to activated damage mechanisms in the measured dynamic tensile strength during spall failure. Peralta et al. [76] and Wayne et al. [77] performed a complete spall study on polycrystalline Cu specimens with the flyer launch techniques detailed by Paisley et al. at the Trident laser facility, using careful fractography and hydrocode simulations to analyze their results. The most recent (2017) spall study done with LDMFP is by Wang et al.[78] where a similar apparatus to ours is used to determine the spall strength of Al, Ni, and Cu thin films. They conclude that further improvements to velocimetry are required to verify that the time-line of failure matches the loading history and to reduce sources of error in their measurement.

This search through the literature suggests ample opportunity to improve lab-bench methods in the laser-driven shock compression community. Though each of the above investigations have had to contend with homogenizing their drive beam to make planar loading conditions, there may be simpler and more cost-effective methods. There are only limited studies that look at spall failure with lab-bench methods, and few have been able to achieve the adequate time resolved measurements found in state of the art spall studies conducted using conventional means. Moreover, the strain rate regime of interest in vehicle and personnel protection applications ($\sim 10^6$ s^{-1}) is below the scope of large facility lasers, but is accessible with lab-bench lasers.

1.4 Organization of the thesis

In this thesis we examine the failure modes of the magnesium alloys AZ31B and Mg-9Al, and the advanced ceramic boron carbide. These studies are conducted with a laser-driven micro-flyer apparatus that we fabricated during the course of this investigation, allowing for high impact velocities (up to 2 km/s is presented in this work) and ultra-high strain rates (below 10^7 s^{-1}) to mimic ballistic loading conditions on the lab bench. The boron carbide and Mg alloys exhibit brittle fragmentation and void mediated failure, respectively. We study these phonomena using in-situ laser based interferometry and post-mortem optical, scanning electron (SEM), and tunneling electron (TEM) microscopy where applicable. In some cases, numerical simulations are used to better understand the loading conditions and failure process.

Chapter 2 introduces the laser-driven micro-flyer facility at the Hopkins Extreme Materials Institute at Johns Hopkins. We present the experimental technique and the validation studies undertaken to confirm the loading conditions generated by the technique. Finally we calculate a launch curve for the apparatus that aids in experiment design.

Chapter 3 describes the velocimetry techniques necessary to obtain in-situ velocity records of the failure process. The laser-driven apparatus imparts ephemeral loading, so time resolution is extremely crucial. Our work has led to the modification of conventional photon Doppler velocimetry through component selection and data processing techniques to develop velocimetry that reliably captures data at the requisite time resolution with adequate signal-to-noise.

Chapter 4 explores the spall failure of extrusion machined AZ31B Mg alloys from void growth and coalescence. First we introduce the mechanics necessary to conduct spall studies. We then describe the AZ31B Mg alloy used in the study and present our results. Post-mortem microscopy using SEM and micro-computed tomography, in addition to analysis of the velocity record, indicates the occurrence of incipient spallation where the material does not completely fail. This feature of the laser-driven technique enables further investigation of the resistance of the bulk material to failure.

Chapter 5 reports on the role of precipitates in spall failure of warm rolled Mg-9Al alloy that is prepared in two forms- (1) fully solutionized without second phase particles, and (2) annealed to form nano and micro-scale precipitates. We begin by introducing the two materials and then presenting the spall data using the laser-driven apparatus. Numerical simulations of the precipitate structure are used to understand the effect of anisotropic plasticity inherent in Mg and its alloys against the role of precipitates during spall failure.

Chapter 6 details our investigation of the brittle fragmentation of boron carbide. This chapter serves two purposes- (1) to first examine the fragmentation response of boron carbide under ballistic loading as expected for a typical application of the material system, and (2) to compare fragmentation between the ballistic case and that generated by the laser-driven technique. After describing the ceramic material and its defect structure and differences between the two loading conditions, we present fragmentation results using both techniques. The hope here is that parallels can be drawn between the two different loading conditions to justify the use of the laser-driven method as a surrogate for ballistic experiments.

We summarize our findings from the work of this thesis in chapter 7. We also suggest possible paths forward in regard to using the laser-driven technique in failure studies, and discuss potential solutions to improve the studied material systems. Appendix A is a manual of operation for the laser-driven micro-flyer facility that includes experiment protocol and data processing protocol. Appendix B outlines the location and organization of all the data used for the investigations herein, and also contains all velocimetry data in a compact fashion for quick reference.

Chapter 2

Laser-Driven Flyer-Plate Facility

Parts of this chapter appear in a research article, Mallick et al. [79], and conference proceeding, Mallick et al. [80]. D.D.M is first and corresponding author for both.

2.1 Introduction

Laser-driven micro-flyer plates offer high velocity (1-10 km/s) loading conditions for shock compression and impact experiments, yet allow a high throughput of tests owing to the small scale of the experiment. The diminished scale of the experiment requires only lab bench-top facilities, improving safety considerations and lowering overall equipment costs. We have already detailed some of the history of direct ablation and laser driven micro-flyer micro-flyer methods in chapter 1 and encourage the reader to review historical details there.

The state-of-the-art launch technique for studies using laser-driven flyers on the lab-bench (for flyers up to 100 μm in thickness) was developed in the past decade by the Dlott group at the University of Illinois Urbana Champagne, allowing for shock Hugoniot measurements of energetic and transparent materials [56, 57, 58, 59, 60, 61]. Our facility is heavily inspired by their efforts and has been constructed with their assistance. To produce a successful impact experiment, an incident laser beam is conditioned through lens optics to produce a laser pulse of a desired duration and spatial profile. The beam duration is on the order of nanoseconds and contains several Joules of energy. The beam then interacts with a confined Al flyer foil of thicknesses between 25 and 100 μm (confined by a transparent borosilicate glass substrate) to ablate a small region. This ablation process creates a rapidly expanding plume of plasma and hot gas that accelerates the flyer away from the confining substrate.

The flyer velocity depends on the standoff distance between the flyer foil and the target specimen. Once the flyer impacts the target, shockwaves propagate through the specimen that are recorded from the back face of the specimen with laser-based interferometry and high speed imaging techniques. Post-mortem microscopy of the impact site identifies the activated mechanisms that lead to failure of the specimen. The flyer geometries and velocities we use are well suited for ballistic impact and spall studies, as we detail in later chapters. In this chapter, we review the laser-driven micro-flyer plate facility at the Hopkins Extreme Materials institute. After reviewing the system, we discuss our approach to beam homogenization to reliably launch good flyers, and then modify a model based on Gurney energy to develop launch curves for our apparatus. Finally, we summarize the facility capabilities.

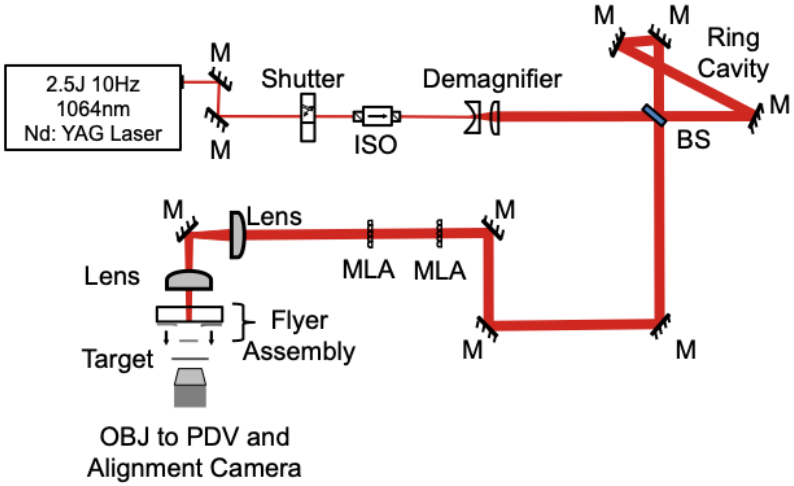

Figure 2.1: System diagram of laser-driven micro flyer-plate launcher. M: Mirror. ISO: Isolator. BS: Beamsplitter.

2.2 Laser-Shock Facility at HEMI

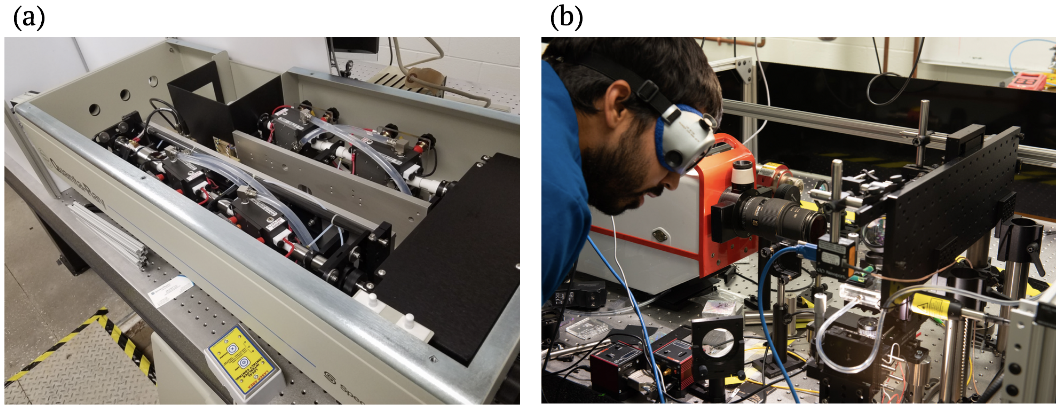

Figure 2.2: (a) Photo of the Nd:YAG laser with the top cover off. (b) Photo of homogenizing optics, diagnostics, and vacuum chamber.

The laser driven micro-flyer facility at the Hopkins Extreme Materials Institute is located in the basement of Malone Hall on the Johns Hopkins University Homewood campus, MD. The facility features the optical system shown in Fig. 2.1 atop a $4' \times 8'$ optical table shown in Fig. 2.2 with overhanging bench space for diagnostic equipment, and two table surfaces for specimen preparation. The core of the laser driven launcher is an incident pulsed laser beam that is conditioned through lens optics to produce a laser pulse of a desired duration and spatial profile. Commissioned in September of 2016, our launching laser is an Nd:YAG pulsed laser (Spectra-Physics Quanta Ray Pro-350) that emits a 1064 nm wavelength pulsed beam with $\sim$10 ns duration and $\sim$13 mm diameter. The laser emits pulses continuously at 10 Hz with $\sim$2.5 Joules of energy per pulse. Flyer launch requires only one pulse from the driving laser, but the laser must run continuously for maximum power output, so a fast shutter mirror (nmLaser, LSTXYW8-1 with CX3000B controller) is used to pick off a single pulse from the pulse train. The shutter system is timed by a delay generator (Berkeley Nucleonics Corp, Model 575) which is triggered from the pulsed laser Q-switch signal and sends a 100 ms open signal to the shutter to open for the next laser pulse. After passing through a magneto-optic isolator (Electro-Optics Technology, 110-10302-0001) to protect the driving laser, the single pulse is spatially expanded with a lens telescope to a nominal 2.5cm diameter to prevent damage of optics further in the drive-train. The delay generator also serves as the trigger system for velocimetry and high speed video diagnostics.

The single pulse is then homogenized in time and space to improve flyer launch (described et seq.) and then focused onto a flyer assembly (Fig. 2.3). This consists of an aluminum foil (Alufoil Inc.) of 25 or 50 μm thickness adhesively bonded (Loctite Ablestik 24) to a 10mm thick glass slide (McMaster-Carr). To further improve flyer uniformity, we machine circles into the aluminum foil using a Clark-MXR femtosecond laser with a translating stage. The laser cuts 1.5mm disks fully through the thickness of the foil with a cut groove width of $\sim$20μm (Fig. 2.4a).

In the current design, specimen coupons must be 3mm diameter disks. To aid in alignment, a 125 μm thick and 3 mm diameter Kapton disk spacer separates the flyer foil from the specimen coupon. The Kapton spacer has a centered 1.5mm diameter through-hole aligned with the cut flyer circles. The hole diameter is the same as the flyer diameter to constrain ablation products for uniform acceleration. The driving laser spot is a 3mm by 4mm rectangle when imaged on the flyer assembly, twice the diameter of the through-hole and the cut flyer, to minimize the chance of misalignment but still provide adequate energy for launch. All of the parts are carefully adhesive bonded. This assembly has the added benefit of ensuring co-linearity between the cut circle flyer, the Kapton spacer, and the target disk (Fig. 2.4a-c). Once the specimen coupon is bonded to the flyer assembly, the entire flyer assembly is placed inside an acrylic vacuum chamber that is pumped down using building vacuum to nominally 75 to 85 percent evacuation, corresponding to 190 to 115 Torr, respectively. The acrylic chamber is used to allow for laser-based diagnostics and high speed imaging, yet remain inexpensive enough to replace panels as they are damaged from repeated impacts and fragmentation.

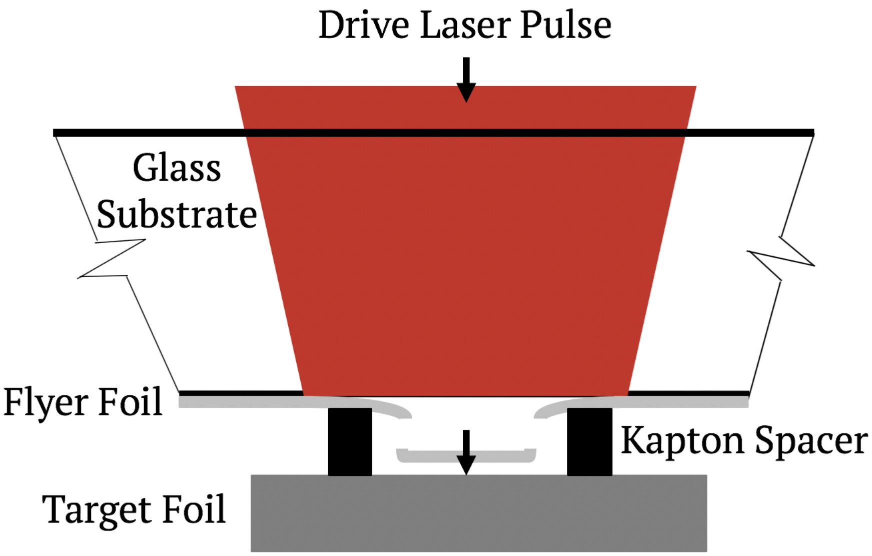

Figure 2.3: Side-view diagram of target and flyer assembly. A 125µm thick spacer separates the flyer from the target disk

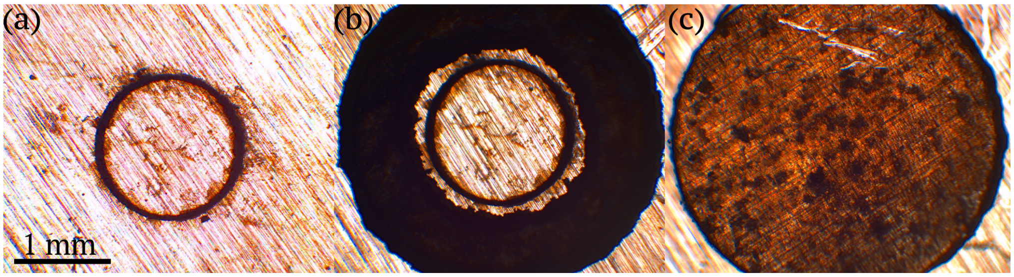

Figure 2.4: (a) Image of femto-second laser cut 1.5mm diam. flyer disk. (b) 3mm outer diameter, 1.5mm inner diameter Kapton spacer placed around the cut flyer before gluing. (c) AZ31B disk glued to spacer, making the final assembly

2.3 Beam Homogenization

If the launching laser pulse duration τ_p is less than the shockwave round-trip time in the launched flyer, i.e. $\tau_p < 2h_{flyer}/c_l$ with c_l denoting the longitudinal wave speed in the flyer material, the ensuing reverberating waves can deform the flyer or cause flyer breakup prior to impact. Following Curtis et al. [60], we employ an optical ring cavity (labeled ”ring cavity” in Fig. 2.1) constructed from a 60:40 beam-splitter (Edmund Optics) and high damage threshold mirrors (CVI Optics) to lengthen the duration of the pulse in time [81] to reduce ringing. The resulting pulse is stretched from ∼13 ns to ∼21 ns and is capable of launching up to 75 µm thick Al flyers without significant ringing in the flyers from drive laser induced shock [80] (scattered light data to characterize the stretched pulse are shown in Fig. 2.5). With the as-received pulse duration from the launching laser and the available optical table space in this facility, the maximum possible pulse duration through employing optical ring cavities will be near the order of the round-trip time in flyers from 25 to 100 µm of thickness. We have successfully launched 100 µm thick flyers with some ringing in the flyer velocity history, but the ringing tends to damp out after the first 100 ns of travel or so. To avoid the effects of the reverberations altogether, flyer thicknesses are held to 25 or 50 μm and we employ standoff distances that impose at least ∼300 ns of flight time between the flyer launch and target impact in the investigations hereafter.

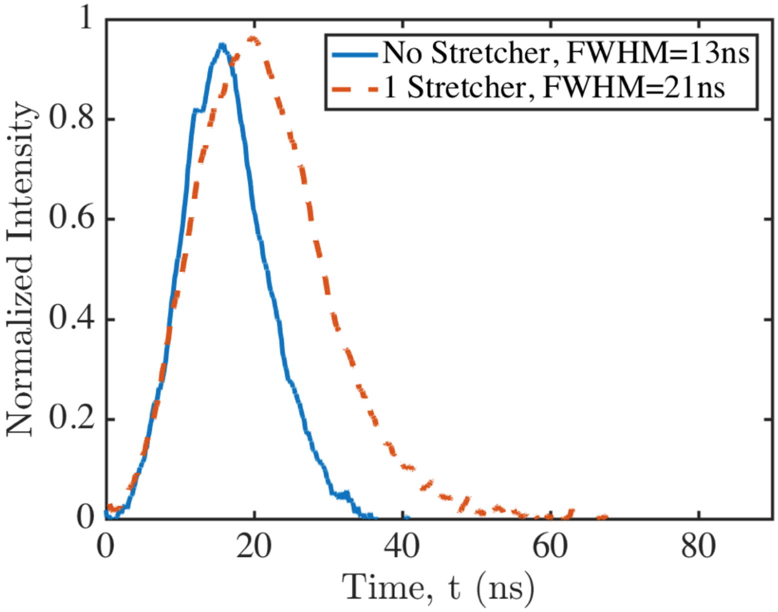

Figure 2.5: Photodiode collected scattered light from optical ring cavity (dashed line) and from the laser without any modification in time (solid line)

Shock compression experiments typically demand planar impacts, so we spatially homogenize the expanded beam with a pair of multi-lens arrays (OptoSigma) in a Kohler integrator configuration [82]. The spatial homogenization assembly operates through discretizing the incident beam (Beam profile after optical ring cavity shown in Fig. 2.6) and superimposing the beam-lets at the image plane (Fig. 2.7a).

Our lens arrays image the homogenized beam as a 4:3 aspect ratio square with the largest dimension as small as several microns and as large as 16mm

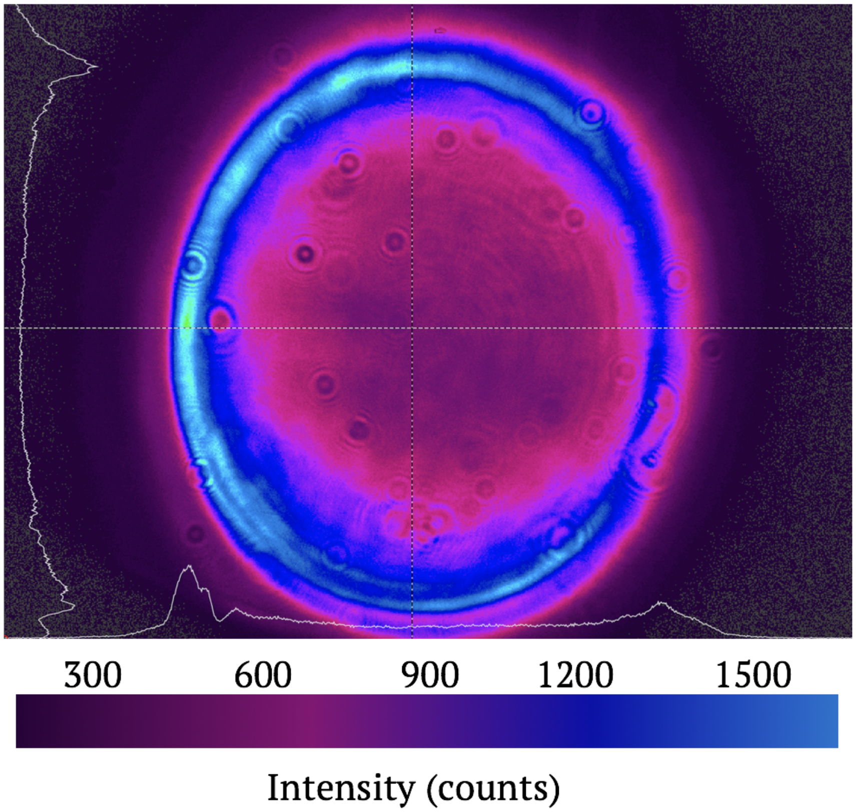

Figure 2.6: Spatial intensity profile of the driving laser pulse after passing through the optical ring cavity shown in a plane view, characterized with a beam profiler (Newport LBP2-VIS2).

as characterized with a beam profiler (Newport LBP2-VIS2) in Fig. 2.7b. The image size D_{Image} is determined by the spacing a_{lens} between the two lens arrays, the focal length f_{LA} of each lens-let, the focal length f_{FL} of the focusing lens, and the size P_{LA} of each lens-let,

$$D_{Image} = \frac{f_{FL} P_{LA} (2 f_{LA} - a_{lens})}{f_{LA}^2}. \tag{2.1}$$

In our experiments, the resulting homogenized image does not exhibit a strong zero order central peak (which occurs in homogenizing schemes that only use one lens system[83]). The homogenized image is of similar quality to those produced by more expensive diffractive optics that operate on similar principles. However, there is certainly room to design the lens array for optimal image size, low divergence angle, and highest Fresnel number for image quality (we note that optic price increases drastically for custom designs). Low divergence angle θ_{div} of the homogenized image is useful for good image quality under high focus, and is given by,

$$\tan\theta_{div} = \frac{D_{Laser} - P_{LA} + D_{Image}}{2f_{LA}}, \tag{2.2}$$

assuming the distance from the array assembly $a_{assy} = 0$, with input laser beam diameter D_{Laser}. Our system has a calculated divergence angle ∼20 degrees, requiring careful flyer to drive-laser alignment to ensure the flyer is in the image plane. A High Fresnel number FN corresponds to a “smoother" homogenized image, where the discretized beamlets have wide Fresnel zones that improve uniformity with input pulse wavelength λ_{drive},

$$FN = \frac{P_{LA} D_{Image}}{4\lambda_{drive} f_{FL}}. \tag{2.3}$$

Our Fresnel number is ∼25, so the driving beam should be adequately homogenized at the image distance f_{FL}. To retain as much fluence as possible, yet to illuminate enough area for a 1.5mm diameter flyer launch, we typically orient the assembly so the homogenized beam has a width of 3 to 4mm.

Despite taking the above steps to homogenize the driving laser pulse, launched flyers have been shown to deform and take on a curved shape

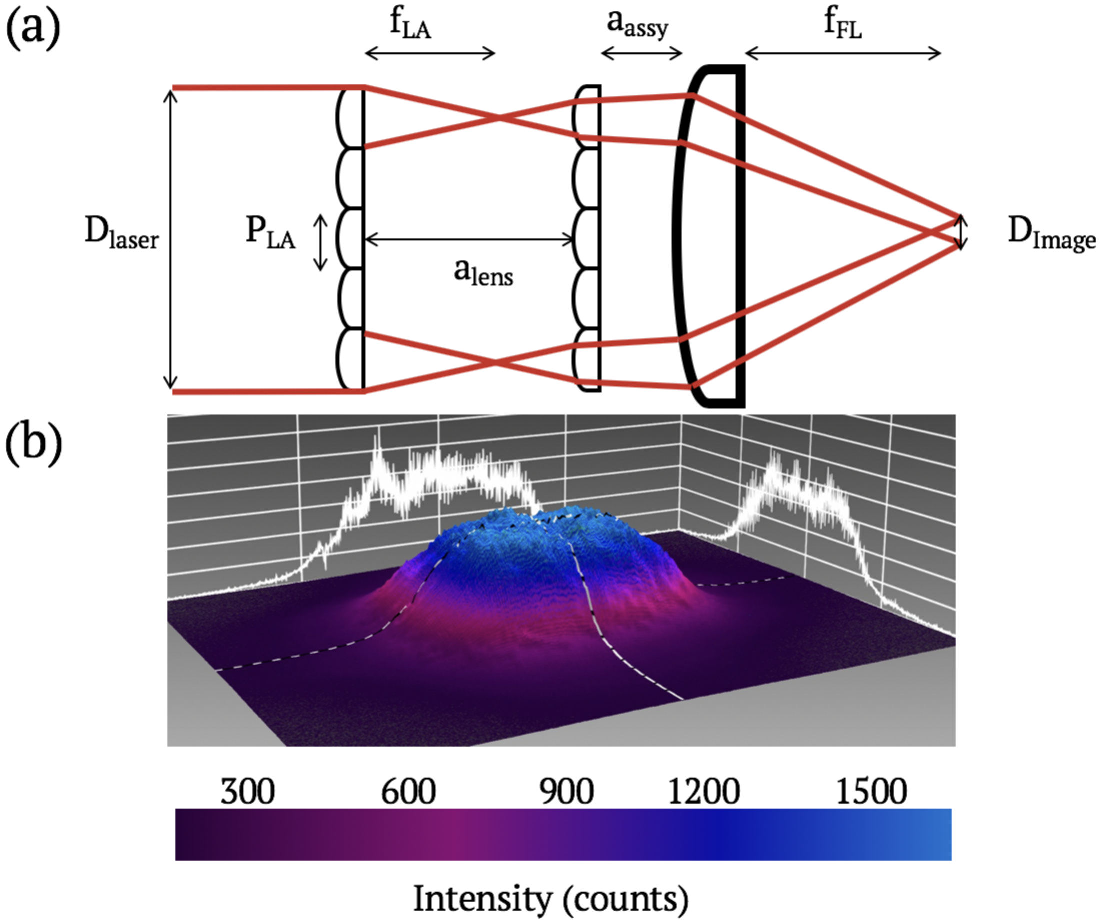

Figure 2.7: (a) Schematic of multi-lens array pair for spatial beam homogenization. (b) Multi-Lens-Array homogenized pulsed laser output at flyer assembly shown in isometric view, characterized with a beam profiler (Newport LBP2-VIS2).

throughout their travel as propulsion products diminish from the edges of the flyer [59] and drag effects take hold in the case of a poorly evacuated experiment chamber. Fig. 2.8b shows several still images from a flyer launch using a 10 MHz high speed camera. The camera shows a side view of the launch process, though the camera is tilted up slightly to get a better view of the femto-second laser cut flyer disk. Radius of curvature measurements made from the high speed imaging stills show excellent planarity for the first 400 nanoseconds of flyer travel, corresponding to $\sim$300µm of flight, after which the flyer begins to deform and take on a curved shape (Fig. 2.9). We note that the slight tilt in the camera will over estimate all reported radius of curvature measurements across the entire time-of-flight.

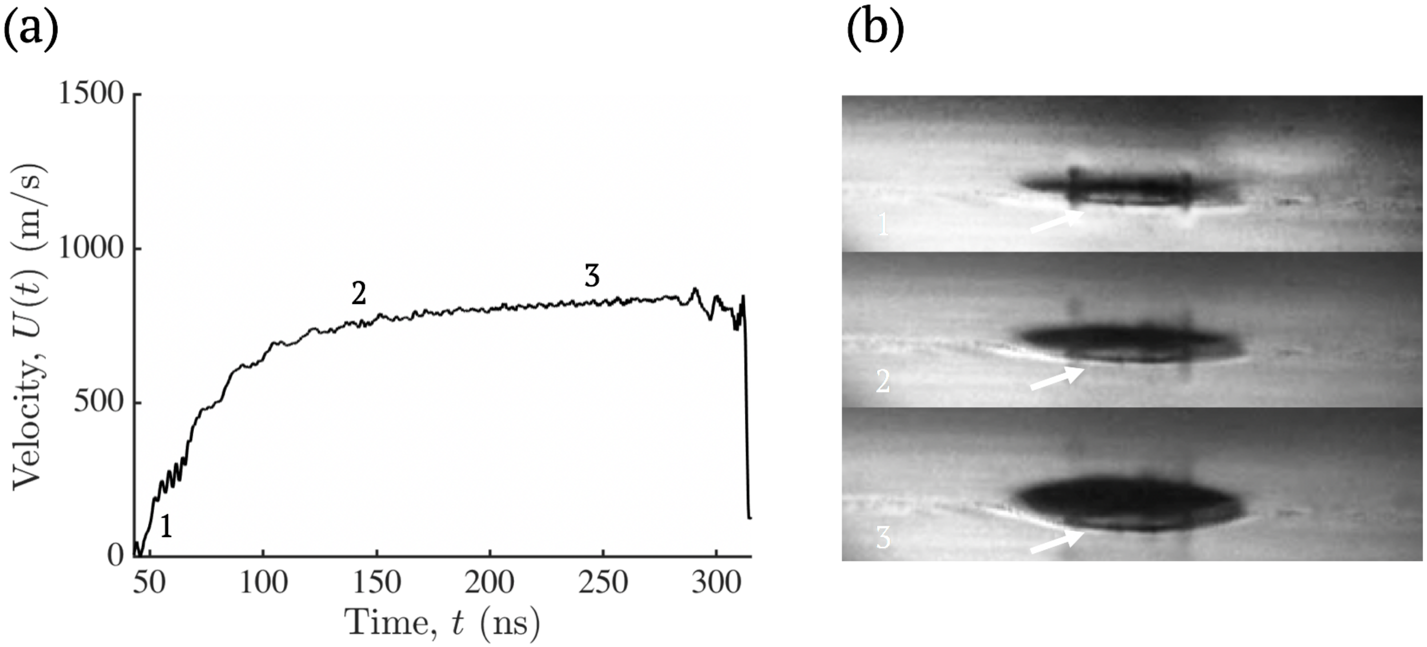

Figure 2.8: (a) Processed velocimetry record of a flyer launch into a glass window to verify flyer planarity at time of impact. (b) 10 MHz high speed imaging of side view of flyer launch. The white numbers correspond to the black numbers in time in the velocity record in Fig. 2.8a. The flyer travel direction is from top of the image to the bottom.

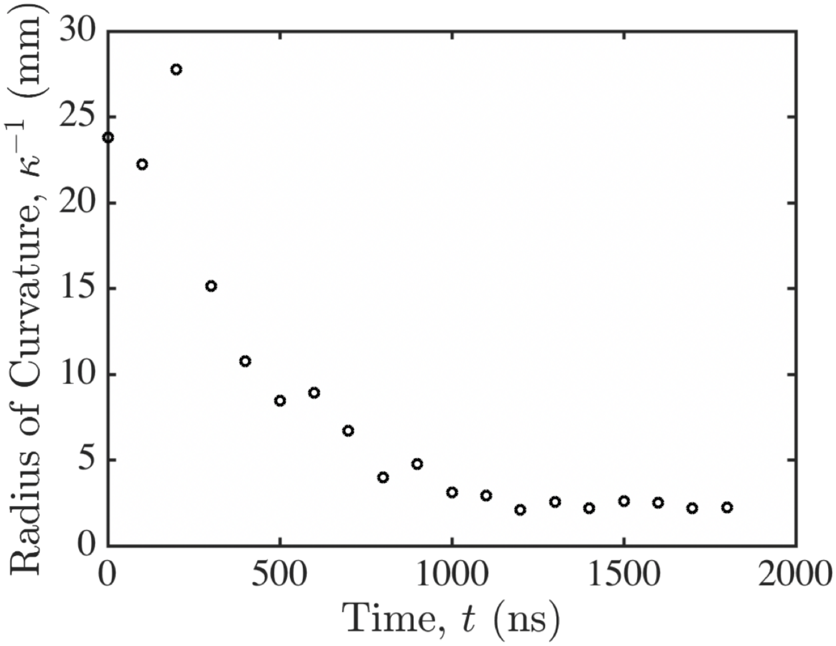

Figure 2.9: Flyer radius of curvature versus time of flight as measured from 10MHz high speed imaging. A higher number indicates a more flat flyer.

2.4 Launch Curve

2.4.1 Launch Model

Laser-driven flyer pioneers Lawrence and Trott [84] developed a simple model for laser-driven flyer velocities. The model applies a Gurney energy analysis, long used in explosively driven flyer plate experiments from the 1940s and onward, to laser-driven micro-flyers. The theory is a simple one-dimensional conservation of energy analysis that compares the available energy in the expanding ablation plume against the sum of the resulting kinetic energy from the flyer and the kinetic energy of flyer material fragments present in the ablation plume itself,

$$\rho h_a \mathcal{E} = \frac{\rho}{2}(h_{flyer} - h_a)U_0^2 + \frac{\rho}{2}\int_0^{h_a}(U_0\frac{h}{h_a})^2 dh, \tag{2.4}$$

with original flyer thickness h_{flyer}, thickness of ablated flyer material h_a, flyer density ρ, launch velocity U_0, and Gurney energy $\mathcal{E}$. Rigid backing of the flyer is assumed for this conservation approach to be valid. Assuming a linear velocity profile for the ablation plume in the final term in (2.4), (2.4) can be solved and then inverted to yield an expression for the launch velocity,

$$U_0 = \sqrt{\frac{\mathcal{E}}{\frac{3h_{flyer}}{2h_a} - 1}}. \tag{2.5}$$

To determine the ablated flyer material depth h_a and Gurney energy $\mathcal{E}$, several assumptions on how much energy gets to the flyer and how much is absorbed into the material thereafter become necessary. We begin by using the laser fluence F_0, an effective absorption coefficient μ_{eff}, a decomposition energy threshold ε_d after which the material becomes ablated and a loss parameter r that accounts for losses between the driving laser pulse and the flyer to estimate the ablated flyer material depth,

$$h_a = \frac{\ln\left(\mu_{eff}F_0(1-r)/\varepsilon_d\right)}{\mu_{eff}\rho}, \tag{2.6}$$

with an effective absorption coefficient derived by,

$$\mu_{eff} = \frac{\mu_a}{1 + k\mu_a\rho\sqrt{\alpha_{th}\tau_p}}, \tag{2.7}$$

using the material mass absorption coefficient μ_a, thermal diffusivity α_{th}, driving laser pulse duration τ_p and fitting parameter k. Finally, we write an expression for the Gurney energy by taking an assumed exponential energy deposition profile using lamberts law, $\mathcal{E} = \int_0^{h_a}(\varepsilon(x) - \varepsilon_d)dx$ with $\varepsilon(x) = \mu_{eff}F_0(1-r)exp(-\mu_{eff}\rho x)$ by Lambert's law, and subtracting the decomposition energy of the flyer material,

$$\mathcal{E} = \frac{F_0(1-r)}{\rho} - \varepsilon_d(1 + \frac{1}{\mu_{eff}\rho h_a}). \tag{2.8}$$

The majority of model parameters are book value material properties identified by Lawrence and Trott [84] (Table 2.1), with the exception of the absorption constant k that is a fitting parameter, and the loss parameter r that can only be experimentally obtained. They employed the model initially to predict the launch velocities of thin flyer foils (25 µm or less) that were launched through a fiber-optic coupling between a 50 mJ launching pulsed laser and the flyer foil with remarkable accuracy. However, the model has not been applied to lens coupled flyer launchers with rigor so we attempt that below.

2.4.2 Launch Velocities for Lens-Coupled Launchers

Curtis et al. [60], Brown et al. [59], and Banishev et al. [61] have published launch velocity data for flyers ranging from 25 to 100 µm over the past

Material Properties [units]	Value
Density ρ [kg/mm^3]	2700
Decompostion Energy ε_d [kJ/kg]	12.0×10^{-3}
Thermal Diffusivity α_{th} [m^2/s]	8×10^{-5}
Absorption Coefficient μ_a [m^2/kg]	4.4×10^{-2}
Absorption Constant k [dimensionless]	0.253

Table 2.1: Model constants used from [84].

decade. They conclude that the velocity insensitivity to transmitted pulse energy suggests launch mechanisms other than flyer material ablation, such as shockwave propagation in the substrate or perhaps ablation of the substrate itself. We can apply the fiber-based launch velocity model to this lens coupled system to understand some of the mechanisms at play. To apply the model to free space lens-coupled systems, we must consider the loss parameter r. In the case of the fiber-optics based launch apparatus, Lawrence and Trott [84] used values between 0.6 and 0.4, depending on the flyer material, to achieve velocity predictions with excellent agreement to data in what were considered state-of-the-art fluences for lab-bench driving laser systems at the time. Easier access to more powerful laser systems in recent years has unlocked a much wider range of fluences (up to and beyond 500 $\mathrm{J/cm^2}$).

Curtis et al. [60] showed that transmission through the transparent substrate in the lens coupled system, likely the most significant contributor to the r parameter in the model, is dictated by damage in the substrate itself. The surface damage threshold on the face of the substrate in contact with the flyer material seems to control the transmittance through the substrate, so the interplay between incident fluence, absorption, transmittance, and damage threshold of the substrate may be optimized to produce higher launch velocities. Above a fluence of $\sim$200 $\mathrm{J/cm^2}$, critical levels of damage develop in the glass substrate where transmittance is reduced to 10 to 20 percent consistently, regardless of glass substrate thickness (Fig. 2.10).

In addition to the varying substrate transmission curve in Fig. 2.10, there are other parameters that introduce loss into the coupling. Lawrence and

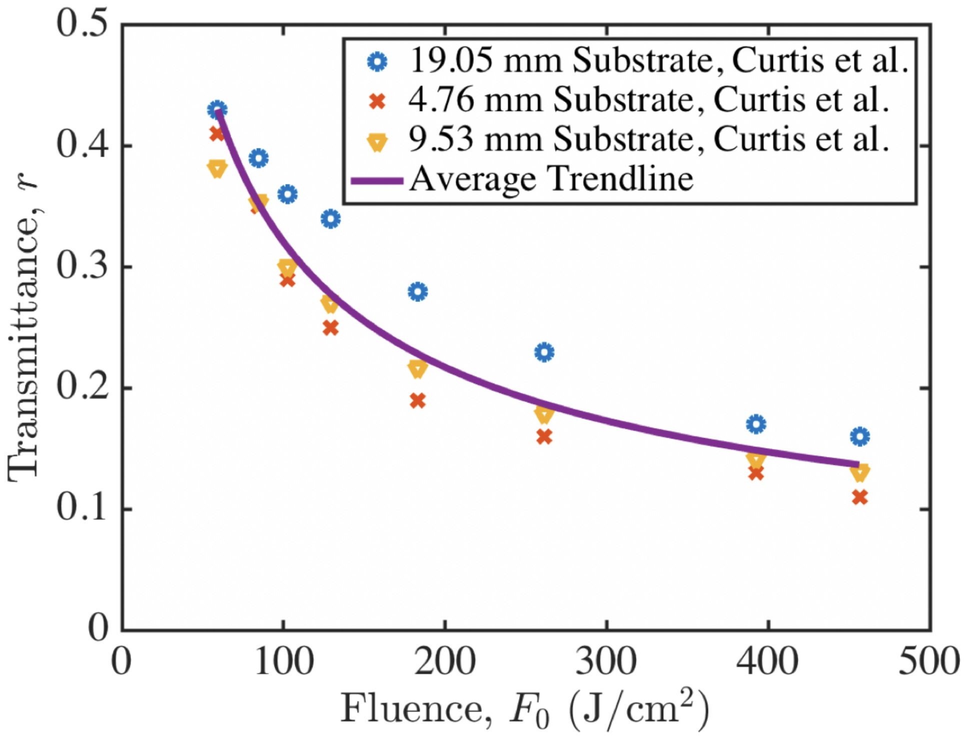

Figure 2.10: Data reproduced from Curtis et al. [60] showing transmittance through bare glass substrates of various thicknesses with respect to pulsed laser fluence.

Trott [84] used an overall loss parameter of $r = 0.5$ to simulate their fiber coupling losses that will compound to the substrate transmission loss in the lens-coupled case. Our foils are adhesive bonded to the glass substrate with an epoxy that likely introduces some transmittance loss, however small. There is also likely some energy lost to tearing the foil away from the launched disk, but we minimize that by cutting the flyer disks with the femto-second machining process in advance. We then propose a form for r,

$$r = 1 - (1 - r_{trans}(F_0, \tau_p))(1 - r_{coupling}). \tag{2.9}$$

Assuming that epoxy absorption and tearing or fracture of the flyer from the

the remaining flyer foil contribute little to the loss parameter, using the same coupling loss from Lawrence and Trott [84], and using a fitted curve to the transmittance data from Curtis et al. [60] ($r_{trans} = 4.26F_0^{-0.562}$), the model can be compared against launch velocity data from Curtis et al. [60]. The model predictions are shown against the launch velocity data in Fig. 2.11, with the predicted velocity envelope being similar to the empirical data. Changing the transmittance by just 3 percent completely brackets the launch velocity data, highlighting the crucial role that transmittance plays in the launch process. Material variability may introduce variance in substrate damage thresholds and can likely account for variability in launch velocities. Examination of the model equations predicts decreasing velocities for increased laser pulse durations τ_p, however, increased durations may prevent or delay substrate damage, suggesting an inflection point where pulse duration and transmitted fluence can launch the optimal speed flyer. Further experiments are necessary to confirm this hypothesis.

Using the same model parameters but accounting for the 10 mm glass substrates and 25 and 50 µm thick Al foils used in this thesis, we can develop a launch curve relating fluence to launch velocity. With 1.5 mm disks, the

Material Properties [units]	Value
Flyer thickness h_{flyer} ρ [m]	5×10^{-5}
Pulse duration τ_p [s]	10×10^{-9}
Incident Fluence F_0 [J/cm^2]	0–500
Absorption Coefficient r [dimensionless]	$1 - 2.13F_0^{-.562}$

Table 2.2: Model parameters used for comparison with launch velocity data.

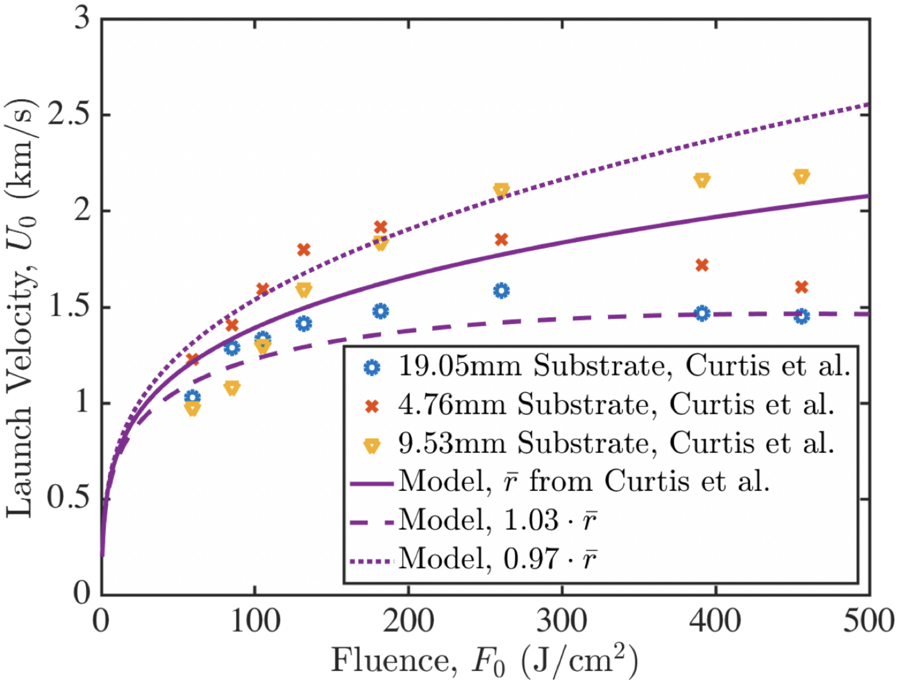

Figure 2.11: The model from Lawrence and Trott [84] applied to launch velocity data from Curtis et al. [60] using the average transmittance from Curtis et al. [60].

maximum fluence we can achieve is ∼100 J/cm^2 resulting in the launch curve shown in Fig. 2.12. With the spot size described in the prior section, we expect launch velocities of ∼1200 m/s for 25 µm thick flyers, and ∼850 m/s for 50 µm thick flyers. In general, the model shows that $U_0 \propto h_{flyer}^{-1/2}$ and $U_0 \propto \rho^{-1/2}$, so Al remains a good choice for flyer material to maximize impact velocity. These relationships do present challenges for shock compression experiments if high shock stresses are desired. With shock stress $\sigma = \rho c_l U/2$, if a high density and high stiffness material can approach similar velocities, higher shock stresses can be unlocked, but further experiments are necessary to find the optimum flyer material and substrate combination.

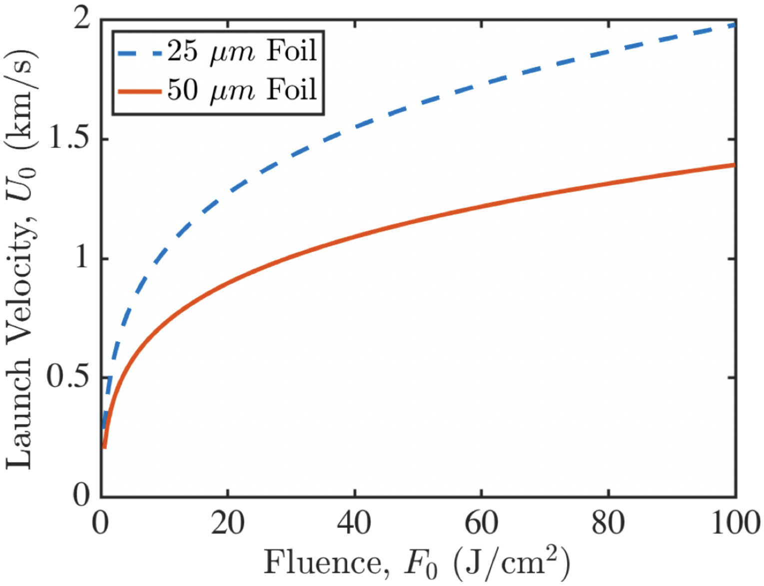

Figure 2.12: Launch curve for 25 and 50 micron thick Al flyers using using the average transmittance from Curtis et al. [60].

2.5 Summary

The apparatus described in this chapter is designed to propel planar Al flyers of thicknesses between 25 and 100 µm to ∼1000 m/s velocities using a pulsed laser to perform shock compression experiments on a target inside a vacuum chamber. The driving pulsed laser emits a single pulse stretched in time to nominally 20 ns using an optical ring cavity, while inexpensive multi-lens arrays are used to homogenize the beam spatially. The vacuum chamber is transparent to allow high speed imaging with a framing camera, and laser based velocimetry. The resulting flyer remains planar within the first ∼300 µm of travel. We modify a Gurney energy launch model, accounting for losses in this lens coupled flyer launcher, to develop a launch curve that predicts flyer velocity with respect to laser spot size and fluence. There remains quite a large space for improvement in the launcher system when considering flyer material, flyer thickness, confining substrate and adhesion to the substrate, and launching laser pulse characteristics that still can be explored to unlock faster or stronger shock compression loading. The shock duration from flyers with these thicknesses will be twice the round trip time of the shockwave in the flyer. Using the longitudinal wave velocity of aluminum, this shock duration is ~ 10 ns, motivating the need for reliable velocimetry with adequate time resolution to resolve failure events during shock experiments, which we discuss et seq.

Chapter 3

Photon Doppler Velocimetry for Shock Experiments

Parts of this chapter appear in a research article, Mallick et al. [79], and a research article, Mallick et al. [85]. D.D.M is first author for both.

3.1 Introduction

Shock compression experiments require velocimetry for an in-situ observation of stress states, particle velocities and shock velocities as they evolve during the experiment. The velocity vector history at the back face of the target package is conventionally measured using free-space lens-coupled tabletop laser interferometry techniques such as normal displacement interferometry (NDI)[86], normal velocity interferometry (NVI)[87], transverse displacement interferometry (TDI)[88], variable sensitivity displacement interferometry (VSDI)[89], and Velocity Interferometer System for Any Reflector (VISAR) [66, 67, 90]. In the past decade, photon Doppler velocimetry (PDV) has gained popularity for dynamic loading experiments[91, 92, 93]. This heterodyne interferometry technique uses telecommunications fiberoptic components to make velocimetry cheaper while making alignments easier, and is commonly employed for normal velocity detection.

In the previous chapter, we looked at 25 and 50 µm thick flyers launched at km/s velocities with our laser-driven launcher. For many shock compression experiment configurations, certainly in the case of the spall experiments described in chapters 4 and 5, the flyer is thinner than the specimen it is loading. If the target thickness is $h_{target} \approx 100\mu m$, and assuming a sound speed of $C_0 \approx 5km/sec$, the velocimetry must be able to resolve shock durations on the order of $\tau_{shock} \approx 20ns$ from a $h_{flyer} \approx 50\mu m$ thick flyer, so time resolution must be on the order of a nanosecond or less. The key question is thus: how does one obtain the desired time-resolved velocimetry? We address this question in this chapter.

3.2 System Principles

To resolve the velocity component along the interferometry laser path, we assume that the probe laser is directly perpendicular to the flyer or specimen surface. In this case, the time dependent velocity vector is assumed to be only in the normal direction of the target surface, $U_n\mathbf{e}_n$. Bold face represents vectors in this notation. The resulting displacement vector is

$$\mathbf{u}(t) = u_n(t)\mathbf{e}_n = \big(\int_0^t U_n(\tau)d\tau\big)\mathbf{e}_n. \tag{3.1}$$

Time-dependent intensity in PDV, a heterodyne interferometer, results from interfering a reference leg of light with a Doppler shifted leg from reflection with a moving object. PDV data analysis techniques typically feature sliding short-time Fourier transform windows [94] that can obscure measurements below 200m/sec due to significant low frequency variations in the interference intensity [92]. Features in the velocity record that are important to shock compression experiments can be below this detection threshold, so investigators have recently resorted to frequency up-shifting the reference leg of the heterodyne interferometer to shift the zero velocity signal above the threshold [93]. Low velocities correspond to low frequency signals which can be confused with DC signal [92], so to aid in the frequency analysis we thermally tune the reference laser to up-shift our reference leg wavelength by roughly 15 picometers in wavelength, generating a carrier upshift of about 2 GHz [93, 95].

We can write the wave equations proportional to the electric field for both the reference $\mathbf{E}_r$ and Doppler shifted $\mathbf{E}_D$ legs to obtain the time-averaged intensity $I = \langle |\mathbf{E}|^2 \rangle$. Each field has amplitude $\mathbf{A}$, wavevector $\mathbf{k}$, angular frequency ω, and initial phase ϕ:

$$\mathbf{E}_r(t, \mathbf{r}) = \mathbf{A}_r \{\exp[i(\mathbf{k}_r \cdot \mathbf{r} - \omega_r t + \phi_r)]\} \tag{3.2}$$

$$\mathbf{E}_D(t, \mathbf{r}) = \mathbf{A}_D \{\exp[i(\mathbf{k}_D \cdot \mathbf{r} + \mathbf{k}_D \cdot 2\mathbf{u}(t) - \omega_D t + \phi_D)]\}. \tag{3.3}$$

Assuming both fields have the same polarization vector, the time-averaged intensity for the interfered reference ($I_r = \langle |\mathbf{E}_r(t, \mathbf{r})|^2 \rangle$) and Doppler shifted

($I_D = \langle |\mathbf{E}_D(t, \mathbf{r})|^2 \rangle$) signals is

$$I(t, \mathbf{r}) = I_r + I_D + 2\sqrt{I_r I_D} \cos[(\mathbf{k}_D - \mathbf{k}_r) \cdot \mathbf{r} + \mathbf{k}_D \cdot 2\mathbf{u}(t) -$$

$$(\omega_D - \omega_r)t + (\phi_D - \phi_r)]. \tag{3.4}$$

The time-dependent phase manifests as wave fringes in the digitizer, which we define as $F(t)$:

$$F(t) = \mathbf{k}_D \cdot 2\mathbf{u}(t) - (\omega_D - \omega_r)t. \tag{3.5}$$

The wavevector $\mathbf{k}_D$ is in the direction of the Poynting vector of the probing laser beam, the surface normal of the target. If we incorporate some Poynting error angle β, this vector has magnitude $\frac{2\pi}{\lambda_D}$. When evaluating the dot product in (3.5) with our approach for a single PDV probing beam, each probe emits and receives its own optical power only. The normalized time derivative of the phase, $\frac{1}{2\pi}\frac{dF(t)}{dt}$, yields the linear signal frequency f for a single probe, where normalization leaves linear frequencies f_D and f_r for the reference and Doppler shifted legs respectively [94]:

$$f(t) = \frac{1}{2\pi}\frac{dF(t)}{dt} = \frac{2}{\lambda_D} U_n(t) \cos\beta - (f_D - f_r). \tag{3.6}$$

The above expression (3.6) is inverted to find a relationship for U_n with respect to the measured signal frequencies from the PDV probes,

$$U_n(t) = \frac{\lambda_D [f(t) + (f_D - f_r)]}{2\cos\beta} \tag{3.7}$$

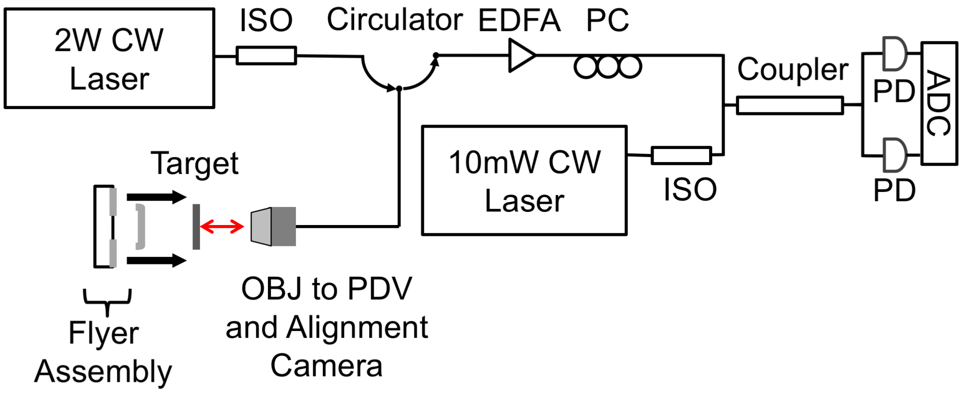

Figure 3.1: System diagram of frequency up-shifted PDV apparatus. Note the low noise amplifier (EDFA) to boost signal. PD: Photodiode. ISO: OpticalIsolator. ADC: Digitizer. PC: Polarization Controller

3.3 System Configuration

We perform normal velocity measurement with a custom-built amplified PDV system. Because of the ephemeral nature of the failure process at such small length scales, we use optics optimized for the 1550 nm wavelength to maximize signal-to-noise (SNR), including the objective (Computar SWIR M2514-SW) that images the velocimetry laser onto a ∼10µm diameter spot on the moving object to reduce signal noise. The PDV system features a single pre-amplified interferometer with a software balanced detector to measure the interference signal from the probe beam and reference oscillator (Fig.3.1). The detector consists of two InGaAs photodiodes (Optilab PD-20) collecting 180 degree out-of-phase light from a 50:50 coupler. PDV signals often feature dynamic amplitude modulations as a result of scattering from the moving target, so we amplify our returned signal with an Erbium Doped Fiber Amplifier (EDFA, Keopsys CEFA-C-PB-LP-CPB15)[96]. The EDFA provides low noise amplification of the returned signal during the measurement. A 45mW fiber laser (NKT Basik) provides optical power to a A 2W CW amplifier (Nuphoton) that supplies the interferometry laser power. The seed laser and amplifier operate at 500mW to prevent optics damage and still return excellent signal ($\geq$ -25dBm). The upshifted reference leg is fed by a second 15mW thermal tuned fiber laser (NKT Basik). The resulting $\geq$ 2GHz carrier frequency enables us to more easily resolve the shock break-out. The frequency offset also avoids signal overlap with leakage interference as a result of reflections from lens-optics and windows or incomplete isolation in system components. We match leg intensities through the amplifier output power control system before each experiment.

3.4 Phase Differentiation

PDV data analysis techniques conventionally feature sliding short-time Fourier transform (STFT) windows[94] of a set number of digitized samples (we capture data at 40GSamples/s) of the raw interference voltage signal to provide adequate velocity resolution[92]. Larger transform windows improve the velocity resolution but reduce time resolution. To resolve changes in velocity history when the applied shocks are on the order of tens of nanoseconds, we require windows on the order of several nanoseconds. Because the nanosecond time window broadens the Doppler signal significantly on the frequency axis of the STFT, extraction of the time-dependent center frequency of interest in the presence of background frequencies and noise becomes difficult. We choose instead to bandpass filter and directly differentiate the phase of the signal (using a MATLAB code) to obtain a velocity history with the

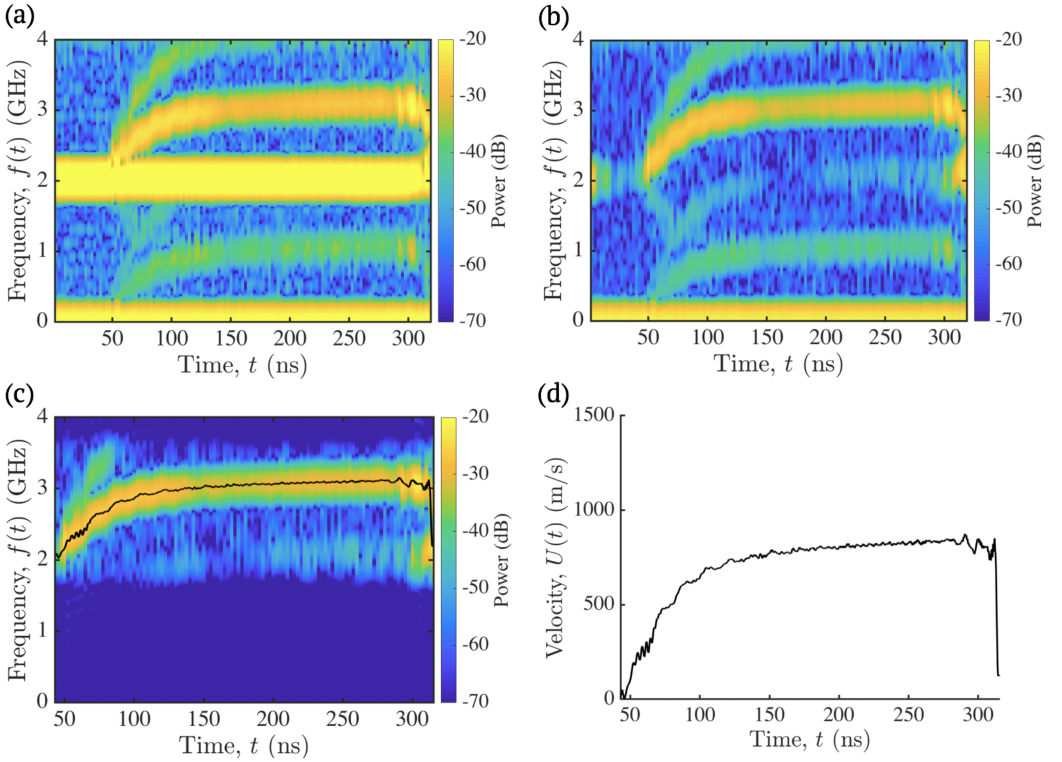

Figure 3.2: (a) Spectrogram of raw interference voltage signal from photodiodes. (b) Spectrogram of interference signal with baseline signal filtered out. (c) Spectrogram of interference signal with bandpass signal applied. (d) Phase differentiated velocity history from interference signal using 3 ns averaging stencil.

granularity of the digitizer sampling rate in time.

The raw PDV data (Fig. 3.2a) is first filtered to remove the up-shifted baseline beat frequency, and then again filtered to attenuate noise that is not the velocity signal. The figure shows a spectrogram of the raw data, where hotter regions indicate the presence of tone corresponding to signal of a particular frequency at a given time. The up-shifted carrier frequency tone is a constant 2GHz across the time of measurement. The baseline removal filter is a sixth order Gaussian notch with an 8MHz rejection band surrounding the beat frequency with strongest intensity in the spectrogram (Fig. 3.2b), while the velocity data isolation filter is a fourth order Gaussian bandpass with a 100 MHz pass-band about the critical data (Fig. 3.2c). After the filtering steps, we use phase angle unwrapping functions in MATLAB and then directly differentiate the unwrapped phase with a smoothing-differentiation stencil [97] to obtain the velocity history (Fig. 3.2d). The temporal width of the stencil can be selected based on the required time resolution but there is still a tradeoff between time and velocity uncertainty discussed in the following uncertainty analysis section.

3.5 Uncertainty Analysis

Uncertainty in the analyzed velocity comes from uncertainties in probing angle, frequency analysis, frequency stability of both reference and Doppler-shifted lasers, and wavelength stability of the Doppler-shifted laser. The first-order second moment (first standard deviation, 95 percent) of each contributing variable as a result of all underlying uncertainties in the normal velocity from (3.7) gives a total velocity uncertainty[98]:

$$\delta U_n = \{ \sum_i [\frac{\partial U_n(X_i)}{\partial X_i} \cdot \delta X_i]^2 \}^{1/2}, \tag{3.8}$$

$$\begin{aligned}\delta U_n = \{ &[\frac{\lambda_D[(f(t) + (f_D - f_r)] \tan\beta \sec\beta}{2} \cdot \delta\theta]^2 + \\ &[\frac{\lambda_D}{2\cos\beta} \cdot \delta f(t)]^2 + [\frac{f(t) + (f_D - f_r)}{2\cos\beta} \cdot \delta\lambda_D]^2 + \\ &[\frac{\lambda_D}{2\cos\beta} \cdot \delta f_D]^2 + [\frac{-\lambda_D}{2\cos\beta} \cdot \delta f_r]^2 \}^{1/2}.\end{aligned} \tag{3.9}$$

Each uncertainty in the budget from (3.9) depends on different variables, though all have a dependence on misalignment angle β:

- The $\delta\beta$ term in (3.9) can play a large role in velocity uncertainty. The Poynting vector error is difficult to measure, though we carefully align the objective that images the probing beam onto the moving object such that the beam path is perpendicular to the object surface. For a 1km/s launch, we expect the ideal frequency to be ~1.29 GHz with carrier wave offset $f_D - f_r = 2$ GHz. We can expect a Poynting error on the order of one degree, but estimate it conservatively as 3 degrees for this analysis. The resulting velocity uncertainty is ~ 7 m/s.

- Uncertainty in $\delta f(t)$ is from the frequency analysis process. A conservative estimate for uncertainty in frequency analysis from the smoothing-differentiation of the signal phase can be made from the Heisenberg-Gabor limit as outlined in Dolan [92] and Kettenbeil et al. [95]. With a

3ns stencil to capture the short duration transients in the velocity record, $\delta f(t) = 1/(4\pi \cdot 3 \times 10^{-9} = 20$ m/s. This uncertainty will be greatest at lower velocities where the smoothing stencil may obfuscate low velocity signals as zero velocity signals.

- $\delta\lambda_D$, δf_D and δf_r all depend on laser stability. The two lasers used in our experiment have less than 1kHz linewidth by specification, corresponding to an 8 attometer (10^{-9} nm) spectral deviation. We also expect the laser center frequencies to be stable over the nanosecond timescale of the experiment, meaning that these variables have very little impact on velocity uncertainty. Perhaps the largest source of uncertainty is determining f_r from the spectrogram, though this frequency is determined from the full trace spectrogram, which contains so many data-points (10 μs at 40 Gsamples/sec) that the estimate is likely very accurate. The sum of uncertainty contributions from λ_D, f_D and f_r is .002 m/s. Most single-frequency lasers with some thermal tunability used in PDV have similar linewidths, so this analysis holds true for most PDV systems[93].

Variations resulting from the laser wavelength and baseline frequencies do not play a significant role in velocity uncertainty, but analysis techniques can have a large effect in the measured frequency.

Time resolution is quite granular- the phase differentiation technique results in velocity histories that are discretized at the sampling rate during data collection (40 GSample/sec for our digitizer). Temporal uncertainty of the velocity history is equivalent to the size of the smoothing-differentiation stencil. In the case of a 3 ns stencil, the smoothing step will introduce a 3 ns group delay. The total uncertainty from (3.9) with a 3 ns smoothing stencil and an assumed 1000 m/s velocity with 2 GHz carrier frequency is ∼28 m/s.

3.6 PDV for Pressure-Shear Plate Impact

In chapter 2, we discussed the higher deviatoric stress associated with a non-planar flyer impact. Excessive magnitudes of deviatoric stress imparted from the non-planar shock compression loading will manifest as shear waves on the free surface of the target specimen. A multi-probe PDV system may be able to decompose the free surface velocity vector into normal and shear velocity components and provide an in-situ verification of flyer planarity, but such a system would be difficult to demonstrate for micro-flyers. To demonstrate the proof of concept, we have implemented such a system in a pressure-shear plate impact experiment (PSPI). PSPI generates deformations with very high

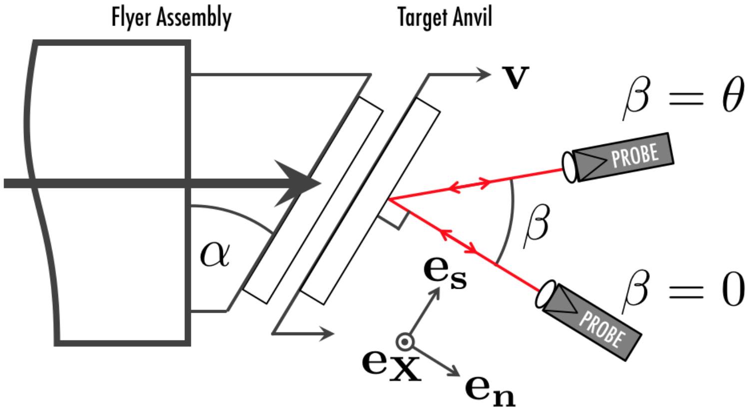

Figure 3.3: Diagram of dual probe alignment with respect to flyer assembly with velocity $\mathbf{v}$, target anvil with normal and transverse velocity components along $\mathbf{e_n}$ and $\mathbf{e_s}$ basis vectors, respectively. The normal probe is aligned along the target surface normal ($\beta = 0$), while the angled probe is aligned at angle θ from the target surface normal

shearing strain rates (between 10^4 s^{-1} and 10^6 s^{-1}) in specimens through impact of an inclined flyer plate with an equally inclined target, resulting in normal and transverse (shear) particle velocities in the system [86]. The velocity vector history at the back face of the target is traditionally measured using diffraction gratings that take careful surface preparation together with free-space lens-coupled tabletop laser interferometry techniques such as normal displacement interferometry (NDI)[86], and transverse displacement interferometry (TDI)[88] which can be cumbersome to align. To resolve both the normal and shear velocity components, we utilize a dual probe PDV system– one probe interrogating normal velocity ($\beta = 0$), while the other has its axis at an angle θ with respect to the target surface normal ($\beta = \theta$) interrogating a combination of normal and transverse velocity (Fig. 3.3). By analyzing both velocity histories we can decompose individual velocity components along the transverse and normal directions.

First, (3.6) must be modified to account for normal and shear velocities based on alignment angle β,

$$f(t) = \frac{1}{2\pi}\frac{dF(t)}{dt} = \frac{2}{\lambda_D}[U_n(t)\cos\beta + U_s(t)\sin\beta] - (f_D - f_r). \tag{3.10}$$

We can now write expressions for the $\beta = 0$ (f_{normal}) and $\beta = \theta$ (f_{angled}) cases and invert them to obtain expressions for the velocities of interest,

$$U_n(t) = \frac{\lambda_D[f_{normal}(t) + (f_D - f_r)]}{2}, \tag{3.11}$$

$$U_s(t,\theta) = \frac{\lambda_D[f_{angled}(t) - f_{normal}(t)\cos\theta + (1-\cos\theta)(f_D - f_r)]}{2\sin\theta}. \tag{3.12}$$

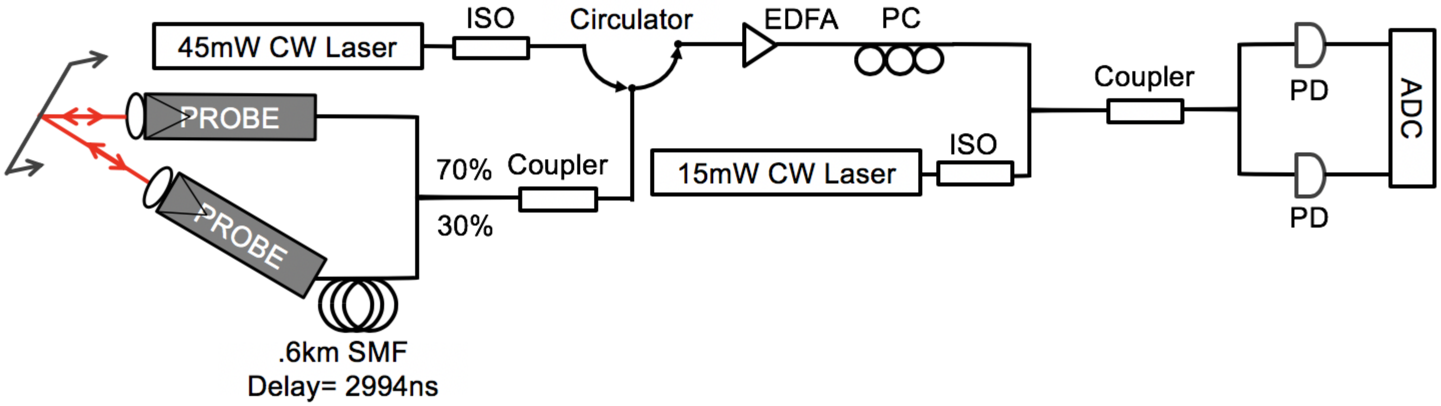

Figure 3.4: System diagram of modified frequency up-shifted PDV apparatus. Note the time multiplexing for two probes and the low noise amplifier (EDFA) to boost signal. PD: Photodiode. ISO: Optical Isolator. ADC: Digitizer. PC: Polarization Controller.

The system configuration requires minor modifications from that shown in Fig. 3.1 because we employ time multiplexing to implement the second PDV probe beam in a cost and complexity efficient manner. To utilize a single amplifier for two independent probe measurements, we time-delay multiplex the two probes, introducing a 70:30 coupler and a 600m single-mode fiber or 2.994μs delay leg at the first probe (Fig. 3.4). Instead of coupling the probes to the moving surface with an objective, disposable GRIN lenses (AC Photonics 1CL15A070LSD01-4m) are placed into a 3-D printed holder with prescribed angles ($\beta = 0^0$ for the normal probe and $\beta = 45^0$ for the angled probe). The single-mode fiber delay between the normal and angled probe data is quantified through a simple experiment with a piezo-actuator that provides a short duration impulsive motion that can be tracked with both probes simultaneously. In our system, this delay was found to be 2.994 $\pm$ .014 μs. This multiplexing procedure concatenates data from the two probes onto a single digitizer trace separated by the prescribed delay. The PSPI experiment timescales are much longer than for our laser driven flyer launcher, so we only require 45mW of optical power and thus we do not use the 2 W amplifier in this configuration.

We now compare the data analysis of the modified two-probe PDV experiment to conventional TDI and NDI. TDI uses lens-coupled visible laser light diffracted off a photo-deposited diffraction grating on the free surface of interest. The grating spacing relates directly to the measured phase, and thus the displacement in the transverse direction by a factor that depends on the diffraction order of the beam. NDI is a lens coupled heterodyne interferometer with the same operating principles as standard PDV. In our demonstration, both TDI and NDI employ a 532nm wavelength solid state laser. A 2cm x 1cm vertical grating with 5μm line spacing is photo-deposited at the center of the target anvil while the PDV probes focus on a spot 1cm away from the center to simplify co-alignment of all interferometry. We demonstrate the technique with several elastic pressure-shear plate impact experiments with our single stage gas gun simultaneously using PDV and traditional free-space lens-coupled TDI and NDI. The experiment uses D3 tool steel tempered at 800F for the flyer and target, keeping the material response elastic at our impact velocity of 100 m/s. The flyer and target are both aligned at an $\alpha = 20^o$ degree angle of inclination (Fig. 3.3). The PDV probes focus on the free surface with two trial surface preparations, (1) a roughly lapped surface, and (2) a surface with femto-second machined grooves using the machining system described in chapter 2.

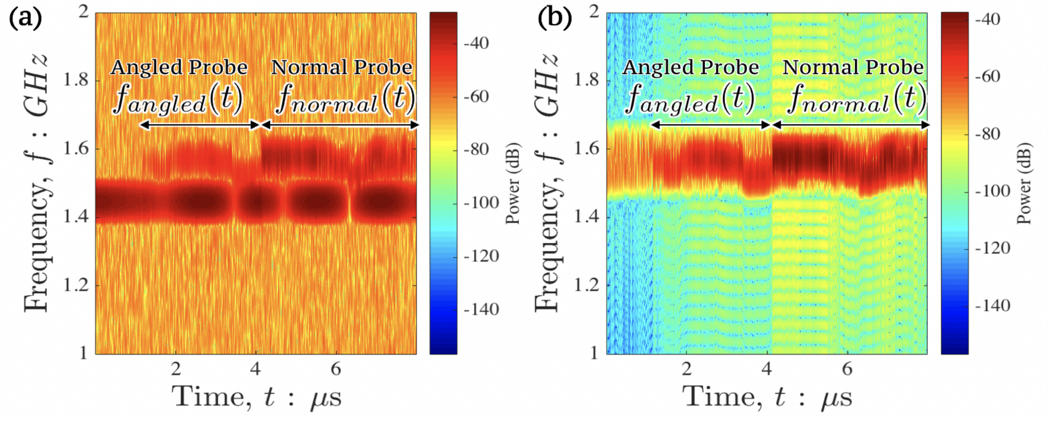

Figure 3.5: (a) Example spectrogram of raw data from the PDV system after 25.6ns FFT window with 50 percent window overlap showing baseline heterodyne beat (around 1.45GHz) below velocity signal tone (around 1.6GHz). (b) Processed spectrogram after applying notch filter to remove baseline beat and notch filter to attenuate noise above and below the flyer velocity data.

The resulting interference voltage signals are processed using the same techniques as in the prior section (example shown in Fig. 3.5). We compare the resulting velocity histories to an elastic prediction made by decomposing the projectile's velocity vector along the shear and normal directions based on the experiment alignment (Fig. 3.6). The PDV and TDI velocity histories agree well with the elastic solutions, considering measurement uncertainty. The lapped surface history is noisier and also shows a slightly lower shear velocity as expected from the slightly lower impact velocity in that experiment

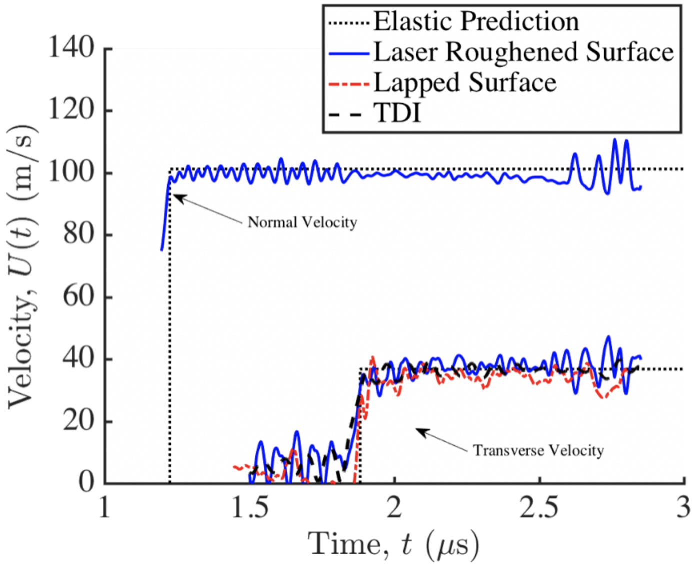

Figure 3.6: Two experiments conducted at the same impact velocity with the custom-built two-probe PDV system. In one experiment, PDV on the laser roughened surface and free-space TDI are concurrently captured for comparison. In the next, only two-probe PDV on a lapped surface is captured. Processed signals for TDI, laser roughened surface, and lapped surface are superimposed. The laser roughened surface data is less noisy due to improved SNR. Note the noise in the first microsecond of the multiplexing-delayed normal signal. This increased noise is from the phase analysis method seeing some of the angled probe data at the same time as the stronger normal probe signal due multiplexing overlap. There is some initial transverse velocity (5 m/s) before shear wave arrival due to tilt closure.

(100 m/s versus 107 m/s). Target surface roughness plays a prominent role in signal to noise ratio. The femto-second laser roughened surface resulted in a 9 percent signal average noise fraction, calculated as the ratio of the mean noise level to the area of its power spectrum in a spectrogram analysis [92]. We ensured that we were not collecting an ordered diffracted beam by shining a laser pointer on the surface to make sure no diffracted spots resulted from our surface processing steps. The barely lapped surface (15 μm surface roughness), resulted in an average 44 percent noise fraction. We noted a large amount of diffuse reflection, in addition to a dim specular reflection spot, with the laser pointer on the lapped surface. These results indicate that the low-noise amplifier is adequate for data collection on a wide variety of surface preparations, but that there are considerable improvements in noise figure with higher surface roughness which generates more scattering.

We also conduct an uncertainty analysis similar to that in the prior section for the shear velocity measurement,

$$\delta U_s = \{ \sum_i [\frac{\partial U_s(X_i)}{\partial X_i} \cdot \delta X_i]^2 \}^{1/2}, \tag{3.13}$$

$$\begin{aligned}
\delta U_s = \{ [& \frac{\lambda_D[(f_{normal}(t) - f_{angled}(t)\cos\theta + (1-\cos\theta)(f_D - f_r)]}{2(\sin\theta)^2} \cdot \delta\theta]^2 + \\
& [\frac{\lambda_D}{2\sin\theta} \cdot \delta f_{angled}]^2 + \\
& [\frac{-\lambda_D \cos\theta}{2\sin\theta} \cdot \delta f_{normal}]^2 + \\
& [\frac{f_{angled}(t) - f_{normal}(t)\cos\theta + (1-\cos\theta)(f_D - f_r)}{2\sin\theta} \cdot \delta\lambda_D]^2 + \\
& [\frac{\lambda_D(1-\cos\theta)}{2\sin\theta} \cdot \delta f_D]^2 + \\
& [\frac{-\lambda_D(1-\cos\theta)}{2\sin\theta} \cdot \delta f_r]^2 \}^{1/2}.
\end{aligned} \tag{3.14}$$

In comparison to the uncertainty analysis for just a single probe in the normal direction, the canting angle θ plays a much larger influence on the shear velocity measurement uncertainty. The disposable GRIN lenses impart a manufactured Poynting error measured as 0.6 ± 0.4 degrees which, when combined with a 3 degree Poynting alignment error estimate, can introduce larger uncertainties. The remaining parameters have the same uncertainty, except a longer smoothing stencil is used (40 ns instead of 3 ns) so measurement uncertainty for ∂f is better in that regard. The results are shown in Fig. 3.7 along with an estimate of shear velocity resolution, indicating an optimized canting angle between 30 and 60 degrees for the angled probe to minimize uncertainty.

Our PDV method requires only knowledge of the probing angle and some preparation of the target surface, while TDI requires a diffraction grating on a mirror finish surface and a careful alignment with diffracted beams. The convenience of our modified PDV method became clear as we performed the experiment– preparation and alignment time for TDI was nearly ten-fold that of our modified PDV.

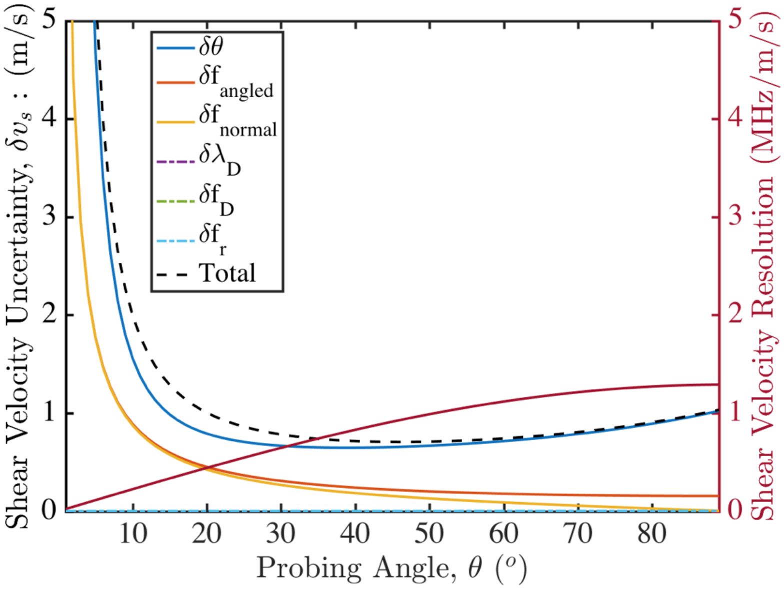

Figure 3.7: (Left) Uncertainty estimates with respect to probing angle. (Right) Transverse velocity resolution from the angled probe signal

The success of the method suggests that such an approach can be applied to the micro-flyer launcher to determine when a non-planar launch has occured, but further planning is necessary to make the apparatus smaller for the smaller diameter flyers which operate on faster timescales than with PSPI.

3.7 Summary

We have demonstrated the capability to impose shock loading with a bench-top laser driven micro flyer plate system and to resolve the resulting impact with laser-based interferometry over the course of tens of nanoseconds with improved processing of photon Doppler velocimetry data. Velocimetry signal-to-noise and time resolution remain the biggest hurdles in performing these experiments as we approach the resolution limits of photon Doppler velocimetry, but this approach presents excellent time resolution on the order of the digitizer sampling rate, and the system employs an erbium doped fiber amplifier with a low noise figure to boost signal-to-noise ratio.

In addition to normal velocity detection, we have developed a novel implementation of PDV for free-surface transverse velocity measurement in pressure-shear plate impact experiments with the hope that shear velocity detection will some day be implemented for laser-driven micro-flyers to infer experiment quality. Time multiplexing allows dual probe measurements without duplicating system components. One probe measures normal velocity directly while the other measures a combination of the normal and transverse velocity. Analysis of the velocity history from both probes then results in decomposed velocity histories for the free surface. We validate the experimental technique through simultaneous free surface velocity measurements with both PDV and traditional free-space transverse displacement interferometry in elastic shots. The PDV and TDI data show good agreement, though PDV offers convenience during alignment and surface preparation owing to its fiber-optics coupling and by not requiring photo-lithography for transverse data, respectively. In the following chapters, we bring the launcher and velocimetry tools to bear to interrogate first the spall failure of magnesium alloys and then the brittle fragmentation of boron carbide ceramics.

Chapter 4

Incipient Spall in Extrusion Machined AZ31B Foils

Parts of this chapter appear in a research article, Mallick et al. [79], where D.D.M is first author.

4.1 Introduction

In the prior chapters we detailed the laser-driven flyer technique available to our laser facility. We now demonstrate the technique to analyze spall failure of Mg alloys which have tremendous weight savings potential for vehicle armors in defense applications. The role of dynamic void growth as a failure mechanism during spall has been the subject of various investigations since Rinehart et al. characterized ultimate tensile strength of steel, brass, Al, and Cu alloys with explosive loading [99]. Spall failure occurs under high-rate loading conditions where stress waves interact to create high tensile pressures in a material, thereafter activating failure mechanisms such as dynamic void growth [7]. In dynamic void growth, the far field load exceeds some criterion thereafter causing unstable nucleation and growth of a cavity [100, 101]. These cavities, or voids, coalesce to degrade the load-bearing capacity of the material. This phenomenon is conventionally studied with gas guns [24, 22, 23] and explosive loading that can achieve strain rates as high as $10^7\ s^{-1}$ or more, but can make specimen recovery difficult due to the large amount of kinetic energy available to such methods. Instead, we use the laser-driven micro-flyer apparatus described in chapters 2 and 3 that imparts four orders of magnitude less kinetic energy than conventional methods into the specimen while retaining similar energy density and strain rate loading, aiding in recovery and allowing for high experimental throughput. Analysis of the specimen free surface velocity history and post-mortem scans of the specimen with micro-computed-tomography techniques reveals the pressure threshold for dynamic void growth that ultimately leads to spall failure in the specimen. The material of interest is extrusion machined AZ31B magnesium alloy, chosen for its high specific strength and subsequent potential application as a lightweight protection material.

4.2 Mechanics of Spall Failure

Here we present the basic mathematical descriptions of wave propagation mechanics necessary to understand the concepts in this chapter. The following primer is not comprehensive and we refer the reader to the thorough treatments in Meyers [68], Drumheller [102], Antoun et al. [7], and Davison [103] for further details.

4.2.1 Wave Propagation in Solids

Impact experiments feature high velocities and rates of deformation, bringing dynamics into the mechanics. Data such as the force or velocity of an impact has a characteristic speed, a wave velocity, through a body, imposing time dependence on any sort of deformation or failure of that body. To understand the propagation of waves in solids leading to spall, we begin with the simplest case by considering a stress wave in one dimension in a linear-elastic isotropic solid. In Einstein notation, generalized hooke's law relates stresses σ_{ij} and strains ε_{ij} to the lame constants λ and μ,

$$\sigma_{ij} = \lambda \delta_{ij} \varepsilon_{kk} + 2\mu \varepsilon_{ij}. \tag{4.1}$$

Assuming small strain kinematics with displacements u_i, i.e.,

$$\varepsilon_{ij} = \frac{1}{2}(u_{i,j} + u_{j,i}), \tag{4.2}$$

the stress in the first basis direction $\mathbf{e}_1$is,

$$\sigma_{11} = (\lambda + 2\mu) u_{1,1}. \tag{4.3}$$

Next, we substitute (4.3) into the linear momentum balance,

$$\sigma_{ij,j} + \rho b_i = \rho \ddot{u}_i \tag{4.4}$$

resulting in the 1-D wave equation,

$$\ddot{u}_1 = \frac{\lambda + 2\mu}{\rho} u_{1,11}. \tag{4.5}$$

This partial differential equation (4.5) contains the longitudinal wave velocity c_l in the case of uniaxial strain as the data propogation velocity,

$$c_l^2 = \frac{\lambda + 2\mu}{\rho}. \tag{4.6}$$

In a similar fashion, wave velocities in the case of uniaxial stress, shear, volumetric and plastic waves can be determined as combination of the reference density and material moduli, i.e. more generally,

$$c^2 = \rho^{-1}\frac{\partial \sigma}{\partial \varepsilon}, \tag{4.7}$$

so the plastic wave in a two wave structure will travel with velocity $c_0 = \sqrt{K/\rho}$ depending on the bulk modulus K and ignoring other modulus associated with shear effects. (4.7) can also explain the "shocking up" of a shockwave wherein the propagation velocity continues to increase in the case where $\frac{\partial}{\partial \varepsilon}(\frac{\partial \sigma}{\partial \varepsilon}) > 0$, such as in the case where a series of waves are traveling one after the other. The pressure following the first wave is higher so the following wave travels faster up to the first wave and so forth, generating a shockwave (Fig. 4.1). The bottom schematic in Fig. 4.1 describes decompressive attenuation of a shock front during impact in the case where a release wave from the rear of the projectile travels through the shocked region at a faster velocity than the compressive shock front, decaying the compressive shock. A similar concept causes rarefaction fans with a tensile wave-train from reflection off a free surface where subsequent wave-packets encounter lower stress and slow down, but the mathematical treatment of this phenomenon isn't addressed here in detail.

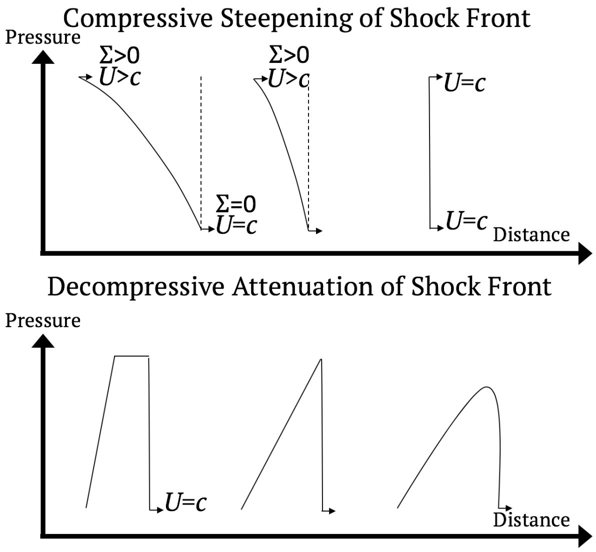

Figure 4.1: (Top) Wave profiles of a compressive wave steepening into a shock. (Bottom) Wave profiles of a decaying wave.

The D'alambert solution to (4.5) is required to develop the method of characteristics which underpins analysis of impact and spall experiments,

$$u = f(c_l t - x) + g(c_l t + x) \tag{4.8}$$

with position coordinate along the $\mathbf{e_1}$ basis vector x. Taking just the component of the solution traveling in the positive x direction in a uniaxial stress case where $c_l = \sqrt{E/\rho}$, i.e. $u = f(c_l t - x)$, we can differentiate this expression with respect to time t and space and then equate the results to relate particle velocities to stresses using the one dimensional Hooke's law $\sigma = E\varepsilon$ with

Young's modulus E,

$$\frac{\partial u}{\partial x} = \varepsilon_x = -f'(c_l t - x),$$

$$\frac{\partial u}{\partial t} = c_l f'(c_l t - x),$$

$$\varepsilon_x = \frac{\sigma}{E} = -c_l^{-1}\frac{\partial u}{\partial t},$$

$$\sigma = -c_l^{-1} E U_p$$

$$\sigma = -\rho c_l U_p, \tag{4.9}$$

where U_p is the particle velocity. (4.9) is the expression describing the forward, often denoted $+$ or C^+, characteristic line of a propagating plane wave and ρc_l is referred to as the acoustic impedance. Similar expressions can be written for waves propagating at other velocities.

4.2.2 The Method of Characteristics in Spall

In the classical spall experiment, the impact of a flyer on a target sends compression waves into the target and backward into the flyer(Fig. 4.2a-b). The propagating compressive shockwaves encounter free surfaces of the target and the flyer and are reflected as rarefaction fans. These two rarefaction fans meet and interact in the target to create a high tensile stress that causes spall failure through void growth and fracture. Diagnostic methods are most conveniently applied at free surfaces in the experiment, so we utilize the measured particle velocity history of the target free surface to interrogate the stress states developed as a result of the impact. A schematic of the particle velocity history measured on the target rear surface is shown in Fig. 4.2c, with labels corresponding to event times shown in Fig. 4.2b.

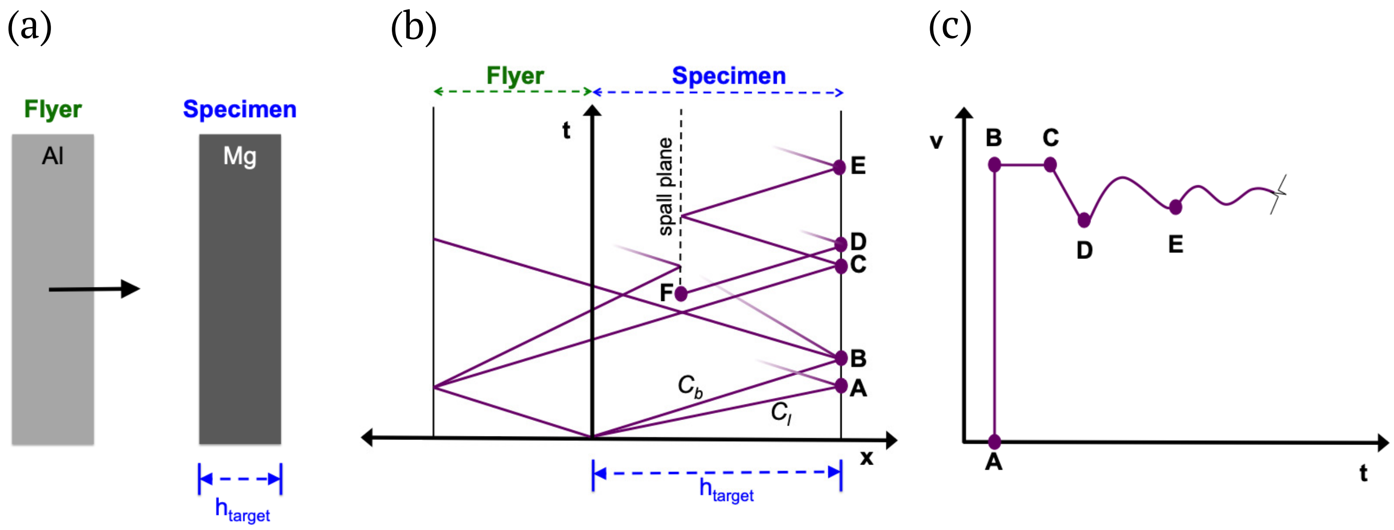

Figure 4.2: (a) Schematic of flyer impact with a target for a spall experiment. (b) Simplified Lagrange (Position vs Time) diagram of spall as a result of flyer impact. Spall failure occurs in the region of high tensile strength caused by interaction rarefaction fans from the flyer and target free surfaces. The longitudinal wave is omitted for clarity. Only the initial longitudinal wave is drawn to illustrate the start of the free surface velocity; Further propagation of the longitudinal wave is omitted otherwise for clarity. (c) Idealized velocity history of spall signal (Pullback velocity is from points B to D). The free surface history is probed at the rear of the target free surface.

Fig. 4.2b shows that the intersection of the rarefaction fans results in the development of a rapidly growing tensile stress state (initially under uniaxial strain). The signature of the development of these tensile stresses and subsequent spall failure is the reduction (”pullback”) of the particle velocity at the rear surface, beginning at point C in Fig. 4.2b-c. As the tension increases, at some time (perhaps at a critical tensile stress) voids begin to nucleate and grow. This spall process takes time, but we assume instantaneous failure for simplicity. After a spalled plane forms suddenly, a recompression shockwave develops and arrives at the rear free surface at time D (Fig 4.2b-c). Point D corresponds to the fully spalled state, so spall strength can be measured by estimating the tensile stress at point F using the velocity history at the rear surface.

The conventional approach to analyzing spall experiments is the method of characteristics [7, 90] where one-dimensional equations describing the particle velocity and pressure assuming uniaxial strain, $U(t)$ and Σ respectively, may be written along characteristic lines for the rearward C^- and forward C^+ traveling characteristics. With reference density ρ and pressure at failure Σ^* corresponding to the state F in Fig. 4.2b,

$$C^+: \int_{\Sigma^*}^{\Sigma(t_D)} d\Sigma = \int_{U(t_F)}^{U(t_D)} \rho c_0 dU \rightarrow \Sigma(t_D) - \Sigma^* = \rho c_0 (U(t_D) - U(t_F)) \tag{4.10}$$

$$C^-: \int_{\Sigma(t_B)}^{\Sigma^*} d\Sigma = -\int_{U(t_B)}^{U(t_F)} \rho c_0 dU \rightarrow \Sigma^* - \Sigma(t_B) = \rho c_0 (U(t_B) - U(t_F)). \tag{4.11}$$

Under the assumptions that the damage information propagates at only the bulk velocity $c_0 = \sqrt{K/\rho}$, the material is linear, and that the spall plane begins after complete release from the rarefaction fan, equations (4.10) and (4.11) are superimposed to give the classical pullback velocity equation for spall strength after imposing traction free boundary conditions at the free surface[104, 105],

$$\begin{aligned} 2\Sigma^* - \Sigma(t_B) + \Sigma(t_D) &= \rho c_0 (U(t_B) - U(t_D)) \\ \Sigma^* &= \frac{1}{2}\rho c_0 (U(t_B) - U(t_D)). \end{aligned} \tag{4.12}$$

The estimated spall strength may be corrected for a more accurate measure of the failure characteristic within the rarefaction fans by a factor δ, which is well understood for plate impacts [24] but is less understood for our laser spall experiments (discussed et seq.).

The approximate tensile strain rate under which spall occurs, assuming the simplest equation of state with bulk modulus $K = C_0^2\rho$, $\sigma_{kk} = K\varepsilon_{kk}$ and that damage information travels with the bulk velocity, can be estimated as,

$$\begin{aligned} \frac{\varepsilon(t_C) - \varepsilon(t_D)}{|t_C - t_D|} &= \frac{\Sigma(t_C)/K - \Sigma(t_D)/K}{|t_C - t_D|}, \\ \dot{\varepsilon} &= \frac{1}{2c_0}\frac{U(t_C) - U(t_D)}{|t_C - t_D|}. \end{aligned} \tag{4.13}$$

The idealized free surface diagram in Fig. 4.2c is rarely the case in actual experiments using most loading methods. Instead, there are typically some artifacts in the signal as a result of loading misalignment, material microstructure, and diagnostic noise. Clear peaks and plateaus become difficult to resolve as the loading duration decreases to values found in our experiments and in direct laser shock experiments because the time between events decreases. To maintain a consistent analysis with the short loading durations in our apparatus, we assume $U(t_B) = U(t_C) = max(U(t < \tau_{shock}))$, where τ_{shock} is a conservative estimate of the shock duration from our experiment using the estimated spalled plate thickness h_{flyer},

$$\tau_{shock} \geq \frac{2h_{flyer}}{C_0}. \tag{4.14}$$

The minimum value $U(t_D)$ is defined as $U(t_D) = min(U(0.5\tau_{shock} < t < 1.5\tau_{shock}))$. Velocimetry must be tuned to account for τ_{shock}, and measurement uncertainty can profoundly impact the uncertainties in the measured spall strength and strain rate (as we explore in the discussion).

The basic configuration described here can be applied to targets of a range of thicknesses, including the thin foils studied here. Since the flyer thickness must be smaller than the target thickness to keep the spall plane inside the specimen, it follows that the loading pulse duration decreases as target thickness decreases. In practice, the flyer is typically half the thickness of the target or less [7]. Resolving the spall process thus requires increasing the time resolution of the velocimetry. If the target thickness is $h_{target} \approx 100$ µm, and assuming a sound speed of $C_0 \approx 5$ km/s, the velocimetry must be able to resolve shock durations on the order of $\tau_{shock} \approx 20$ ns from a $h_{flyer} \approx 50$ µm thick flyer, so time resolution must be on the order of a nanosecond or less. The key questions are thus: (1) How does one launch flyers of such small thicknesses, and (2) how does one obtain the desired time-resolved velocimetry? We address each of these questions in the next two sections.

4.3 Extrusion Machined AZ31B Mg Alloy

We investigate the spall response of the Mg alloy, AZ31B, which has been studied through plate impact spall experiments by Farbaniec et al. [24], Williams et al. [106], and Yu et al. [22]. AZ31B Mg alloy thin foil targets of 175 and 100 μm thicknesses are prepared using a shear-based deformation process termed extrusion-machining that exploits large strains intrinsic to machining with the dimensional control of extrusion [107]. In this process, a sheet or foil of predetermined thickness is removed from the surface of a bulk workpiece via simultaneous cutting and extrusion [108]. The underlying deformation is simple shear, with the corresponding strain and strain rate conditions determined by the cutting velocity and tool geometry. This process therefore provides a convenient approach to process thin specimens with controlled thickness (±1μm) over a range of different strain/strain rate conditions. In this study, two AZ31B Mg foils, of 175 μm and 100 μm thick, were produced using the extrusion-machining method. The 175 μm sample was processed at a nominal (von Mises) strain of 0.6 and strain rate of 6×10^3 s^{-1}, while the corresponding conditions for the 100 μm foil were 1.1 and 10^5 s^{-1}. The 100 μm foil has a dynamically recrystallized, equiaxed microstructure with an average grain size of $\sim$ 3.3 μm, likely because of the high strain and strain rate conditions (and attendant adiabatic heating). In contrast, the 175 μm thick foil was characterized by a more twinned and highly-sheared microstructure with an average grain size of $\sim$2.4 μm with a more uniform distribution (some larger sheared grains). However, both of these samples are characterized by tilted-basal type textures with the (0001) basal planes aligned at an angle with respect to the foil surface [107] (EBSD scans shown in Fig. 4.3 and Fig. 4.4). Specimen coupons are cut from the as-received foils using a 3mm diameter Transmission Electron Microscope sample punch for use in the shock loading apparatus.

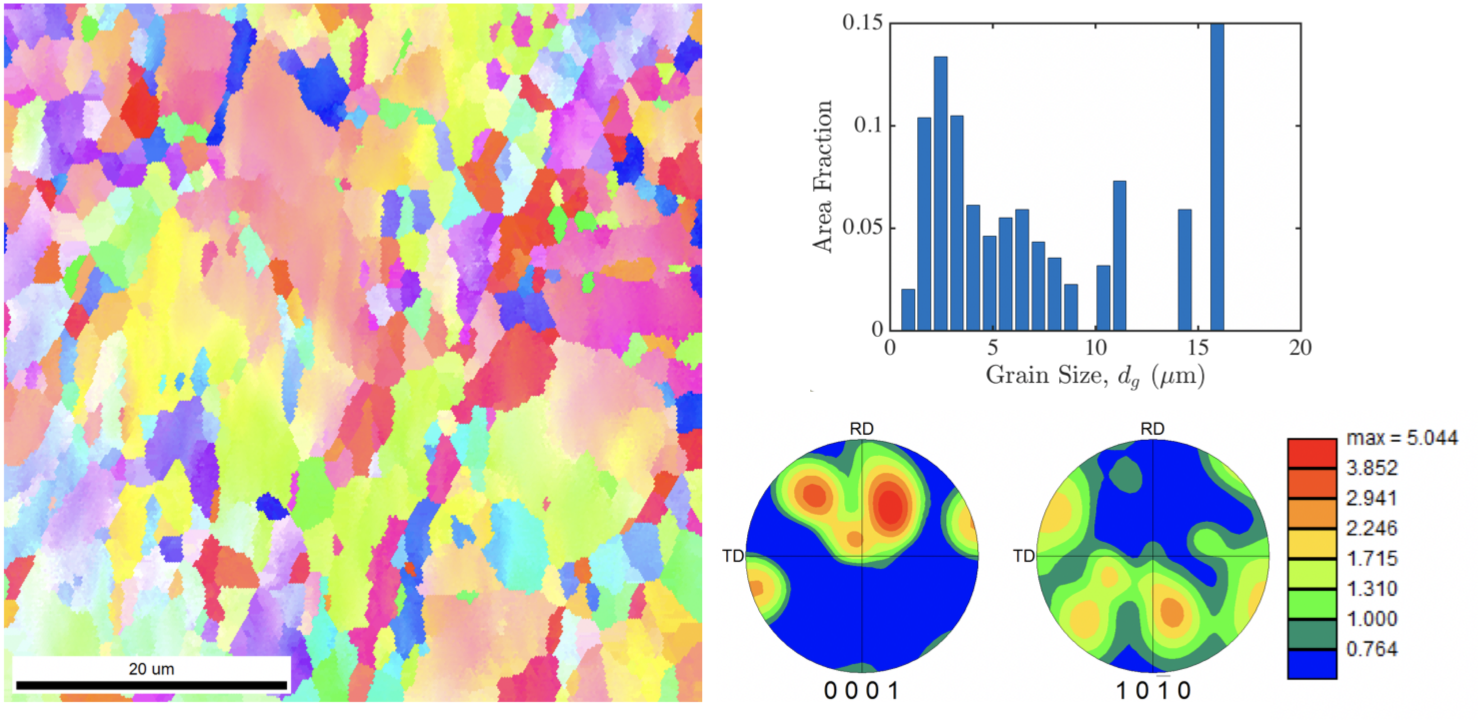

Figure 4.3: Inverse pole figure, grain size distribution, and texture plot of 175 μm thick AZ31B foil.

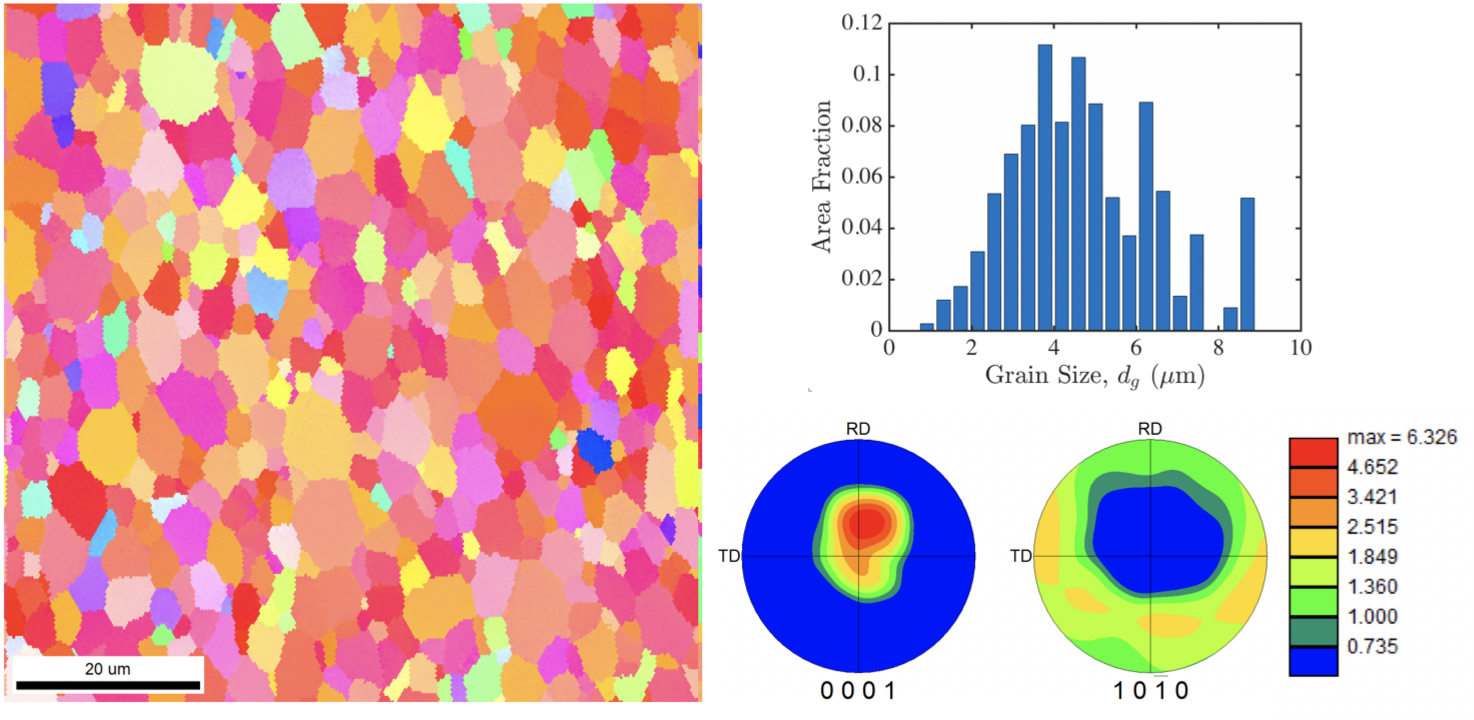

Figure 4.4: Inverse pole figure, grain size distribution, and texture plot of 175 µm thick AZ31B foil.

4.4 Experiment Procedure

Most spall experiments employ symmetric impacts where the flyer material is the same as the target material, so that the impact velocity is the same as the peak velocity in the target under standard experiment geometries, and then separate measurement of impact velocity is unnecessary. However, as we discuss in chapter 2, LDMFP experiments with lab-bench lasers offer a limited fluence, or pulse energy per unit area for flyer launch, so flyer materials have to be chosen to optimize impact velocity. Modeling of LDMFP launches in that chapter show relationships between flyer thickness h_{flyer}, flyer material density ρ_{flyer}, and launch velocity U_0. Now, $U_0 \propto h_{flyer}^{-1/2}$ and $U_0 \propto \rho_{flyer}^{-1/2}$ based on the available launch energy from (2.5) and (2.8). Aluminum is a good choice for the flyer material to maximize impact velocities with 50 μm thick flyers, and is also a fairly strong metal that is ubiquitous in thickness controlled foil format. Using Al flyers against Mg alloys makes the impact non-symmetric, so knowing the impact velocity is helpful for verifying success of an experiment. Unfortunately, the small scales of the flyer, target, and stand-off distance in LDMFP spall experiments coupled with the high launch velocities makes capturing the impact velocity of the flyer difficult in-situ. We therefore warm up the laser for consistent energy output and then measure launch velocities in independent experiments with a transparent target before performing the spall experiment. Using the estimated launch curve in chapter 2, we verify launch velocity by performing a launch into an optically transparent glass target at the same stand-off distance as the specimen. We then assume that impact velocity for the spall experiment on the specimen itself. As per the captured velocimetry and application of (3.7), a full laser power launch of a 50 µm thick flyer is about 850 m/s, but the velocity can vary fairly widely (±100 m/s) if the laser is not adequately warmed up (We note that laser fluences were adjusted to achieve different strain rates with limited variance in this chapter, from 600 m/s up to a maximum velocity of 900 m/s). After the impact velocity on the transparent target is determined, we perform the experiment with the specimen coupon adhesively bonded to the flyer package through a Kapton spacer with a 1.5 mm through hole.

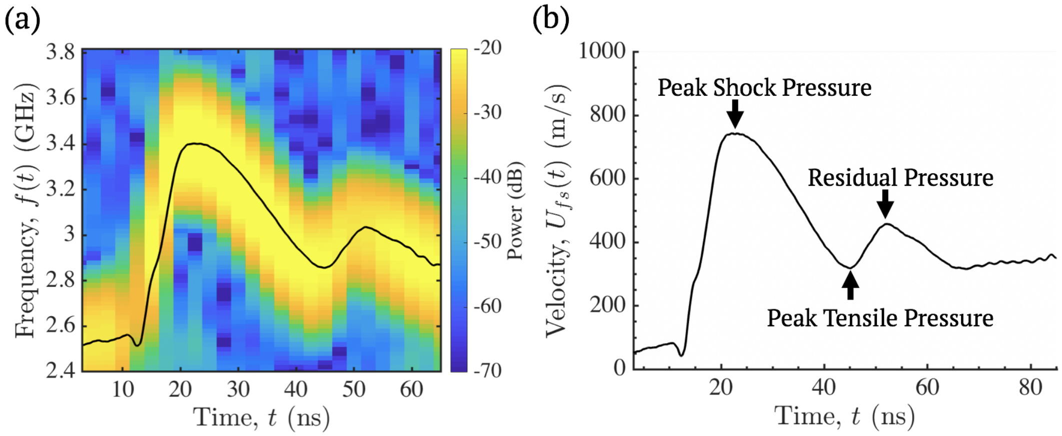

Figure 4.5: (a) MATLAB spectrogram of impact experiment on 175 µm thick AZ31B thin foil after filtering steps to isolate velocity history tone (Shot number 2018.10.08.00003). The black overlay is the phase differentiated frequency-time history of the signal. (b) The frequency-time history is converted into a velocity-time history of the target free surface. Note the presence of a small air shock from 0 to 13ns from the not fully evacuated chamber

The spectrogram shown in Fig. 4.5a has been filtered to remove the up-shifted baseline at ∼2.4GHz, leaving only the up-shifted tone corresponding to the measured free surface velocity. The velocity record shown in Fig. 4.5b exhibits a low velocity rumble for the first ∼20 ns preceding the shock break-out, resulting from sub-optimal chamber evacuation leading to a small air shock. The subsequent velocity record can then be analyzed to determine spall strength from velocity pullback (4.12) and tensile loading rate from the time duration of the velocity pullback (4.13) (From ∼35 ns to ∼55 ns in Fig. 4.5b corresponding to t_B to t_D in Fig. 4.2c). The spalled pulse duration can be estimated from the duration of the following peak in the velocity signal as waves ring in the spalled plate (From ∼55 ns to ∼75 ns in Fig. 4.5b corresponding to t_D to t_E in Fig. 4.2c).

4.5 Results: Spall Strength of AZ31B Mg Alloy

4.5.1 Velocimetry

The pullback velocity analysis in (4.12) and (4.13) is applied to ten experiments, five on 175 µm thick AZ31B Mg targets, and five on 100 µm thick targets. Fig. 4.6 shows the calculated spall strength against the estimated tensile loading rate. The thicker targets exhibit higher spall strength (averages are 1.69 ± 0.06 GPa vs 1.44 ± 0.11 GPa for 175 and 100 µm thick targets respectively). A lower unloading strain rate develops in the thicker targets (averages are $2.8 \times 10^6 \pm 5.6 \times 10^5$ s^{-1} vs $3.15 \pm 1.2 \times 10^6$ s^{-1} for 175 and 100 µm thick targets respectively). There is a single higher velocity experiment on the 100 µm thick foils shown as the rightmost data-point from an attempt to increase impact velocity (∼1200 m/s) to obtain a higher strain rate by reducing the drive laser spot size on the flyer (we note that based on the divergence of the drive laser with our homogenization technique, decreasing the spot size of the drive laser past the spot size for ∼850 m/s launch velocity does increase the launch velocity, but also increases difficulty of alignment). After excluding

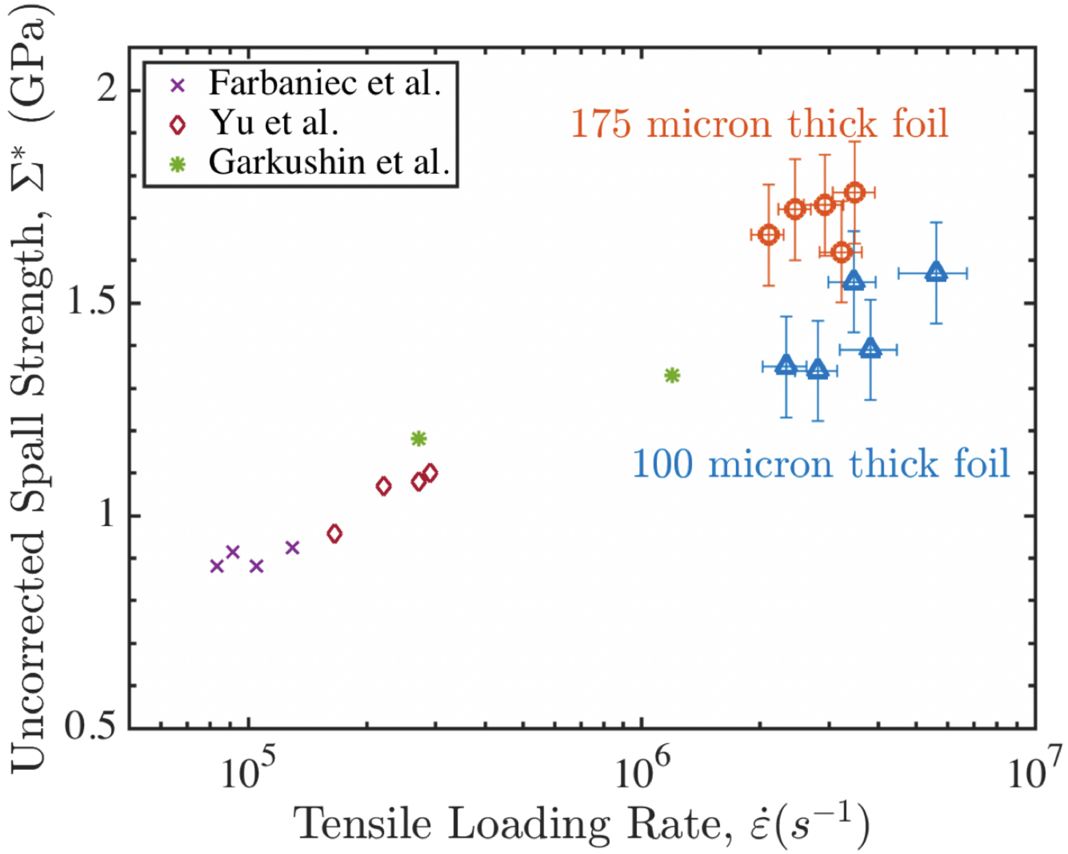

Figure 4.6: Spall strength versus strain rate for two different AZ31B target foil thicknesses. Superimposed are spall strength data from Farbaniec et al. [24], Garkushin et al. [23], and Yu et al. [22]. Error bars denote measurement uncertainty by the analysis in the discussion et seq.

the higher velocity datapoint, the average strain rate for the 100 µm thick foils is $3.11 \times 10^6 \pm 6.7 \times 10^5$ s^{-1}.

Fig. 4.6 also shows spall data from Farbaniec et al. [24], Yu et al. [22], and Garkushin et al. [23] superimposed on our results. Farbaniec et al. [24] performed gas-gun spall studies on equal channel angular extruded AZ31B-H24 Mg alloy with a nominal grain size of ∼3 µm. While their grain size is similar to our material, the processing strain rate is 3 orders of magnitude lower and the grains are equiaxed with a strong basal texture along the loading direction. Yu et al. [22] performed gas-gun spall studies at higher rates on equal channel angular pressed AZ31B Mg alloy with a tilted basal texture similar to the Mg alloy in this study. The grain sizes in their work also ranged between 1.5 and 5 µm. Garkushin et al. [23] performed gas-gun studies on equal channel angular pressed Ma2-1 Mg alloy with a larger average grain size at ∼7 µm with an unreported texture. Though the alloy microstructures are different from case to case, the overall trend of rising spall strength with strain rate remains consistent.

We now turn to analyze the velocity record of the experiment in Fig. 4.5 in greater detail to understand the stress history in the target throughout the spall failure process. At $\sim$ 25 ns, the peak compressive pressure, $\Sigma_{peak} = \frac{\sigma_{kk}}{3}|_{t\sim 25ns}$ is achieved (at the point denoted "Peak Shock Pressure" in Fig. 4.5) and can be estimated as,

$$\Sigma_{peak} = -\frac{1}{2}\rho c_0 U_{max}. \tag{4.15}$$

This peak shock stress is ~ -2.99 GPa where the negative sign denotes compression. The velocity "pullback" signal occurs at $\sim$ 45 ns (the "pullback" velocity minimum, U_{min}, denoted "Peak Tensile Pressure" in Fig. 4.5) allowing for an estimate of the spall strength $\Sigma^*|_{t\sim 45ns}$ by (4.12).

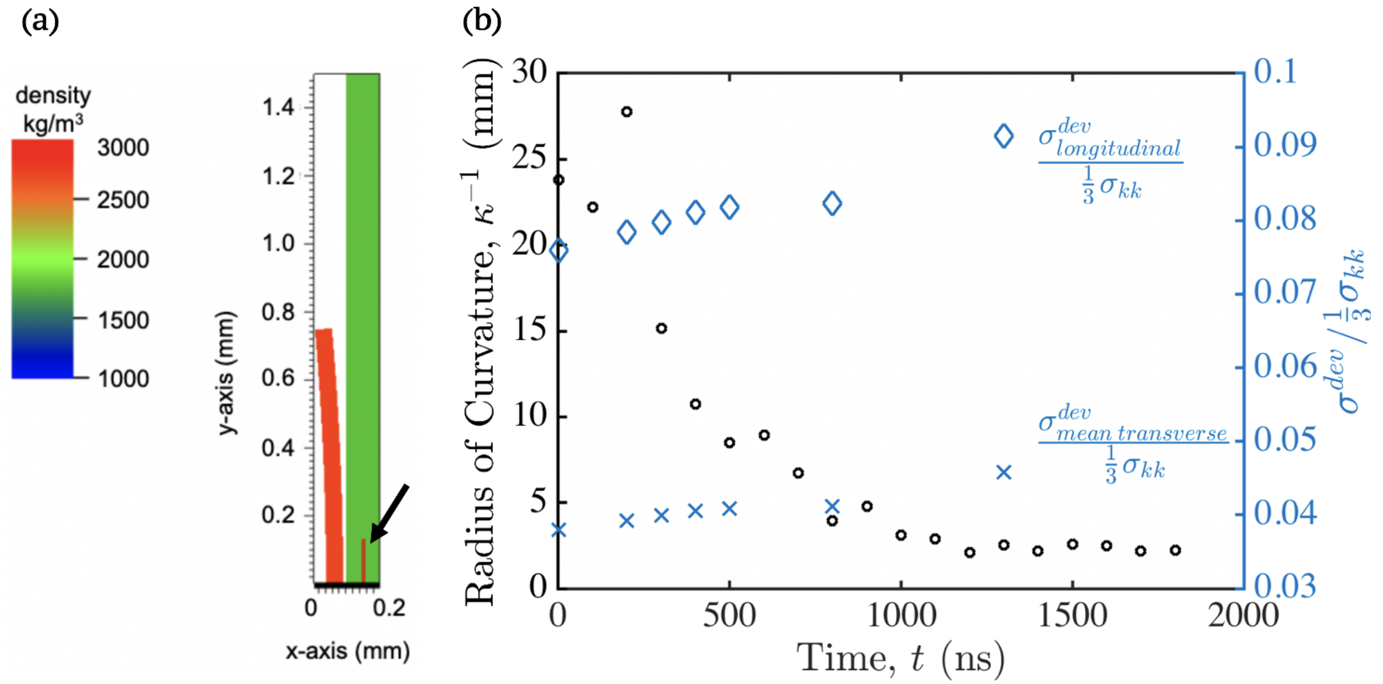

Figure 4.7: (a) Diagram of finite element simulation. The red region is the aluminum flyer with some radius of curvature. The green region is the magnesium target. The black arrow points at the region of the spall plane where we analyze the pressure history in Fig. 4.7b. (b) Flyer radius of curvature versus time of flight as measured from 10MHz high speed imaging. A higher number indicates a more flat flyer. Superimposed is the ratio of longitudinal and average transverse deviatoric stresses to the pressure, calculated from the numerical simulations, averaged in the region highlighted by the black arrow in (a), indicating a significant departure from a hydrostatic stress state after 750 to 1000 ns of flyer travel and associated deformation of the flyer.

We have performed finite element simulations to assess the consequences of curved flyer impact on the spall strength measurement. We examine the stress state at the spall plane and the velocity history at the back surface of the target during the impact while varying the radius of curvature of the flyer by experimentally observed values from Fig. 2.9. The simulations are run in an explicit arbitrary Lagrange-Eulerian finite element framework (ALE3D [109]) that can represent multiple materials in each element to prevent significant distortion of the mesh associated with large deformations like those found in impact scenarios.

Fig. 4.7a shows a diagram of the 2-dimensional simulation with an axisymmetry boundary condition about the x-axis. The red region is the 50 µm thick and 0.75 mm radius Al flyer with some prescribed radius of curvature from high speed imaging measurements, a rigid contact boundary, and a median prescribed velocity of 850 m/s. The green region is the 100 µm thick and 1.5 mm radius specimen.

The Al flyer material is modeled as elastically isotropic (shear modulus is 27.6 GPa) with a von Mises yield criterion for Steinberg-Guinan hardening ($f = 290\text{ MPa}\cdot(1 + 125(\varepsilon_{plastic})^{0.1} \leq 680\text{ MPa}$)[110]. To reduce computational burden, the equation of state is assumed to be linear (K=74.2 GPa). The Mg alloy target material is also modeled as elastically isotropic (shear modulus is 16.5 GPa) with a von Mises yield criterion for Steinberg-Guinan hardening ($f = 150\text{ MPa}\cdot(1 + 1100(\varepsilon_{plastic})^{0.12} \leq 480\text{ MPa}$) [110]. The equation of state of the Mg alloy is Mie-Gruneisen using $K = 38.867$ GPa as the reference bulk modulus and 1.28 as the slope parameter in the $U_{shock} - U_{particle}$ relationship[111]. The Gruneisen parameter is 1.54 with a linear-shear coefficient of 0.33. The failure criterion is a simple pressure model where strength drops to zero upon achieving the critical pressure $p_{min} = \frac{1}{3}\sigma_{kk}$. The critical pressure is set to the measured spall strength from the experiments detailed in chapter 4.

As we detailed in chapter 3, our velocimetry probe diameter of tens of microns might probe a region of ∼250 µm radius on the free surface assuming conservative alignment error. We average the pressure ($\frac{1}{3}\sigma_{kk}$ and deviatoric stresses ($\sigma_{ij}^{dev} = \sigma_{ij} - \frac{1}{3}\sigma_{kk}$) in a 2.5 µm thick, 250 µm diameter region at the expected spall plane in the simulations, highlighted by the black arrow in Fig. 4.7a, to examine the ratio of deviatoric stress to pressure ($\sigma_{ij}^{dev}/\frac{1}{3}\sigma_{kk}$). The diamonds and crosses in Fig. 4.7b mark these ratios as a function of radius of curvature of the impacting flyer, showing a sizeable jump in deviatoric stress after ∼800 ns of flyer travel. The conservative radius of curvature measurements correspond to fairly constant deviatoric stress ratios until that point, indicating that the experiment can be considered as a uniaxial strain condition for a fairly large range of stand-off distances or projectile flight times. Based on the standoff-distance in this study, we expect the uniaxial strain assumption to hold in the above experiments.

Fig. 4.8 shows the spalled pulse duration with respect to impact velocity for 175 µm thick specimens, corresponding to the imposed shock stress. As the shock stress increases, we expect the associated increase in particle velocity to drive a faster shockwave, leading to a linear decrease in spall pulse duration. The linearity of the fit suggests good quality flyer impacts for all the

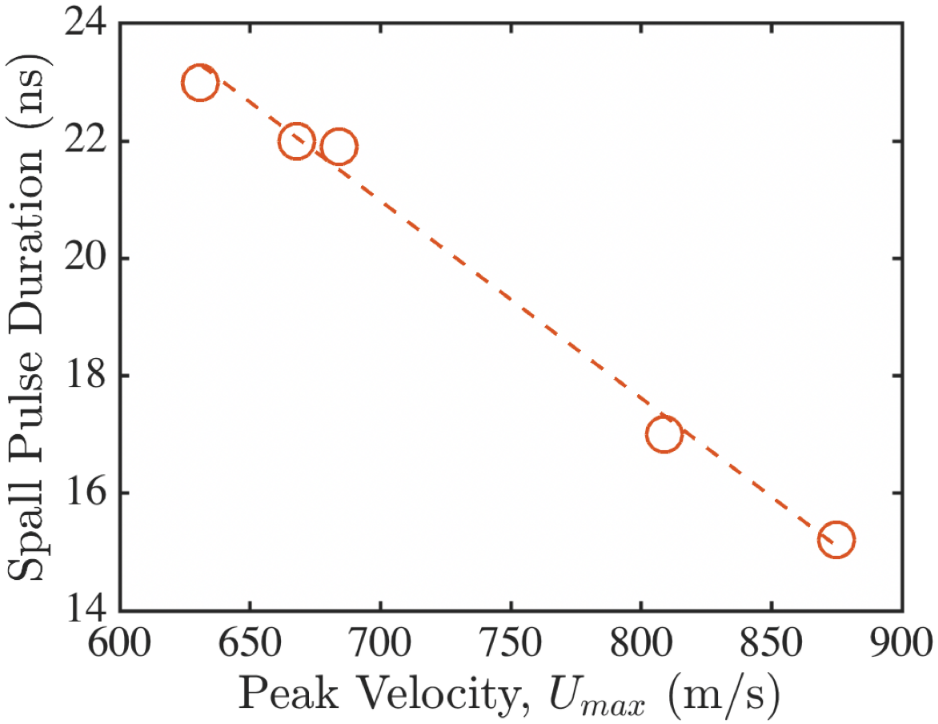

Figure 4.8: The pulse duration decreases as the shock velocities are faster from higher impact stresses.

experiments. The spalled pulse duration can serve as a metric for experiment quality in lieu of in-situ flyer quality characterization.

Also shown in Fig. 4.5 is the spall pulse ($U_{residual}$ denoted "Residual Pressure") corresponding to the residual stress in the separated spalled plate. This velocity approaches U_{t_B} in over-driven spall experiments where the magnitude and duration of the original shockwave nucleates and grows failure mechanisms to full coalescence in the spall plane [112]. In the case of limited nucleation and growth of failure mechanisms due to short shock durations and lower shock magnitudes imposed by the laser driven experiment in this work, there is a residual stress in the spall plane corresponding to (4.12) with

$U_{residual}$ substituted for U_{t_D} (i.e. $U_{residual} < U_{t_B}$ resulting in a residual tensile pressure of $\sim$ 1.15 GPa) [113, 114].

The existence of the residual stress is confirmed by the flyer planarity simulations. Fig. 4.9 shows both the velocity record and the simulated velocity record for comparison. The void growth dynamics of the real experiment prevent full spall plane coalescence, so the free surface velocity does not rebound to the shock stress as happens in the simulation.

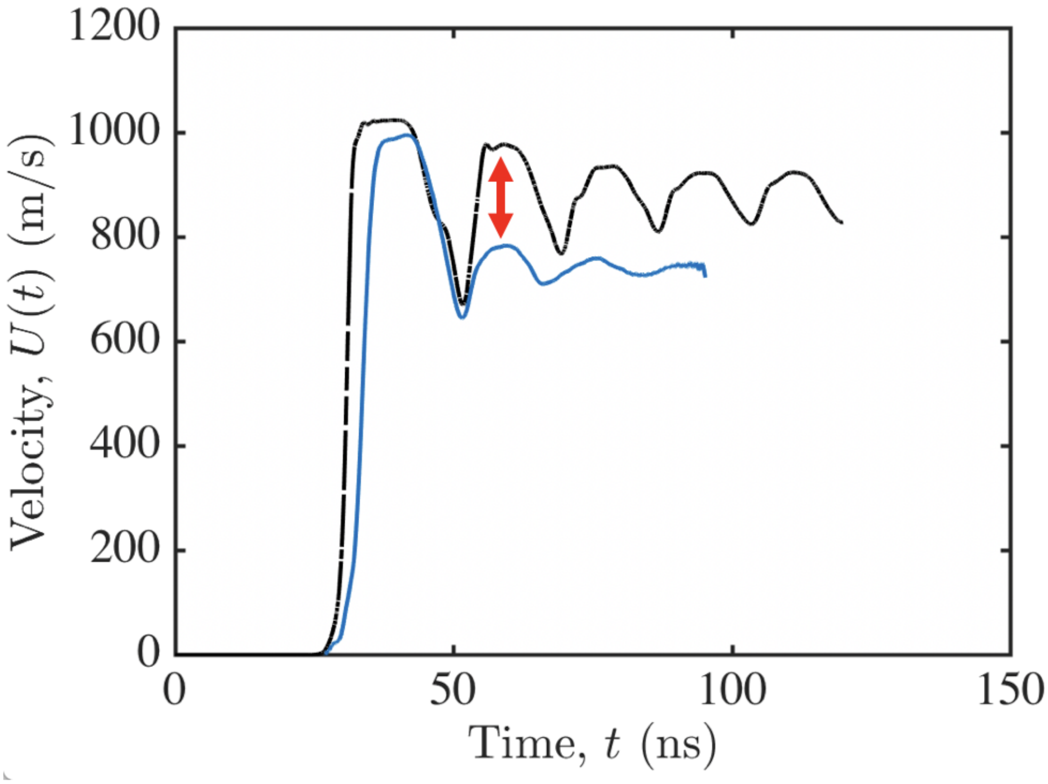

Figure 4.9: Free surface history from experiment number 2018.07.18.00011 on a 100 µm foil (blue) plotted against the simulation free surface history (black). Notice the difference in spall pulse magnitude highlighted with a red arrow indicating the presence of residual stress in the spall plane after peak tension.

The duration of tensile pressure is estimated from Fig. 4.5 by determining the crossover point between compression to tension from Σ_{peak} to Σ^* using the calculated pressures from (4.12) and (4.15) and the difference in time between the two events in the velocity history ($\sim$ 19 ns). The resulting tensile pressure history is assumed to be monotonically increasing from 0 to 1.69 GPa over $\sim$ 7 ns, effectively assuming a constant modulus between elastic and plastic behavior as the material moves from peak compression into peak tension. The velocity record indicates residual tensile pressure of about $\sim$ 1.15 GPa after peak tension, but duration and variations in residual history cannot be easily determined as the interactions between the residual pressure wave and the partially separated spall plane are very complex. We will apply this understanding of the stress history to some models for void-mediated nucleation and growth in the discussion.

4.5.2 Fractography

Fig. 4.10a-b shows SEM micrographs of 175 and 100 μm specimens with increasing magnification. The spalled plate has not delaminated in the 175 μm thick sample shown in Fig. 4.10a so the image is of the target free surface where interferometry measurements are made. There are various cracks across the surface indicating that failure has not completely linked up in the spall plane. A micro-computed tomography (μ-CT) scan is taken of this sample to better understand the damage level in the target that cannot be characterized through SEM (Fig. 4.11). The 100 μm thick samples frequently separated into two or three large fragments with a crack running through the center of the sample where the flyer impacts. These fragments often featured regions where the spalled plate dynamically tore away during the deformation process or during impacts with the acrylic test chamber just after the experiment during recovery. Fig. 4.10b shows one such fragment of a 100 µm thick sample where the spalled plate tore away during the experiment revealing the spall surface below. The exposed principal spall plane is visibly rough, yet stops at the ends of the torn away region, indicating localized failure. The spalled regions show voids of $\sim$2.5 µm diameter, but we perform a more rigorous analysis on void sizes using the μ-CT scan.

A micro-computed tomography scan of the 175µm sample in Fig. 4.10a is shown in Fig. 4.11. The scan is segmented to show low density regions in red. A Bruker Skyscan 1172 micro-CT (Kontich, Belgium) was used to scan the sample with a voxel size of 0.81 µm^3. The reconstructed micro-CT scan indicates the existence of a principal spall plane where voids are clustered. The spall plane consists of a $\sim$1 mm diameter and $\sim$20 µm thick disk containing a confluence of voids. The diameter of the spall plane is less than the flyer diameter, as expected, due to the confinement from the outer edges of the $\sim$1.5 mm diameter impacted region from the $\sim$3 mm diameter specimen. All of the void growth is along the principal spall plane, but is not linked up completely, indicating that void growth and coalescence initiates and progresses at regions in the microstructure where a void, inclusion, precipitate, grain boundary, or other inhomogeneity existed, but perhaps did not have the requisite energy to completely link the entire spall plane together. To obtain void statistics from the experiment shown in fig. 4.5, the reconstructed scan is segmented in MATLAB using Otsu thresholding. A morphological closing operation using

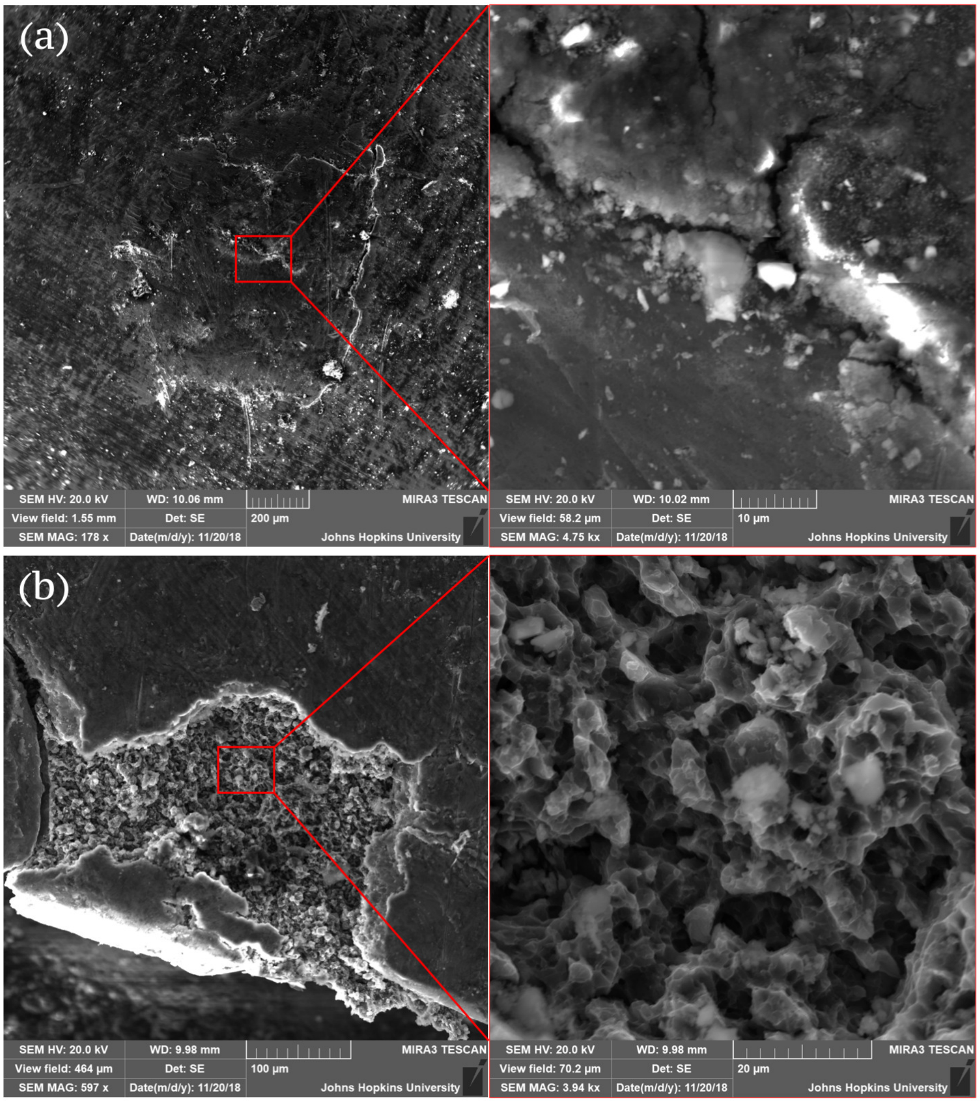

Figure 4.10: (a) SEM images of specimen surface after spall experiment on 175 µm thick foil. The specimen exhibits incipient spall, as evidenced by the lack of complete separation of the spalled plate. (b) SEM images of a 100 µm thick foil that fractured after impact. Despite the catastrophic failure of the specimen, localized regions of void growth did not completely link up to form a full spall plane. Instead only some regions of the spalled plate delaminated.

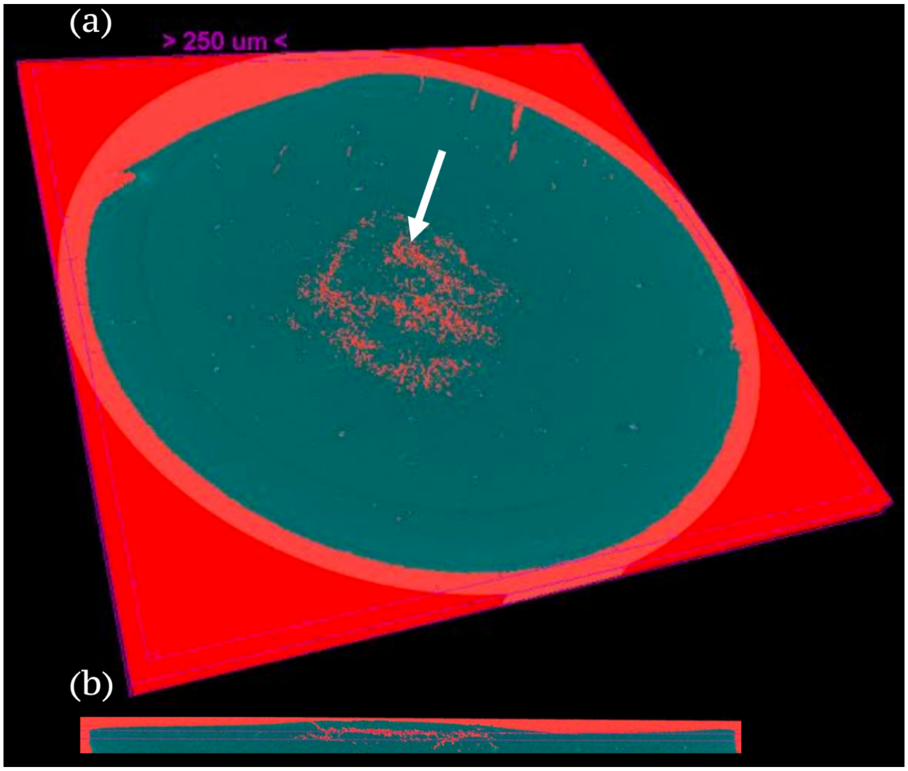

Figure 4.11: (a) Isometric view of a CT scan of a specimen exhibiting incipient spall low density regions (air and voids) colored red. The fully dense un-deformed regions surrounding the spall plane are colored in gray. The white arrow denotes a region of voids corresponding to a crack that reaches the free surface of the specimen (Fig. 4.10a). (b) Side view a CT scan of the same specimen exhibiting incipient spall. The white arrow denotes a region of voids corresponding to a crack that reaches the free surface of the specimen (Fig. 4.10a)

a disk structuring element is performed to eliminate mis-classified pixels due to noise. The size of the structuring element is chosen by examining mean void radius from the segmented scan while changing the structuring element size. The structuring element was varied between 2 pixels and 5 pixels. The smallest changes in mean void size with respect to changes in filter threshold occur with a structuring element size of 3 pixels.

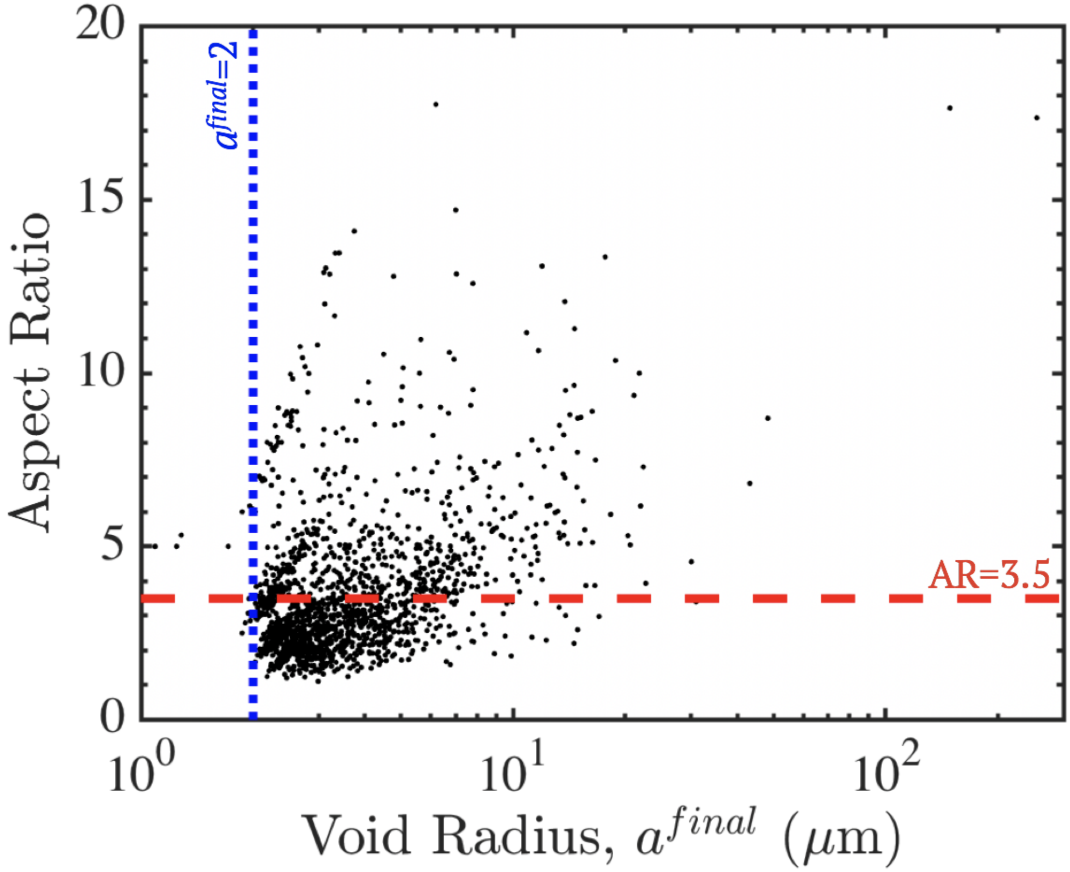

Figure 4.12: Void radius and aspect ratio data from filtered μ-CT scan of deformed target. The void radius is the average of the principle radii of each void. A dashed line is shown where data is excluded above aspect ratios of 3.5. A dotted line is shown where data is excluded below void radii of 2 µm.

The resulting data captures $\sim$ 2500 voids with radii, a^{final}, (average of principle radii of each void) from 1 µm to 148 µm and aspect ratios (ratio of largest principle radius to smallest principle radius of each void) from unity to 17.75 as shown in Fig. 4.12. Notice that the scan voxel size will make sub-micron voids impossible to resolve in this dataset. Some of the captured void data undoubtedly consists of individual voids that have impinged upon each other to create a coalesced void. To isolate individual voids, we leverage the simulations reported by Selvarajou, Joshi, and Benzerga [115] that consider plastic anisotropy and orientation-dependent activation of deformation mechanisms in pure Mg to estimate individual void aspect ratios under far field loading of various triaxialities. Their results indicate a maximum aspect ratio of 3.5 for a single deforming void as a result of directional plastic strain accumulation from the wide variance in critically resolved shear stress for slip systems and deformation twinning in Mg, so we remove those voids from the μ-CT dataset with larger aspect ratios (remove data above red dashed line in Fig. 4.12). The empirical cumulative distribution of the void radii data for aspect ratios underneath 3.5 is shown in Fig. 4.13 (solid blue line). A bounded power law distribution is fitted to the data,

$$g(a^{final}) = \frac{\beta(a^{final})^{-\alpha}}{((a^{final}_{max})^{\beta} - (a^{final}_{min})^{\beta})}, \tag{4.16}$$

with $\beta = 1 - \alpha$ and $\alpha = 3$ (the α and β parameters are used to make notation compact and represent the shape factor of the power law), shown as a red dashed line in Fig. 4.13. This fit shows reasonable agreement with the experimentally observed voids until void radii exceed $\sim$ 6 µm. The inset in Fig. 4.13

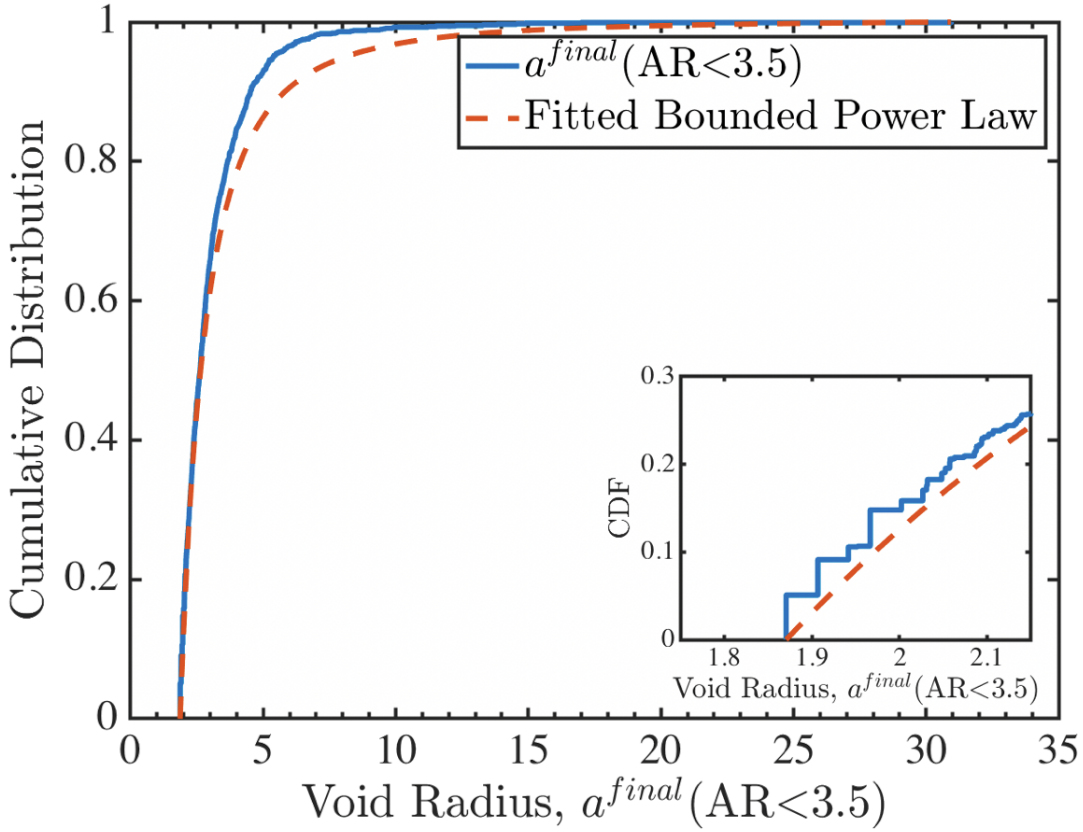

Figure 4.13: Experimental cumulative distribution function of void radii data when the void is under aspect ratios of 3.5 shown in solid blue. The dashed red line is the cumulative distribution of a fitted bounded power law distribution. The inset shows voids with radii<2 µm are mixed with noise, so we exclude that data as shown in Fig. 4.12 (red dashed line)

shows data clustering for void radii smaller than 2 µm, suggesting that data under that threshold is mixed wtih noise from measurements near the μ-CT instrument resolution limit. Those $\sim$ 150 voids are to the left of the dotted blue line in Fig. 4.12.

4.6 Discussion

4.6.1 Uncertainty Analysis

Analysis of the target free-surface velocity history is the primary method of understanding the experiments we have performed. Accordingly, errors and uncertainties in the free-surface velocity history will propagate into the reported values of spall strength, and tensile loading strain rate through (4.12) and (4.13). In addition to velocity history errors, microstructure variability in such a fine grained magnesium specimen will inevitably lead to variability in the spall strength, leading to another source of uncertainty in the results. We now perform a sensitivity analysis to understand the envelope of error propagation similar to that from chapter 3.

4.6.1.1 Spall Strength

Uncertainty in the reported spall strength comes from uncertainties in velocimetry, variation in material, and variation in loading conditions. Velocimetry uncertainty can potentially originate from uncertainty in velocimetry alignment angle $\mathcal{B}$, frequency and wavelength stability of interferometry lasers f_D, f_r, and λ_D, and frequency analysis methodology $f(t)$. Uncertainty in material parameters ρ and c_0 will also affect the measurement. To analyze the bounds of this uncertainty, we substitute the expression for normal velocity detection (3.7) into (4.12),

$$\begin{aligned}\Sigma^* =&\frac{1}{2}\rho c_0(U(t_B)-U(t_D)),\\ =&\frac{1}{2}\rho c_0\frac{\lambda_D}{2\cos\mathcal{B}}(f(t_B)-f(t_D)),\end{aligned} \tag{4.17}$$

where t_B and t_D denote times from the velocity record corresponding to the spall pullback shown in Fig. 4.2c. The first-order second moment (first standard deviation, 95 percent) of each contributing variable in (4.17) as a result of all underlying uncertainties in the velocity record provides a complete spall strength uncertainty figure,

$$\begin{aligned}\delta\Sigma^* =& \{\sum_i[\frac{\partial\Sigma^*(X_i)}{\partial X_i}\cdot\delta X_i]^2\}^{1/2},\\ \delta\Sigma^* =& \{[-\frac{1}{2}\rho c_0\frac{\lambda_D}{2}\tan\mathcal{B}\sec\mathcal{B}(f(t_B)-f(t_D))\cdot\delta\theta]^2+\\ &[\frac{1}{2}\rho c_0\frac{\lambda_D}{2\cos\mathcal{B}}\cdot\delta f(t_B)]^2+[-\frac{1}{2}\rho c_0\frac{\lambda_D}{2\cos\mathcal{B}}\cdot\delta f(t_D)]^2+\\ &[0\cdot\delta f_D]^2+[0\cdot\delta f_r]^2+[\frac{1}{2}\rho c_0\frac{1}{2\cos\mathcal{B}}(f(t_B)-f(t_D))\cdot\delta\lambda_D]^2+\\ &[\frac{1}{2}\rho\frac{\lambda_D}{2\cos\mathcal{B}}(f(t_B)-f(t_D))\cdot\delta c_0]^2+\\ &[\frac{1}{2}c_0\frac{\lambda_D}{2\cos\mathcal{B}}(f(t_B)-f(t_D))\cdot\delta\rho]^2\}^{1/2},\end{aligned} \tag{4.18}$$

By this analysis, the measurement is not sensitive to frequency stability of the interferometry lasers δf_D and δf_r, but does have a relationship with the wavelength stability $\delta\lambda_D$. The two lasers used in our experiment have less than 1kHz linewidth by specification, corresponding to an 8 attometer (10^{-9}

nm) spectral deviation, an insignificant contribution to the uncertainty budget. In contrast, misalignment angle $\mathcal{B}$ can play a major role, but we expect this Poynting error to be under a degree at most as both the interferometry objective and the target itself are carefully aligned prior to each experiment. A conservative estimate of 3 degree error corresponds to a $\sim$12 MPa uncertainty in the AZ31B spall strength assuming a 0.5 GHz pullback signal frequency, an uncertainty that is two orders of magnitude below spall strength. Material properties ρ and c_0 are assumed to have very little deviation ($\leq$ 0.5 percent [24]) and will not have a significant effect on measurement uncertainty ($\sim$14 MPa from material specification deviations).

The largest source of uncertainty is from the frequency analysis method, resulting in uncertainty in $f_{(t_B)}$ and $f_{(t_D)}$. The Heisenberg-Gabor limit is an estimate for velocity uncertainty with respect to the time averaging done in a frequency analysis [92, 95],

$$\Delta t \Delta f \geq \frac{1}{4\pi}. \tag{4.19}$$

Our interferometry captures data at 40GSamples per second, and the phase differentiation of the signal frequency occurs over 120 sample or 3 nanosecond windows, so an estimate for the frequency uncertainty is then $\delta f(t_B) = \delta f(t_D) \sim$ 26.5MHz or a $\sim$160 MPa deviation in spall strength, which is significant, but on the order of uncertainties commonly reported in spall strength experiments at similar strain rates [116].

4.6.1.2 Strain Rate

The strain rate can be very roughly estimated as U_{impact}/h_{target} (8.5×10^6 s^{-1} for 100 µm thick foils and 4.9×10^6 s^{-1} for 175 µm thick foils). The tensile loading rate of each experiment can be more specifically estimated by (4.13) after substituting (3.7) and taking into account the misalignment angle $\mathcal{B}$, but we near the time resolution limitations of the heterodyne interferometer with our digitizing sampling rate, so considerable challenges remain with respect to measurement uncertainty. Following the same process above, the uncertainty budget is,

$$\delta\dot{\varepsilon} = \{\sum_i [\frac{\partial\dot{\varepsilon}(X_i)}{\partial X_i} \cdot \delta X_i]^2\}^{1/2}, \tag{4.20}$$

$$\begin{aligned}
\delta\dot{\varepsilon} = \{[-\frac{\lambda_D}{4C_0^2 \cos\mathcal{B}} \frac{f(t_C) - f(t_D)}{|t_C - t_D|} \cdot \delta c_0]^2 + \\
[\frac{1}{4c_0 \cos\mathcal{B}} \frac{f(t_C) - f(t_D)}{|t_C - t_D|} \cdot \delta\lambda_D]^2 + \\
[\frac{\lambda_D \tan\mathcal{B} \sec\mathcal{B}}{4c_0} \frac{f(t_C) - f(t_D)}{|t_C - t_D|} \cdot \delta\theta]^2 + \\
[\frac{\lambda_D}{4c_0 \cos\mathcal{B}} \frac{1}{|t_C - t_D|} \cdot \delta f(t_C)]^2 + \\
[-\frac{\lambda_D}{4c_0 \cos\mathcal{B}} \frac{1}{|t_C - t_D|} \cdot \delta f(t_D)]^2 + \\
[-\frac{\lambda_D}{4c_0 \cos\mathcal{B}} \frac{f(t_C) - f(t_D)}{|t_C - t_D|^2} \cdot \delta t_C]^2 + \\
[\frac{\lambda_D}{4c_0 \cos\mathcal{B}} \frac{f(t_C) - f(t_D)}{|t_C - t_D|^2} \cdot \delta t_D]^2\}^{1/2}.
\end{aligned} \tag{4.21}$$

Assuming a duration of $\tau_{shock} = t_C - t_D = 22ns$ and a 0.5 GHz pullback frequency once again, the largest source of measurement uncertainty is from measuring times t_C and t_D. The material constant uncertainty in c_0 only contributes a uncertainty of $9.7e3s^{-1}$, three orders of magnitude below the estimated experiment strain rate. Interferometer laser stability (δf_D, δf_r, $\delta \lambda_D$) contributes negligible uncertainty to strain rate and are thus omitted from (4.21). A conservative estimate of 3 degrees of alignment error results in 1.5×10^4 s^{-1} uncertainty, two orders of magnitude below the expected strain rate.

The largest contributors to uncertainty in strain rate are from the velocity and time measurements from the velocity history. Once again, the competition between time and velocity uncertainty comes into play, but this time with greater effect. If the data is processed with a 120 sample or 3 nanosecond differentiation stencil, the combined uncertainty from $\delta f(t_C)$, $\delta f(t_D)$, δt_C, and δt_D is 2.7×10^5 s^{-1}, only an order of magnitude under the expected strain rate. By inspection of (4.21), the uncertainty is exacerbated by decreasing τ_{shock}, so higher strain rate experiments will feature higher uncertainties in strain rate. This effect is reflected in Fig. 4.6 where the strain rate error bar size increases with strain rate. To keep the uncertainty within a reasonable bound, we process the velocity history using a 3ns differentiation stencil, but process the event times using a 1ns differentiation stencil to reduce the uncertainties δt_C and δt_D. This approach does result in an estimated decrease in uncertainty and is the method applied to present error bars in strain rate for our results in Fig. 4.6.

4.6.2 Void Growth Dynamics and Critical Nucleation Pressure

The stability criterion of a single void in an infinite, elastic, perfectly-plastic matrix under far-field hydrostatic tension was proposed first by Hill [117] and extended by Huang, Hutchinson, and Tvergaard [118] and then modified by Wilkerson and Ramesh [119] to incorporate Hall-Petch strengthening effects as a function of material grain size,

$$\mathcal{R}_y = \frac{2}{3}(\sigma_0 + \frac{k_y}{\sqrt{d_g}})\{1 - ln\frac{3}{2}(\frac{\sigma_0}{E}) + \frac{k_y}{E\sqrt{d_g}}\}, \tag{4.22}$$

where the critical pressure for unstable growth $\mathcal{R}_y$ depends on Hall-Petch reference strength σ_0, Hall-Petch strengthening constant k_y, grain size d_g, and Young's modulus E. To incorporate nucleation into a critical pressure threshold, Wilkerson and Ramesh [119] consider the maximum possible pressure for lattice instability as the ideal tensile strength of the material, $\mathcal{R}_{eos} = \rho C_0^2/4S$ with S as the linear parameter of the shock-velocity to particle-velocity equation-of-state, and assume that the critical nucleation pressure at any random position, $\mathcal{R}_{cr}$, in the material lies between these two values. The stochastic distribution of the critical pressures between $\mathcal{R}_y$ and $\mathcal{R}_{eos}$ remains difficult to determine for a given material, so we attempt to characterize it here.

Molinari and Wright [101] have reported a solution to an evolution law for inertia mediated void growth in an infinite, elastic, perfectly-plastic matrix under monotonically increasing far-field hydrostatic tension, giving the final void radius of an initially infinitely small void as,

$$a^* = \sqrt{\frac{8}{33}}(\dot{\Sigma}^* \sqrt{\rho})^{-1} \langle \Sigma^* - \mathcal{R}_{cr} \rangle^{3/2}. \tag{4.23}$$

Notice that (4.23) gives the void radius at the moment of peak tension a^*, but that our captured void radius statistics, for a^{final}, are from the recovered sample after any post-spall loading. We examine the statistics of the a^{final} void radius distribution to learn the extent of the difference between a^{final} and a^*. Following Molinari and Wright [101] to examine irrecoverable porosity from the distribution of voids at spall, the plastic change in specific volume, $\Delta v_p / v_0$, when porosity is low ($\sim$ 10 percent or less), is estimated as [101],

$$\frac{\Delta v_p}{v_0} = \frac{4\pi}{3} N_v \int_0^\infty g(a) a^3 da, \tag{4.24}$$

with number density N_v, and probability density of void size $g(a)$. In the simplest possible equation of state, $\Sigma = K \frac{\Delta v_e}{v_0}$, using the recoverable change in specific volume $\Delta v_e / v_0$, the peak tension is achieved when $\dot{\Sigma} = 0$, or,

$$\dot{\Sigma} = \dot{K} \frac{\Delta v_e}{v_0} + K(\frac{\dot{v}}{v_0} - \frac{\Delta \dot{v}_p}{v_0}) = 0, \tag{4.25}$$

where $v = v_e + v_p$ is the total volume [120]. In the case when $\Delta v_e = 0$, the time derivative of (4.24) now results in an expression relating volumetric strain rate to the time derivative of porosity at spall. The subset of void data is now approximated by the bounded power law distribution in (4.16) from $a_{min}^{final} = 1.87$ µm until $a_{max}^{final} = 6$ µm. After substituting this density function into (4.24) and taking the time derivative as per (4.25), the resulting expression equating the volumetric strain rate to the porosity is, assuming that the number density N_v does not change during the loading,

$$\frac{\dot{v}}{v_0} = -\frac{4\pi}{3} N_v \frac{2}{(a_{max}^{final})^{-2} - (a_{min}^{final})^{-2}} \dot{a^*}. \tag{4.26}$$

The time derivative of (4.23) under monotonically increasing tension is $\dot{a^*} = \sqrt{6/11}\sqrt{\langle \Sigma^* - \mathcal{R}_y \rangle / \rho}$ [101], so (4.26) can be inverted to find the spall strength as a function of the void distribution:

$$\Sigma^* = \mathcal{R}_y + \Big(-\frac{\dot{v}}{\pi v_0} N_v^{-1} ((a_{max}^{final})^{-2} - (a_{min}^{final})^{-2}) \sqrt{\frac{99}{384}} \sqrt{\rho} \Big)^2. \tag{4.27}$$

Using the reference density $\rho = 1773.75$ Kg/m^3 [24], strain rate measured from the velocity record $\dot{v}/v_0 = 3 \times 10^6$ s^{-1}, $\sigma_0 = 12.2$ MPa [121], $k_y = 7.2$ MPa $\cdot$ mm$^{1/2}$ [121] and $d_g = 3$ µm [79], only the number density is required to estimate the spall strength from the final void distribution. We estimate the number density by examining mean void spacing l_{nn} from the reconstructed μ-CT data for this subset of final voids, and then calculating the number density as $N_v = 1/l_{nn}^3 \sim 1.3 \times 10^{14}$ m^3 to obtain an estimate for the spall strength as 1.79 GPa. This is on the order of the spall strength measured from the velocity record (1.69 GPa) but we note that this spall strength estimate has a wide margin of deviation- the maximum and minimum void sizes and mean void spacing have large standard deviations. The analytically estimated strength is higher than the strength from the velocity record, suggesting that the subset of voids used in (4.27) may not be correct.

In all likelihood, there is further void growth after reaching peak tension during the spall event because the velocity record indicates residual tension in the spall plane. The post-mortem recovery and analysis indicates regions of voids that have not linked up (incipient spall), preventing relaxation of the high tensile stress at the spall plane, so $a^{final} > a^*$ from further growth driven by the residual tension after peak. Even in the case of over-driven spall, there is a short transient of tension after peak tension as the coalescing failure relaxes stress in the spall plane, growing the voids so that $a^{final} > a^*$. We must consider the input void distribution when estimating the critical nucleation pressures. Wilkerson and Ramesh [122] have demonstrated that under a transitional void radius a^*_{trans}, void growth is limited by dislocation drag mediated resistance. They present a closed form expression for $a^*_{trans} = \frac{3}{bN_m c_s}\sqrt{\frac{6}{11}\langle \Sigma^* - R_y \rangle}$ with Burgers vector $b = 0.321$ nm [121], mobile dislocation density $N_m =\sim 1 - 10 \times 10^{15}$ m^{-2} [123], and shear wave speed $c_s = 3065$ m/s [24], resulting in a transitional void radius between 1.7 and 0.17 µm depending on the mobile dislocation density. When above this transitional void radius, void growth rates are controlled by inertial resistance. Inertia mediated void growth rates are uniform across initial void radii, implying that both $a^{final}_{min} = \Delta a + a^*_{min}$ and $a^{final}_{max} = \Delta a + a^*_{max}$. To determine Δa, we consider the largest possible void radius during spall, a^*_{max}, which is generated when $\mathcal{R}_{cr} = \mathcal{R}_y$ in (4.23). After substituting the remaining parameters from the material properties and from the velocity record, ($\dot{\Sigma}^* = 2.46 \times 10^8$ GPa/s,

$\Sigma^* = 1.69$ GPa) the resulting maximum void radius is $a^*_{max} = 1.702$ μm. Measured radii over this value are assumed to be voids that have coalesced to generate an effective radii larger than for a single void. To account for this, we assume that $\Delta a = a^{final}_{min} = 2$μm to filter noise out of small voids and discriminate against void radii larger than $a^{final}_{min} + a^*_{max} = 3.702$ μm, leaving $\sim$ 800 voids in the dataset.

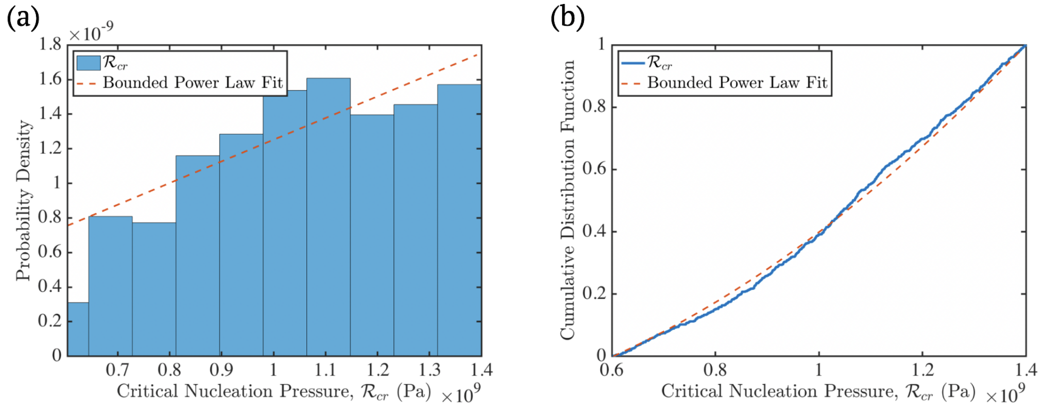

Figure 4.14: (a) Probability distribution function of critical nucleation pressures $\mathcal{R}_{cr}$ calculated from observed void radii a^{final}. The dashed line is a bounded power law distribution fit. (b) Cumulative distribution function of critical nucleation pressures $\mathcal{R}_{cr}$ calculated from observed void radii a^{final}. The dashed line is a bounded power law distribution fit.

The resulting subset of void radii is sampled randomly a million times with sampled a^* radii inserted into (4.23), inverting the expression to obtain an estimate for $\mathcal{R}_{cr}$. The probability density and cumulative distribution of resulting nucleation pressures from this monte carlo procedure are shown in Fig. 4.14a-b (solid blue) with an overlaid bounded power law fitted to the data (dashed red line). The resulting experimental distribution begins at $\mathcal{R}_y$ and ends at Σ^* as expected. The fitted bounded power law $g(\mathcal{R}_{cr})$ follows the same analytical form of the probability density for a^{final} in (4.16) but with

$\beta = 1 - \alpha$ and $\alpha = -1$. The fit stops at nucleation pressures higher than ~ 1.4 GPa, corresponding to smaller void radii where errors in the μ-CT technique are the largest, so that data is omitted from Fig. 4.14a-b.

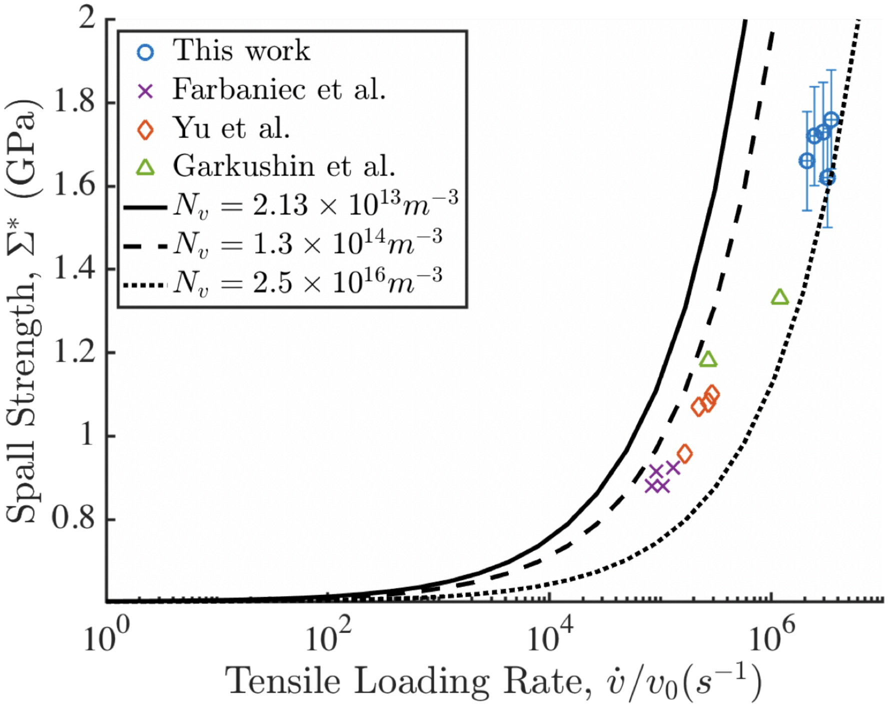

Figure 4.15: Modeled trend in spall strength with respect to strain rate using measured cavity number densities N_v and critical nucleation pressure probability density (black lines). Experimental spall strength measurements on similar Mg alloys are overlaid.

Assuming that the shape of the nucleation pressure threshold distribution remains the same from Σ^* to $\mathcal{R}_{eos}$, an analytical model is applied to estimate spall strengths across various strain rates (see Wilkerson and Ramesh [119] for complete details),

$$\Sigma^* = \mathcal{R}_y + \frac{K}{\zeta} \sqrt[\beta+7/2]{\frac{(\mathcal{R}_{eos} - \mathcal{R}_y)^{\beta} \frac{\dot{v}}{v_0}}{\frac{4}{3}\pi(\frac{8}{33})^{\frac{3}{2}} C_0^3 K^{\beta} \xi N_v}} (\frac{\dot{v}}{v_0})^{\frac{2}{\beta+7/2}}, \tag{4.28}$$

with $\zeta = \frac{9+2\beta}{7+2\beta}$ and $\xi = (\beta + 9/2)2^{\beta}\Gamma(\beta)\prod_{i=1}^{\beta}(9+2i)^{-1}$. The standard deviation when calculating l_{nn} in N_v prescribes a wide range of possible void number densities from $2.13 \times 10^{13}\ m^{-3}$ to $2.5 \times 10^{16}\ m^{-3}$, so each bound and the mean is plotted as lines in Fig. 4.15. Though the alloy microstructures are different from the literature cases, the overall trend of rising spall strength with strain rate is nicely captured by the model (overlaid on Fig. 4.15). Our specimens feature a more deformed microstructure, so the potential number of cavitation sites perhaps trends higher and our spall strength data more closely follows the larger number density trend (dotted black line).

We acknowledge that the resulting distribution of nucleation pressures relies heavily on the selection of Δa, and that the simulated distribution cannot describe pressures above the spall strength of the material, even though the critical nucleation pressure in regions where void growth did not occur is obviously higher than the measured spall strength. Nevertheless, this novel approach provides an experimentally observed distribution of cavitation nucleation pressures- giving at the very least a sense of the shape of the distribution- that is conventionally only reported as a single peak tensile pressure value in spall experiments. Additionally, over half of the measured void radii are proposed to be a combination of two or more impinged voids and tend to be larger than 3.7 μm, far past the transitional void radius between dislocation-drag mediated and micro-intertia mediated void growth, suggesting that the growth of large voids that are responsible for spall failure is micro-inertia dominated.

4.6.3 Variability in Spall Strength

The measured spall strengths are not consistent between the two sample thicknesses in this study, and there is some variability within each microstructure as well. One possibility is that geometries in the experiment configuration can interact with the imposed loading conditions to cause variation in the measured spall strength. Another possibility is variation in material properties of the two thicknesses such that the spall strength of the 175 µm thick samples is indeed larger than the 100 µm thick samples as shown in Fig. 4.6. Both possibilities are explored in this section.

The ratio of flyer thickness to sample thickness can affect the loading condition at the spall plane. Conventional flyer plate experiments have been shown to build stress loading in a more trapezoidal fashion where the peak stress is achieved over a short period of time and plateaus before receding or unloading. The thin flyers in LDMFP experiments imply a loading condition where stress quickly builds and recedes in a potentially triangular fashion (τ_{shock} is on the order of tens of nanoseconds), but the true loading condition is difficult to infer. The differences in loading history manifest in the spall strength through the propagation velocity in (4.12)), where a truly triangular loading history entails peak tensile stress on the wave characteristic directly between the longitudinal (with velocity $c_l = \sqrt{E/\rho}$) and bulk wave characteristics in the rarefaction fans shown in Fig. 4.2b.

The unloading tail of any imposed shock will overtake the head after some amount of time, so a triangular loading condition can be assumed for large ratios ($\geq\sim$5:1) of target thickness to flyer. In the case of a smaller thickness ratio, Kanel [124] suggested a correction factor to estimate the peak tensile load characteristic using the velocity time gradient before and after the spall event in the velocity record ($\dot{U}_1 = (U(t_C) - U(t_D))/(t_D - t_C)$ and $\dot{U}_2 = (U(t_E) - U(t_D))/(t_E - t_D)$ in Fig. 4.2c),

$$\Sigma^* = \frac{1}{2}\rho c_0(U(t_B) - U(t_D)) + \delta \tag{4.29}$$

$$\delta = \frac{h_{flyer}}{2}\rho c_0(c_0^{-1} - c_l^{-1})\frac{\dot{U}_1\dot{U}_2}{\dot{U}_1 + \dot{U}_2}.$$

In our experiments, applying the correction factor does not significantly affect any trends in measured spall strengths except to increase them by approximately 11 percent, indicating that the thickness ratios do not play a large role in the range of spall strengths.

SEM and μ-CT fractography of the AZ31B specimens indicates that our high strain rate impacts always cause some spall failure, though impact velocities are not varied much below 700 m/s in this study. Even at such a high impact velocity, the regions of coalesced voids rarely link up (from recovered specimens when the sample is not fractured), indicating damage at or just past an incipient stage. In addition, the velocity records indicate residual stress in the spall plane after peak tension, implying an absence of large scale damage. It is possible that the short loading duration causes isolated and localized void nucleation and growth, inducing scattered spall strength measurements from specimen to specimen. This scatter from the short load duration may represent the ”true” spall strength of the material as over-driven spall experiments have been shown to potentially misrepresent the spall strength because the process of linking damage completely in the spall plane diminishes the magnitude of the peak tensile pulse before reaching the target free surface for measurement with interferometry [104, 125, 77, 76]. Inertia mediated void growth models have shown excellent agreement with final void sizes in other studies [122, 126], indicating that inertial effects play a large role in void growth dynamics- these local effects will not propagate to the free surface for interferometry based measurement.

Finally, it is possible that microstructure differences detailed in the materials and specimens section are causing the difference in spall strength. In both specimen microstructures, the grain size is much smaller than the imposed shock compression, so the shock front generated will have roughness to it and will not be completely planar. Our velocimetry probes a $\sim$10 µm region on the specimen, so multiple grains will be probed during the spall event. If we focus on a region that has a weaker homogeneity in it, like a second phase particle or multiple grain boundaries, the probed strength in that region may be lower than the remaining bulk. The 175 µm thick samples consistently exhibit greater spall strength, potentially from strengthening mechanisms and from different deformation mechanisms generating different failure nucleation sites. With a somewhat smaller grain size and without dynamic recrystallization during processing to homogenize developed dislocations, grain boundaries, and other strengthening mechanisms, the 175 µm thick foils may simply have a higher resistance to void nucleation through higher yield strength from un-recovered work hardening [119]. Additionally, all experiments are shock compressed along the normal direction where both foil thicknesses feature a tilted basal texture (Fig. 4.3-4.4), but the 175 µm thick foils also show some twinned regions and more varied texture as received. The 100 μm thick foils likely feature dominant extension twinning on release, a low strength deformation mechanism often linked to low spall strength[127, 128], but some of the varied texture grains in the 175 μm thick foils may require higher resolved stress to activate deformation mechanisms to generate failure nucleation sites. In the cases of both foils, the highly deformed fine-grained microstructures present many possible failure nucleation sites and in turn can introduce some scatter into reported spall strengths.

4.7 Conclusion

In summary, we have demonstrated the capability to perform spall experiments with our laser-driven flyer launcher on thin AZ31B Mg alloy foils. We can resolve the failure process over the course of tens of nanoseconds with improved processing of photon Doppler velocimetry data and high speed imaging. Velocimetry resolution remains the most difficult hurdle in performing these experiments as we approach the resolution limits of photon Doppler velocimetry. To overcome this challenge, we modify averaging windows for different parts of the spall strength calculation to minimize measurement uncertainty. The experiment imparts a small time duration shock load that likely introduces some stochasticity to the measured spall strength through limited activation of failure mechanisms.

The shocked AZ31B Mg alloy fails at peak tensile loads that are greater than previously reported figures for fine grained Mg alloys, though the LDMFP system achieves higher strain rate loading than in previous literature. Fractography using SEM and micro-CT of the deformed specimens shows regions of void growth and coalescence in the spall plane. Ultimately, this fine grained alloy presents a wide array of microstructure features that can act as failure nucleation sites, but the tested foil with a more deformed microstructure exhibits higher spall strength.

We have also introduced a methodology to estimate the critical nucleation pressure for unstable cavitation in AZ31B Mg alloy undergoing spall failure. We use the micro-computed tomography scans of the deformed specimens to obtain final void radius statistics. Inertia mediated void growth laws allow reverse calculation from the void radius statistics to the critical pressure distribution of the Mg alloy. The measured void statistics and critical pressure distribution inform a model that captures rate dependent strength behavior. This technique provides the first ever experimentally reported distribution of cavitation nucleation pressures that are typically only reported as a single peak value from spall experiments. In the next chapter, we explore the role of second phase particles in spall failure of Mg9 wt. % Al Mg alloy.

Chapter 5

Precipitate Structure in Spall of Mg-9Al Binary Alloy

Parts of this chapter appear in a research article in preparation, where D.D.M is first author. D.D.M. conducted the spall experiments and received assistance in microscopy from Dr. M. Zhao and S. Eswarappa Prameela (Hopkins Extreme Materials Institute, Johns Hopkins University), and performed the simulations with assistance from Dr. J. T. Lloyd (U.S. Army Research Lab) on the Department of Defense High Performance Computing Modernization Program system.

5.1 Introduction

In the prior chapter we examined void growth dynamics during spall failure of AZ31B magnesium alloys. In this chapter we examine the microstructure-dependent spall failure of the Mg-9 wt.% Al alloy. Protection materials benefit from high strength, especially at the high rates of deformation that they must withstand. Magnesium and its alloys feature high specific stiffness and specific strength, coupled with low density, making them attractive for use as protection materials, but they suffer from low failure strains. The reasons for the low failure strains are not well understood, but optimizing strength and resistance to failure (at quasi-static strain rates) of Mg and alloys has been the focus of research for some time. There are several strengthening mechanisms that increase the yield threshold by harnessing different strengthening routes:

- The Peierls-Nabarro stress defines how dislocations interact with the crystal lattice of the material [129].
- Solid solution strengthening comes about as dislocations must interact with solute atoms in the lattice [130].
- Dislocations can interact with themselves and twinned lattices in forest hardening [131].
- Dislocation motion is impeded by grain boundaries which are controlled by grain size in the Hall-Petch relationship [132].
- Reheating a solutionized alloy will disperse the super-saturated alloyed elements into precipitates that act as obstacles during slip in precipitation strengthening.

In the case of precipitation strengthening, dislocations must either bow around second phase particles or cut through those particles in the microstructure, leading to strengthening behavior. In chapter 1, we discussed the widely varied critically resolved shear stresses (CRSS) for activating different deformation mechanisms in Mg that lead to so-called plastic anisotropy. The second phase particles introduced into the microstructure of Mg alloys through thermal processing (aging) may affect the effective CRSS for specific deformation mechanisms and can diminish the anisotropy [133, 134]. Although there is a strengthening effect from introducing these defects, defects may also act as the nucleation sites for dynamic failure during spall [135, 136]. To optimize a microstructure to withstand ultra-high rate loading, we desire to understand the contributions of these microstructural features to the failure strength of the material under spall.

The Mg-9 wt.% Al binary alloy has received considerable attention because of the potential to introduce second phase particles through aging (Shown as black lath precipitates in the micrograph in Fig. 5.1). The $Mg_{17}Al_{12}$ second phase particles in this alloy are easily formed through warm aging to create high volume fractions [137] with body centered crystal structure, and are stronger and stiffer than the surrounding matrix. The precipitation strengthening effect presents differently depending on loading direction in the crystal lattice owing to the plastic anisotropy in Mg and alloys, and these precipitates are continuous within grains [138], and discontinuous at grain boundaries [139, 140]. Studies of deformation mechanisms in Mg-9Al alloys have shown changes in the CRSS of basal and prismatic slip that depend on precipitate shape and habit plane, but their contribution to the dynamic tensile strength is not known [141, 142]. This simple model binary alloy is an excellent choice for

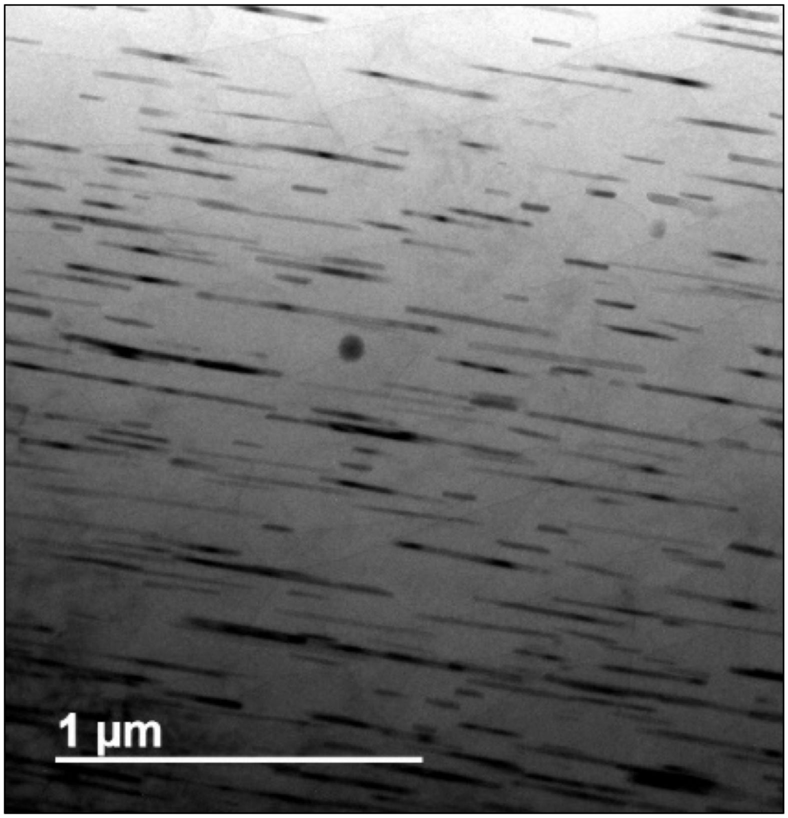

Figure 5.1: Transmission electron microscopy images of $Mg_{17}Al_{12}$ precipitates (black) in the Mg-9Al matrix.

such an investigation as the formed second phase can only take on one composition, allowing easier identification of crucial microstructure features. In this chapter we perform spall experiments using the laser-driven flyer apparatus on Mg-9Al alloy materials in two processing conditions: fully solutionized at 450° for 24 hours with no second phase particles, and peak aged to generate high aspect-ratio lath precipitates.

5.2 Mg-9Al Material

Mg-9wt%Al alloy is procured from Magnesium Elektron North America (MENA). The cast ingot is warm rolled to 60% rolling reduction to produce a strong basal texture (X-ray diffraction data is presented in Fig. 5.4). The alloy then undergoes solution treatment in a furnace at 450° C for 24 hours in Ar atmosphere followed by cold water quenching. Peak aged samples are aged at 150° C for 163 hours.

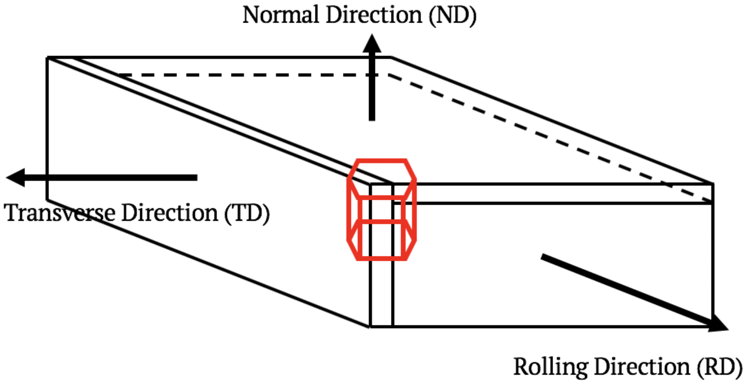

Figure 5.2: Samples cut from ingot in different orientations. These sample plates are then polished down to 200 micron thickness sheets and specimen coupons are cut using a 3 mm diameter TEM punch thereafter.

Our samples are first obtained as an ingot and warm rolled and then peak-aged (PA) or left un-aged. The processed ingot is then sectioned into 2 mm thick sheets using a wire Electro Discharge machine (EDM) with normal direction (ND) and transverse direction (TD) sheet normals (See Fig. 5.2 for a schematic of the wire EDM cut sample sheets). The specimens are then carefully polished to present a flat and planar surface for the spall experiment with increasing grits of polishing papers from 400, to 600, to 800, to 1200. The final thickness of the sheets is nominally 200 μm; however there are variations from sheet to sheet as further polishing is done to ensure planarity of the entire sheet (checked with a micrometer).

Electron backscatter diffraction (EBSD) is performed to obtain the grain sizes in the sample after both processing routes. Specimen coupons are further polished with colloidal silica solution and then electropolished using a Struers twin-jet electro-polishing machine with a solution of lithium chloride, magnesium perchlorate and 2-butoxy-ethanol in methanol as an electrolyte at 100 V and ∼40° C bath temperature. A final cleaning step is performed using a Fischione Instruments (Model 1060) ion mill at 1-2 kV driving voltage with the Ar ion guns inclined at 3° to the sample surface before mounting it into the scanning electron microscope (SEM). The resulting scans are shown for the solutionized (Fig. 5.3a) and peak aged samples (Fig. 5.3b). The solutionized samples present ∼200 μm grains while peak aging grows the grains to nominally ∼500 μm. These estimates are made through making major axis measurements while scanning different regions. We note that the introduction of the second phase makes indexing difficult for the peak aged sample. The large grained microstructure necessitates a macro-texture measurement method, so we employ x-ray diffraction to make texture measurements.

We examine the texture of the solution treated and peak aged thin foils with a symmetric X-ray diffraction analysis using a Bruker D8 Focus diffractometer. A two-theta scan is used in the range of 30-80° with a step size of 3 μm and 0.5 s dwell time. Fig. 5.4 shows the x-ray diffraction data for both solutionized and peak aged samples. Both samples exhibit strong basal texture with the

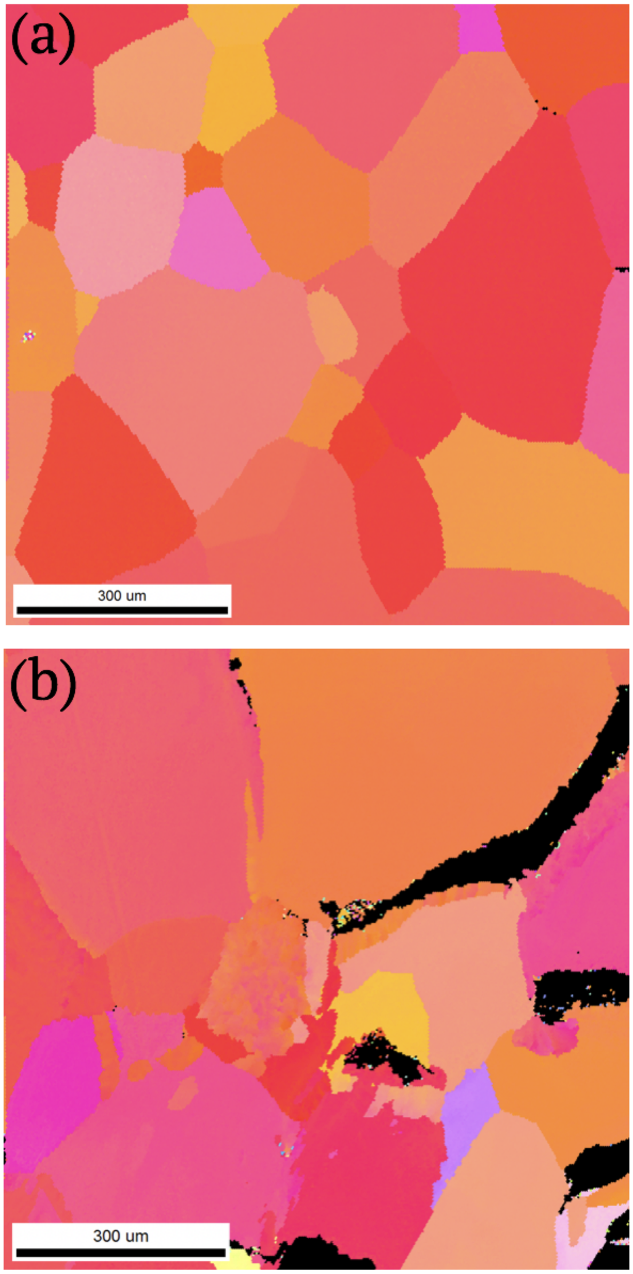

Figure 5.3: Electron backscatter diffraction (EBSD) inverse pole figures for (a) the hot rolled and solutionized material and (b) the peak aged sample.

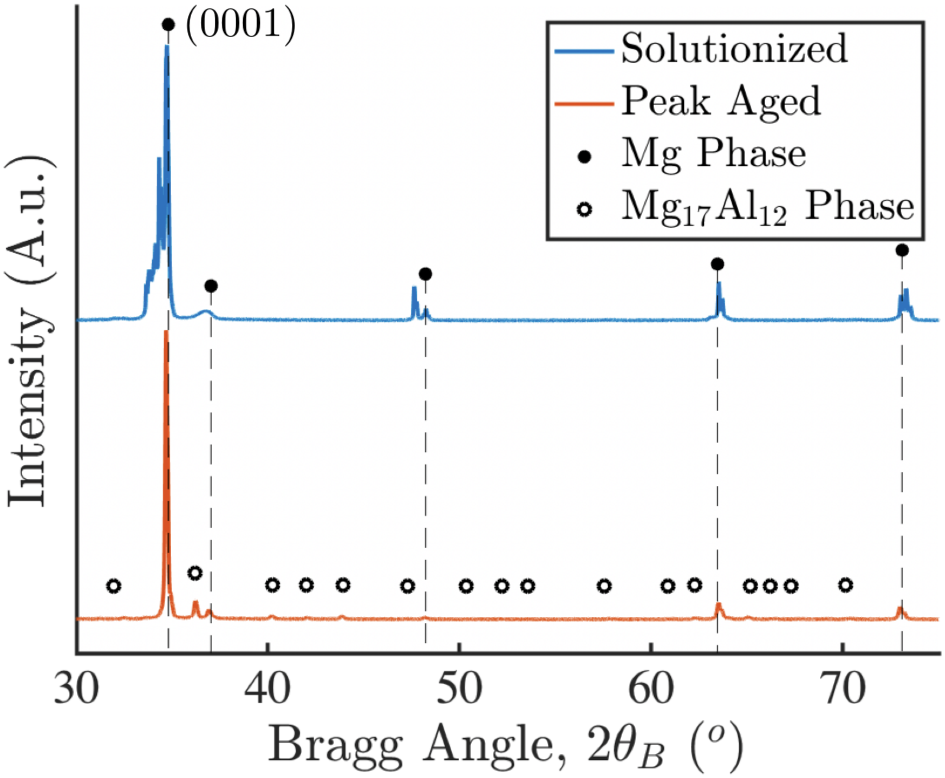

Figure 5.4: X-Ray diffraction experiments on the solutionized and peak aged samples showing a basal rolling texture for both preparations. Lattice indices are shown for the dominant (0001) Mg phase.

(0001) Mg phase having the highest relative intensity, though the aging process seems to reorient grains to show an even stronger basal texture than in the solutionized samples. Notice the small offsets from the expected Mg peaks in both scans due to the presence of fully solutionized Al atoms.

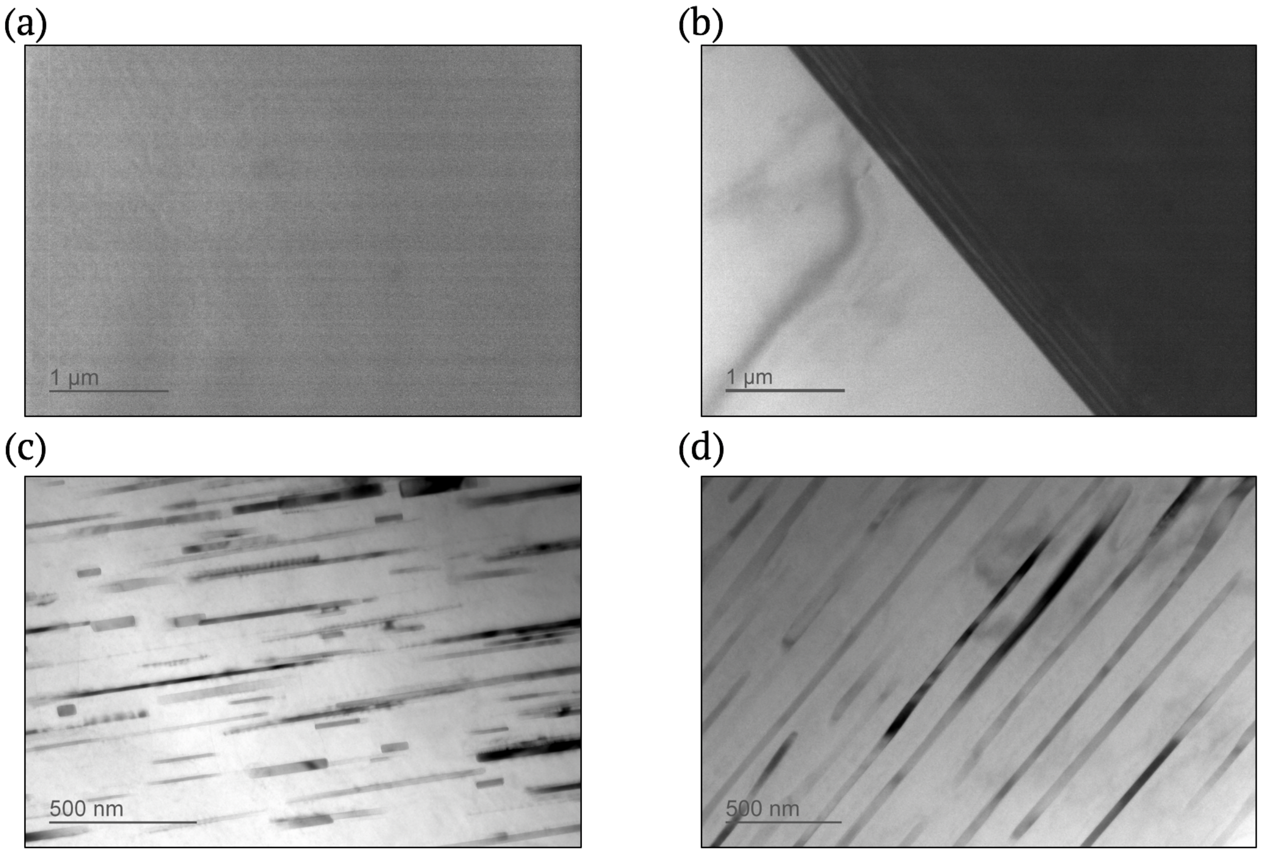

Figure 5.5: Transmission electron microscopy images of the samples taken from the TD direction. (a) Grain interior of solutionized sample. (b) Grain boundary of solutionized sample. (c) Continuous precipitates in grain interior of peak-aged sample. (d) Discontinuous precipitates at grain boundary of peak-aged sample. Notice that the grain boundary itself is not shown.

We use Transmission Electron Microscope (TEM) imaging to observe the continuous and discontinuous precipitate structure in grain interiors and grain boundaries in Fig. 5.5. Samples for TEM are taken from 3 mm diameter specimen coupons punched from the 200 μm thick foil. We then mechanically polish the coupons to 50 μm thickness using silicon carbide paper and waterless colloidal suspension. The specimen is ion-milled using a GATAN PIPS II system to create a perforation for TEM observation in a Tecnai TF 30 microscope at 300 kV. The TEM imaging indicates the presence of lath precipitates on the basal habit planes. The average width of the precipitates is 20 ± 6.2 nm with an average length of 0.73 ± 0.18 μm. In the transverse direction, the spacing between basal habit planes for the precipitates is an average of 130 ± 42 nm (Fig. 5.5c-d). The mean spacing between precipitates on the basal habit plane when looking at ND specimens is 314 ± 149 nm. These spacing measurements suggest a volumetric density of 1.56×10^{11} mm^{-3}, directly in line with measurements by Prameelaa et al. [143] of aged Mg-9Al alloy. Notice that these averages are taken from TEM images of both continuous precipitates in grain interiors and discontinuous precipitates that grow at the grain boundaries.

5.3 Results

5.3.1 Laser-Driven Spall Experiments

We use the laser-driven launcher described in chapter 2 and 3 to conduct spall experiments at impact velocities between 750 and 1000 m/s. The resulting stress state and strain rate during spall is estimated using (4.12) and (4.13) respectively, and shown in Fig. 5.6. All the experiments are conducted at tensile loading rates between 1 to 5×10^6 s^{-1}. The solutionized specimens shocked along the normal direction show spall strengths on average of 1.75±0.13 GPa over 12 experiments. Along the transverse direction, the solutionized specimens have spall strengths of 1.71±0.11 GPa over 12 experiments. The peak aged specimens shocked along the normal direction show spall strengths of 1.23±0.10 GPa over 10 experiments, while the peak aged transverse direction specimens have spall strengths of 1.44±0.15 GPa over 11 experiments. The error bars shown in Fig. 5.6 correspond to the error analysis in chapter 4, and filled regions corresponding to the total error bounds are shown for emphasis of overall trends. The number of experiments conducted (46) create a dataset with sometimes 15 % standard deviations, a function of not being able to perform EBSD analysis for each specimen prior to the experiment. It is very likely that some experiments probe misaligned grains, and the wide deviations reflect this. Even with the wide standard deviations, some trends emerge; The solutionized samples do not exhibit spall strength anisotropy, while the aged samples show a clear dependence in spall strength on loading direction where the TD orientation is stronger.

We also use optical microscopy to find the average fragment size from the recovered fragments (typically between 0, or unfragmented, up to 4 fragments per experiment) after the spall experiment has concluded. The resulting averages are shown in Fig. 5.7 and indicate larger fragments for the solutionized samples. Chhabildas et al. [144] have shown a proportional correlation between fragment size and spall strength during brittle spall that may explain our data, though we do not examine any transition between ductile and brittle spall in this study. Altogether, our results indicate little difference in spall strength with orientation for the solutionized samples, but a significant difference in spall strength with orientation for the peak aged samples. To understand the effect of orientation on the failure process, we set up numerical simulations of the precipitates undergoing shock loading in the following section.

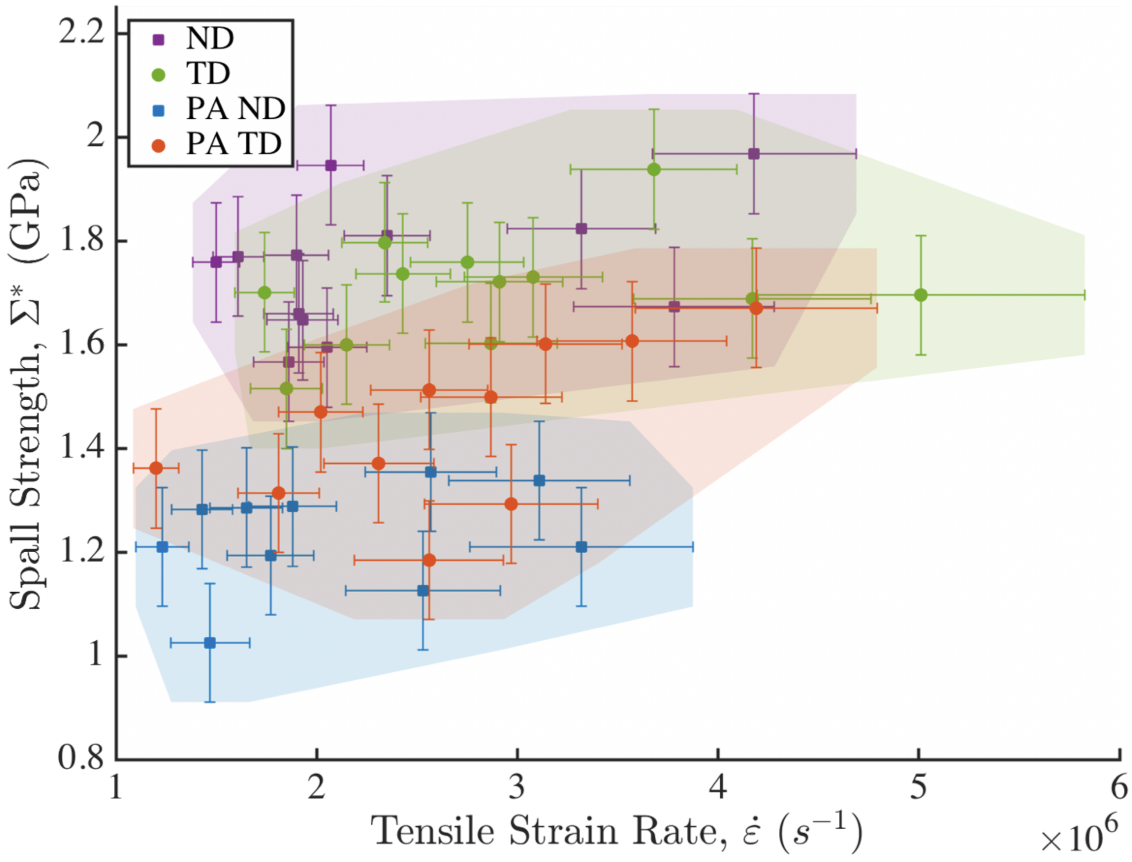

Figure 5.6: Spall strength measurements using (4.12) and strain rate estimates using (4.13) of solutionized (ND and TD) and peak aged (PA ND and PA TD) samples. The translucent boxes surround the minimum and maximum measured values for emphasis. Error bars are calculated using the measurement error discussed in chapter 4.

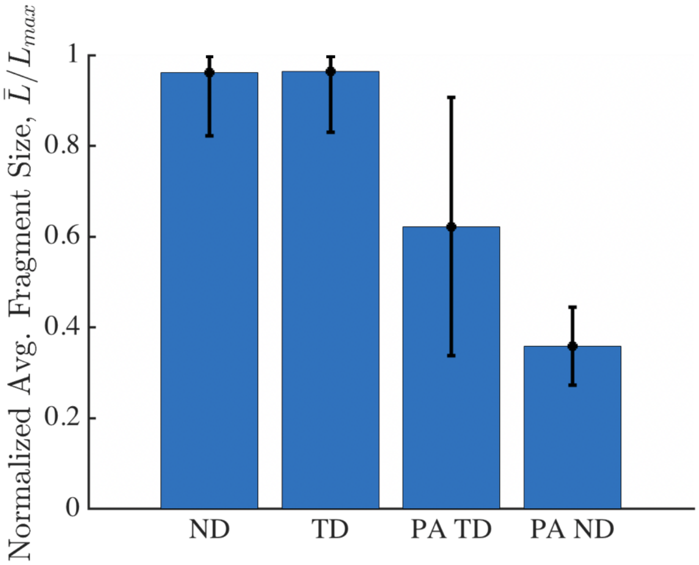

Figure 5.7: Fragments during spall experiments are measured for area by major axis and normalized against the maximum axis size (3 mm) with black bars showing standard deviation.

5.3.2 Numerical Simulations of Peak Aged Mg-9Al

We perform numerical simulations that harness the TEM observations in Fig. 5.5 to understand the anisotropy in spall strength in the peak aged Mg-9Al alloy. The simulations are run in an explicit arbitrary Lagrange-Eulerian finite element framework (ALE3D [109]) that can represent multiple materials in each element to prevent significant distortion of the mesh associated with large deformations like those found in impact scenarios. A 3-dimensional mesh is initialized with a randomized precipitate structure conforming to morphology statistics from TEM imaging. The matrix material is considered isotropic with material property selection discussed et seq. We retain the 130 nm spacing between habit planes, but place 0.730 μm long and 20 nm wide lath precipitates in $\langle a \rangle$ directions on each habit plane with uniform randomness (there is an equal chance that we place a lath in the direction of one of the three $\langle a \rangle$ axes in the habit plane) in the simulation. The aspect ratio between lath length and width approaches 40, necessitating a very fine mesh to capture individual laths (10 nm long sides for each cuboidal element). Such small elements limit the computational domain when we want to run multiple simulations to see the impact of the randomness in the generated precipitate structure, so we choose a simulation domain of $5 \times 1 \times 1\ \mu\text{m}^3$ consisting of 5 million elements. Notice that this domain is considerably smaller than in the actual experiment. The precipitate number density of $\sim 1.5 \times 10^{11}\ \text{mm}^{-3}$ from Prameelaa et al. [143] and our own observations is used to determine the number of precipitates to place on each habit plane (21 precipitates per plane) (Fig. 5.8).

We utilize the same material and failure models as in the numerical simulations in chapter 4, but the simulation is now run in a 3-dimensional framework. In the preceding section we presented evidence that at these high shock stresses and rates, the ultimate tensile failure strength is isotropic, so the model reflects this. The material is magnesium, modeled as elastically isotropic (shear modulus is 16.5 GPa), with a rate-independent Von-Mises yield criterion and Steinberg-Guinan hardening for the flow strength $\bar{\sigma}$ [110],

$$\bar{\sigma} = \sigma_0 (1 + \mathcal{A} \varepsilon_p)^n \frac{G}{G_0}, \tag{5.1}$$

with $\sigma_0 = 152$ MPa initial flow strength, $\mathcal{A} = 1100$ and $n = 0.12$ strain hardening parameters, ε_p equivalent plastic strain, and $G_0 = 16.5$ GPa initial shear modulus. There is a cap of 480 MPa to prevent unbounded hardening.

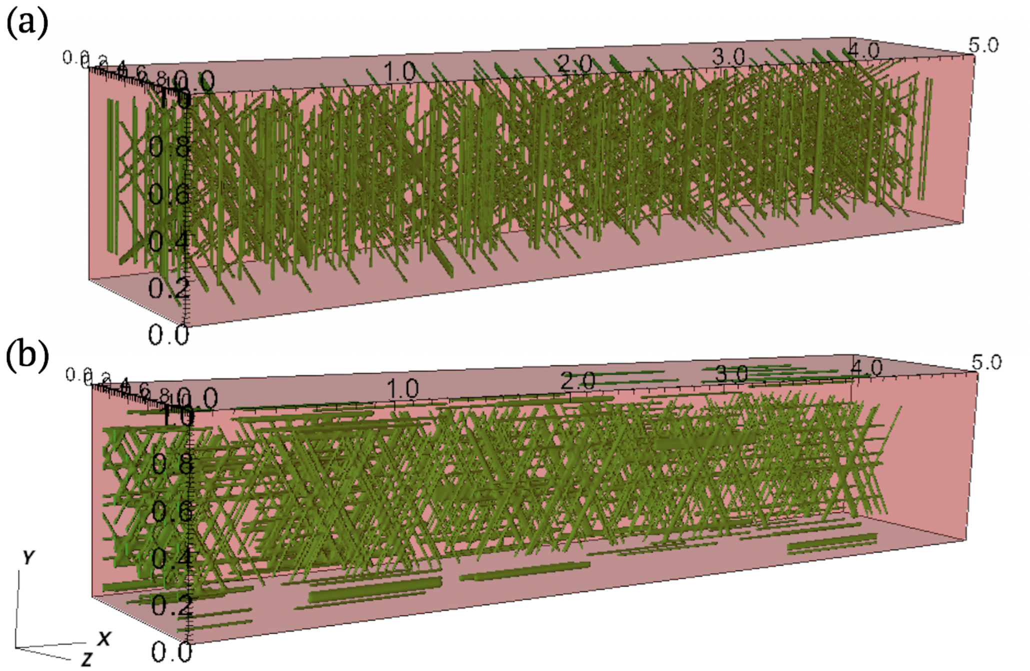

Figure 5.8: (a) 1×1×5µm Simulation domain for ND specimen shock loading. Load is applied at x=0 and free surface velocity is tracked at x=5 µm. The matrix (red) contains randomly distributed precipitates (green) that lay on evenly spaced habit planes with their plane normal vectors parallel to the shock direction. (b) Simulation domain for TD specimen shock loading. Load is applied at x=0 and free surface velocity is tracked at x=5 µm. The matrix (red) contains randomly distributed precipitates (green) that lay on evenly spaced habit planes with their plane normal vectors in the z direction.

The shear modulus evolves with further deformation as,

$$G = G_0(1 + \mathcal{C}\Sigma - \mathcal{D}T), \tag{5.2}$$

with scaling parameter $\mathcal{C} = 10.3 \times 10^{-5}$ MPa^{-1} that scales with pressure Σ and scaling parameter $\mathcal{D} = 5.09 \times 10^{-4}$ K^{-1} that scales with temperature T. These values are the same as in the flyer curvature simulations in chapter 4 and the numerical simulation of dynamic tensile failure of AZ31B Mg alloy in Lloyd et al. [145].

The equation of state is Mie-Gruneisen,

$$\Sigma = \begin{cases} \frac{\rho c_0^2 \mu (1+(1-\gamma_0/2)\mu - \mathcal{L}\mu^2/2))}{(1-(S_1-1)\mu)^2} + (\gamma_0 + \mathcal{L}\mu)\mathcal{E}, & \text{if } \mu \geq 0 \\ \rho c_0^2 \mu + (\gamma_0 + \mathcal{L}\mu)\mathcal{E}, & \text{otherwise,} \end{cases} \tag{5.3}$$

where,

$$\mu = (\frac{\rho}{\rho_0} - 1), \tag{5.4}$$

with current density ρ, reference density $\rho_0 = 1780$ kg/m^3, bulk wave speed $c_0 = 4540$ m/s, Gruneisen parameter $\gamma_0 = 1.54$, density scaling parameter $\mathcal{L} = 0.33$, linear equation of state parameter $S_1 = 1.242$ [111], and internal energy per unit reference volume $\mathcal{E}$.

The matrix has no failure model, but the precipitates have a simple failure criterion of $\Sigma = \Sigma_{min} = 2.7$ GPa to model precipitate decohesion, after which the failed material has no strength, transferring load to surrounding regions. The failed material is replaced with void material when $\mu < -0.1$ to model void growth in the failed material. The Σ_{min} value is chosen such that simulated pullback velocities match the average pullback velocities from our experiments, while the density criterion is chosen based on nominal porosity from post-mortem micro-computed tomography of AZ31B samples using our apparatus from chapter 4. We note that the trends in strength discussed hereafter did not change with different failure criterion Σ_{min} values and that the critical value is expected to deviate from measured spall strengths because the damage model does not account for micro-inertia mediated void growth. Fig. 5.9 shows the insertion of void material (blue) into the precipitate (green) laden matrix (red) as a result of achieving the failure and replacement conditions.

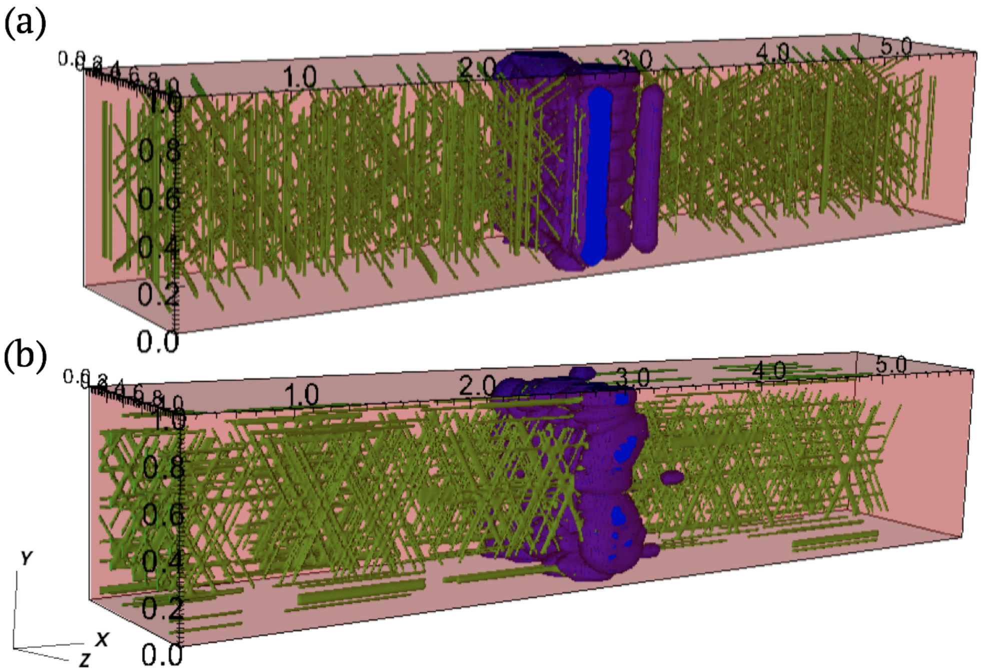

Figure 5.9: At t=1.95ns, the pressure has surpassed the critical threshold and has caused failure in the precipitates, leading to void insertion in the model (blue). At this stage, the voids have coalesced to create a complete spall plane in the model. The mesh is shown with the matrix (red) and precipitates (green) in the (a) ND orientation and (b) TD orientation.

To model the impact loading, the face of the domain where $x = 0$ sees a square velocity pulse of 425 m/s for 1 ns, after which that surface has a velocity of 0, corresponding to a 850 m/s impact with a flyer plate that has an acoustic round-trip time of 1 ns. Notice the order of magnitude decrease in flyer plate round trip time that must be used to account for the computationally expensive 5 μm long domain, and the resulting increase in loading strain rate by the same magnitude up to $\sim 10^7$ s^{-1}. The average velocity of the free surface at x =5 μm is where pullback velocities are measured during the simulation (Free surface velocities shown in Fig. 5.10). The other surfaces in the simulation domain have symmetry boundary conditions to prevent unloading waves from interfering with the loading condition, creating a uniaxial strain state in the *x* direction.

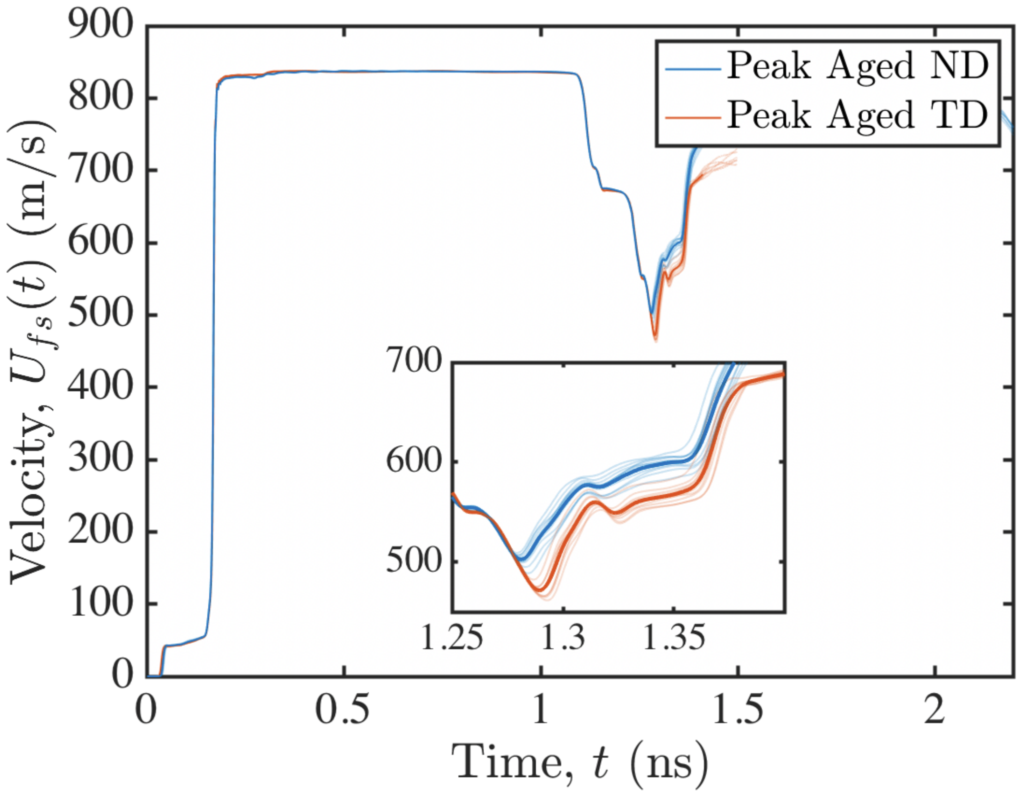

Figure 5.10: Free surface velocity history for 10 simulations with randomized microstructures for ND (blue) and TD (red) orientations. The bold lines are the averaged histories within each orientation. The inset highlights the difference in peak tension signals in the velocity history.

To understand the effect of the randomness in populating the habit plane with precipitates, we perform the simulation 10 times for each loading orientation. These runs are shown as lighter hues in Fig. 5.10. In the case of the ND oriented specimen (blue), the simulation consistently shows a lower peak tensile stress at failure when compared to the TD oriented specimen (red). The average of all ten histories for each orientation are overlaid in darker hues to emphasize this trend. The average spall strength calculated from the simulated velocity histories is 1.35 ± 0.02 GPa for the ND oriented specimens, and 1.47± 0.02 GPa for the TD oriented specimens (an 8 percent reduction for the ND case). These results imply that the precipitate structure imposes weakness in ultimate dynamic tensile strength when the precipitate habit planes are parallel to the propagating shock front, where previously there was little to no anisotropy in the un-aged samples.

5.4 Discussion

5.4.1 Spall Strength Isotropy in Solutionized Mg-9Al

Kanel et al. [146] show anisotropy in high rate spall strength with respect to the direction of loading on the crystal lattice in Mg single crystals, but we do not see evidence of such strong anisotropy in our experiments in the solutionized samples. The binary alloy in this work features grain sizes that are barely an order below the flyer diameter, and the velocimetry probe diameter is in the tens of microns, so the probe is at least an order of magnitude smaller than the average grain size. Thus our experiments on the binary alloy can be compared to the single crystal based on the strong basal texture of the material, especially in light of the large number of experiments we conducted. Fig. 5.11 shows our spall experiments as colored and filled symbols along with the single crystal work from Kanel et al. [146] and Resseguier et al. [128]. Notice the difference in tensile loading rate between our experiments and in

Kanel et al. [146], and that our material is polycrystalline, though the material characterization done in this work indicates large grains and strong basal texture in the Mg-9Al material. The strengths of solutionized ND and TD (Purple and green symbols) specimens overlap for most of our measurements, especially at higher strain rates where shock stress is highest. One possible explanation for the loading direction independent spall strength lies in the shock strains and the rates that our experiment imposes.

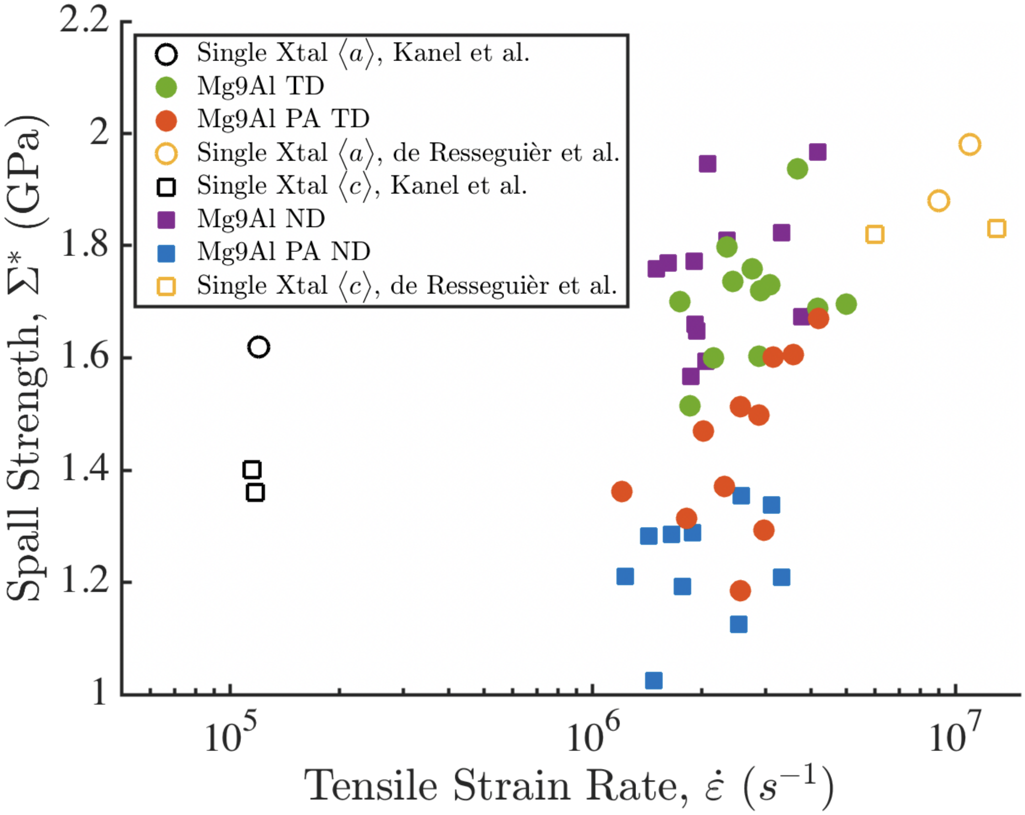

Figure 5.11: Spall strengths from experiments in this study (colored filled symbols with squares for normal direction and circles for transverse direction) for solutionized (Mg-9Al TD and ND) and aged (Mg-9Al PA ND and TD). Also plotted are single crystal spall strengths by Kanel et al.[146] (Left black), and single crystal spall strengths by Resseguier et al. [128] (Right black).

The effective strain under an arbitrary load is,

$$\varepsilon_{eff} = \frac{\sqrt{2}}{3}((\varepsilon_1 - \varepsilon_2)^2 + (\varepsilon_2 - \varepsilon_3)^2 + (\varepsilon_3 - \varepsilon_1)^2)^{1/2}. \tag{5.5}$$

Under uniaxial strain conditions from laser-flyer loading where the edges of the specimen confine lateral strains, $\varepsilon_2 = \varepsilon_3 = 0$, so $\varepsilon_{eff} = 2\varepsilon_1/3$. The volumetric strain depends only on the strain in the primary basis direction under these conditions, so $\varepsilon_1 = \frac{\Delta v_e}{v_0}$ with reference volume v_0 and elastic volume change Δv_e. The resulting effective strain from the laser-flyer is,

$$\varepsilon_{eff} = \frac{2\Delta v_e}{3v_0}. \tag{5.6}$$

Assuming the simplest equation of state, $\Sigma = K\frac{\Delta v_e}{v_0}$, and substituting into (5.6), the effective strain imposed by uniaxial strain deformation under shock loading can be estimated as [68],

$$\varepsilon_{eff} = \frac{2\Sigma}{3K} \tag{5.7}$$

with bulk modulus K and pressure Σ estimated by (4.15) during the peak of the velocity history. A better estimate in the case of spall is then,

$$\varepsilon = \frac{2\Sigma_{peak}}{3K} + \frac{2\Sigma_{peak}}{3K} + \frac{2\Sigma^*}{3K}, \tag{5.8}$$

with terms representing the shock compression, decompression to zero pressure, and then tension until spall failure, in that order.

Both Kanel et al. [146]'s single crystal data and our experiments are conducted at similar shock stresses for ND or $\langle c \rangle$-axis compression, with peak free surface velocity histories that are near 800 m/s. In TD or $\langle a \rangle$-axis compression, Kanel et al. [146]'s experiments again have peak free surface velocities near 800 m/s while our TD experiments have some shock stresses at that level but also have higher free surface velocities that near 1100 m/s (higher rate experiments in green shown in Fig. 5.11). All of our experiments are performed at higher strain rates, so the combination of the higher shock stresses and spall strengths means that strain at failure is slightly higher in the case of the binary alloy experiments by (5.8) (strain from only the combination of initial compression and decompression to zero stress for the shock stress in Kanel et al. [146] is shown as the black vertical line in Fig. 5.12). Perhaps the strain levels are in a regime where we "shock out" the plastic anisotropy when spall failure occurs and flow stress levels are at or near the same, based on the quasistatic (10^{-4} s^{-1}) stress and strain relationships shown in Fig. 5.12 [147, 148, 149].

We do not have much stress-strain data for the Mg-9Al binary alloy, so we must extrapolate using the available data and compare with AZ31B and single crystal data where flow stresses are similar at strains nearing $\sim$0.1 between the two different loading directions. This feature may enable us to probe only the effects of the precipitate structure in plastically anisotropic materials. Note that Zhao, Kannan, and Ramesh [147] show stress-strain relationships that match the quasi-static data at dynamic rates, (10^3 to 10^5 s^{-1}) suggesting that these relationships may hold true for Mg and Mg alloys at the higher strain rates we achieve. Resseguier et al. [128] present direct ablation laser-shock spall experiments on Mg single crystals that are also plotted in Fig. 5.11. They conclude that further experiments are necessary to confirm the lack of directional anisotropy in spall strength, but their experiments are

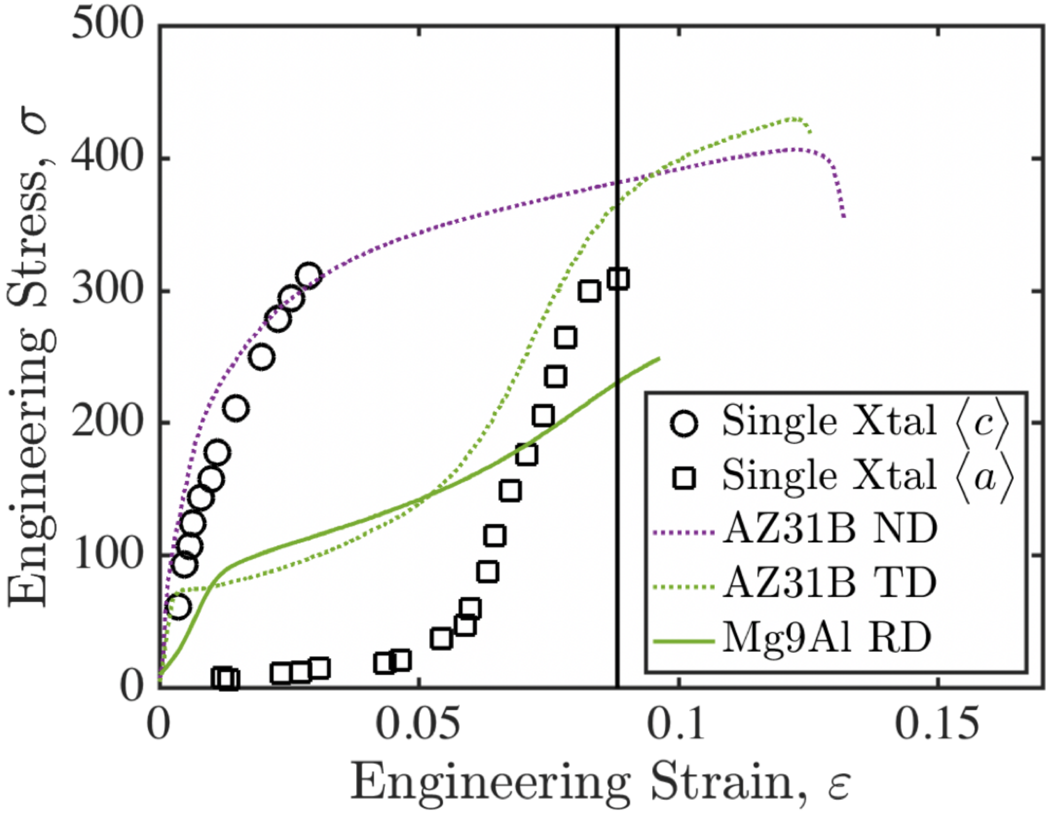

Figure 5.12: Stress strain curves for single crystal Mg from selected quasi-static compression experiments in [149] (black symbols). Stress strain curves for rolled AZ31B Mg alloy from quasi-static compression experiments in [147] (dashed lines). Stress strain curve for quasi-static compression of the Mg-9Al alloy in this study in the rolling direction from [148] (solid line). The black vertical line denotes the average plastic strain achieved in our experiments.

performed on "clean" single crystal microstructures. Our results confirm this high rate strength isotropy for the solutionized samples which have a relatively clean microstructure (Fig. 5.5) and very strong basal texture (Fig. 5.4). It is possible that a single experiment probes a misaligned grain, but we have performed a large number of experiments that mostly confirm the isotropy in measured spall strengths. Mechanism based reasoning for this strength isotropy remains unclear, but could be related to rate sensitivities of dislocation slip and twinning at the high rates of the laser-driven shock experiments.

5.4.2 Spall Strength Anisotropy from Precipitate Structure

Fig. 5.13 shows a cutaway view through the simulation domain at the $y =$0.5 µm plane colorized with the longitudinal stress profile in the x direction at $t = 1.35$ ns. The white regions are where Mg material has been replaced by voids. When shocking along the presumed $\langle c \rangle$ axis in Fig. 5.13a, the precipitate habit planes are parallel to the propagating shockwave front, so failure tends to occur simultaneously across the habit planes in the region of high tension. Any intact material sees very high stress concentrations thereafter. In Fig. 5.13b, the habit planes are perpendicular to the shock front, so fewer precipitates debond or fracture and less void material is inserted. The remaining intact material sees lower stress concentrations as a result, and the bulk response is stronger. Notice the generally localized stress distribution in the ND case when compared to the TD loading that results in a higher spall strength. The final void fraction is larger at the end of the simulation in the ND case when failure from multiple habit planes links up (visually discernable from Fig. 5.9), perhaps supporting the experimental observation of smaller average fragment sizes for that loading orientation in Fig. 5.7. From the velocity histories in Fig. 5.10, the ND orientation is on average 8 percent weaker than the TD orientation.

These experiments and simulation results stand in contrast to the conventional wisdom that the introduction of second phase particles causes an

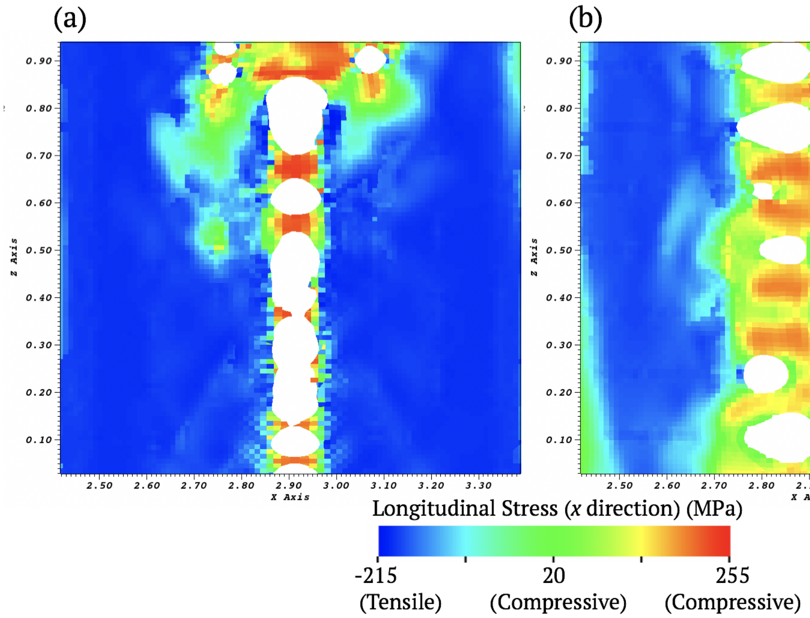

Figure 5.13: At t =1.35ns, the pressure has surpassed the critical threshold and has caused failure in the precipitates, leading to void insertion in the model. Voids are beginning to coalesce (white regions), leading to stress concentrations near other precipitates in the spall plane. This image is a colorized representation of longitudinal stress in the x direction on a cutaway down the y=0.5 μm plane for the (a) ND orientation and (b) TD orientation.

increase in strength in lower rate or quasi-static loading. Though the grain size increases through the aging process which should decrease the yield strength through the Hall-Petch relationship as in eq. (4.22), Prameelaa et al. [143] present quasi-static hardness data that indicates a 40 to 50 % increase in strength for the precipitate laden material. In quasi-static loading, the precipitates can act as obstacles for slip and twinning mechanisms. As the strain rate increases, the microstructure defect distribution comes into play as the second phase particles act as nucleation sites for failure. A larger quasi-static strengthening effect is likely necessary to see an improvement in spall strength where finer precipitates, much smaller grains, large dislocation densities, and pre-twinning may improve the yield strength to an extent where it can overtake the introduction of failure nucleation sites [143].

The simulations confirm the trends in the experimental results and suggest that the orientation of preferred precipitate habit planes to the shock front affects the maximum capacity of the material to withstand dynamic tensile loading. The simulations showed an average reduction in spall strength of 8 percent for ND oriented loading, whereas our experiments showed a reduction closer to 15 percent for the same loading condition. There are several potential sources for this discrepancy between the experimental result and these simulations. First, all the simulations are conducted at the same shock stress and strain rate. Due to computational expense, our simulation domain is much smaller than the experiment, so the shockwave we propagate is nearly 20 times shorter in the x direction (and has a much higher strain rate as a result, $\sim 10^7$ s^{-1}). Perhaps a longer region of high tensile stress will activate failure in more habit planes in the ND orientation, causing a faster failure and lower spall strength more in line with the experimental result. Additionally, though we aim to implement physically realistic representations of the precipitate morphology in this work and randomize placement on habit planes, the variance in lath precipitate length and width is not accounted for in these simulations (as well as a mathematical constraint that brings spacings between randomly placed laths to the values observed on the habit planes themselves). We could also be under or overestimating the number density of precipitates based on TEM observation, which is an extremely local microscopy technique. The result of these modeling assumptions could create differences in connectivity between failure prone precipitates in the microstructure once void growth kicks off. The lower spall strength in the ND orientation may also barely bring the transient shock strain back into a level where we are not completely ”shocking out” the strength anisotropy by the third term in (5.8), so the TD oriented specimens may return to having a matrix that is more resistant to spall failure as in Kanel et al. [146]. We cannot evaluate this hypothesis without implementing an anisotropic plasticity model for the alloy such as in the work of Lloyd et al. [145].

5.5 Concluding Remarks

In this chapter we have demonstrated the high throughput capability of the apparatus, presenting one of the largest volumes of spall experiments on one material system in one work, to the author’s knowledge. The high strain rate loading, coupled with the high strains imposed during the experiment, may shock the plastically anisotropic solutionized Mg alloy into a state where it exhibits isotropy in spall strength. When peak aging introduces precipitates into the microstructure, we observe a strong loading direction correlation in spall strength. Though plate impacts impose large stress triaxiality loading conditions with high pressures, there is still an asymmetry (likely from stress concentrations at the precipitate-matrix interface and increased volume of precipitates in the region of peak tension) that presents as a lower failure strength for the Mg-9Al alloy in the normal direction when precipitate habit planes are parallel to the propagating shock front. Numerical simulations using physically realistic representations of the precipitates bolster this hypothesis. Further fractography is necessary to discern the nucleation sites of the failure process and to confirm the precipitate volume correlation to the spall strength.

Chapter 6

Fragmentation of Boron Carbide

Parts of this chapter appear in a research article, Hogan et al. [150], and a conference proceeding, Mallick and Ramesh [151], where D.D.M. is third author and first author, respectively. D.D.M. performed the ballistic experiments and obtained the fragmentation statistics through optical microscopy in Hogan et al. [150].

6.1 Introduction

In the prior two chapters, we examined spall failure using the laser-driven apparatus. We now investigate the fragmentation behavior of advanced ceramics typically used for body armor in defense applications. Impacts into protection materials activate deformation mechanisms such as plasticity and phase transformations and failure mechanisms such as void growth and coalescence and dynamic fracture originating from defects in the material. Dynamic fragmentation through high rate impact generates large numbers of fragments of various sizes and shapes. The fragmentation failure mode is an important part of the impact performance of advanced ceramics which feature high strengths and low density but fail in brittle modes. The protective capability of a protection material has been linked to the sizes and shapes of fragments by Krell and Strassburger [5], who observed that particular size and shape combinations more effectively erode the projectile, improving resistance to penetration. Their fragmentation results stand in contrast to studies that look at penetration resistance and material properties, such as fracture toughness or stiffness, which have yielded contradictory correlations [5]. We build on this fragmentation concept here by instead linking microstructure properties to impact fragmentation.

Laser-driven projectile launchers have demonstrated effectiveness as a way to probe novel protection materials such as graphene sheets on the lab-bench, but have not been utilized to evaluate mass-produced protection materials such as ceramics with larger geometries [62]. Instead, fragmentation studies of protection materials are typically conducted using dynamic loading apparatuses such as Kolsky bars [32, 33, 39], and powder or gas guns [5, 43, 42, 41, 40]. Widespread adoption of laser driven methods is only reasonable if there is sufficient evidence that the impact from a laser driven apparatus generates a comparable loading condition to ballistic loading with a conventional gun. In this chapter, we explore the impact-induced fragmentation of a commercially available hot-pressed boron carbide using the laser-driven flyer apparatus and velocimetry described in chapters 2 and 3 and a conventional powder gun. We present fragment size and shape distribution data from laser driven and ballistic experiments. These are some of the first comparisons between laser-driven impacts and ballistic impacts on protection ceramics, certainly when studying dynamic fragmentation.

6.2 Material

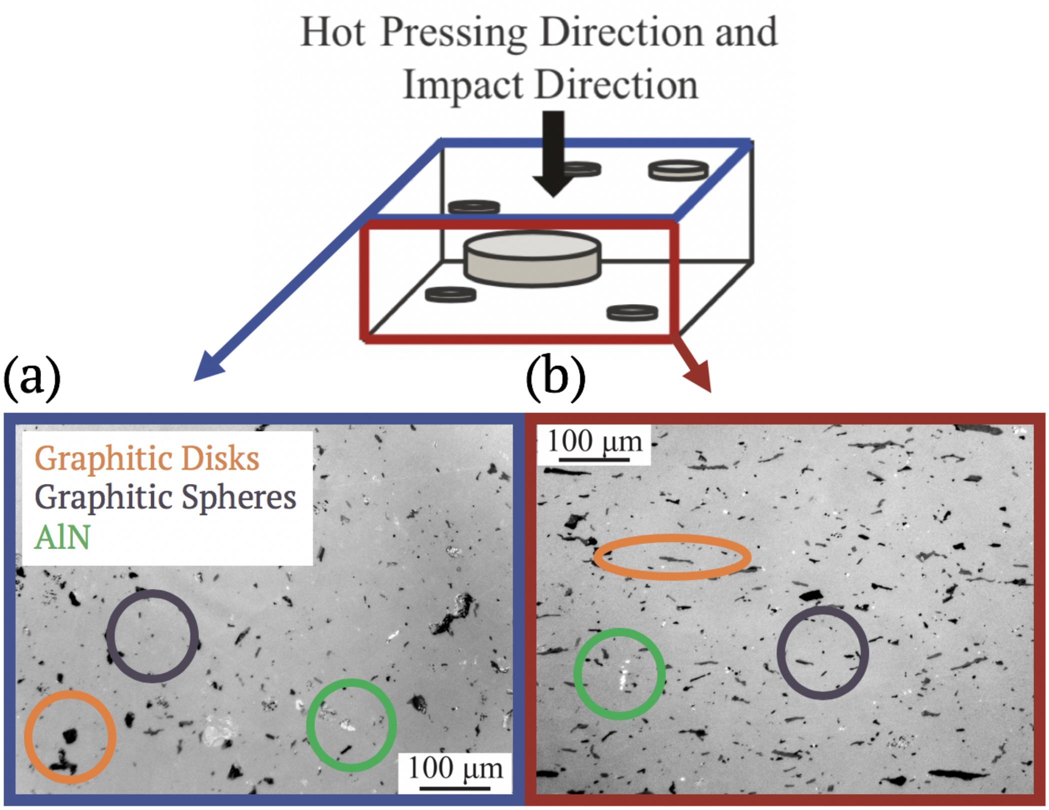

Figure 6.1: (top middle) Schematic of boron carbide tile with hot-pressing direction labeled and conceptual graphite disk defects. Optical microscope images of boron carbide microstructure for (a) through-thickness direction, looking along the shot-line, and (b) in-plane direction, viewed transverse to the hot-pressing direction. Labeled in these images are microstructure features (defined in top left of image (a)) and the impact direction of the spherical projectile (the dark circular object).

Boron carbide has received considerable attention in the literature as a protection material because of its high specific strength in comparison to other ceramics [32, 33, 31]. Boron carbide is particularly interesting because of an observed phase transformation, termed "amorphization", that has been associated with a decrease in resistance to ballistic penetration [29]. Several threshold parameters have been suggested for this response such as a critical impact velocity of 850 m/s [29], or unloading in shear after high hydrostatic loads [30, 34].

We investigate fragmentation of a hot-pressed boron carbide ceramic (Coorstek, Inc.) with a Young's modulus of 430 GPa and a density of $\rho = 2,510$ kg/m^3. The target plate is conceptualized in the schematic in Fig. 6.1 with the projectile impact direction along the hot-pressing direction. Fig. 6.1a-b shows shows optical micrographs of the material normal-to and transverse-to the hot-pressing direction, highlighting large carbonaceous inclusions that present as circular in the hot-pressing direction and needle-like when viewed transverse to the hot-pressing direction. These inclusions are disk-like in three dimensions with a preferred orientation that is normal to the hot-pressing direction (as in the orange circle). The microstructure also has smaller spherical features that are primarily carbonaceous in composition, although sometimes they are pores (black circles), and brighter ceramic phases that have been identified as aluminum nitride and boron nitride (green circles) [32, 33, 31]. All optical microscope images were taken using a Zeiss optical microscope with an AxioCam MRC camera. A detailed description of the microstructure is described in previous literature [32, 33, 31], but we emphasize the measured statistics of carbonaceous defect spacing from that work in Fig. 6.2.

Fig. 6.2 shows the empirical cumulative distribution function (eCDF),

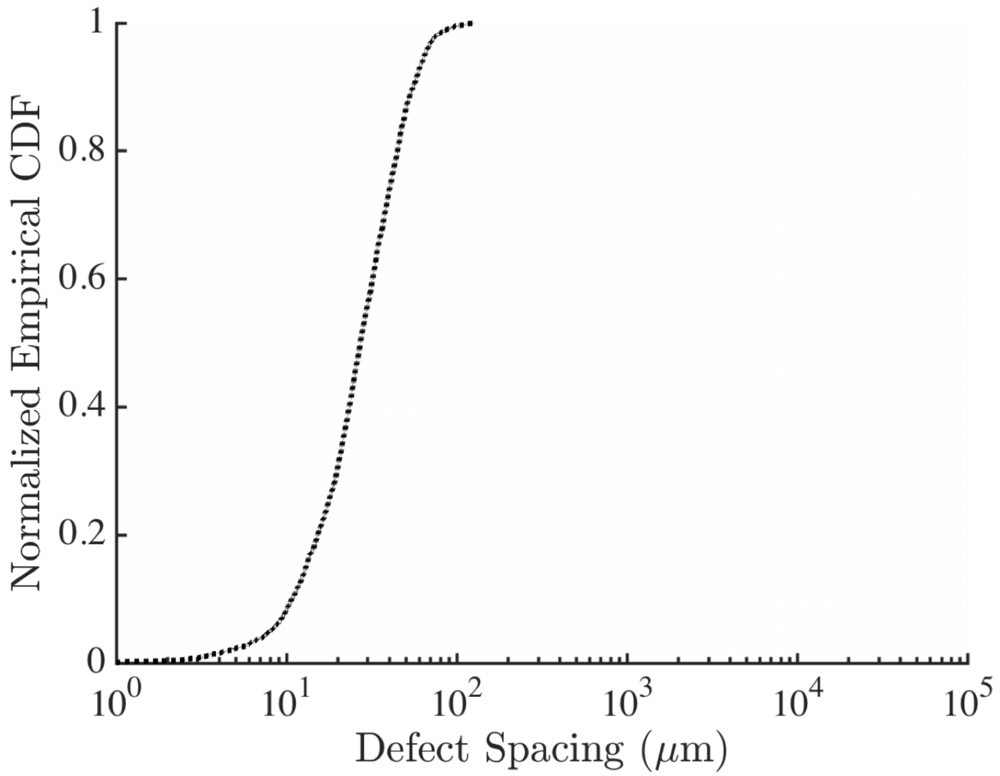

Figure 6.2: Empirical cumulative distribution function (eCDF) of spacing between carbonaceous disk-like defects in the as-received microstructure as obtained from optical microscopy images analyzed by MATLAB thresholding techniques.

where for n measured minimum nearest neighbor distances l_i (for the ith measured spacing), the eCDF is $G(l) = n^{-1} \sum_{i=1}^{n} \mathbf{1}(l_i \leq l)$. $\mathbf{1}$ is the indicator function with value 1 if $l_i \leq l$ and 0 otherwise. We expect that the finest fragments are generated by cracks between these inclusions during high rate loading, so the generated fragment distribution should correlate to the defect spacing statistics of the material.

Fig. 6.1 also shows the impact direction along the hot pressing direction of the plate. We perform laser-driven impacts on 3 mm diameter, 50 µm thick disks manufactured from the as-received 8 mm thick plate by first cutting a

1.2 cm x 1.2 cm sample that is 1 mm thick (along the hot-pressing direction) and then mechanically polishing (Bomas Machine Specialties, Inc.) to a 50 µm thick and 1 cm x 1 cm sample. Notice that at this machining thickness, the specimens will only contain up to 90 percent of the measured defects as per Fig. 6.2. We cut 3 mm diameter disk-shaped specimens from the sample using a femto-second pulsed-laser based machining procedure outlined in Mallick et al. [85] and chapter 2. For the conventional gun driven impacts, we took the as-received 8 mm (along hot-pressing direction) thick plate and cut 55 mm × 70 mm coupons from the plate using a high-speed saw.

6.3 Experimental Configuration

6.3.1 Laser-Driven Flyer Experiment

The laser-driven flyer apparatus, described in chapter 2, is configured to generate two different flyer profiles by changing the stand-off distance between the flyer and the target as shown schematically in Fig. 6.3a. The flyer loses launch products at the edges, so the edges travel at a slower velocity inducing curvature in the flyer. Because the stand-off distance required to generate a flyer with a high radius-of-curvature (ROC) is rather large, these experiments were conducted in air rather than under vacuum. This has the benefit of inducing a faster deformation due to air drag. The 125 µm stand off distance is the same as used in Chs. 4-5, achieved with a 3 mm OD, 1.5 mm ID Kapton spacer. A 700 µm thick Kapton spacer provides the longer stand-off distance for the more curved flyer. The outer diameters of both spacers are the same as the diameters of the specimen coupons to ensure co-linearity during alignment and impact. The spacers are omitted in the schematic in Fig. 6.3a for clarity.

To characterize the evolving curvature of the flyer, a 10MHz framing camera (Shimadzu HPV-X2 camera, 100 ns exposure time, with Specialized Imaging SiLux 640 laser back lighting) is used to image the flyer in the absence of the Kapton spacers in Fig. 6.3b. We use imaging software (ImageJ) to process the frames and obtain radius of curvature (ROC) estimates for the two experiment configurations (overlaid in Fig. 6.3b). We note that the Kapton spacer may provide confinement for ablated launch products and thus a more uniform launching load, so the true ROC in the presence of the spacer is likely higher than the reported values here (i.e. flyers are likely more planar when using the spacer). We use 25 µm thick flyers in this study to maximize impact velocity and thus develop the highest shock stress, but this has the added benefit of increasing the ROC at impact when compared to reported values in chapter 2 as the thinner flyers are more susceptible to the bending that generates flyer curvature.

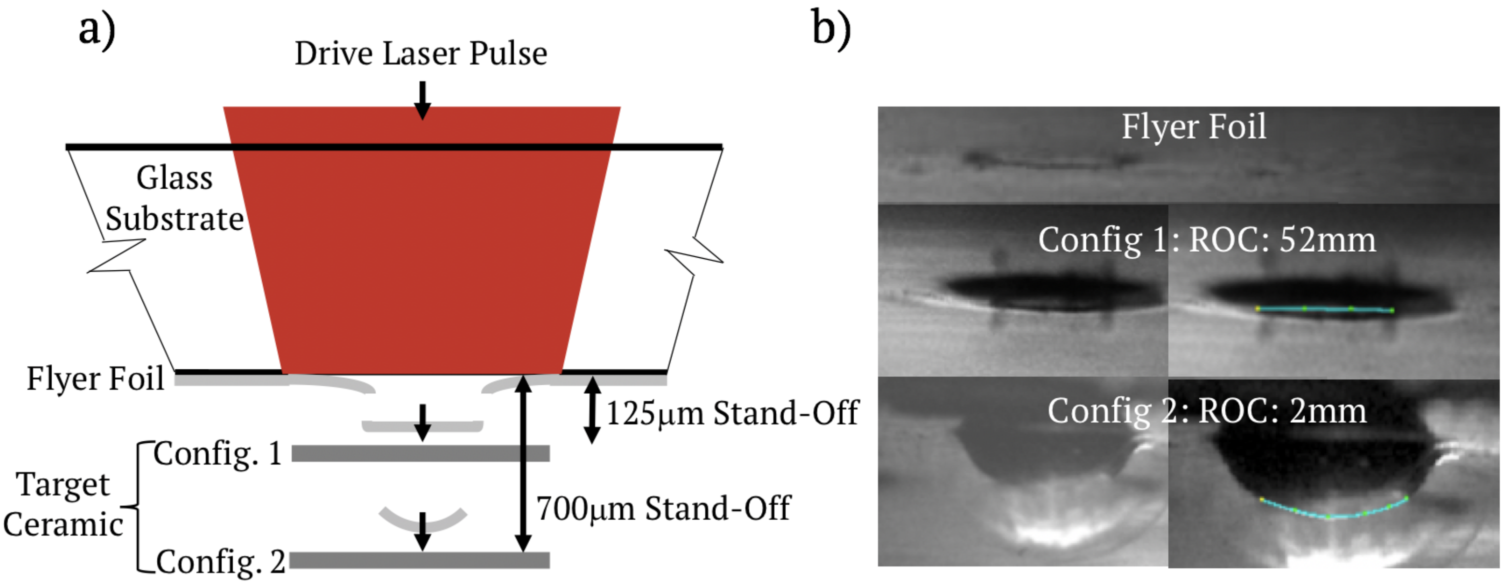

Figure 6.3: (a) Schematic of the laser-driven launch and evolving deformation of the launched flyer. (b) 100 ns exposure still images taken with a Shimadzu HPV-X2 high speed camera at 10 MHz framing rate showing the launched flyer in the left column. Radius-of-curvature (ROC) measurements obtained by image analysis with ImageJ Kappa plugin in the right column. The radius of curvature measurement for the flat flyer is considered extremely conservative because of the pixel sizes in the image (the actual radius of curvature is likely much higher, i.e. more planar).

We employ photon Doppler velocimetry (PDV) to interrogate the back-surface velocity history of the ceramic target during failure (see chapter 3 for details on the velocimetry techniques used to achieve nanosecond time resolution). To characterize the impact velocity in the presence of both spacers, we replace the target with a NBK7 glass slide and probe only the flyer travel with PDV. The longer stand-off distance causes a loss from 1200 to 1100 m/s in velocity prior to impact due to the extended flight time of the projectile in air. We then perform the impact experiment immediately after the impact velocity characterization with the specimen in place. The PDV probe laser is focused onto the specimen free surface through an optically transparent 2 mm thick layer of Polydimethylsiloxane (PDMS) at the bottom of an optically transparent 35 mm diameter petri dish in a "soft-catch" configuration such that fragments of the target become embedded in the PDMS layer post target failure without further deformation to the fragments. Post-experiment, we image the fragments using a Zeiss optical microscope with an AxioCam MRC camera and use image processing techniques developed in previous works [32] to determine fragment size (longest spanning dimension) and aspect ratio (ratio between longest and smallest spanning dimension). We then perform Raman spectroscopy on the recovered fragments to look for amorphization signals. The fragmentation data from the laser-driven launcher is compared against fragmentation data from ballistic experiments with a gun described et seq.

6.3.2 Ballistic Experiment

The ballistic impact experiments were conducted at the U.S. Army Research Laboratory, Aberdeen Proving Ground, MD, USA. A 6.35 mm diameter spherical projectile made of 93% tungsten carbide, 6% cobalt, and 1% nickel is impacted at velocities of 275 m/s and 930 m/s (measured using flash x-ray) into the larger target coupons cut with a high speed saw. Targets are mounted inside an acrylic box that is 200 mm long in the direction of impact, 460 mm in height, and 460 mm wide. The box walls are 10 mm thick and lined with 38 mm thick ballistic gelatin in a "soft-catch" configuration. The gelatin captures some of the fragments, while the rest remain within the box during the impact event. With this configuration, greater than 90% of the original target mass is recovered. The same optical microscopy techniques are used to image and quantify fragments as in above.

6.3.3 Methods Comparison

With some a priori analysis, we have designed the two experimental technique applications for this problem to generate similar fragmentation regimes. Grady [152] has shown excellent capability to predict mean fragment size from a fragmentation event using an energy analysis. The imparted strain energy from the impact drives the creation of fracture surfaces during fragmentation, so the fracture surface energy serves as a fragmentation criterion that counteracts the loading. The mass and density of the ballistic projectile (0.002 kg and 14500 kg/m^3 respectively) is much greater than for the laser driven impact (1.2 $\times 10^{-7}$ kg and 2700 kg/m^3 respectively), so the kinetic energy and shock stress is much higher. The target thickness is two orders of magnitude thinner in the case of the laser driven impact, resulting in a macroscopic strain rate increase in order of magnitude by two decades. Though it is impossible to match the stresses, kinetic energies, and strain rates between the two methods, the energy density can be matched to create a similar mean fragment size within a particular projectile-target interaction zone.

For the ballistic impact, the tungsten carbide sphere generates approximately 840.6 J of kinetic energy in the case of a 930 m/s impact. Assuming that the entire thickness of the target is fragmented, the region directly interfacing with the projectile has a volume of 2.5×10^{-7} m^3, resulting in an energy density of 3.32 GJ/m^3. In contrast, the 25 μm thick Al flyer generates 0.09 J of kinetic energy for a 1200 m/s impact, resulting in an energy density of 0.97 GJ/m^3 at the projectile-target interface for the 50 μm thick target. By this analysis, the two energy densities are within the same order of magnitude, suggesting that laser-driven impacts in this configuration can approach the fragmentation behavior in the ballistic experiment, provided that fragmentation is analyzed for these projectile-target interaction zones specifically.

6.4 Results

6.4.1 Ballistic Fragmentation

The processed optical microscopy from the ballistic and laser-driven impacts result in a dataset of fragment sizes (longest major axis) and aspect ratios (ratio of longest major axis to shortest perpendicular axis). One set is shown for the 930 m/s ballistic case in Fig. 6.4. The cluster of larger fragments on

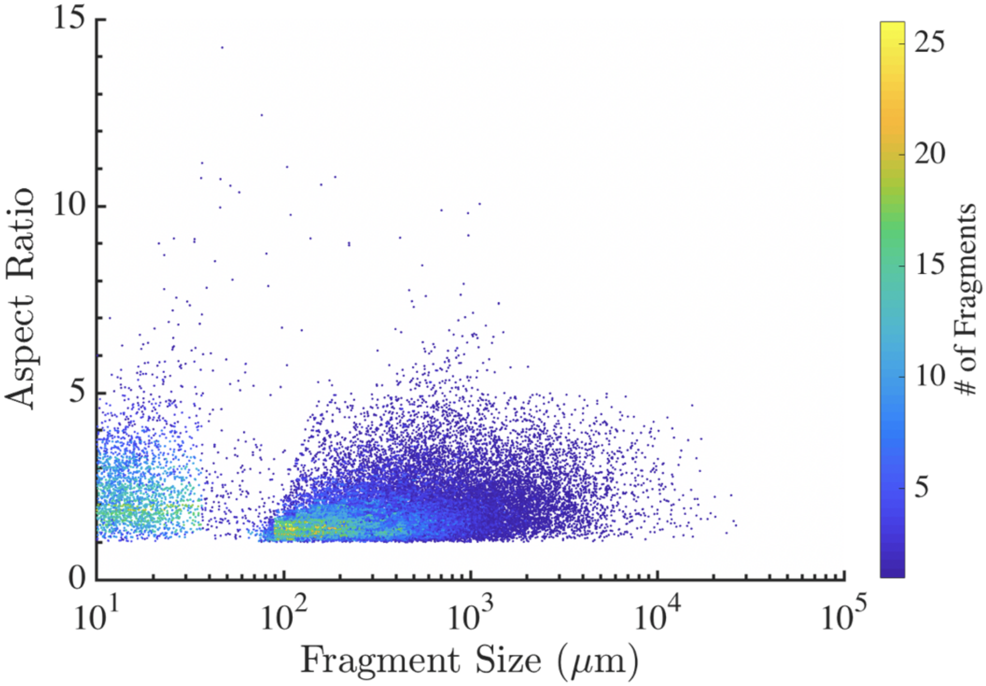

Figure 6.4: Heat scatter plot of fragment size and aspect ratio distribution for the 930 m/s ballistic impact case. Hotter colors indicate more than one fragment overlapping in the scatter plot.

the right tends to have aspect ratios closer to 1, indicating a more "blocky" fragment, while the cluster of fragments on the left has a more uniform distribution of aspect ratios. There are clearly two populations as exhibited by the clusters, small fragments less than ~30 µm to the left, and fragments larger than ~70 µm to the right. Comparable results exist for the 275 m/s ballistic impact case.

In lieu of showing more scatter plots that poorly present trends, we present eCDFs of the two ballistic impact cases in Fig. 6.5a-b. The 930 m/s ballistic impact results in a larger fraction of the smaller fragment regime than in the case of the 275 m/s impact where only several percent of the recovered number of fragments are smaller than 70 µm. The remainder of the eCDF

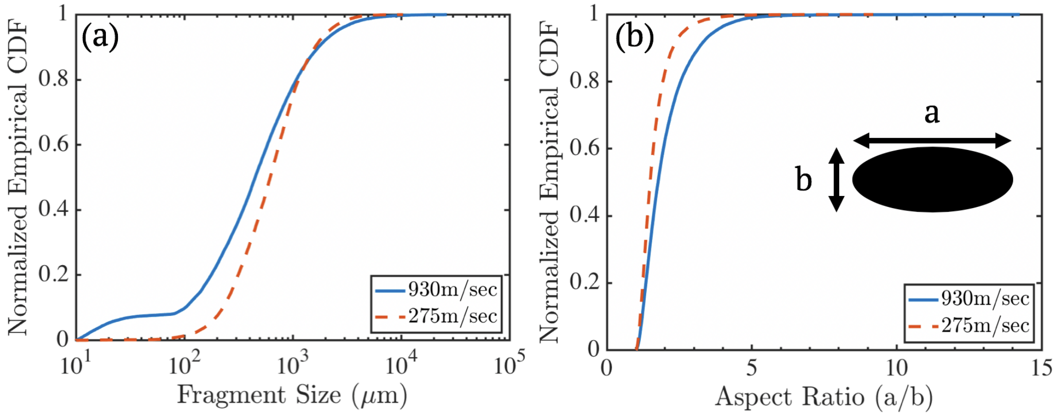

Figure 6.5: (a) Normalized cumulative distribution of fragment sizes for the ballistic impact cases, (b) normalized cumulative distribution of fragment aspect ratios (a/b) for the ballistic impact cases.

shifts to the left in the 930 m/s case as expected because of the additional cracking necessary to dissipate the additional strain energy for the higher impact velocity, and the associated activation of more defects due to the increased loading rate. The increase in activated flaws should also increase the amount of crack coalescence resulting in smaller fragments. The aspect ratio eCDF indicates a shift to elongated fragments with increasing impact velocity in Fig. 6.5b.

We can link microstructure length scales to fragment sizes by examining eCDFs of each. Fig. 6.6 shows the eCDF for fragment sizes in the 930 m/s ballistic impact case with the eCDF for carbonaceous disk spacing from optical microscopy of the as-received hot-pressed plate overlaid from [32]. The comparison suggests that the inflection point in the fragment size eCDF at $\sim$ 70 µm coincides with the maximum spacing of the carbonaceous disk-like flaws in the microstructure. A red arrow in the figure highlights the link between microstructure and fragmentation. A similar result can be found for

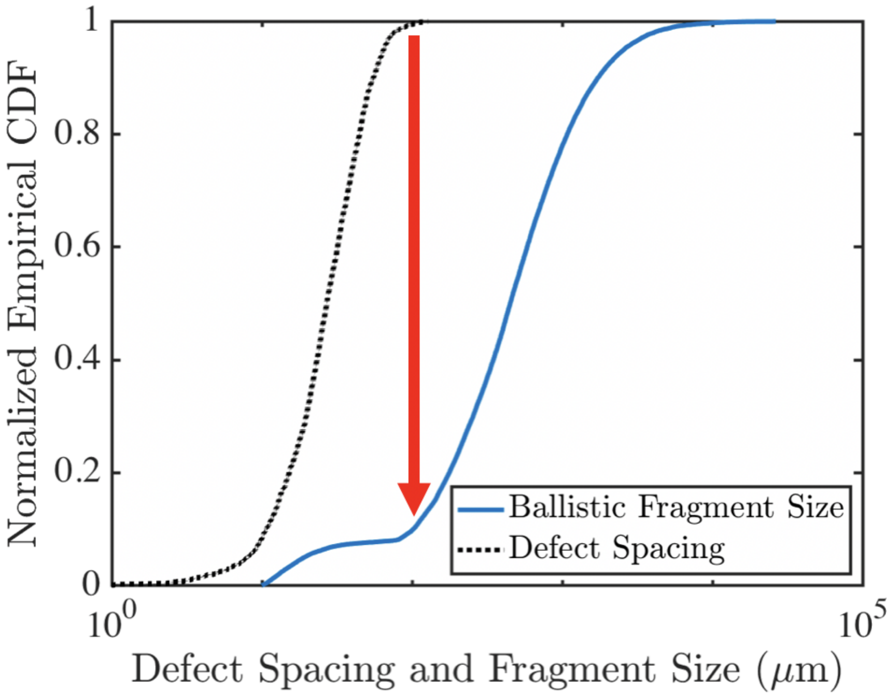

Figure 6.6: Cumulative distribution of fragment sizes (solid blue curve) and spacing between graphitic disks in the in-plane direction of the as-recieved boron carbide plate (black dotted curve). We extend an arrow from the defect spacing distribution through the fragment size distribution to show that they are similar in value, suggesting a link may exist between fragment size and defect spacing.

the 275 m/s case, though the number of fragments under the maximum defect spacing is much lower in this case, owing to the lower strain energy from the slower impact velocity.

6.4.2 Laser-Driven Flyer Generated Fragmentation

We present impact experiments with the laser-driven flyer launcher with the two different flyer geometries shown in Fig. 6.3a-b. Both the flat and curved flyer geometries impact at between 1100 and 1200 m/s. The ceramic free surface velocity histories are shown in Fig. 6.7a-b. The curved flyer

(Fig. 6.7b) imparts a rise time that is 6-8 times longer than for the flat flyer. The peak surface velocity is slightly lower (50 m/s) for the curved flyer, as expected by the numerical simulations for radius of curvature in Mg target experiments shown in chapter 2 and also seen in boron carbide experiments with varying radius impactors [153]. At these impact velocities with a 25 μm flat flyer impacting a 50 μm target, we expect spallation behavior in the ceramic target, but the thin flyer imparts a very short shock duration (8 ns) that makes the spall behavior difficult to resolve with our velocimetry. Additionally, the ceramic target becomes somewhat optically transparent at these target thicknesses, making velocimetry signals very poor. With these caveats, an estimate for the spall pullback from the flat flyer impact is 60 m/s, corresponding to a spall strength of 0.71 GPa (using (4.12) as derived in chapter 4) at a shock stress of 10 GPa, directly in line with reported values for boron carbide [154]. The 2 mm radius of curvature of the curved flyer (estimated from analysis of high speed imaging) should impart a 140 μm closure distance for the flyer (estimated using a 1.5 mm flyer diameter), corresponding to an expected rise time of 115 ns at a 1200 m/s impact velocity. The measured rise time of 50 ns indicates a radius of curvature of 4 mm instead, suggesting that the Kapton spacer creates a more uniform launch process than launches without any confinement.

Over 225 optical microscopy images of collected fragments are processed in MATLAB to obtain an aspect ratio (ratio between major and perpendicular minor axes) and fragment size (major axis dimension) for each fragment captured in the experiment. The data encompasses fragments larger than 6 μm.

All fragments are believed to be contained within the petri dish post-impact (4000 fragments for the flat case and 3000 for the curved case). The measured statistics are thus representative of the general fragmentation behavior during impact with the exception of incomplete fragmentation in the case of the curved flyer. For the curved flyer, the outer ring of the target remained mostly intact while the inner 1.5 mm diameter region of the target fragmented; the intact outer ring is not reflected in the following fragmentation data. The flat flyer impact completely fragmented and the resulting fragments are completely characterized. We note that this data only considers fragments larger than 6 µm, or 10 pixels. Below this size, signal to noise ratio becomes small due to the MATLAB thresholding procedure. Fragment size and aspect ratio data are shown as a scatter-plot in Fig. 6.8a-b where hotter colors indicate multiple instances of a data-point with (a) showing data from the flat flyer impact and (b) showing data from the curved flyer impact. The data indicates that the flat flyer impact generates larger fragments, but the data does not account for the non-fractured region for the curved flyer case. Aspect ratios are well distributed but fragments become less elongated and more uniform in major and minor dimensions as fragment sizes approach 50 µm.

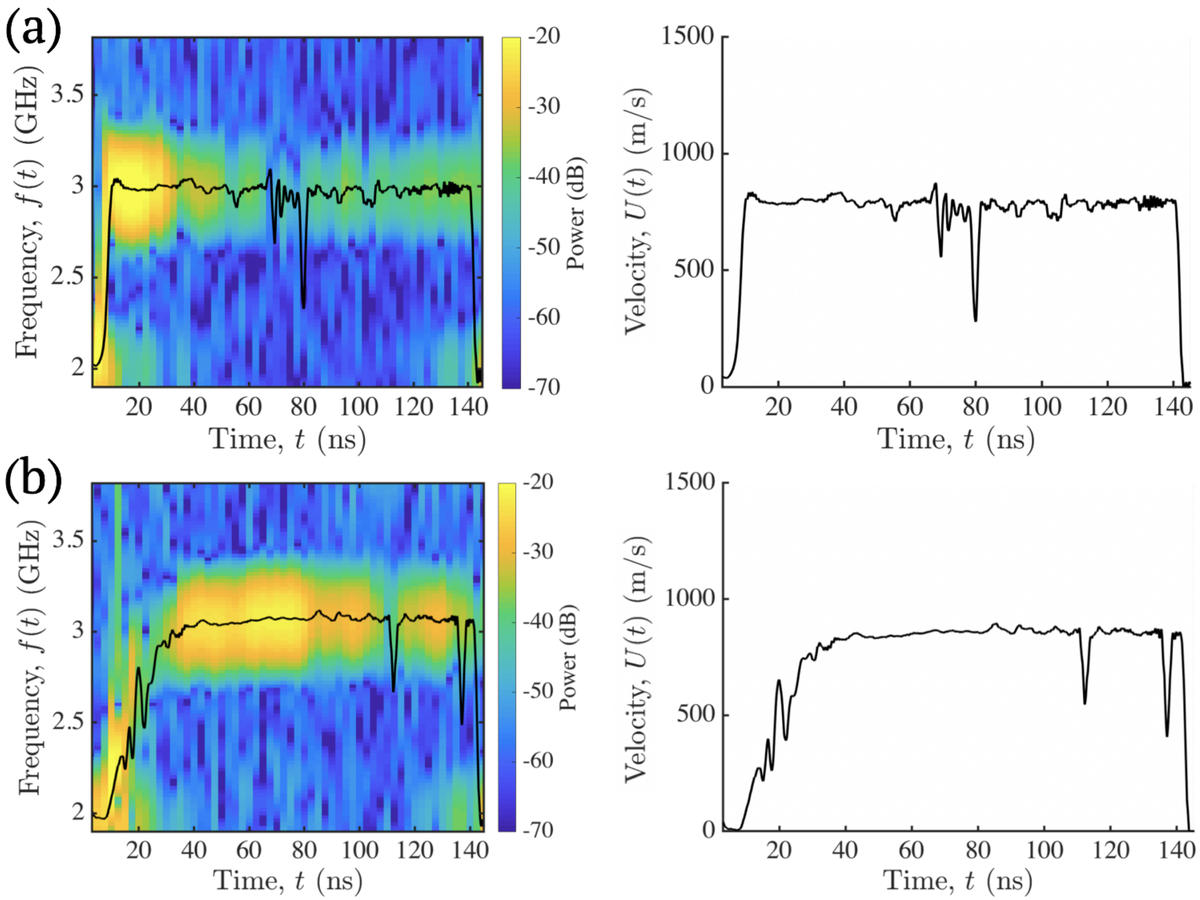

Figure 6.7: (a) Left, spectrogram of interferometry voltage signal for boron carbide target free surface velocity history from flat Al flyer with overlaid peak frequency tone history in black. Right, processed velocity history. (b) Left, spectrogram of interferometry voltage signal for boron carbide target free surface velocity history from curved Al flyer with overlaid peak frequency tone history in black. Right, processed velocity history.

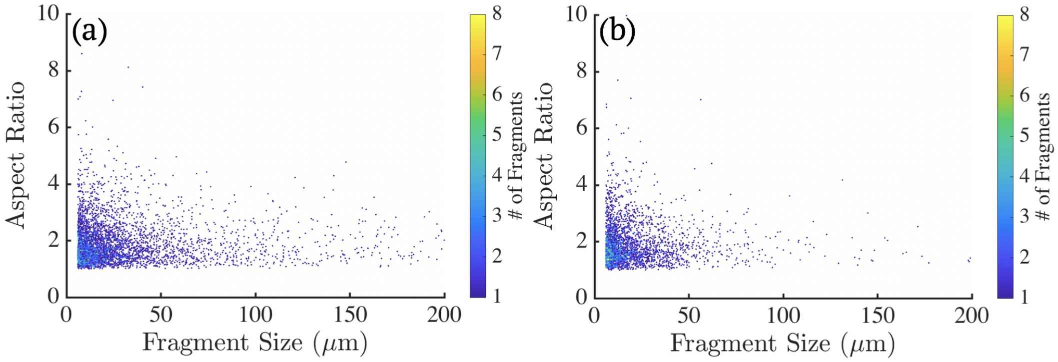

Figure 6.8: (a) Fragment data scatterplot showing size vs. aspect ratio for flat Al flyer impact. (b) Fragment data showing size vs. aspect ratio for curved Al flyer impact.

The aspect ratios do not show strong trends in both the laser-driven and ballistic experiments, so we instead compare the fragment size data between the two cases in Fig. 6.9a-b. The use of cumulative distribution functions and ”Mott” plots [152] for fragment distribution analysis is effective when examining strongly differentiated behavior like in the case of the defect-controlled and structural fragmentation regimes in Fig. 6.6, but can homogenize small differences in distributed data. To compare the differences in laser-driven and ballistic fragmentation in greatest detail, we show the complete fragment size data as a histogram normalized to one in Fig. 6.9a. Notice that this is type of analysis not a probability density function which is further normalized over the histogram integral. The ballistic experiment data shows the transition between defect spacing controlled and structural controlled fragmentation between 30 and 70 µm through the separation between two fragment size populations in Fig. 6.9a. The curved Al flyer line indicates smaller fragments than in the flat Al flyer case but reasonably matches the small fragmentation regime in the ballistic case.

Fig. 6.9b shows the probability histogram of fragmentation data with fragments selected by specific size criteria. The ballistic experiment data is shown for fragment sizes below 75 µm when the defect-controlled fragmentation regime begins. For the flat Al flyer impact, fragments underneath 50 µm are shown to discriminate against fragments larger than the target thickness and 90 percent of microstructure defect spacings in the as-received material. The curved flyer fragmentation data is unchanged as the fragmented region is only at the interface between the projectile and target. This subset of the data aligns particularly well with each other, and as this region of fragment size data is thought to correspond to defect spacing in the ballistic experiment, perhaps this discrimination technique is a viable method to probe the defect driven fragmentation regime with the laser-driven system.

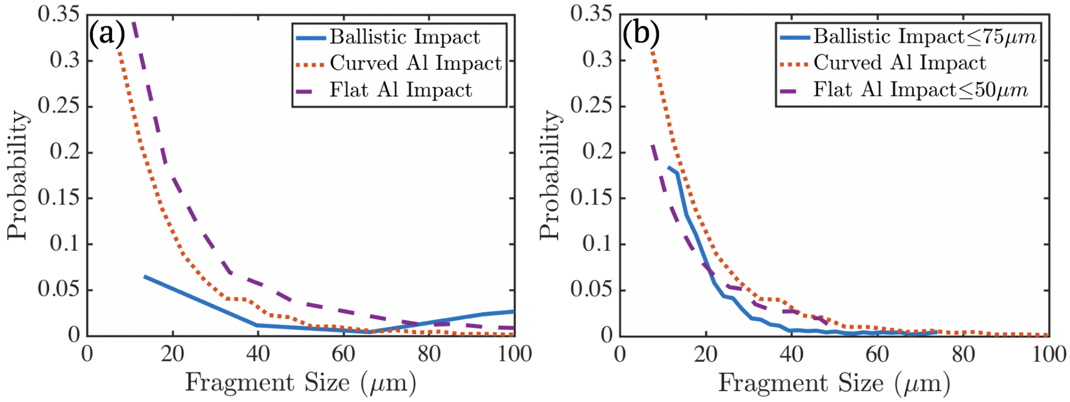

Figure 6.9: (a) Normalized histograms for all three impact cases. (b) Normalized histograms with subsets of fragment size data from the ballistic and flat flyer cases.

Shown in Fig. 6.10 are representative Raman Spectroscopy measurements on the as-received material and on fragments from the laser-driven tests. Like in the ballistic case presented in previous work [150], Raman spectroscopy of the fragments does not reveal any amorphization signal, though with shock

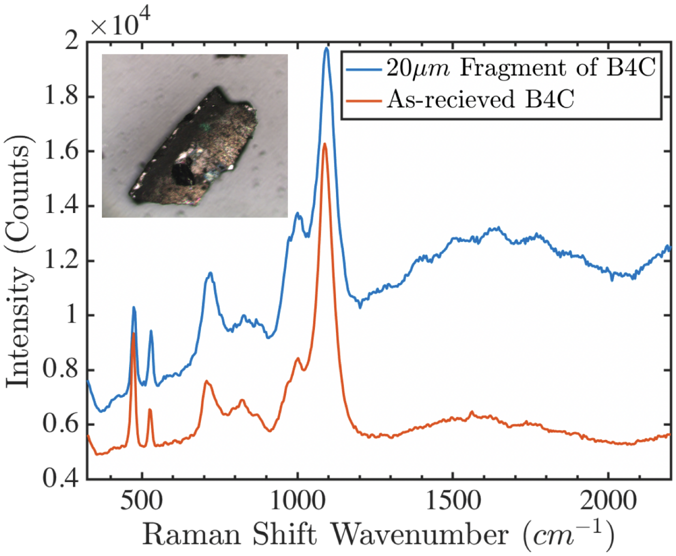

Figure 6.10: Representative Raman spectroscopy scan for as-received boron carbide target and a fragment from a flat flyer impact. No amorphization is observed. The shown fragment major axis is 50 µm.

pressures at 10 GPa and below (analysis et seq.), the Al flyers will likely not generate amorphization favorable stress states [30]. We note that this result is from a larger fragment that likely is from structure-dominated fragmentation where amorphization volume fraction will likely be low, but that Raman spectroscopy was performed on a large number of fragments of various sizes without observed amorphization spectra for both flat and curved Al flyers.

6.5 Discussion

The energy balance approach described in the methods section developed by Grady [152] takes an analytical form for the characteristic mean fragment length. Assuming fragmentation begins at the elastic limit, the peak elastic strain energy from loading is equated to the critical fracture energy, resulting in an expression for the mean fragment size,

$$L = (\frac{ZG_C}{\rho})^{1/3}\dot{\varepsilon}^{-2/3}, \tag{6.1}$$

where L is the generated mean fragment size, G_C is the critical Griffith's fracture energy, Z is a constant related to the target geometry and problem dimensionality, and $\dot{\varepsilon}$ is the strain rate.

The fragment sizes and shapes from ballistic loading reveal two distinct fragmentation regimes from the impact, separated by the fragmentation mechanism that causes each regime:

- Small fragments from coalescence of fracture originating from the entire defect population in the material where high local stresses and strain rates develop. In this regime, the defect population statistics can control the resulting fragment size distribution as seen in Fig. 6.6. The onset of this regime is under a fragment size of 70 µm.

- Larger fragments associated with structural failure from the multi-axial loading state (e.g., radial and circumferential cracking away from the projectile-target interface zone where strain rates are nominally lower as per (6.1).

Both regimes contain fragments that are mostly uniform in shape with low aspect ratios and elongated fragments with higher aspect ratios.

When comparing with the laser-driven impact, the longitudinal impact stress σ can be roughly approximated using the longitudinal sound speed c_l, impactor density ρ, and impact velocity U_0 as $\sigma = (1/2)\rho c_l U_0$ (this assumption holds best under one-dimensional loading conditions like in uniaxial strain). Using an Al projectile instead of tungsten carbide with the impact velocities in this study results in a peak stress decrease by a factor of $\sim$6 compared to the ballistic case. As discussed in the methods section, the smaller thicknesses of the impactor and target result in a higher strain rate, roughly approximated by two orders of magnitude increase for the Al flyer case ($\sim 10^7$ s^{-1}). The Al flyers have a large interaction region relative to the size of the target because the flyer diameter is half that of the target, in contrast to the ballistic case where the tungsten carbide projectile is much smaller than the target ($\sim$1:2 ratio vs $\sim$1:10 ratio, respectively).

With the smaller target volume, lower peak pressure, and larger interaction area, we expect a reduction in total strain energy across the entire volume that will greatly reduce the overall number of large fragments associated with structural bending for the laser-driven impacts. In the region where the strain energy density is comparable to the ballistic case, the majority of the generated fragments corresponds to defect spacing in the material. The laser-driven impact specimen thickness captures 90 percent of microstructure defect spacings and the majority of defects initiate and grow cracks due to the high strain rate and high stress loading. Because the projectile-target interaction region is roughly half of the target volume for the flyer impacts, examining if fragmentation statistics remain consistent with the microstructure controlled defects from ballistic fragmentation is an important consideration.

Between the flat and curved Al flyer cases, the curved Al flyer achieves peak longitudinal stress after a longer rise time and thus a slower strain rate than the flat Al flyer. The flat Al flyer creates a planar stress state associated with uniaxial strain where the ratio of longitudinal stress in the impact direction to transverse stress is $(1-\nu)/\nu$ with Poisson's ratio ν. In contrast, the curved Al flyer (and the spherical ballistic projectile) develop stress states with large deviatoric stresses throughout the interaction area. The developed shockwave is spherical in nature with a radius less than the radius of curvature of the sphere or the curved flyer, and the wave structure consists of a longitudinal wave followed immediately by a shear wave, introducing large deviatoric stresses under the projectile-target interaction region between the longitudinal and shear waves [155]. Kanel et al. [155] solve the balance of momentum equations to show that the magnitude of stress is inversely proportional to the radius away from the center of the projectile, so the imposed loading condition is extremely localized in comparison to the planar case.

The curved flyer generates a larger gradient of strain rates because of the localized stress state it imparts on the target. As a result, there should be large fragments at the outer radius of the curved flyer where strain rates are lower while the flat Al flyer will generate a more uniform distribution of fragmentation. In both cases, the compressive stress pulse from the laser-driven launcher is short (on the order of 10 to 50 ns), which is adequate to achieve full fragmentation through the thickness of the target assuming crack speeds on the order of acoustic velocities in the material. Fig. 6.9a shows that the laser-driven launches both primarily access the defect statistics controlled fragmentation regime, though ~20 percent of recovered fragments are larger than the target thickness in the flat flyer case, indicating that these fragments are created through radial cracking that may correlate to structural failure outside the projectile-target interface zone.

At first, this result is in contrast to the expected behavior from (6.1), but the localized stress state for the curved flyer induces such low strain rates near the outside edges of the flyer, that the region outside of the projectile-target interface does not fragment at all and is not reflected in the fragmentation data. Instead, the region of the target in direct contact with the flyer fails, and the majority of collected fragments are defect-spacing controlled. Fig. 6.9b suggests that the laser-driven impact experiments performed in this study generate fewer fragments with size distributions that are similar to the small fragment regime in ballistic experiments despite the differences in imposed stress state and strain rate, especially in the case of the curved Al flyer.

Altogether, these results indicate that probing microstructure-dependent fragmentation with the laser-driven launcher is best done with the highest possible peak stress and a curved flyer geometry. That said, all launch conditions induce some level of fragmentation that may be linked to the microstructure, indicating that the microstructure controlled fragmentation regime may be invariant to stress triaxiality, magnitude, and strain rate once the energy threshold for fragmentation is surpassed. Larger fragments in the defect-controlled regime have been shown to better erode impactors (and thus provide better penetration resistance) by Krell and Strassburger [5], while large fragments have also been shown to be an indicator of higher resistance to tensile failure at high rates in brittle modes by Chhabildas et al. [144]. Accordingly, finding methods to increase defect spacing and decrease defect count while retaining high densification may have a significant effect in curbing small fragment generation across a variety of loading conditions and thus may present an opportunity to improve ceramic protection capability.

6.6 Conclusions

We have investigated the impact-induced fragmentation of a hot-pressed boron carbide with ballistic impacts using a conventional gun and laser-driven flyer impacts to compare their resulting fragmentation distributions. The ballistic experiments reveal a structural failure regime with larger fragments and a microstructure defect controlled failure regime that generates smaller fragments. We have harnessed the evolving curvature of laser-driven microflyers to both perform a planar plate impact by conducting the impact early during the launch process, and also have generated a stress state similar to the ballistic case with a hemispherical nose by increasing the flight path length. In all cases, the defect spacing length scales inherent to the material microstructure affect failure and fragmentation sizes and shapes of at least some of the captured fragmentation distribution. The localized stress state in the case of the curved flyer directly probes microstructure-controlled fragmentation, while the planar impact also generates larger structural fragments like in the case of ballistic impact, though not to the same extent. Overall, the results presented in this paper demonstrate the capability of the laser-driven microflyer apparatus for fragmentation studies comparable to those possible with ballistic experiments and can offer insight into the impact induced failure of ceramics. In the following chapter, we turn away from experimental results that demonstrate the capabilities of the laser-driven flyer launcher to summarize the key findings in this thesis and present some perspectives on unanswered questions and potential future directions with this facility and technique.

Chapter 7

Conclusion

7.1 Summary of Chapters

This thesis has detailed a laser-driven launcher for shock compression experiments, and then presented studies on the spall failure of AZ31B magnesium alloy and Mg-9Al Mg alloy and brittle fragmentation of boron carbide. The key findings of this work are summarized below.

We began by describing the laser-driven micro-flyer launcher facility in chapter 2. Our measurements showed that the launcher accelerates sufficiently planar flyers of considerable thickness (25 to 100 μm) to velocities of 1-2 km/s to perform spall and impact experiments. In addition to this, we showed that a conservation of energy approach using parameters from the driving pulsed laser and the flyer material can accurately predict the launch velocity of the flyers. We described the modifications to the standard photon Doppler velocimetry system and processing procedure that are necessary to resolve shock compression events that occur over tens of nanoseconds in chapter 3. We also proposed and developed a proof of concept to detect shear velocities on a probed surface, which could provide a method to check impact planarity, but that technique has yet to be transitioned to the micro-flyer experiment.

Next we demonstrated the inaugural use of this facility for studies in several model protection material systems. In chapter 4 we showcased the capability of the apparatus to cause and resolve spall failure in extrusion machined AZ31B magnesium alloy. The apparatus generates a loading strain rate higher than most spall strength measurement regimes and we observe an increase in strength when compared with data on similar alloys tested at lower strain rates. The extrusion machined AZ31B Mg alloy was recieved in two cases, (1) a heavily deformed microstructure with weak rolling texture, and (2) a recrystallized microstructure with strong rolling texture. The heavily deformed microstructure consistently exhibited higher spall strength, indicating that the deformed microstructure may impede void growth. The deformed microstructure featured a higher dislocation density, higher twin volume fraction, and a weaker texture that together may provide a synergistic improvement in spall strength. We then used post-mortem fractography (micro-computed-tomography scans) to obtain void statistics in the spalled specimen. These statistics were used to back out the distribution of critical nucleation pressures in the material, and then were leveraged as inputs into a model that captured the rate dependent strength of the material.

Next, we interrogated the role of precipitate morphology during spall failure in Mg-9Al Mg alloy in chapter 5. The apparatus imposed plastic strains during shock compression that caused saturation of the flow stress at the point of spall failure, reducing spall strength anisotropy that is typically found in Mg alloys. This allowed for a study of the role of second phase particles in the microstructure. We found that the presence of precipitates causes a noticeable decrease in spall strength as the precipitates supply many void nucleation sites during peak tension. In addition to this, we found that the loading orientation with respect to the precipitates controls the spall strength, where presented volume of precipitates in the region of peak tension correlates to spall strength inversely. In the case of shock loading along the $\langle c \rangle$-axis, the spall strength was lower than in the case of shock loading in the transverse direction. Numerical simulations confirmed the orientation dependent spall strength. Further fractography is necessary to better understand the failure process and to confirm the precipitate volume correlation to spall strength, but our results indicate that second phase particles with just one dimension in the micron length-scale are detrimental to spall strength, even though such particles can improve yield strength.

Finally, we compared brittle fragmentation events caused by the laser-driven launcher with boron carbide targets to that caused by a powder gun in chapter 6. Both the laser-driven flyer system and the powder gun produced fragmentation statistics that indicated fragment sizes are correlated to the spacing between defects in the boron carbide microstructure. This implies that the laser-driven flyer system can access the same microstructure-controlled fragmentation as conventional methods, but can potentially do so in a manner where high throughput of experiments can improve collected datasets. Additionally, the correlation between microstructure and fragmentation length-scales suggests that increasing the spacing between inclusions in the microstructure may generate larger fragments with improved ballistic penetration resistance. Several drawbacks to our laser-driven flyer approach became apparent during the course of performing the aforementioned studies, which we now consider in detail.

7.2 Applicability and Limitations of Laser-Driven Flyers

The spall experiments and fragmentation studies in this thesis have revealed some limitations to the laser-driven micro-flyer-plate technique as a shock compression tool:

- First and foremost is the inability to characterize the state of the flyer just prior to impact. Gun-driven flyers utilize high speed imaging, high speed flash x-rays, or tilt closure pins to discern the tilt, planarity, and integrity of the flyer prior to impact, but the compact nature of our experiment and the requirement to perform the impact at short stand-off distances for planar impact makes such characterization an impossibility with our facility. In chapter 2 we detailed our high speed imaging characterization of the flyer in the absence of a target and use that data to design our experiment for optimum tilt and planarity. We also increase the pulse duration of the laser with a ring cavity to improve flyer integrity. Beyond these considerations, there is little else that can be done to confirm low-tilt and planar impacts without implementing multi-point velocimetry as we discuss in the next sub-section. Figs. 4.6 and 5.11 confirm matching trends for the spall experiments when comparing our technique to published data from gun-driven flyers. Fig. 6.6 also shows positive correlation for fragmentation results when compared to gun experiments, altogether suggesting that our understanding of laser-driven impact conditions is likely correct.

- Experiment design must be considered based on the small scale of the experiment and our velocimetry probe size. Our velocimetry probe from chapter 3 has a diameter spanning tens of microns (∼30 µm). This makes bulk material measurements impossible when microstructure features are larger than (at most) ∼10 µm. In the AZ31B Mg alloy study from chapter 4, the grain size is sufficiently below the probe diameter so we can make comments on the bulk material response. The data features somewhat less scatter as a result when compared to the Mg-9Al study in chapter 5. In the Mg-9Al study, our answer to probing a large grain size material is to design the experiment to compare with single crystal experiments and to perform a large number of experiments. The boron carbide study in chapter 6 uses a sample thickness that captures 85 to 90 percent of the defect spacings in the microstructure to ensure that fragmentation results from a microstructure that represents the bulk material. We again benefit from our spall results maintaining trends with published data despite the differences in experiment scale. As a rule of thumb, the velocimetry probe region must be 10 times larger (or more) than the characteristic length scale of the target material grain size to make measurements of the bulk material. In the absence of this condition, the experiment is closer to a single crystal measurement.

- Specimen preparation in laser-shock experiments has always been a concern. Large-scale laser facilities employ entire teams of specimen preparation specialists for this reason. During the course of performing these experiments, it has become clear that preparing planar specimens is a non-trivial task. The velocimetry works best when some of the light is scattered, so mirror-finish specimens are not ideal. The result is that the high throughput potential of the experiment is throttled by specimen preparation time. In the case of the AZ31B Mg alloy experiments in chapter 4, the extrusion machining technique provide exceptionally well controlled sample thicknesses with sufficient surface finishes for velocimetry, but the remaining studies require time-consuming specimen preparation. Either the as-received material must be adequate for the experiment, or considerable time and expense must be expended to achieve high throughput with the apparatus. We have found success in using a mirror finish (1200 grit or finer) for surfaces in contact with the flyer, but using no finer than a 1200 grit finish for free surfaces where velocimetry measurements are made.

- As in any experiment that uses optics, alignment is crucial to a successful experiment. At this time, the majority of the alignment steps are easily controlled through kinematic optics mounts, but care must be taken to ensure the alignment is maintained as a whole. In addition to this, our approach operates at the very limit of photon Doppler velocimetry time resolution, so impact events under 10 ns will be quite difficult to resolve. Perhaps a higher digitizer sampling rate can improve the time resolution to a degree, but generally experiments must be designed to have higher event durations in the tens of nanoseconds.

Despite these drawbacks, there are several aspects of the apparatus that may be improved, and some potential studies which could employ the technique that we now outline.

7.3 Future Work

- The velocimetry techniques detailed in this thesis have excellent velocity and time resolutions, but the velocity record is insufficient to examine shock-induced changes in microstructure (Such as the Hugoniot elastic limit in the elastic regime, or crystal lattice strains resulting from the shock loading). Post-mortem fractography can only be obtained after all deformation has occurred, and the effects from the primary spall fragmentation are mixed with later deformations in the experiment. Researchers have coupled time-resolved diffraction to laser shock experiments in recent years to obtain histories of texture and lattice strain [156, 157], and such an approach could certainly improve studies here, like in the case of spall experiments on magnesium alloys where the spall failure occurs during tension in a microstructure that has been shock compressed. As nanosecond period x-ray sources become more commonplace in research facilities, our expectation is that most shock compression techniques will move toward employing simultaneous diffraction methods.

- We selected Al as the flyer material for its low cost and low density, but in the case of the boron carbide study (chapter 6), we found that the aluminum flyers would not allow us to achieve the proposed amorphization threshold in the literature. There are some studies that have looked at various flyer materials [158], but there is no comprehensive study that relates flyer material density and laser coupling potential to launch velocity. We provided evidence that the damage threshold of the confining substrate in the flyer assembly plays a large role in the transmitted energy from the laser to the flyer (chapter 2. During the course of developing the facility, we performed some preliminary studies on substrate material and found a marked difference in launch velocity based on the material. Fig. 7.1 shows velocimetry data from a study comparing borosilicate glass and fused silica as the substrate. The overlaid model was fitted using measured transmittance data for each substrate. There is a $\sim$15 percent difference in launch velocity based on substrate choice that suggests there could be a substrate material that improves on the launch velocities presented in this work. It would be fruitful to perform a study on alternative structural metals such as tungsten carbide or tungsten, titanium, or magnesium.

- The material studies performed here were done with single point velocimetry. It would be extremely convenient to have a “line” velocimetry measurement to understand the planarity of any experiment. This would provide an in-situ method of knowing experiment quality. In addition to convenience, two dimensional or three dimensional velocimetry would

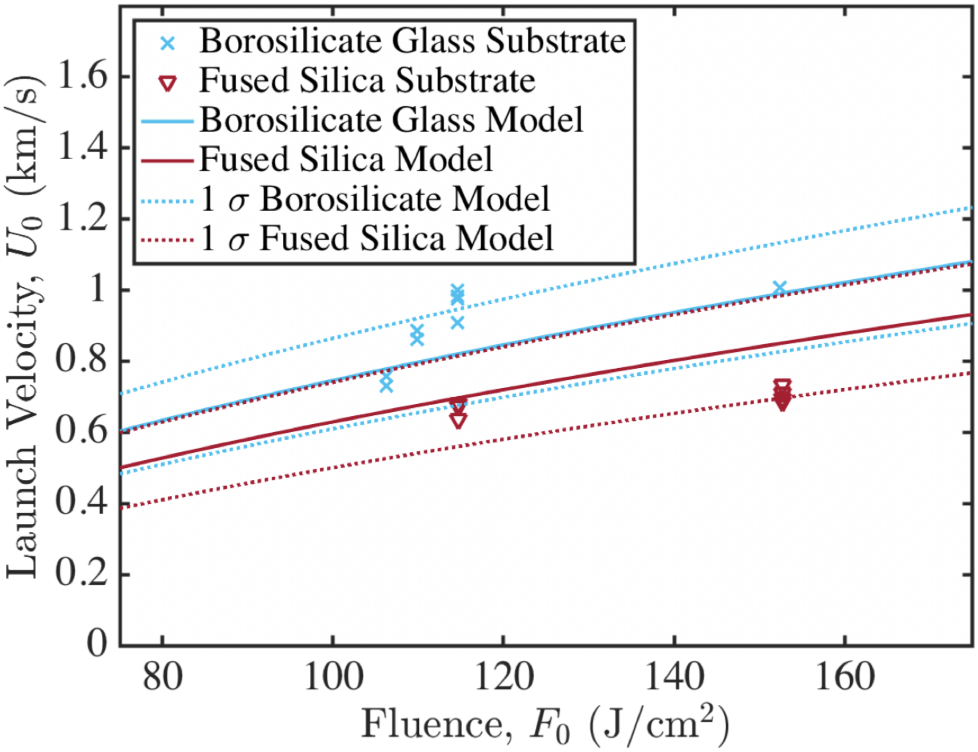

Figure 7.1: Experimental data for launch with two different substrate materials (Borosilicate glass and fused silica) compared with model predictions from Chapter 3.

be useful for experiments on materials where the grain size is much smaller than the flyer diameter, or when the material is very heterogenous and a non-planar shockwave is not expected as a result. We have begun to develop multi-point velocimetry by modifying the photon Doppler velocimetry system to either send more wavelengths of laser light and sort spatially by wavelength (Fig. 7.2), or to use time multiplexing to superimpose multiple velocity histories with just one interferometer, but both approaches have significant hurdles with respect to returned power and imaging of the multiple beams onto the target surface.

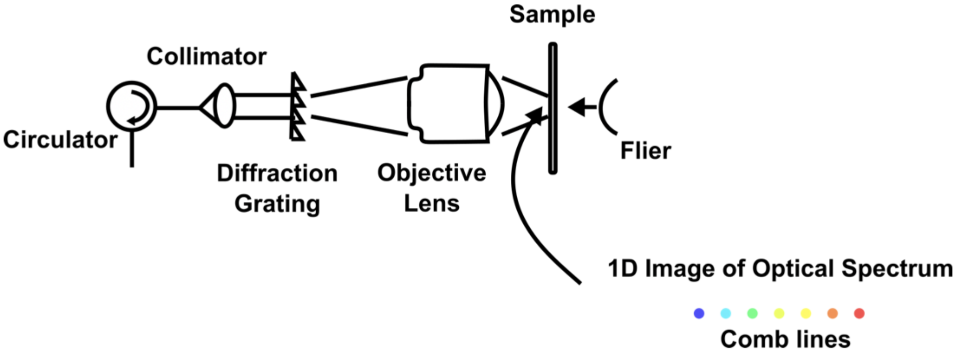

Figure 7.2: Schematic of possible multi-point velocimetry system that uses a diffraction grating to map different wavelengths onto different areas of the flyer or specimen.

- Upon developing some form of multi-point velocimetry, flyer impacts into common window materials such as LiF or quartz could be characterized for impact tilt and planarity (with no target apart from the window material). In addition, careful selection of a buffer material between the flyer and the target can be used to only examine changes in material structure from just the shock compression loading by exploiting the acoustic impedance mismatch of the buffer material like in studies performed by Winey, Renganathan, and Gupta [159] and Renganathan, Winey, and Gupta [160].

- In chapter 4 we showed spall strength differences between Mg alloys that were extrusion machined to different strains and strain rates, and thus different thicknesses. Though we saw a clear difference between the two cases we presented, it would be interesting to do a parametric study on varying strain and strain rate processing between the two extreme microstructures in this study to better understand the reasons why the spall strengths are different in this work. In the same fashion, taking a single microstructure and machining it to different thicknesses could rule out thickness effects on the variations in spall strength.

- In chapter 5 we showed spall strength dependency on precipitate orientation in Mg-9Al alloy. The shock pressures used in that study induce strains that are outside of the plastic anisotropy regime in Mg. With a high throughput apparatus, the impact velocities could be decreased to return the shock pressures into the anisotropic plasticity regime, and then many experiments could be performed to examine the role of the anisotropy on spall strength. This study could be performed across various strain rates to complement studies that have shown the presence of plastic anisotropy even under high rates, such as by Zhao, Kannan, and Ramesh [147].

Appendix A

Appendix: LDMFP Facility Guide

A.1 Experiment Protocol

This is an experiment protocol for the laser-driven micro-flyer facility at the Hopkins Extreme Materials Institute. Note that the facility can be dangerous if the guide is not followed completely and in the following order. An updated copy of this guide with images can be found at HEMI LDMFP Guide. The version of the guide at the link above supercedes this document as the facility is under continuous development.

- Before turning on pulsed laser:
  1. Turn on delay generator.
  2. Turn on shutter control. ALERT: MAKE SURE SHUTTER IS CLOSED BEFORE TURNING ON PULSED LASER.
- Turning on the pulsed laser:
  1. PUT ON YOUR SAFETY GOGGLES.
  2. ALERT: ARE YOUR GOGGLES ON? MAKE SURE.

3. Make sure the oscillator and amplifier dials on the pulsed laser are set to zero power.
4. Check to make sure your safety goggles are on, then turn on the pulsed laser.

- While the laser warms up:

1. Turn on PDV low-noise EDFA power source.
2. Plug in PDV photodiode power source.
3. Turn on PDV seed lasers through oscilloscope control.
4. Turn on PDV main EDFA, but set to 100 mW. ALERT: YOUR GOGGLES SHOULD BE ON AT THIS POINT.
5. Turn on motorized stages.
6. Turn on room vacuum to vacuum chamber.
7. Turn on other diagnostics such as high speed camera and pulsed laser illumination. Check to make sure these diagnostics are interfaced with the delay generator.
8. Turn on PDV camera. Place an IR card above the PDV objective and draw a circle using the camera software where the PDV spot is being emitted.
9. Are your goggles on? Is the shutter closed? Turn on the oscillator and amplifier in the pulsed laser to full for ten minutes, and keep running for consistent power delivery.

- Alignment check:

    1. Place an acrylic sheet over the foil of a target assembly, and place just the target assembly without the vacuum chamber onto the motorized stage.
    2. Align the PDV camera drawn circle with a cut flyer disk on the flyer assembly foil surface.
    3. Are your goggles on?
    4. Make sure the PDV objective is covered by glass or plastic.
    5. Follow the shooting checklist, then fire the laser from the delay generator once.
    6. Align the PDV objective stage so that the PDV camera circle is in the center of the imaged driving laser pulse.

- Shooting:
    1. Epoxy a spacer around the pre-cut flyer disk on a flyer assembly.
    2. Epoxy a target onto the spacer.
    3. Place flyer assembly inside vacuum chamber, and seal vacuum chamber with gasket from above.
    4. Align the PDV camera circle with the center of the target.
    5. Adjust Z-axis on the PDV objective stage so that the target surface comes into focus.
    6. Stop the PDV objective down to 16 for best depth of field during shot.

7. Follow shooting checklist, then fire the laser from the delay generator once.

- After the shot:
  1. DO NOT REMOVE YOUR GOGGLES.
  2. Save your data.
  3. If there are subsequent shots, do not turn down or turn off the laser for best repeatability.
- Deactivating the facility:
  1. Turn off the pulsed laser only when the oscillator and amplifier are not running.
  2. Turn off the low-noise EDFA and turn off its power source.
  3. Unplug the PDV photodiodes.
  4. Turn off the motorized stage controllers.
  5. Make the PDV lasers stop emitting through the oscilloscope control, but do not turn them off. The oscilloscope can be turned off as required.
  6. Turn off the shutter control.
  7. Turn off other diagnostics.

A.2 Firing Checklist- DO THIS EVERY TIME

☐ Everyone has appropriate eyewear on.

☐ Pulsed laser is on and shutter is closed.

☐ Delay generator is on with timing settings intact.

☐ Drive-train is clear of objects that could impede the laser pulse (loose cables etc.).

☐ PDV main power is set correctly (500mW is typical during firing).

☐ PDV low-noise EDFA is on and is amplifying correctly.

☐ Oscilloscope is waiting for trigger.

☐ Vacuum gauge is reading at least 75 percent evacuation.

☐ The PDV objective is covered by a glass slide or is otherwise protected.

☐ All other diagnostics are activated and waiting for trigger.

☐ FIRE.

A.3 Data Analysis

The MATLAB code used to analyse collected PDV data can be found for each individual saved experiment in the next appendix, but we will review the procedure here:

A.3.1 Load File and Determine Carrier Frequency

This section loads the data and shows a spectrogram of the full signal to help determine the points where data truncation needs to occur.

```
clear all;
nCol=2; %Read in file
fid = fopen('/Users/debjoymallick/Google Drive/experiments/DATE/FILE.txt');
%fid = fopen('Interferometer(4).txt');
cen=0;
for i=1:5
firstRowString = fgetl(fid);
end
%Visualize raw data in spectrogram
data = textscan(fid, repmat('%f',1,nCol),'Delimiter',',','CollectOutput', true);
fclose(fid);
time1=data{1}(:,1);
voltage1=data{1}(:,2);
N=1600/8; %window size 256*4
noverlap=round(.5*N);
nfft=N*10;
spectrogram(voltage1, N, noverlap, nfft, 1/(time1(2)-time1(1)),'yaxis','Power'); colormap jet;
npts=size(voltage1,1);
spectra=fft(voltage1);
spectra=abs(spectra/npts);
spectra=spectra(1:npts/2+1);
spectra(2:end-1)=2*spectra(2:end-1);
w=(1/(time1(2)-time1(1)))*(0:(npts/2))/npts;
% figure();
% plot(w,spectra);
[dummy,index]=max(spectra(100:end));
cen=w(index+99); %Find peak signal tone for heterodyne 0 frequency.
```

A.3.2 Truncate Raw Signal in Time

This section truncates the raw signal in time so we only examine the data of interest.

```
%% Truncate signal in time
%[c index] = min(abs(time1-(.0599500001+val)))
[dummy starti]=min(abs(time1-(.0599500001+50e-6))); % Start
[dummy endi]=min(abs(time1-(.0599500001+50.905e-6))); % Finish

cutt=time1(starti:endi);
cutv=voltage1(starti:endi);

spectrogram(cutv, N, noverlap, nfft, 1/(time1(2)-time1(1)),'yaxis','Power'); colormap parula;
ylim([0e9 4]);
caxis([-70 -20]);
ylabel('Frequency, $f(t)$ (GHz)','interpreter','latex');
xlabel('Time, $t$ (ns)','interpreter','latex');
pbaspect([4 3 1]);

%% Save truncated signal
time1=cutt;
voltage1=cutv;
```

A.3.3 Filter out Carrier Frequency

In this section we filter out the baseline carrier frequency that corresponds to the zero velocity from heterodyne-mixing the Doppler shifted signal with an up-shifted local oscillator.

```
%% Filter out heterodyne 0 signal
samplerate = 1/(time1(2) - time1(1));
freq = fftshift(((-length(time1)/2):(length(time1)/2-1)) * samplerate/length(time1))';

wid = 0.04e9;
ord = 6;
filt = 1-exp(-(freq - cen).^ord / wid^ord) - exp(-(freq + cen).^ord / wid^ord);
```

```

[dummy fixt]=min(abs(time1-(time1(1)+1.229e-6)));
voltagefilt = ifft(fft(voltage1) .* filt);

spectrogram(voltagefilt, N, noverlap, nfft, 1/(time1(2)-time1(1)),'yaxis','Power'); colormap parula;
ylim([0e9 4]);
caxis([-70 -20]);
ylabel('Frequency, $f(t)$ (GHz)','interpreter','latex');
xlabel('Time, $t$ (ns)','interpreter','latex');
pbaspect([4 3 1]);

%% Set filtered signal into voltagefilt
voltage1=voltagefilt;
```

A.3.4 Perform Phase Differentiation

In this section we filter out all signals outside of a pass band that contains the frequency information of interest. Then the unwrap command returns the phase angles with respect to time, which we then differentiate with a central difference routine with a user defined stencil size. The resulting traces give the measured velocity.

```
%% Spectrogram to determine filter limits
spectrogram(voltagefilt, hamming(N), noverlap, nfft, 1/(time1(2)-time1(1)),'yaxis','Power'); colormap jet;
set(gca, 'FontName','Serif','FontSize', 14)
%% phase diff
%check for number of points to be even
ns=3; %Central Difference Window
figure();
numpts=size(time1,1);
if mod(numpts,2)==1
    time1=cat(1,time1,time1(size(time1,1))+time1(2)-time1(1));
    voltage1=cat(1,voltage1,voltage1(size(voltage1,1)));
```

```
end
numpts=size(time1,1);
phas = unwrap(angle(voltage1));

freq = fftshift(((-numpts/2):(numpts/2-1)) * samplerate/numpts)';
filt=freq > 1.9e9 & freq < 3.5e9; %Set Filter Limits Here
voltagefilt = ifft(fft(voltage1).*filt);

phas = unwrap(angle(voltagefilt));

hold on;
sub1=subplot(1,2,1);
spectrogram(voltagefilt, hamming(N), noverlap, nfft, 1/(time1(2)-time1(1)),'yaxis','Power'); colormap parula;

for j=ns:ns

phasD2 = filter(-smooth_diff(40*j),1,phas)/(time1(2)-time1(1)) / 2 /pi;
sub2=subplot(1,2,2);
hold on;
vel=775*((phasD2/1e9)-cen/1e9)-offset;
plot((time1-time1(1))/1e-9, vel,'k','DisplayName',num2str(i),'linewidth',2);
xlabel('Time, $t$ (ns)','interpreter','latex');
ylabel('Velocity, $U(t)$ (m/s)','interpreter','latex');
xt = get(gca, 'XTick');
time=(time1-time1(1))./1e-6;
ylim([0 1500]);
xlim([43 time(end-200)*1000]);
pbaspect([4 3 1]);

subplot(1,2,1);
hold on;
plot(time./1e-3,phasD2./1e9,'k','linewidth',2);
ylim([0 4]);
```

```
xlim([3 time(end-200)/1e-3]);
caxis([-70 -20]);
xlabel('Time, $t$ (ns)','interpreter','latex');
ylabel('Frequency, $f(t)$ (GHz)','interpreter','latex');
xlim([43 time(end-200)*1000]);
pbaspect([4 3 1]);
end
```

Appendix B

Appendix B: Data Repository

B.1 Location and Organization of Data

The organization of data in this thesis, and throughout my time as a Ph.D student, is detailed herein. All of the data I have collected can be accessed through this link. All files are organized by date of collection within that folder. The dates correspond to entries in my lab notebook, stored as a PDF and accessible through this link. I will also detail links to the exact location of data and MATLAB files used to generate the figures from this thesis below. In case these hyperlinks are not accessible in print copies of this thesis, or in the case that the online database does not transfer links over correctly, a copy of this manuscript in PDF and LaTeX source with the links intact is available at https://ramesh-lab.craedl.org/directory/166099/

B.1.1 Chapter 1

Figures from chapter 1 are in this compilation file of chapter 1 figures.

B.1.2 Chapter 2

Figures from chapter 2 are in this compilation file of chapter 2 figures. The data and MATLAB script used to generate Fig. 2.5 are in this directory. The images of intensity profiles taken for Fig. 2.6 are in this folder. The images of intensity profiles taken for Fig. 2.7 are in this folder. The data for Fig. 2.8 showing the velocity history of a flyer launch and several videos of flyer launches for curvature analysis are in this folder. The data and MATLAB file to generate Fig. 2.9 is in this file. The data and MATLAB file to generate Fig. 2.10 is in this file. The data and MATLAB file to generate Fig. 2.11 is in this file. The data and MATLAB file to generate Fig. 2.12 is in this file.

B.1.3 Chapter 3

Figures from chapter 3 are in this compilation file of chapter 3 figures. The MATLAB script to generate the images in Fig. 3.2 can be accessed through this link. The MATLAB script and data files to generate Fig. 3.5 are in this folder. The MATLAB script and data files to generate Fig. 3.6 are in this folder. The MATLAB script to generate Fig. 3.7 can be accessed through this link.

B.1.4 Chapter 4

Figures from chapter 4 are in this compilation file of chapter 4 figures. Velocimetry raw data and processing MATLAB files are found in 2018.10.08, 2018.07.18, and 2018.07.24 as per the tables showing shot numbers in the subsequent section. The MATLAB script used to generate Fig. 4.6 can be accessed through this link. The MATLAB script used to generate Fig. 4.7

can be accessed through this link. The MATLAB script used to generate Fig. 4.8 can be accessed through this link. The data and MATLAB script used to generate Fig. 4.9 can be accessed through this directory. The MATLAB script and data used to generate Figs. 4.12, 4.13, and 4.14 can be found in this folder. The MATLAB script used to generate Fig. 4.15 can be accessed from this link.

B.1.5 Chapter 5

Figures from chapter 5 are in this compilation file of chapter 5 figures. Velocimetry raw data and processing MATLAB files are found in these two folders: 2019.02.11 and 2019.02.13. The data and MATLAB script used to generate Fig. 5.4 can be found in this directory. The MATLAB script used to generate Figs. 5.6 and 5.11 can be accessed by this link. The MATLAB script used to generate Fig. 5.7 can be accessed by this link. The data and MATLAB script used to generate Fig. 5.10 can be found in this directory. The MATLAB script used to generate Fig. 5.12 can be accessed through this link.

B.1.6 Chapter 6

Figures from chapter 6 are in this compilation file of chapter 6 figures. The data and MATLAB scripts used to generate Figs. 6.2, 6.4, 6.5, and 6.6 are located in this directory. The data and MATLAB scripts used to generate Fig. 6.7 are located in this directory. The data and MATLAB scripts necessary to generate Figs. 6.8, 6.9, and 6.10 are in this directory.

B.1.7 Chapter 7

The figures in chapter 7 are in this compilation file of chapter 7 figures. The data and MATLAB script used to generate Fig. 7.1 is accessible through this link.

B.2 Experiment Velocimetry Data

B.2.1 Velocity Histories from Chapter 4

The velocity histories for the AZ31B Mg Alloy spall experiments are presented below. The data for the 100 µm thick specimens is presented first, followed by the data for the 175 µm specimens.

Shot Number	Flyer Thickness (μm)	Target Thickness (μm)	Peak Velocity (m/s)	Shock Stress (GPa)	Pullback (m/s)	Uncorrected Spall Strength (GPa)	Strain Rate (s^{-1})	Pulse Duration (ns)
2018.10.08.00009	50	100	742	3.29	344	1.36	2.4E+06	31
2018.10.08.00011	50	100	870	3.86	330	1.30	2.8E+06	16
2018.07.18.00007	50	100	1563	6.94	387	1.53	5.5E+06	14
2018.07.18.00009	50	100	1060	4.70	398	1.57	3.5E+06	15
2018.07.18.00011	50	100	1026	4.55	351	1.39	3.8E+06	14

Table B.1: AZ31B 100 µm Mg Alloy Spall Strength Data Summary (Chapter 4).

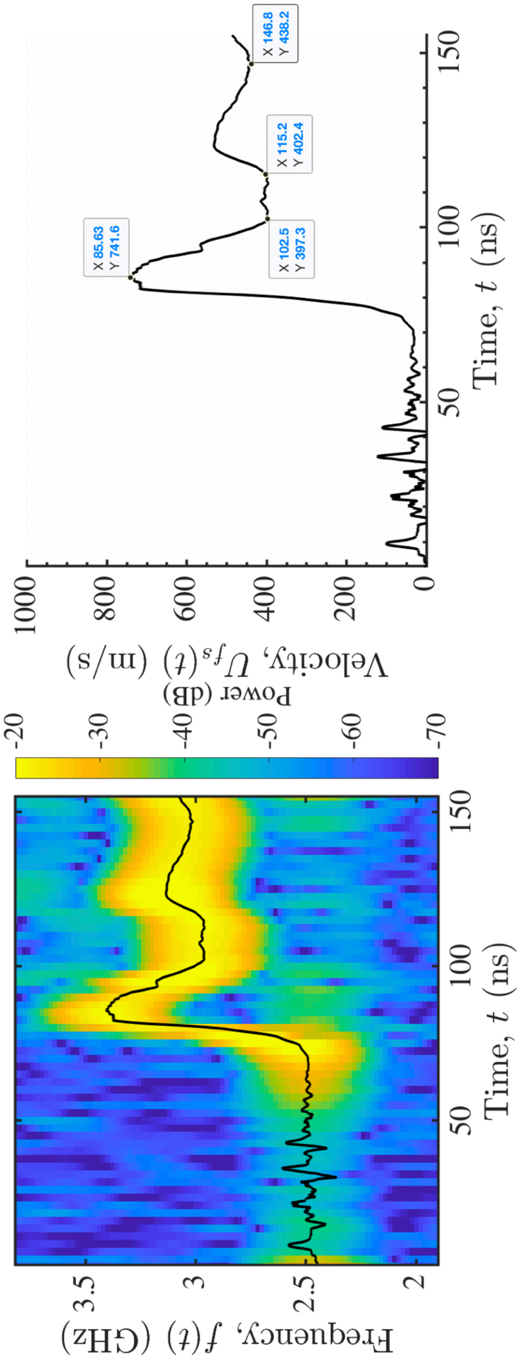

Figure B.1: Data from shot number 2018.10.08.00009

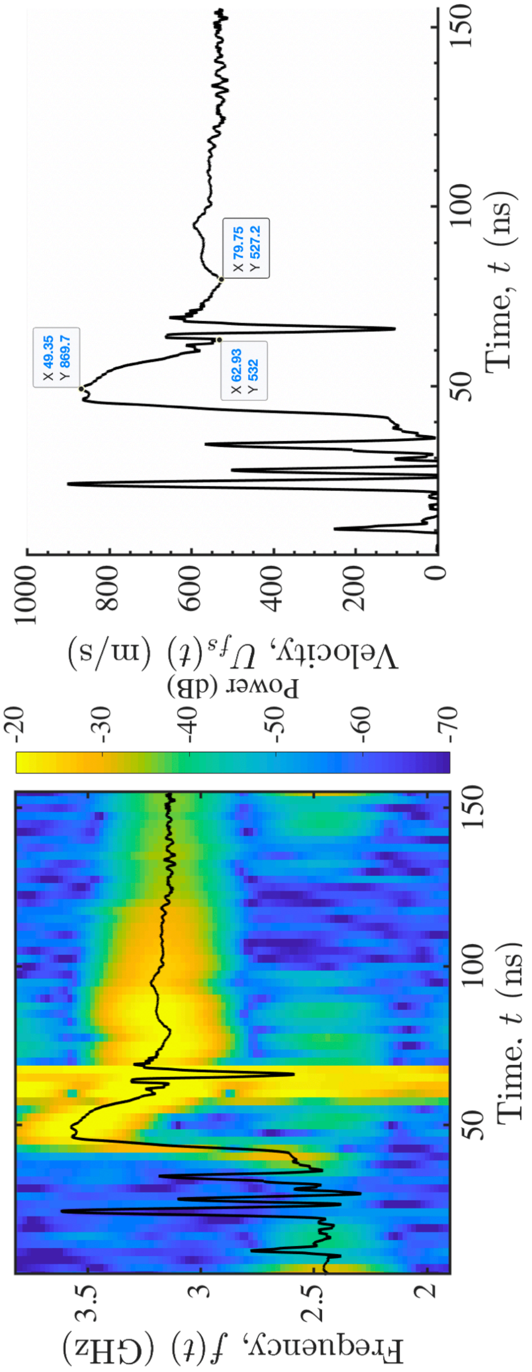

Figure B.2: Data from shot number 2018.10.08.00011

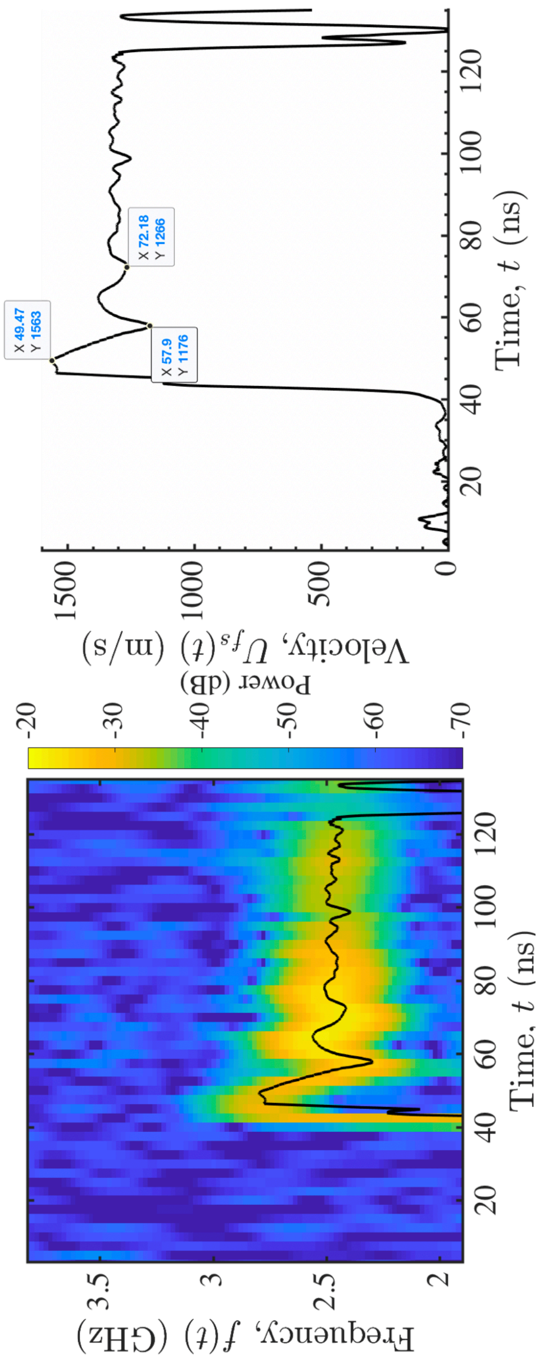

Figure B.3: Data from shot number 2018.07.18.00007

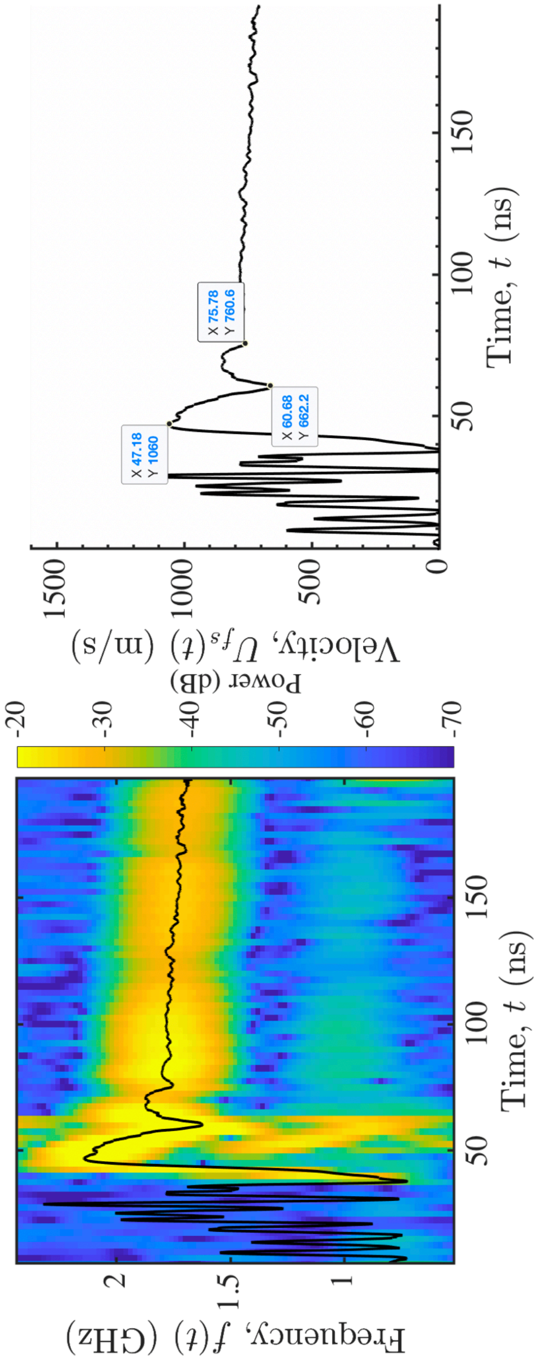

Figure B.4: Data from shot number 2018.07.18.00009

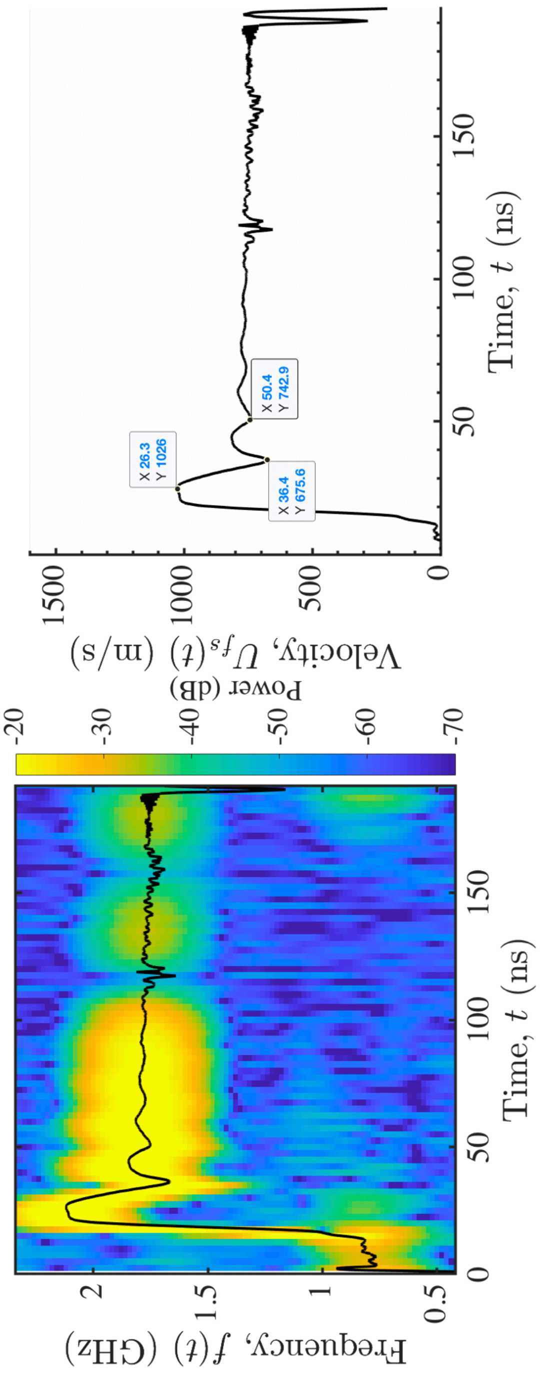

Figure B.5: Data from shot number 2018.07.18.00011

Shot Number	Flyer Thickness (μm)	Target Thickness (μm)	Peak Velocity (m/s)	Shock Stress (GPa)	Pullback (m/s)	Uncorrected Spall Strength (GPa)	Strain Rate (s^{-1})	Pulse Duration (ns)
2018.10.08.00003	50	175	744	3.30	426	1.68	2.1E+06	22
2018.10.08.00004	50	175	741	3.29	449	1.77	3.5E+06	23
2018.10.08.00005	50	175	757	3.36	430	1.70	2.4E+06	22
2018.10.08.00007	50	175	895	3.97	412	1.63	3.2E+06	14
2018.07.24.00001	50	175	949	4.21	423	1.67	2.8E+06	15

Table B.2: AZ31B 175 µm Thick Mg Alloy Spall Strength Data Summary (Chapter 4).

B.2.2 Velocity Histories from Chapter 5

The velocity histories for the Mg-9Al Alloy spall experiments are presented below. The data for warm-rolled and solutionized samples in the normal direction is presented first, followed by the data for warm-rolled and solutionized samples in the transverse direction. Next, the data for warm-rolled, solutionized, and peak aged samples in the normal direction is presented, followed by the data for warm-rolled, solutionized, and peak aged samples in the transverse direction.

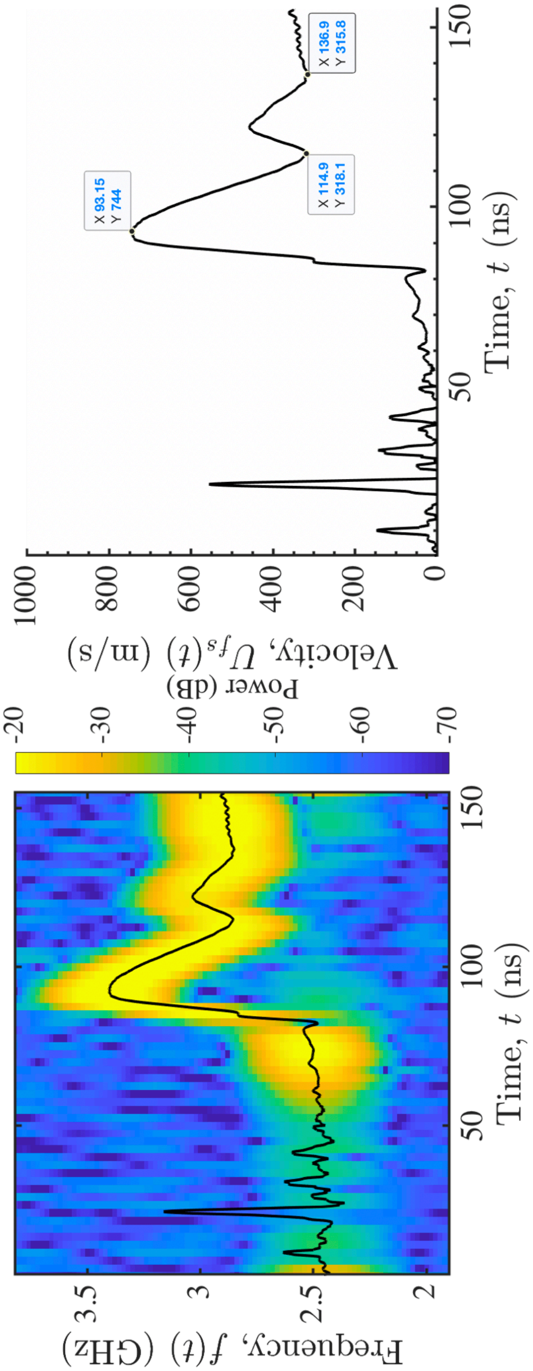

Figure B.6: Data from shot number 2018.10.08.00003

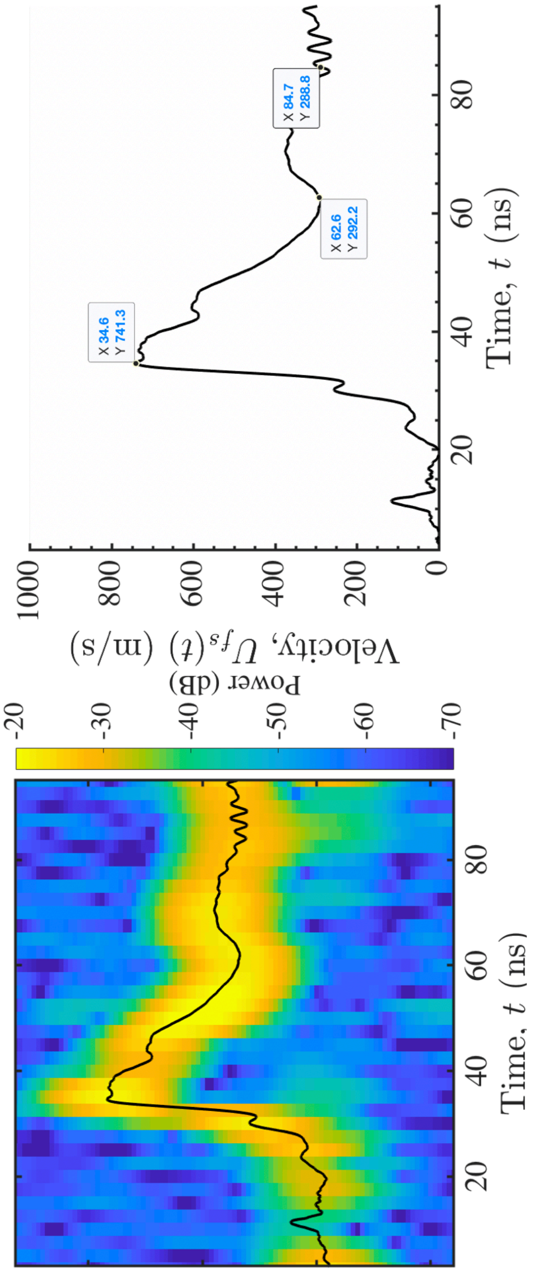

Figure B.7: Data from shot number 2018.10.08.00004

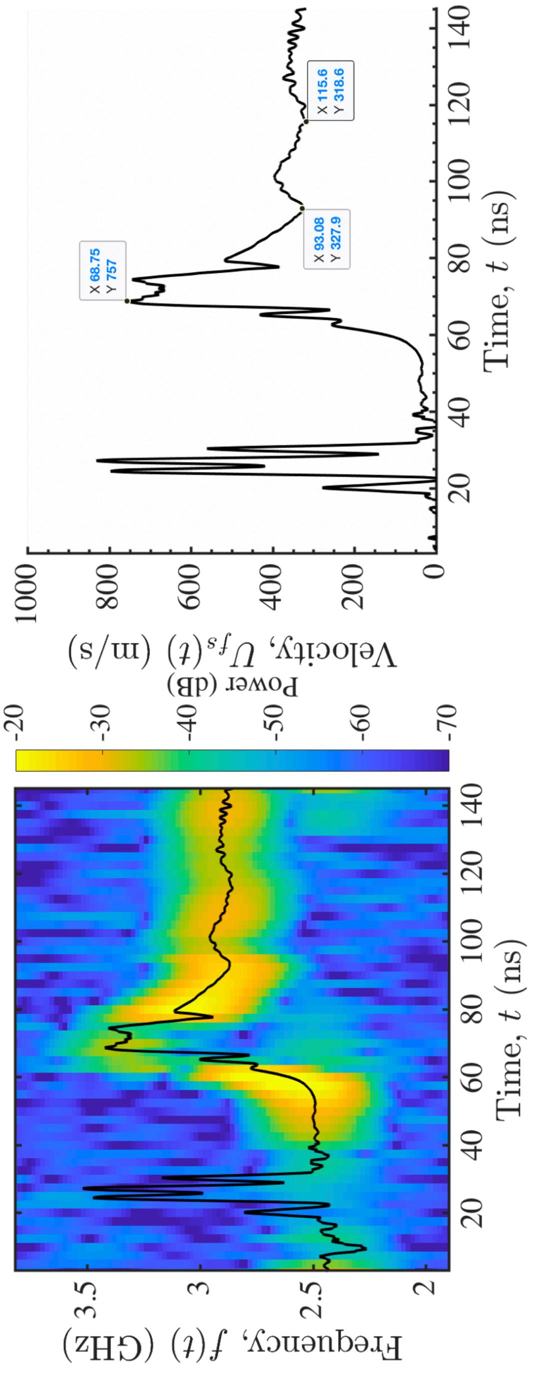

Figure B.8: Data from shot number 2018.10.08.00005

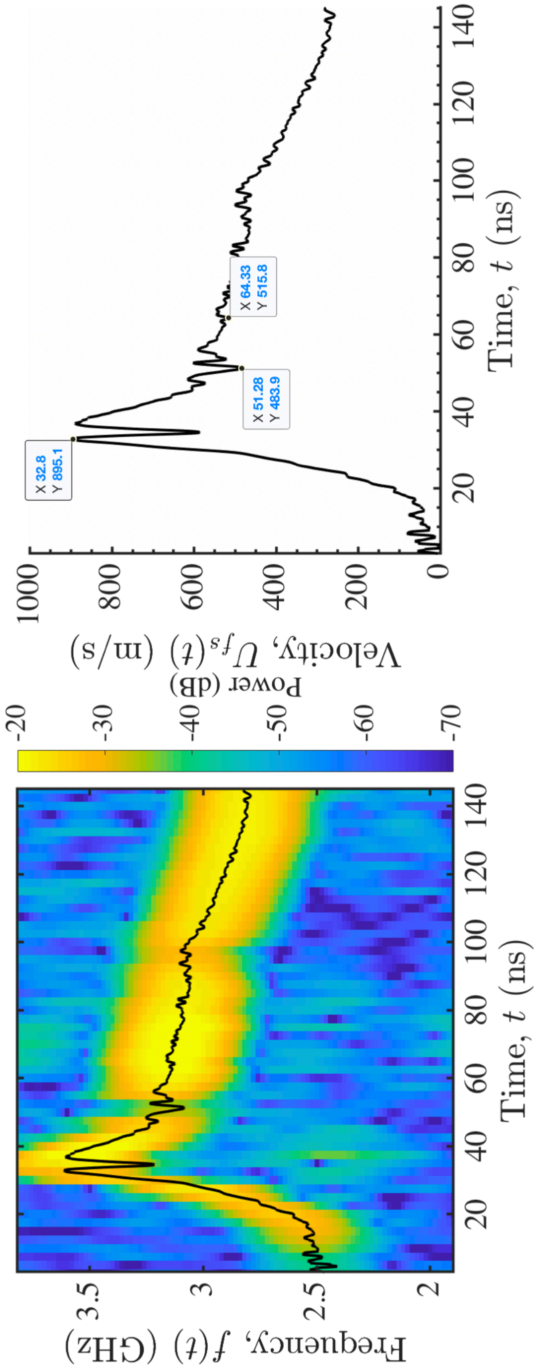

Figure B.9: Data from shot number 2018.10.08.00007

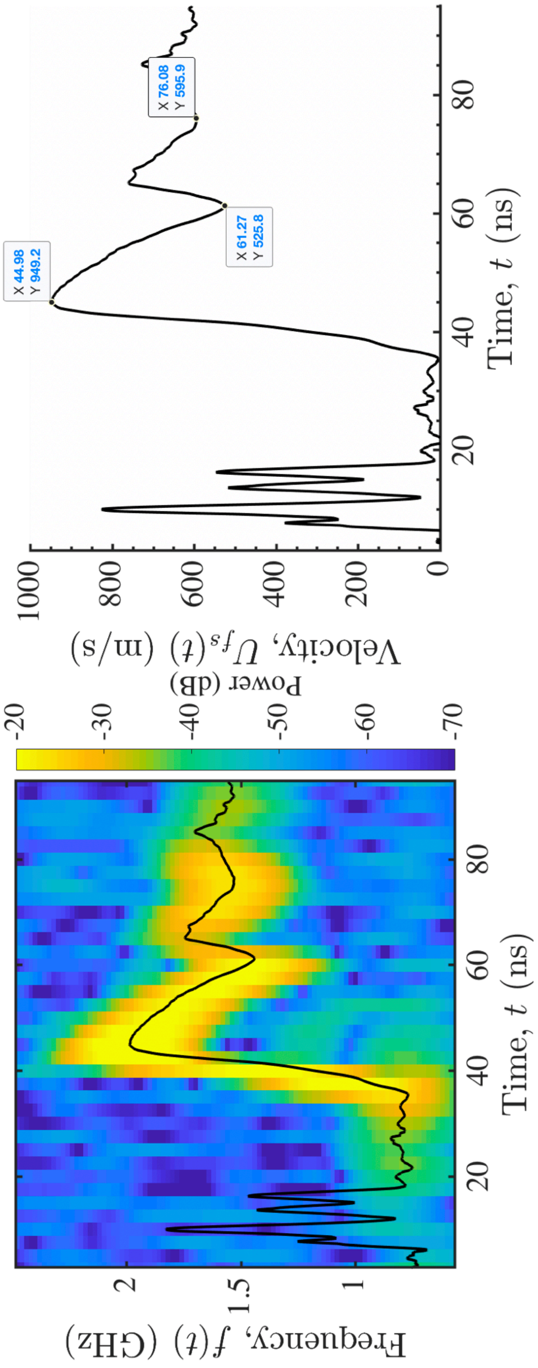

Figure B.10: Data from shot number 2018.07.24.00001

Shot Number	Flyer Thickness (μm)	Target Thickness (μm)	Peak Velocity (m/s)	Shock Stress (GPa)	Pullback (m/s)	Uncorrected Spall Strength (GPa)	Strain Rate (s^{-1})	Pulse Duration (ns)
2019.02.11.00001	50	200	710	2.79	423	1.66	1.91E+06	23
2019.02.11.00010	50	200	761	2.99	496	1.95	2.07E+06	30
2019.02.11.00018	50	191	759	2.98	464	1.82	3.32E+06	15
2019.02.11.00021	50	195	727	2.85	461	1.81	2.35E+06	19
2019.02.11.00027	50	190	741	2.91	420	1.65	1.93E+06	30
2019.02.11.00031	50	193	677	2.66	451	1.77	1.90E+06	25
2019.02.11.00037	50	185	979	3.85	501	1.97	4.18E+06	15
2019.02.11.00042	50	187	728	2.86	406	1.59	2.05E+06	30
2019.02.11.00052	50	183	731	2.87	448	1.76	1.50E+06	32
2019.02.13.00001	50	178	720	2.83	451	1.77	1.61E+06	29
2019.02.13.00002	50	177	936	3.68	426	1.67	3.78E+06	16
2019.02.13.00003	50	178	643	2.53	399	1.57	1.86E+06	27

Table B.3: Warm-Rolled, Solutionized, Mg-9Al Alloy Normal Direction Spall Strength Data Summary (Chapter 5).

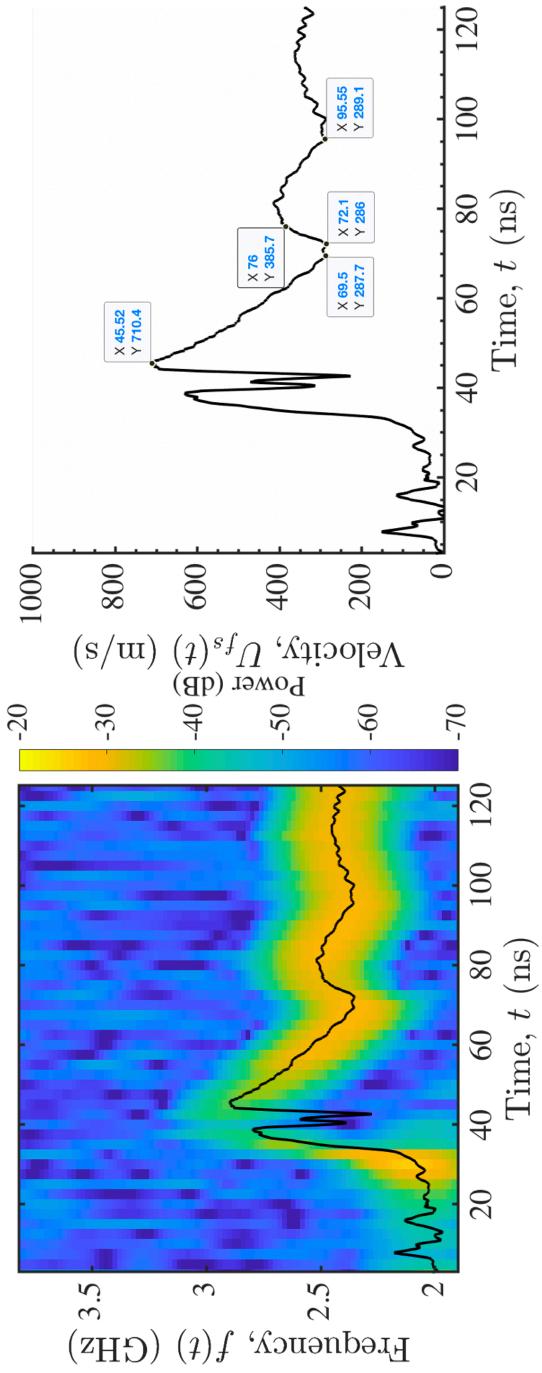

Figure B.11: Data from shot number 2019.02.11.00001

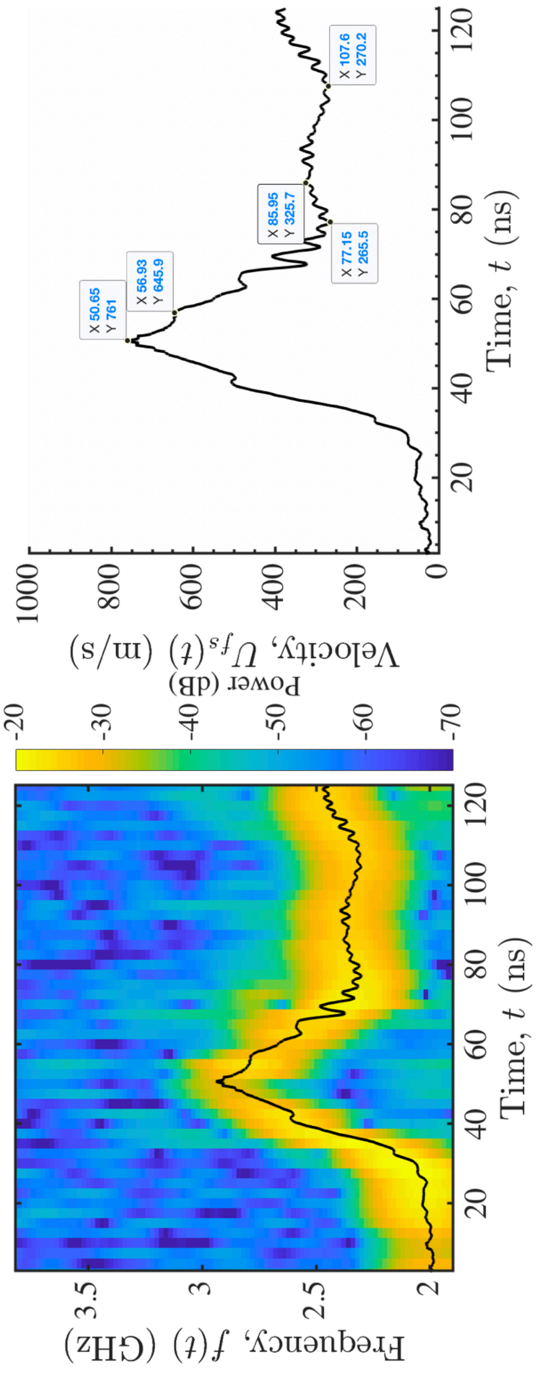

Figure B.12: Data from shot number 2019.02.11.00010

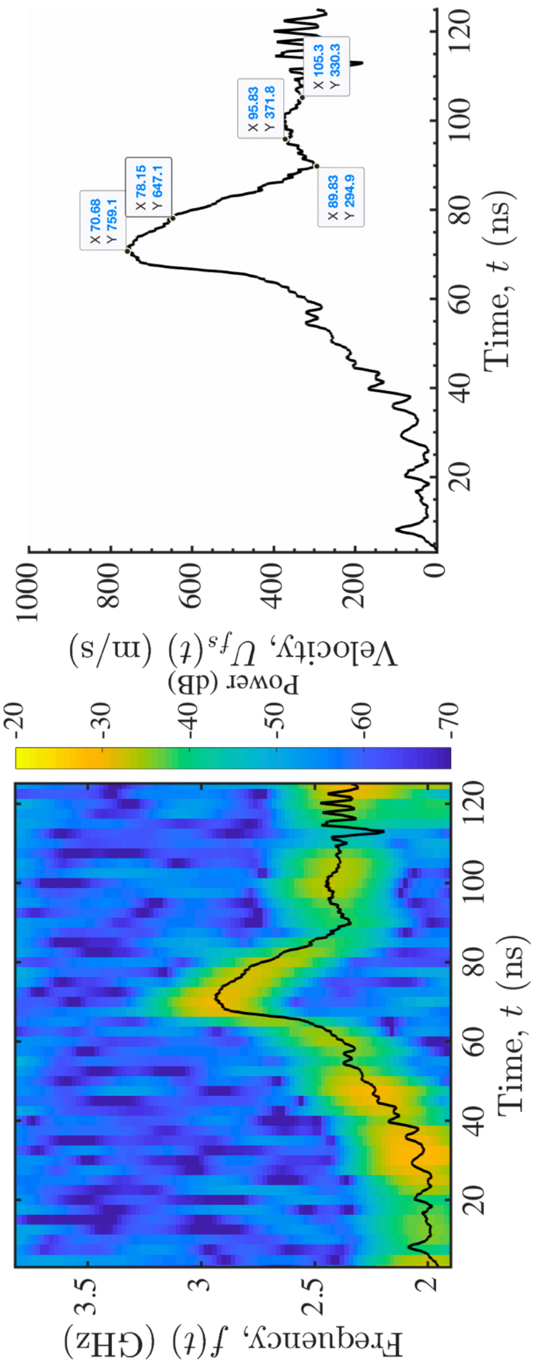

Figure B.13: Data from shot number 2019.02.11.00018

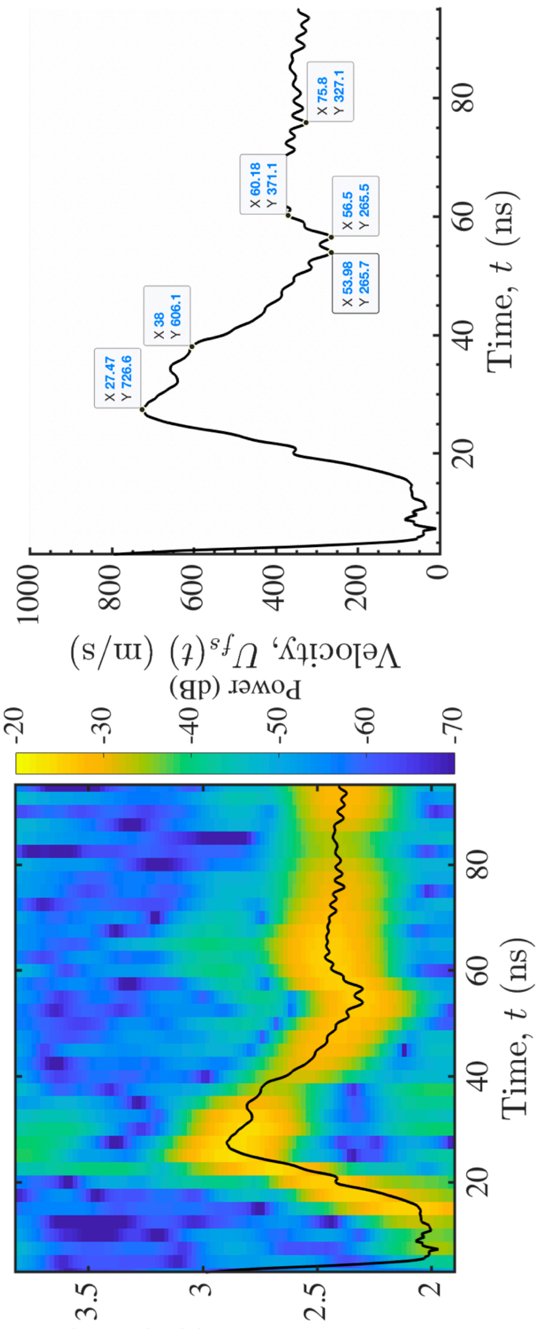

Figure B.14: Data from shot number 2019.02.11.00021

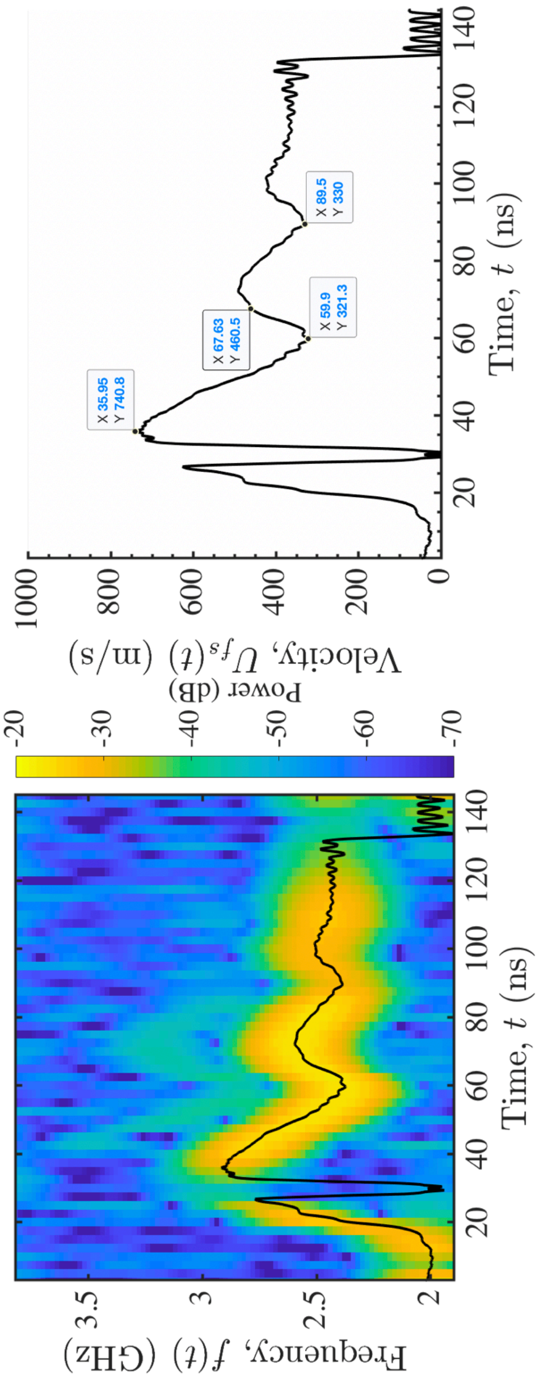

Figure B.15: Data from shot number 2019.02.11.00027

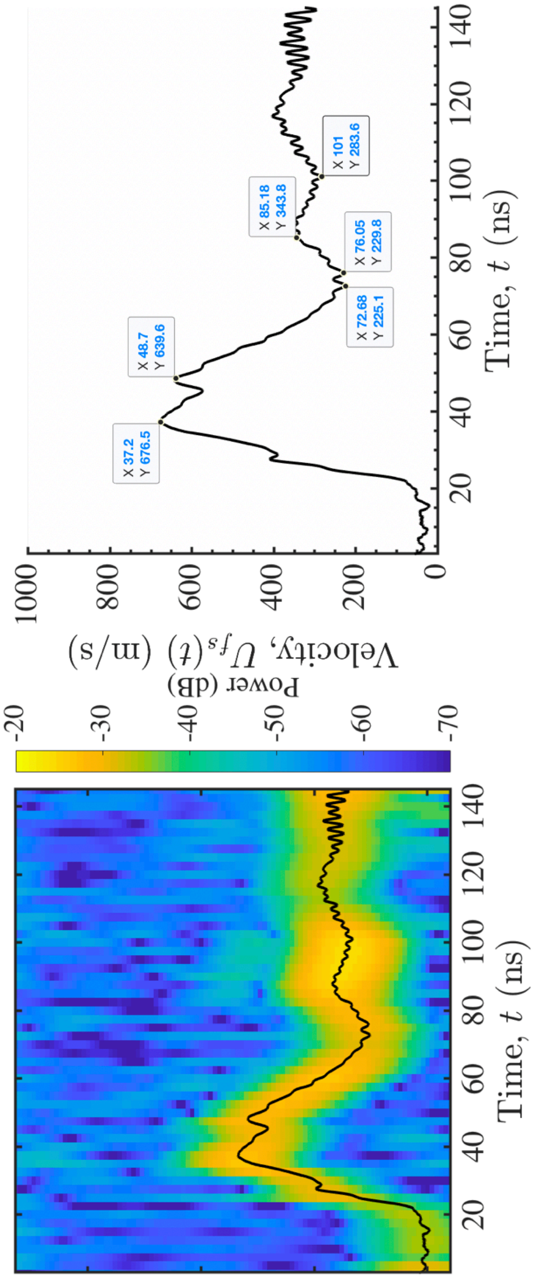

Figure B.16: Data from shot number 2019.02.11.00031

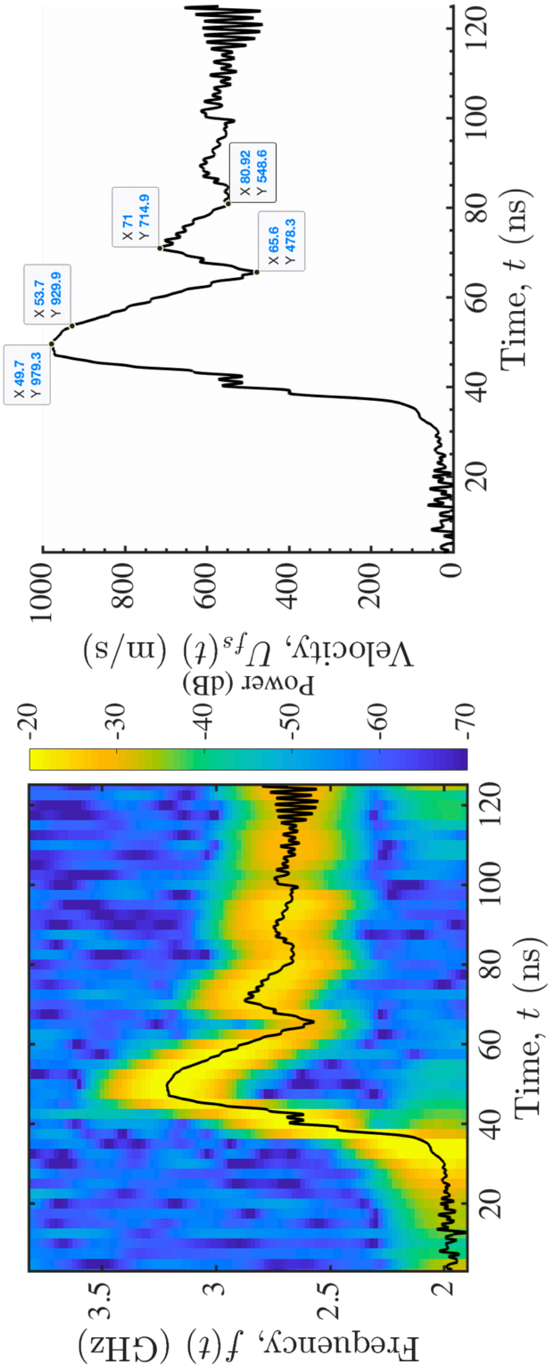

Figure B.17: Data from shot number 2019.02.11.00037

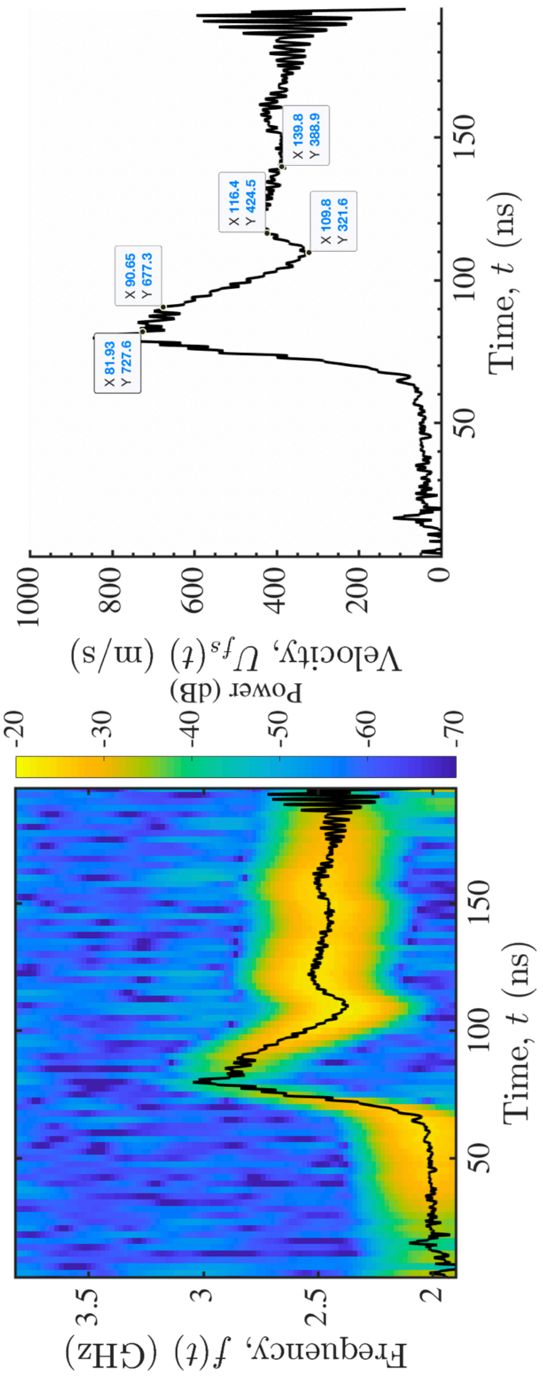

Figure B.18: Data from shot number 2019.02.11.00042

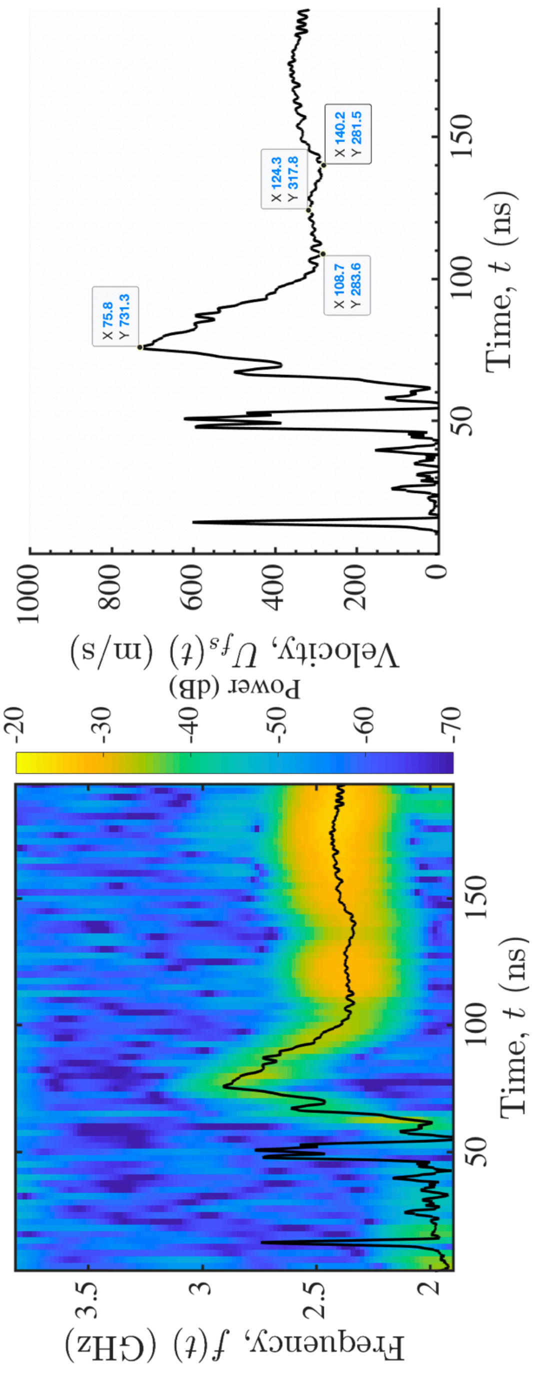

Figure B.19: Data from shot number 2019.02.11.00052

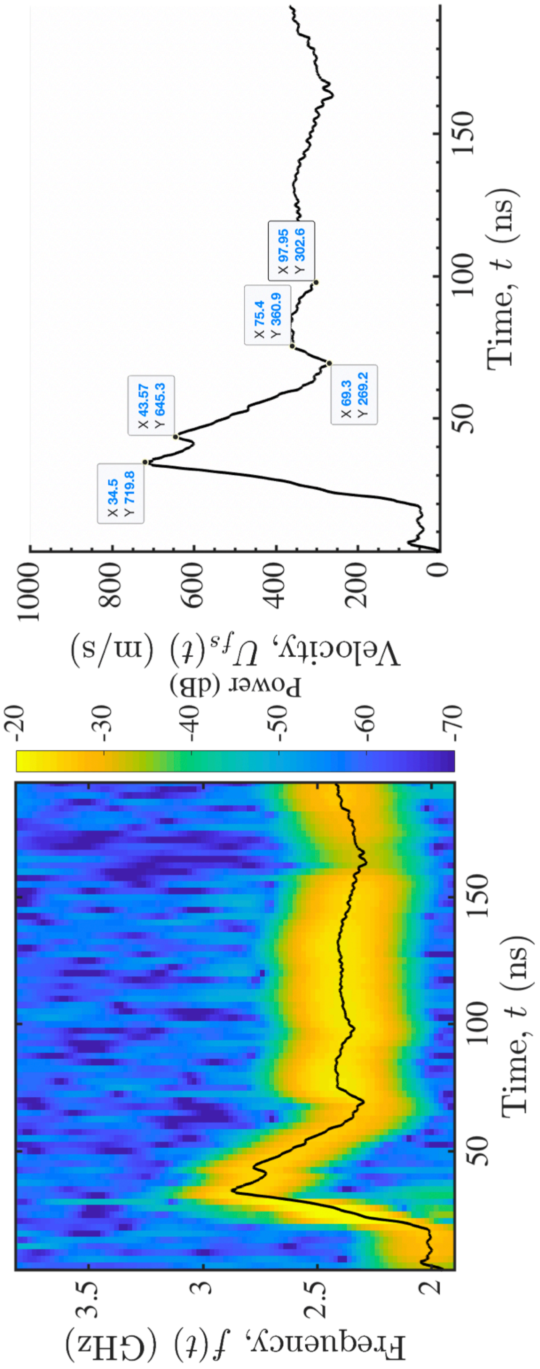

Figure B.20: Data from shot number 2019.02.13.00001

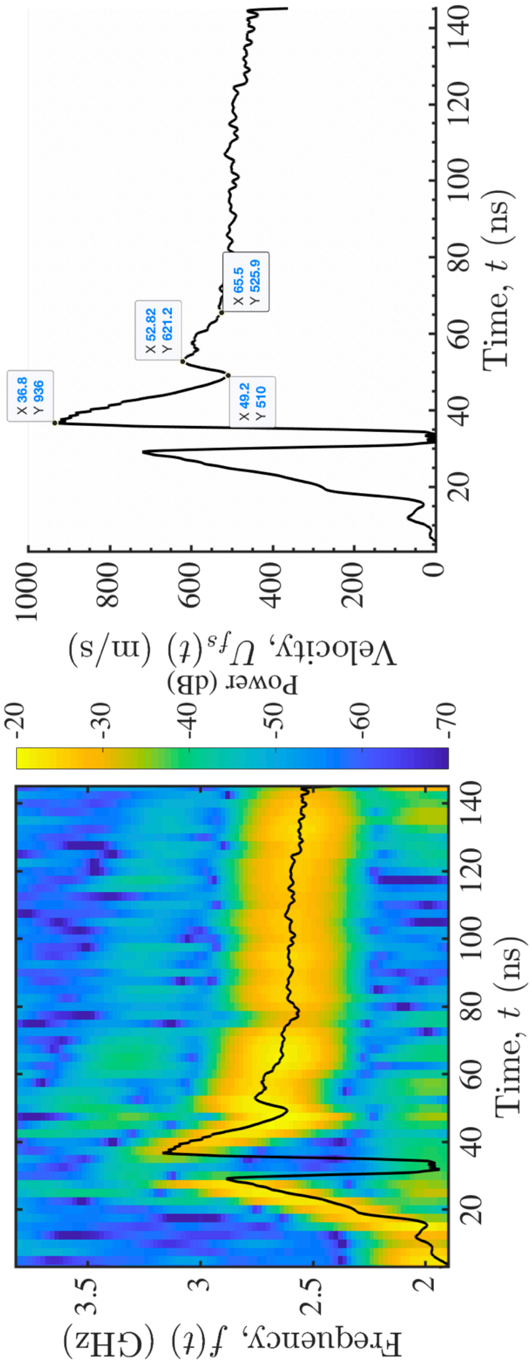

Figure B.21: Data from shot number 2019.02.13.00002

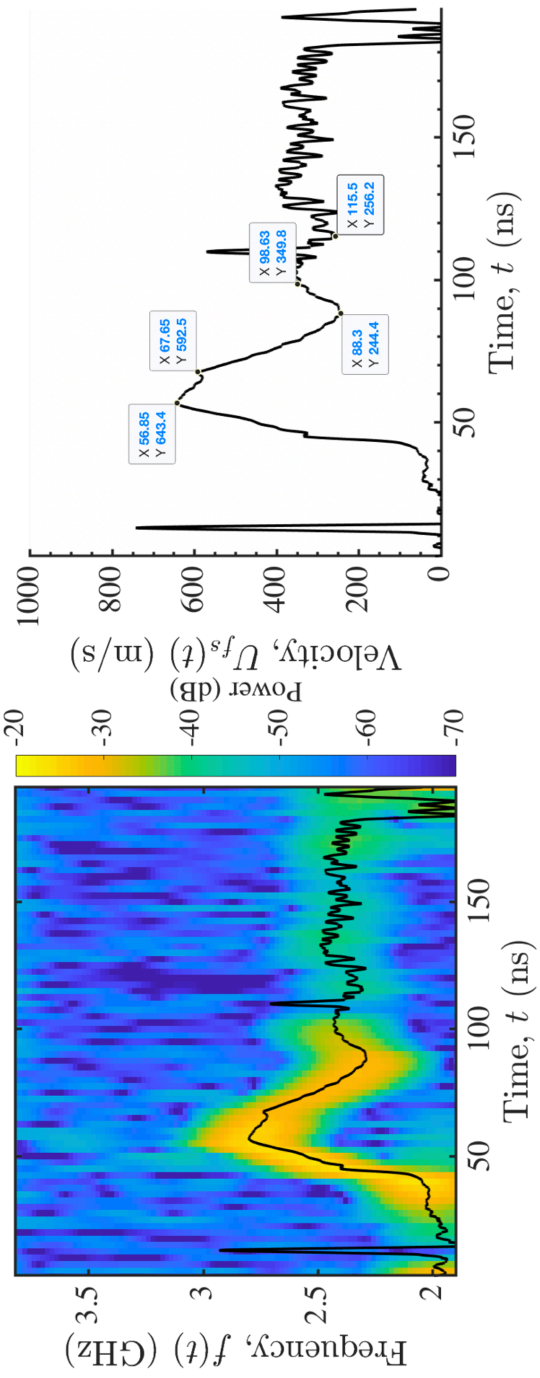

Figure B.22: Data from shot number 2019.02.13.00003

Shot Number	Flyer Thickness (μm)	Target Thickness (μm)	Peak Velocity (m/s)	Shock Stress (GPa)	Pullback (m/s)	Uncorrected Spall Strength (GPa)	Strain Rate (s^{-1})	Pulse Duration (ns)
2019.02.11.00002	50	210	843	3.31	448	1.76	2.75E+06	11
2019.02.11.00011	50	201	709	2.78	433	1.70	1.74E+06	LOS
2019.02.11.00013	50	206	578	2.27	386	1.51	1.85E+06	16
2019.02.11.00014	50	201	780	3.06	442	1.74	2.43E+06	22
2019.02.11.00015	50	200	792	3.11	407	1.60	2.15E+06	14
2019.02.11.00023	50	204	879	3.45	430	1.69	4.17E+06	18
2019.02.11.00028	50	200	984	3.86	441	1.73	3.08E+06	18
2019.02.11.00030	50	200	780	3.06	458	1.80	2.34E+06	18
2019.02.11.00039	50	200	1117	4.39	432	1.70	5.01E+06	13
2019.02.11.00041	50	199	1023	4.02	438	1.72	2.91E+06	15
2019.02.11.00049	50	185	826	3.24	408	1.60	2.87E+06	19
2019.02.11.00051	50	198	929	3.65	493	1.94	3.68E+06	16

Table B.4: Warm-Rolled, Solutionized, Mg-9Al Alloy Transverse Direction Spall Strength Data Summary (Chapter 5).

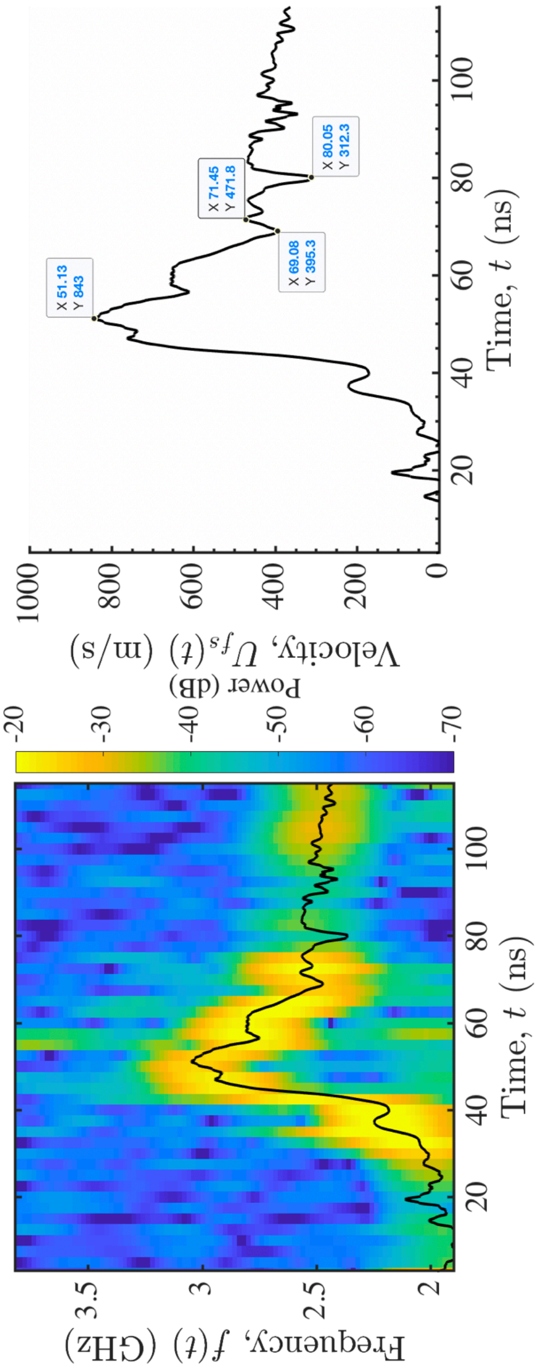

Figure B.23: Data from shot number 2019.02.11.00002

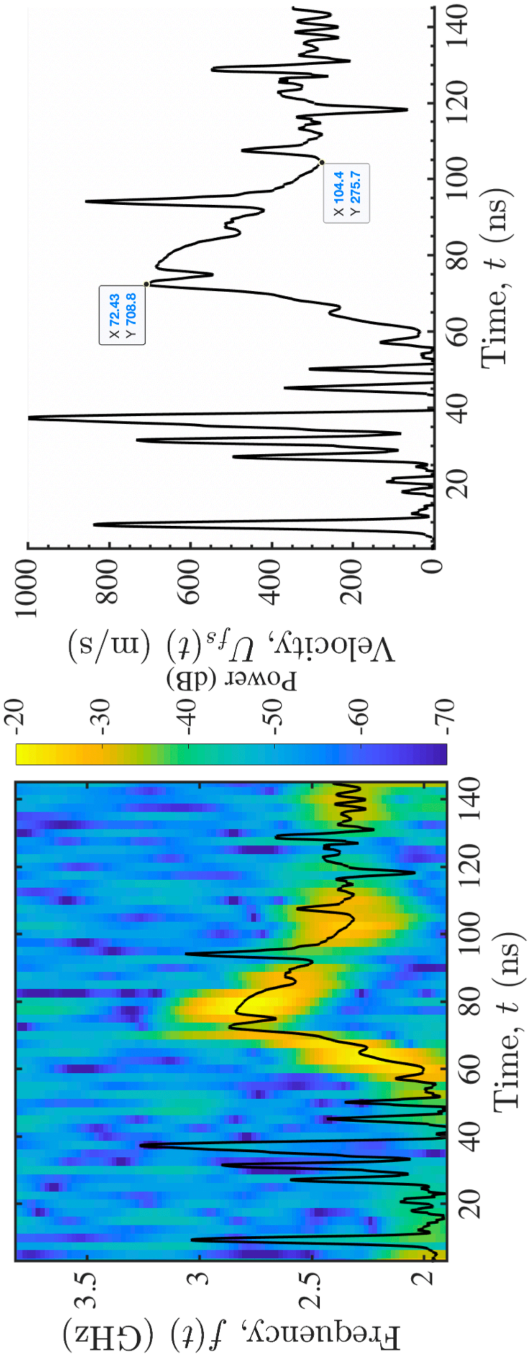

Figure B.24: Data from shot number 2019.02.11.00011

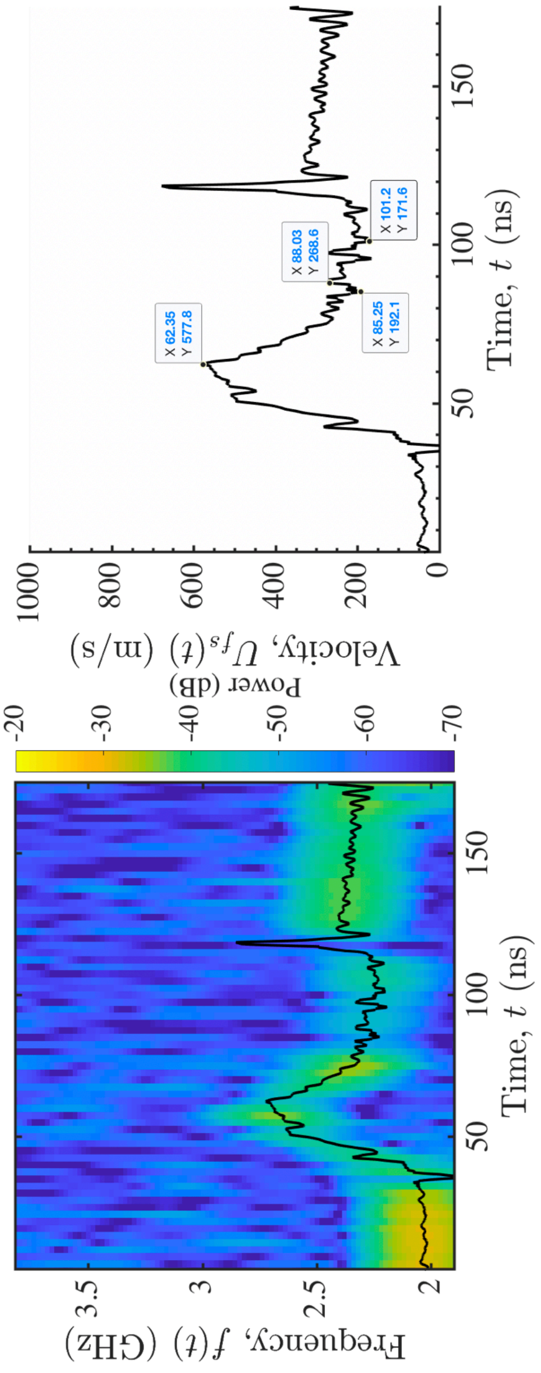

Figure B.25: Data from shot number 2019.02.11.00013

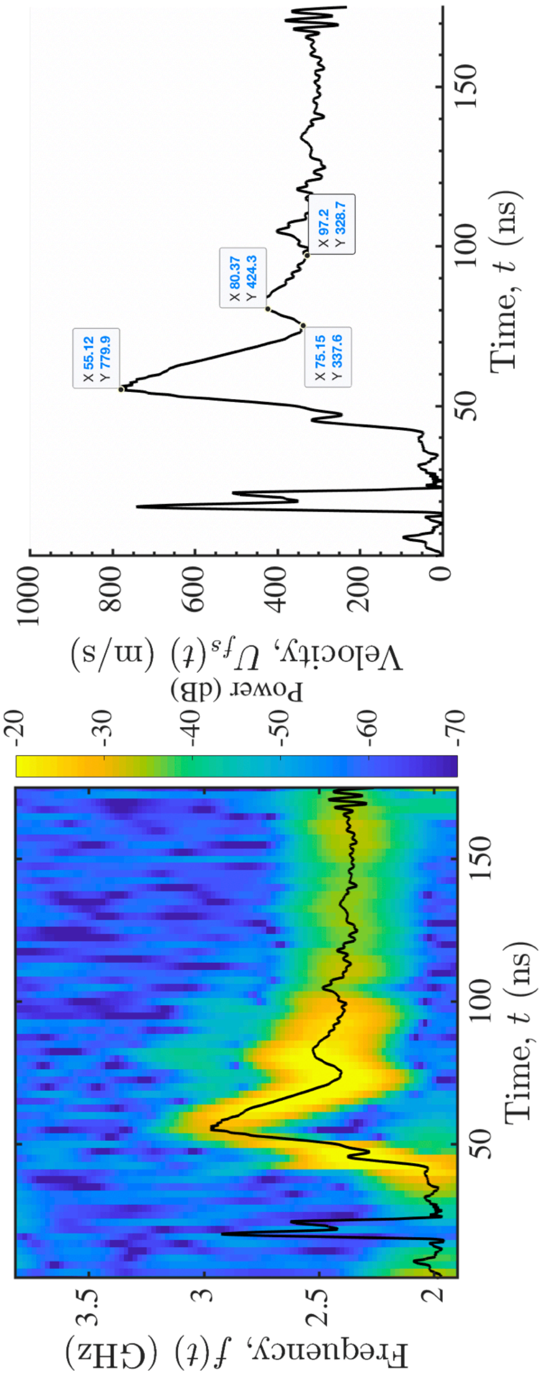

Figure B.26: Data from shot number 2019.02.11.00014

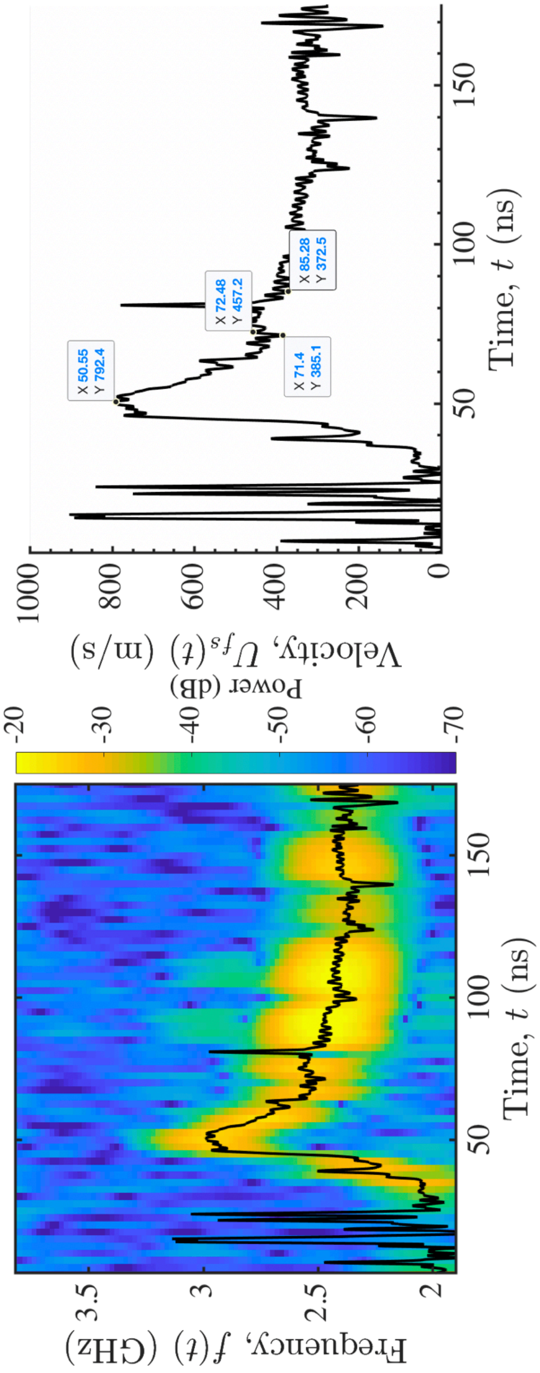

Figure B.27: Data from shot number 2019.02.11.00015

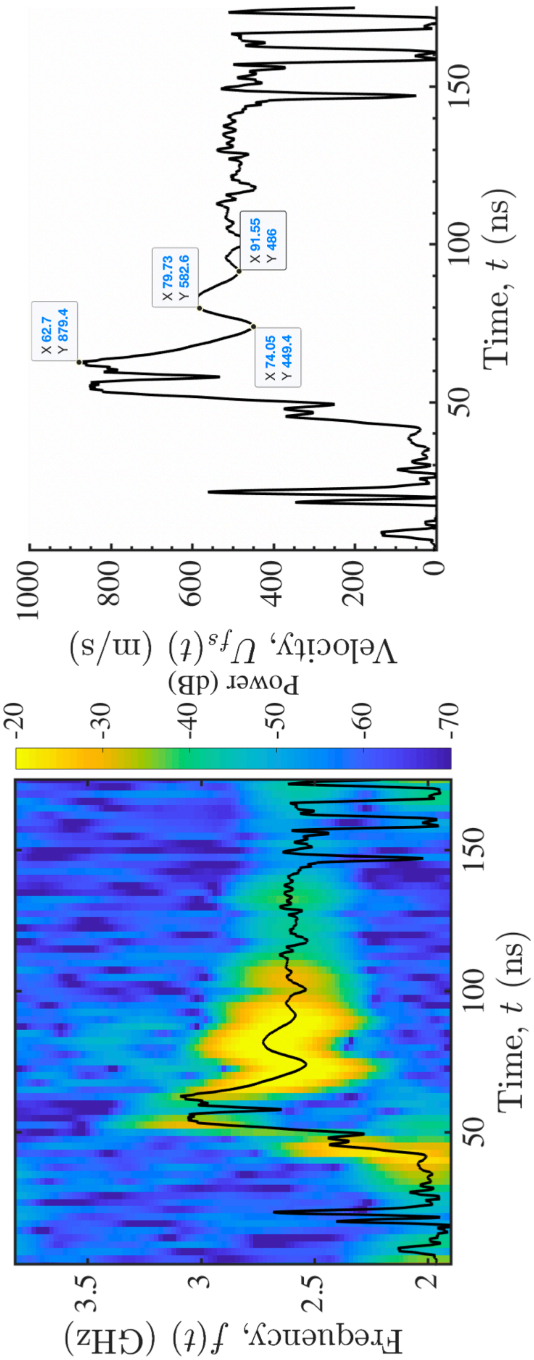

Figure B.28: Data from shot number 2019.02.11.00023

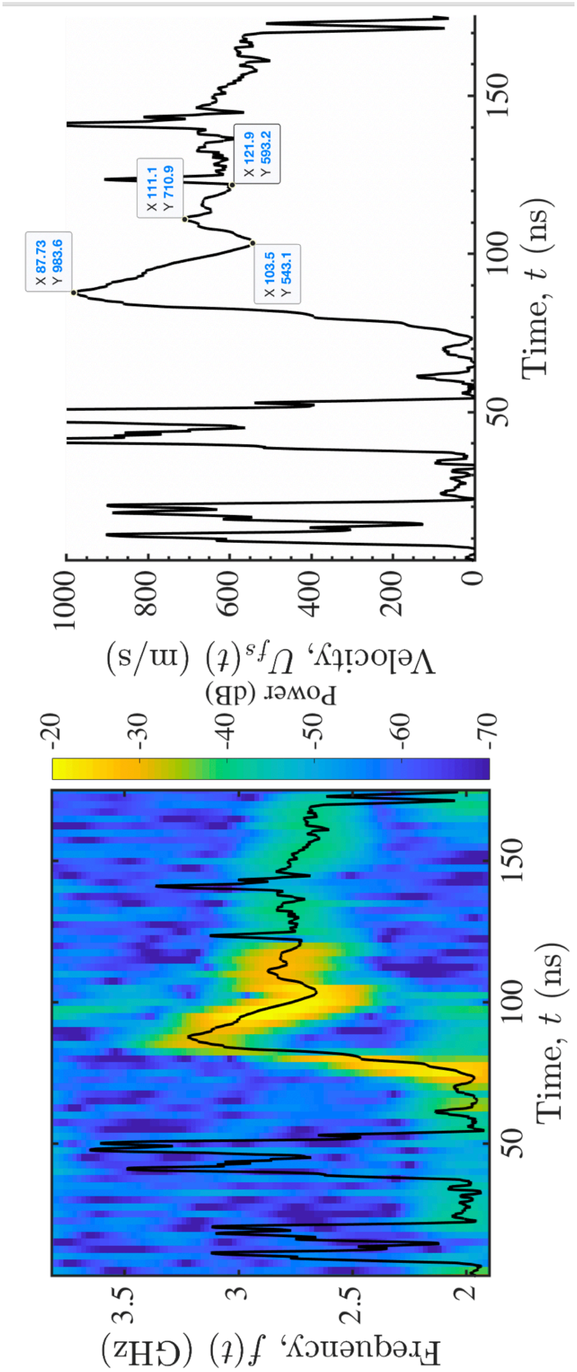

Figure B.29: Data from shot number 2019.02.11.00028

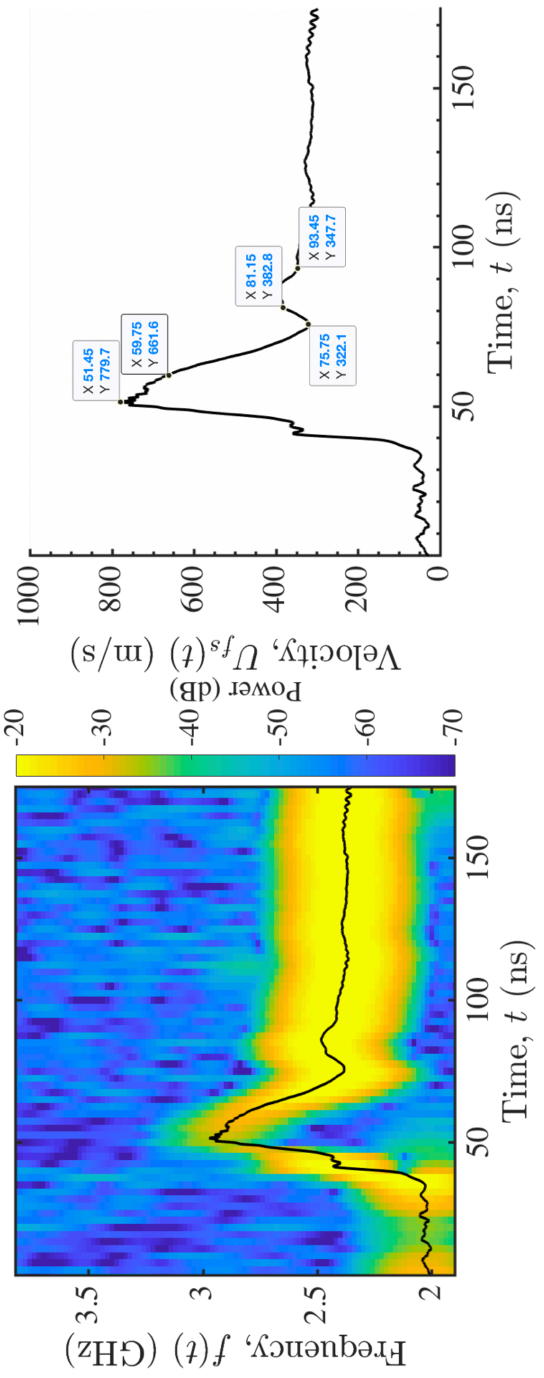

Figure B.30: Data from shot number 2019.02.11.00030

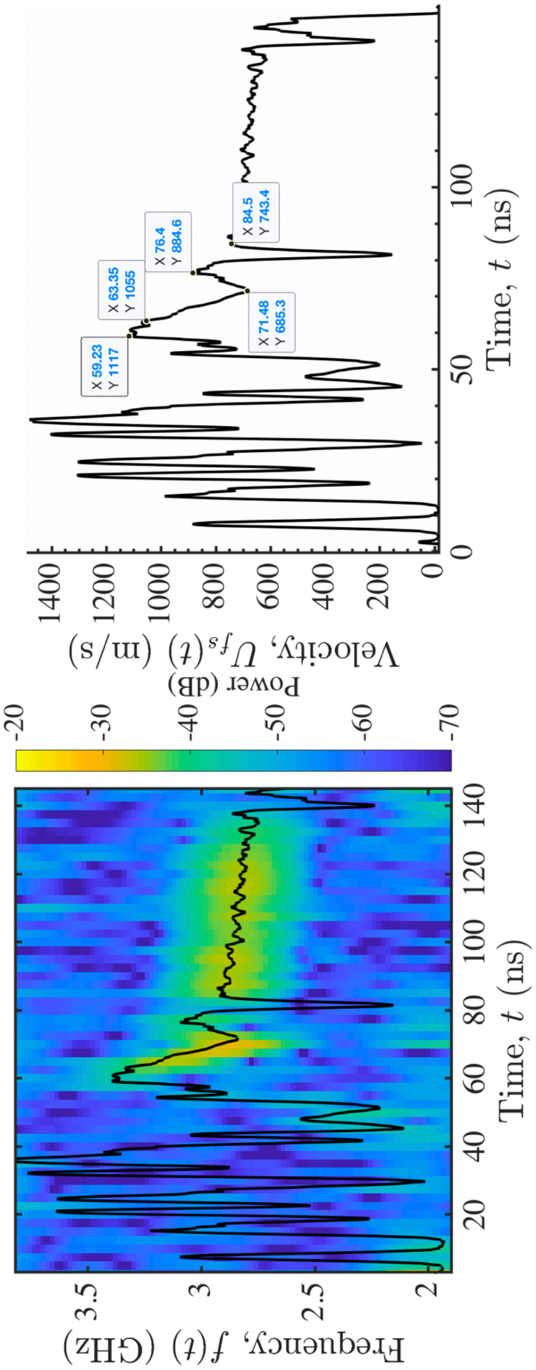

Figure B.31: Data from shot number 2019.02.11.00039

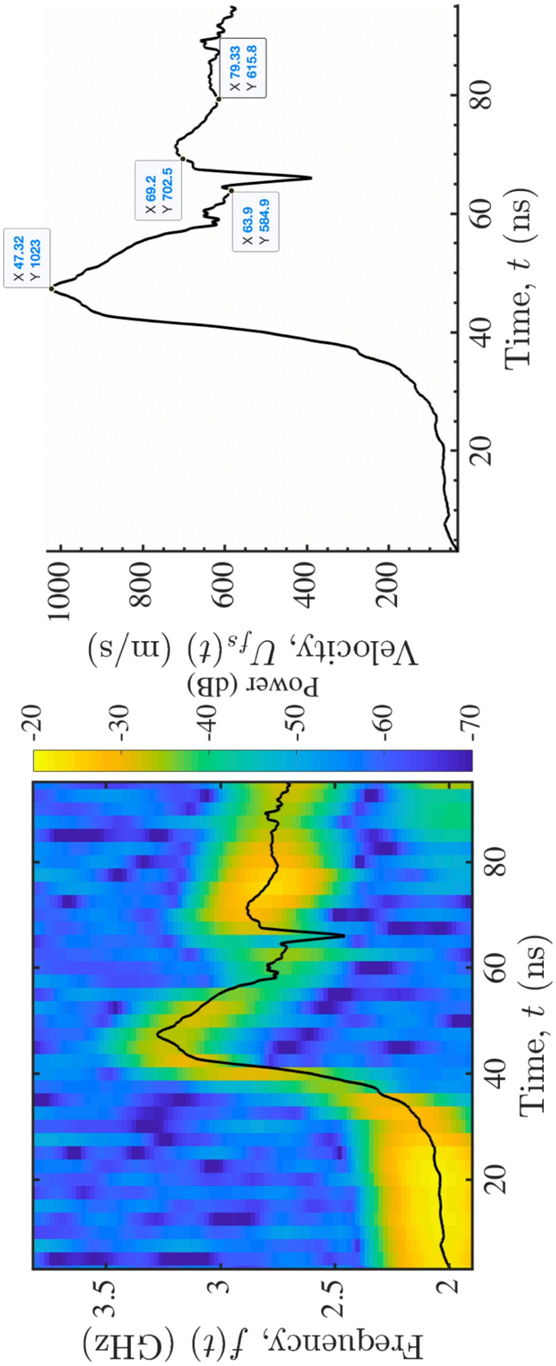

Figure B.32: Data from shot number 2019.02.11.00041

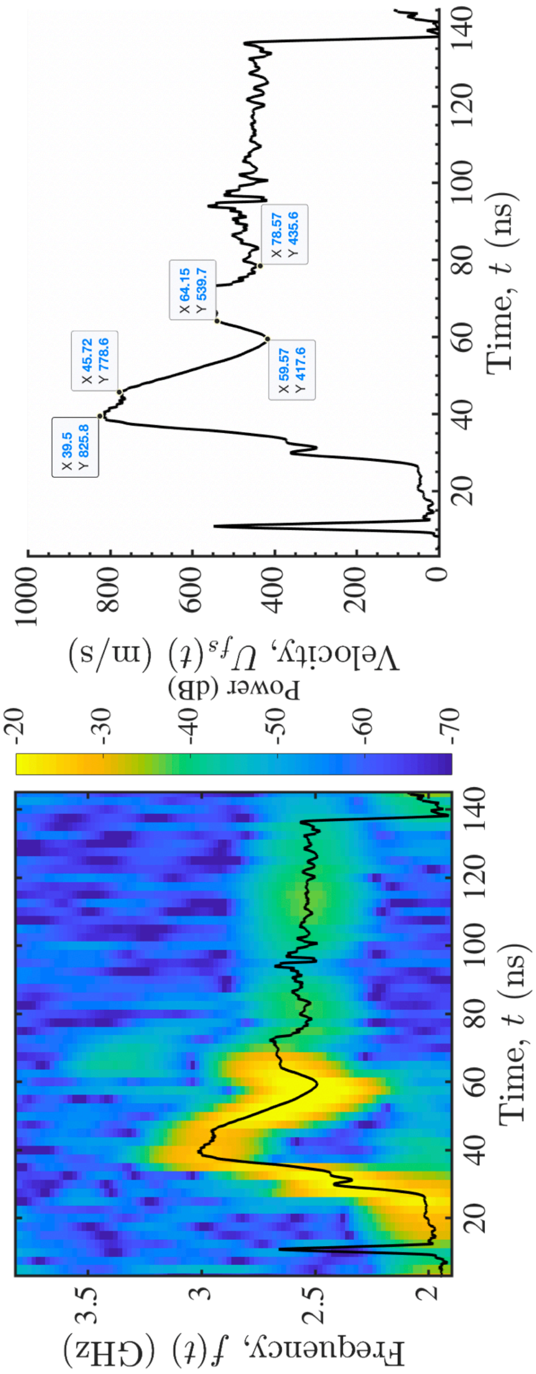

Figure B.33: Data from shot number 2019.02.11.00049

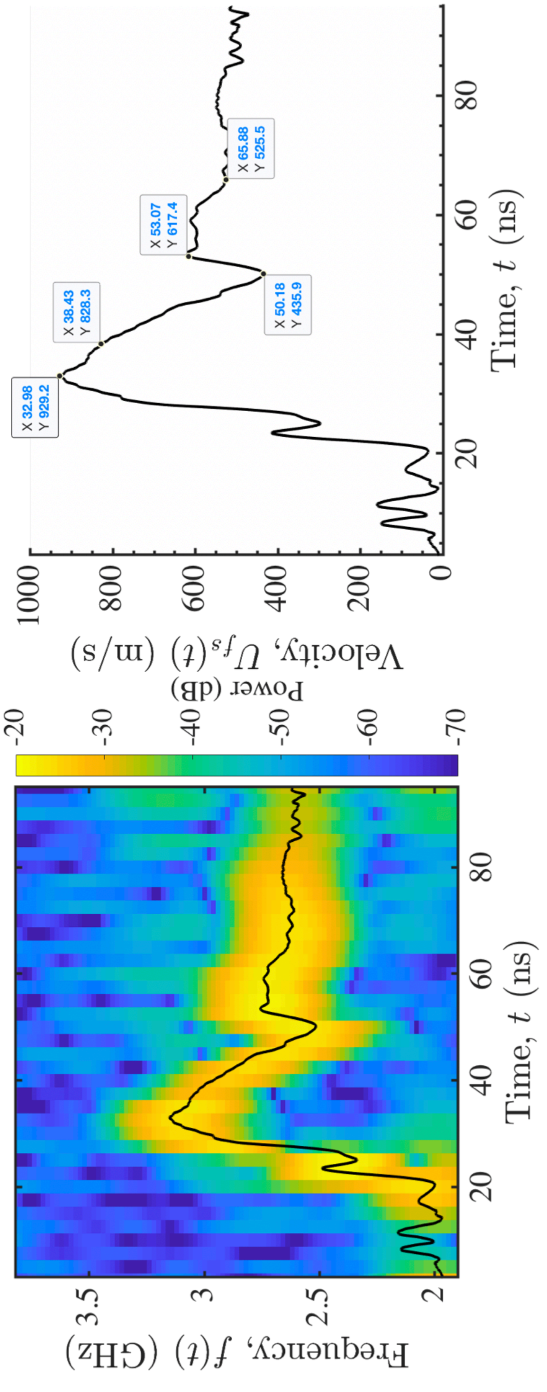

Figure B.34: Data from shot number 2019.02.11.00051

Shot Number	Flyer Thickness (μm)	Target Thickness (μm)	Peak Velocity (m/s)	Shock Stress (GPa)	Pullback (m/s)	Uncorrected Spall Strength (GPa)	Strain Rate (s^{-1})	Pulse Duration (ns)
2019.02.11.00004	50	200	862	3.39	308	1.21	3.32E+06	14
2019.02.11.00017	50	198	639	2.51	327	1.28	1.43E+06	17
2019.02.11.00022	50	200	824	3.24	287	1.13	2.53E+06	15
2019.02.11.00026	50	203	629	2.47	261	1.03	1.47E+06	20
2019.02.11.00032	50	191	999	3.92	341	1.34	3.11E+06	15
2019.02.11.00043	50	185	717	2.82	304	1.19	1.77E+06	20
2019.02.11.00047	50	185	654	2.57	328	1.29	1.88E+06	24
2019.02.11.00053	50	191	586	2.30	308	1.21	1.23E+06	19
2019.02.13.00005	50	173	828	3.25	345	1.35	2.57E+06	17
2019.02.13.00006	50	184	690	2.71	327	1.29	1.65E+06	22

Table B.5: Warm-Rolled, Solutionized, Peak Aged, Mg-9Al Alloy Normal Direction Spall Strength Data Summary (Chapter 5).

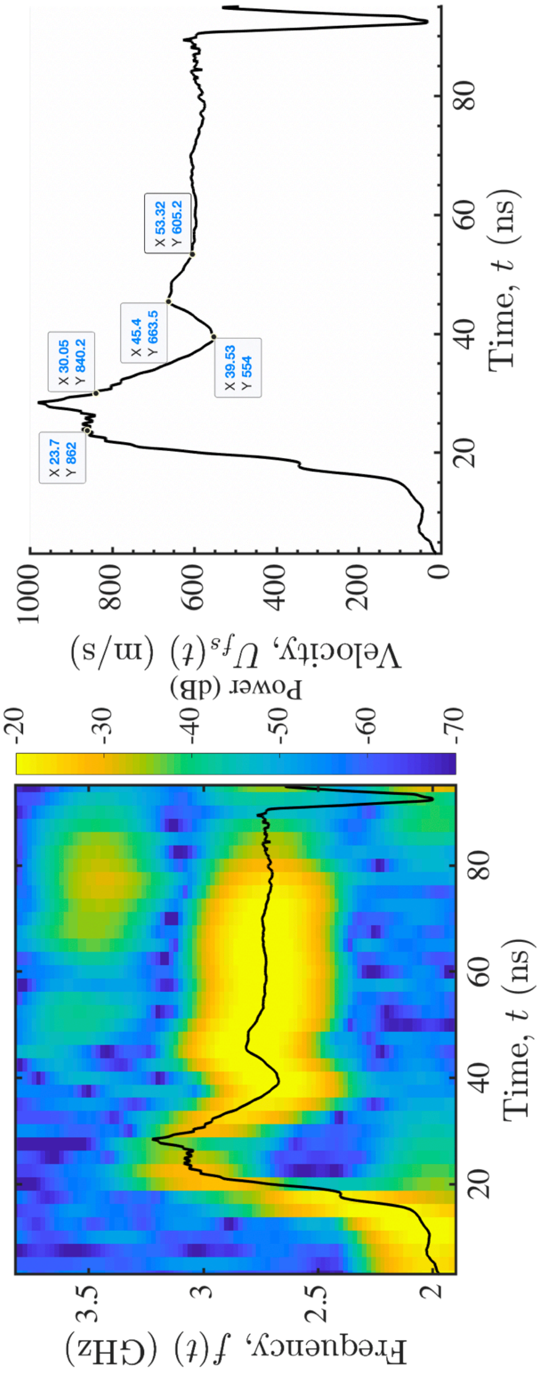

Figure B.35: Data from shot number 2019.02.11.00004

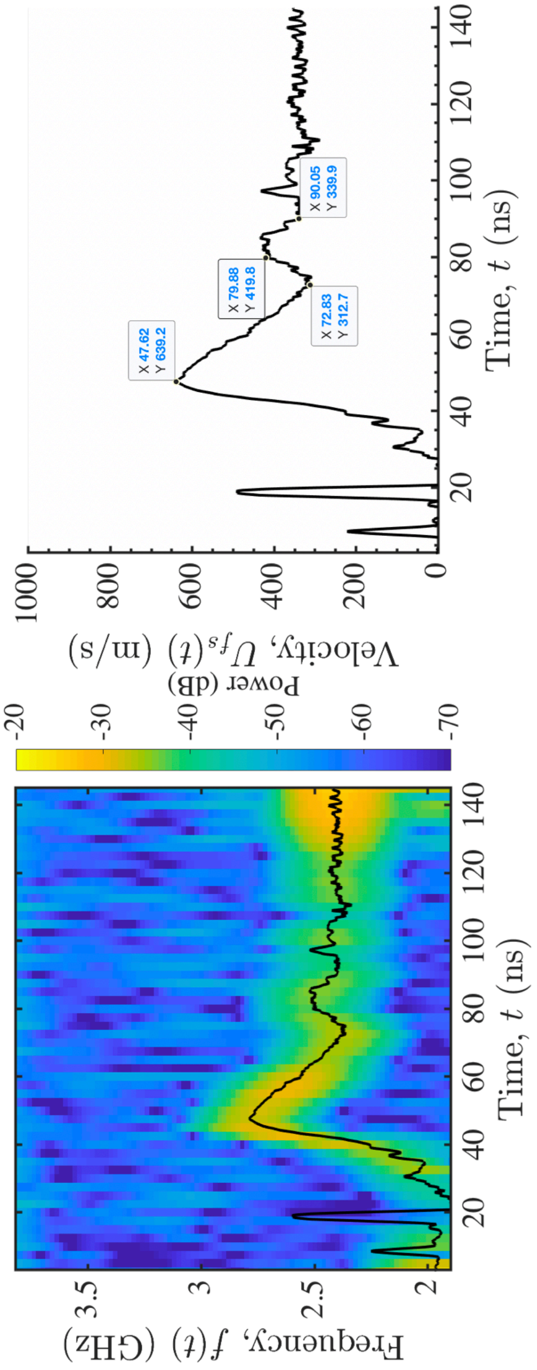

Figure B.36: Data from shot number 2019.02.11.00017

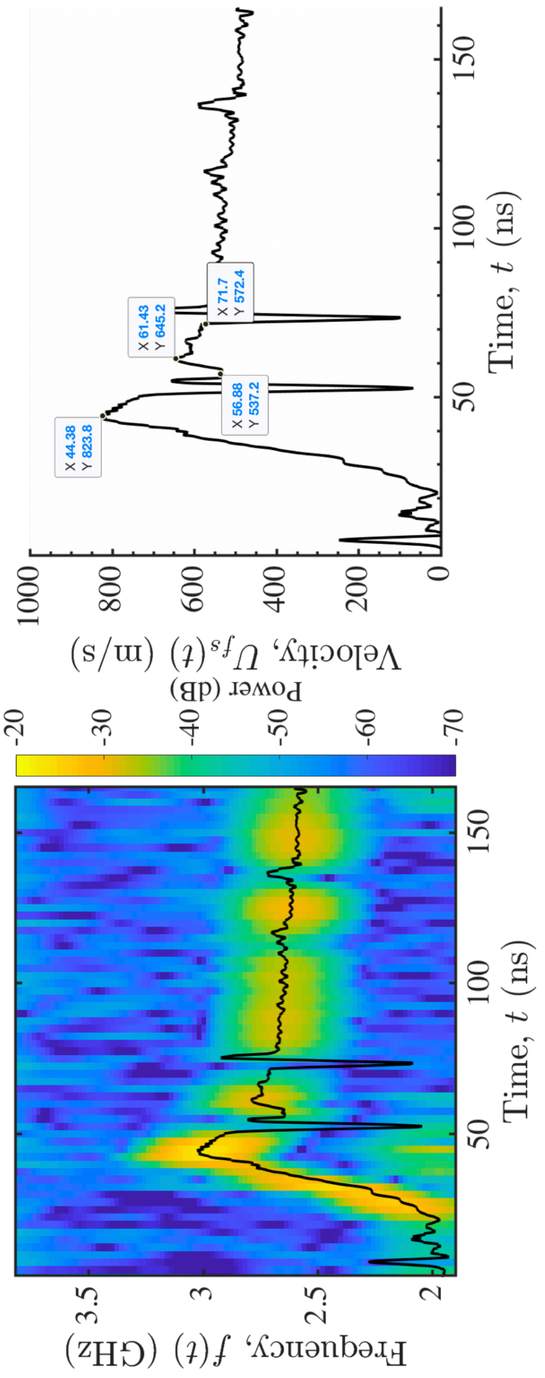

Figure B.37: Data from shot number 2019.02.11.00022

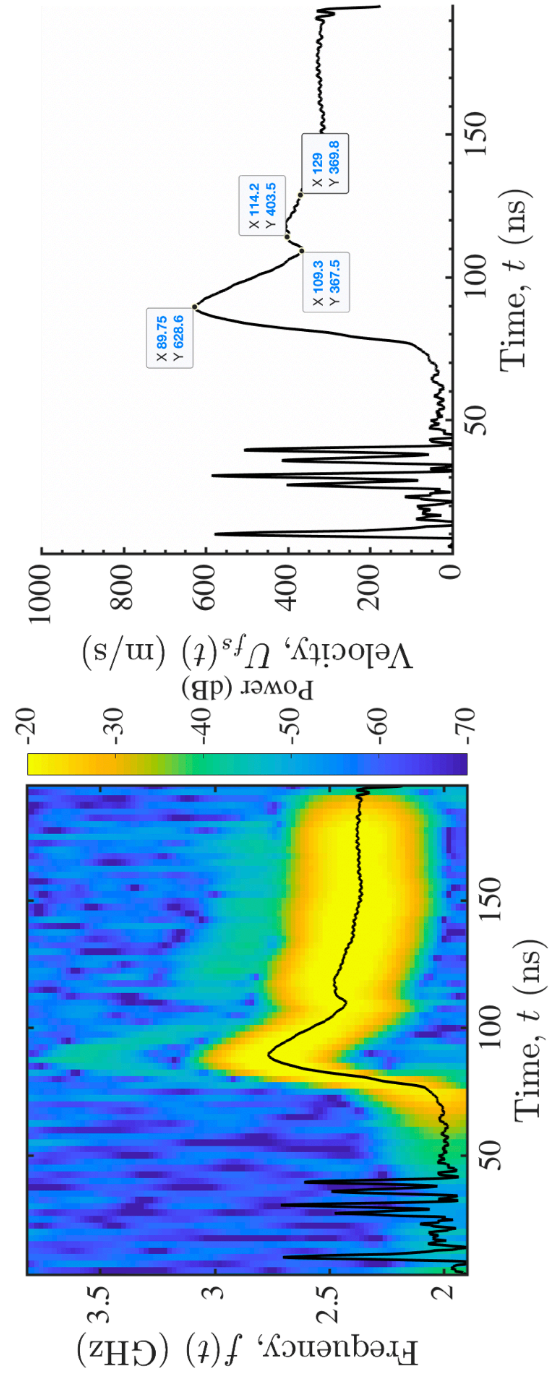

Figure B.38: Data from shot number 2019.02.11.00026

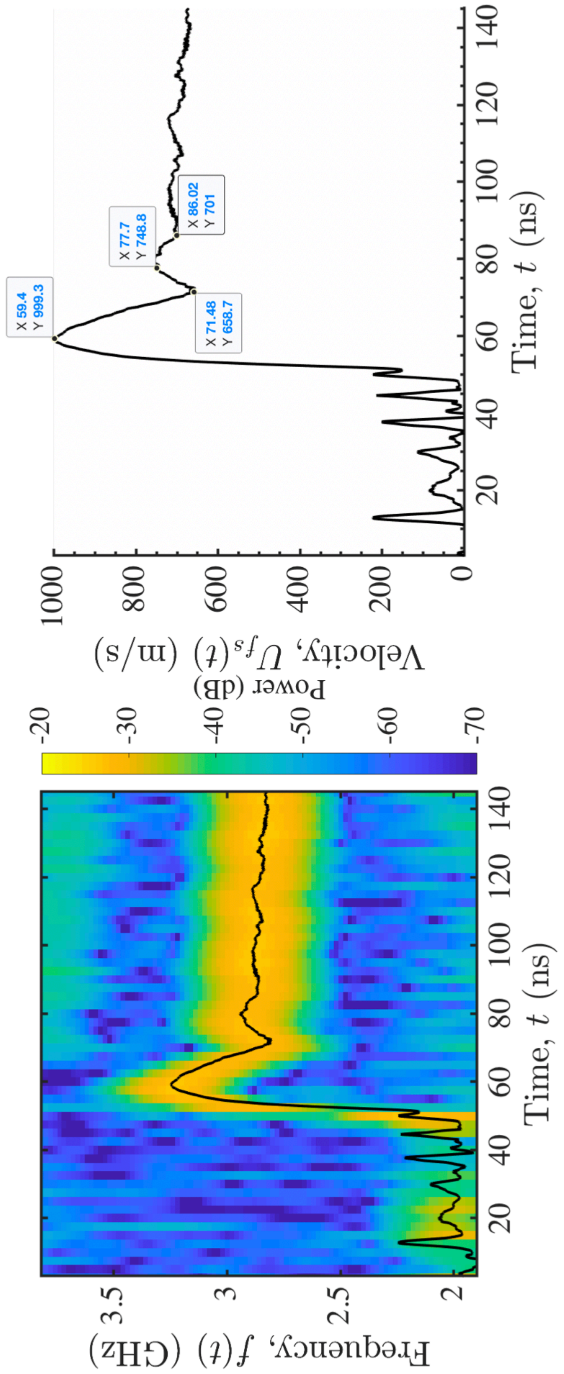

Figure B.39: Data from shot number 2019.02.11.00032

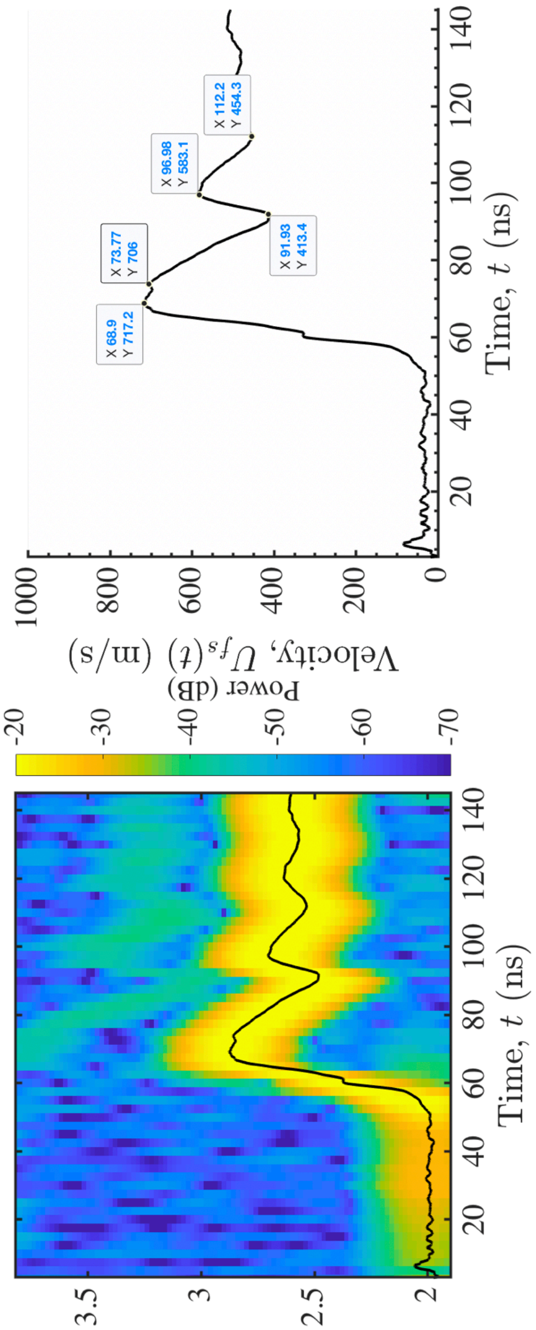

Figure B.40: Data from shot number 2019.02.11.00043

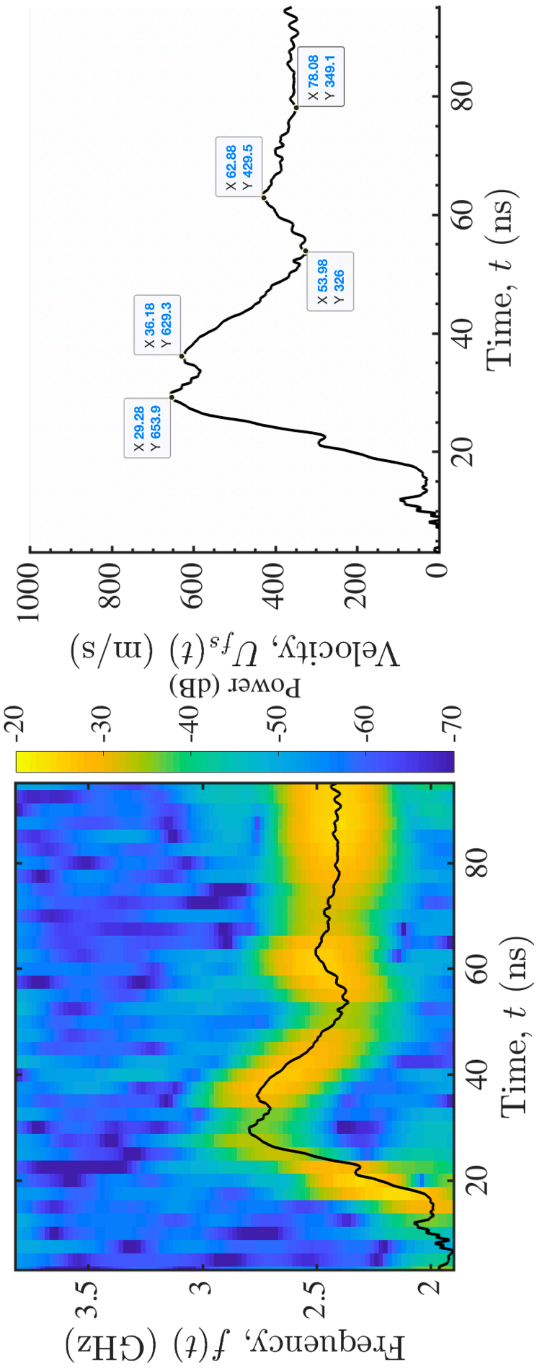

Figure B.41: Data from shot number 2019.02.11.00047

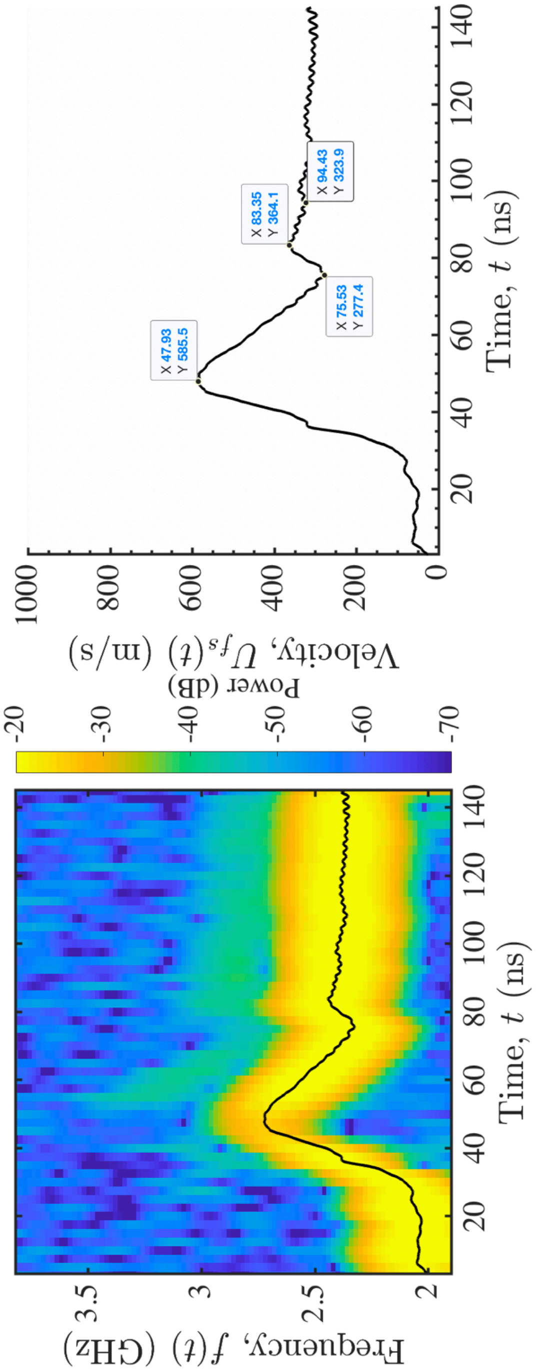

Figure B.42: Data from shot number 2019.02.11.00053

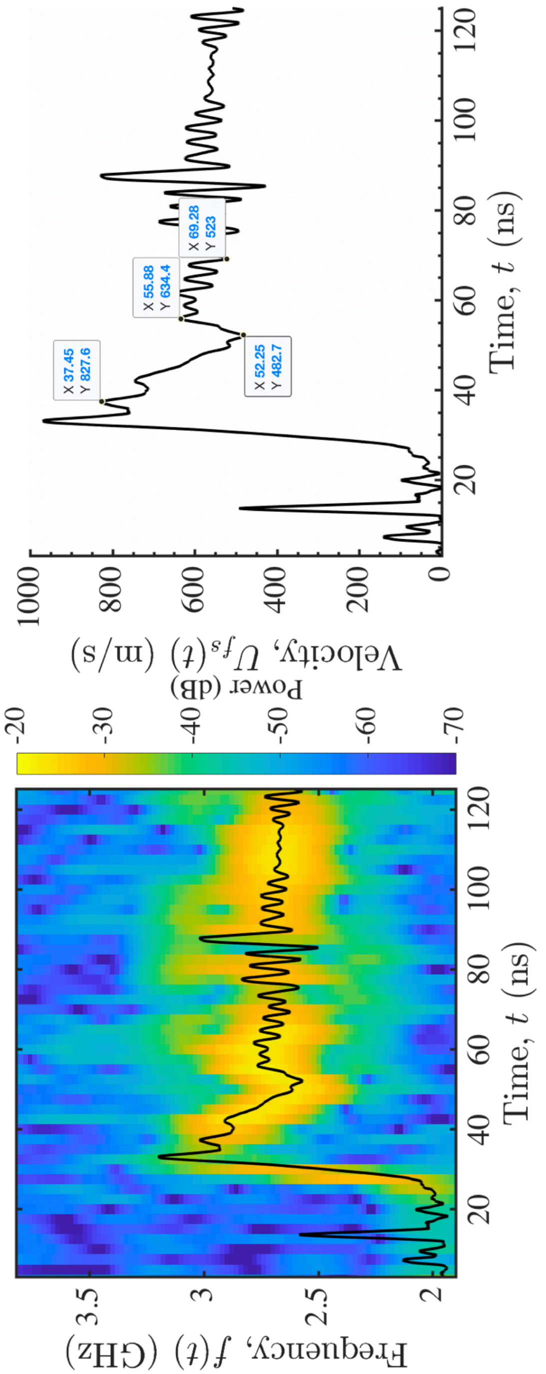

Figure B.43: Data from shot number 2019.02.13.00005

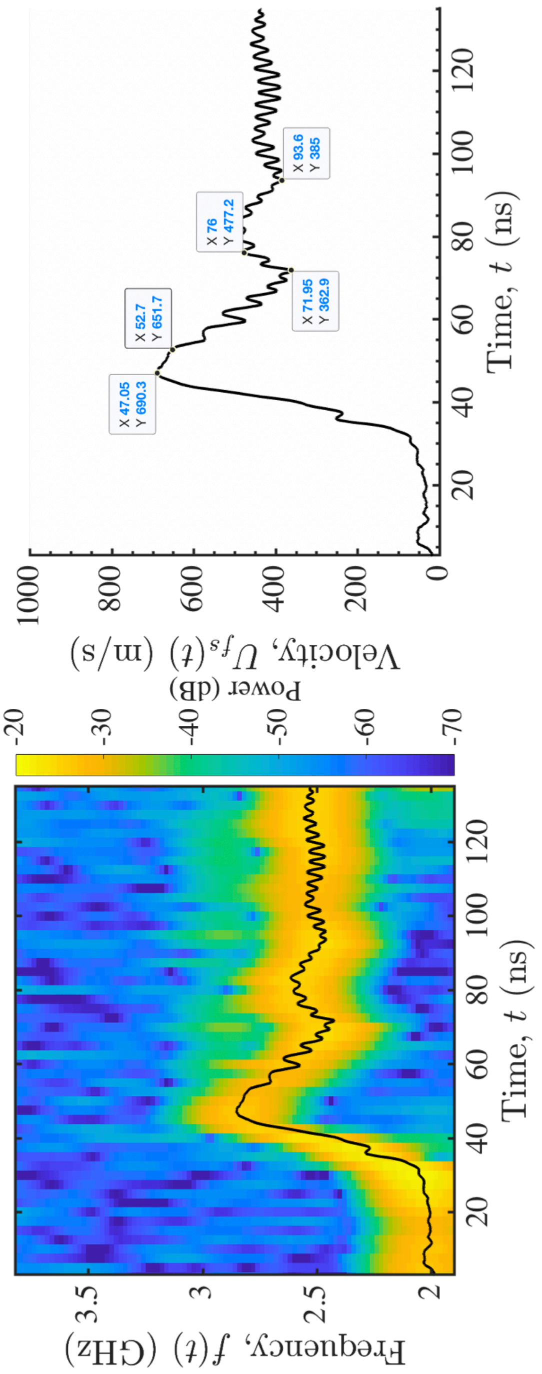

Figure B.44: Data from shot number 2019.02.13.00006

Shot Number	Flyer Thickness (μm)	Target Thickness (μm)	Peak Velocity (m/s)	Shock Stress (GPa)	Pullback (m/s)	Uncorrected Spall Strength (GPa)	Strain Rate (s^{-1})	Pulse Duration (ns)
2019.02.11.00006	50	204	614	2.41	347	1.36	1.52E+06	12
2019.02.11.00007	50	200	850	3.34	382	1.50	2.87E+06	16
2019.02.11.00016	50	202	735	2.89	302	1.18	2.56E+06	12
2019.02.11.00020	50	203	778	3.05	385	1.51	2.56E+06	17
2019.02.11.00025	50	203	825	3.24	409	1.61	3.56E+06	17
2019.02.11.00033	50	203	1118	4.39	425	1.67	4.19E+06	10
2019.02.11.00044	50	203	786	3.09	374	1.47	2.02E+06	18
2019.02.11.00046	50	205	786	3.09	349	1.37	2.31E+06	15
2019.02.11.00054	50	197	812	3.19	329	1.29	2.97E+06	16
2019.02.13.00008	50	193	1052	4.13	408	1.60	3.14E+06	16
2019.02.13.00009	50	193	682	2.68	335	1.31	1.81E+06	20

Table B.6: Warm-Rolled, Solutionized, Peak Aged, Mg-9Al Alloy Transverse Direction Spall Strength Data Summary (Chapter 5).

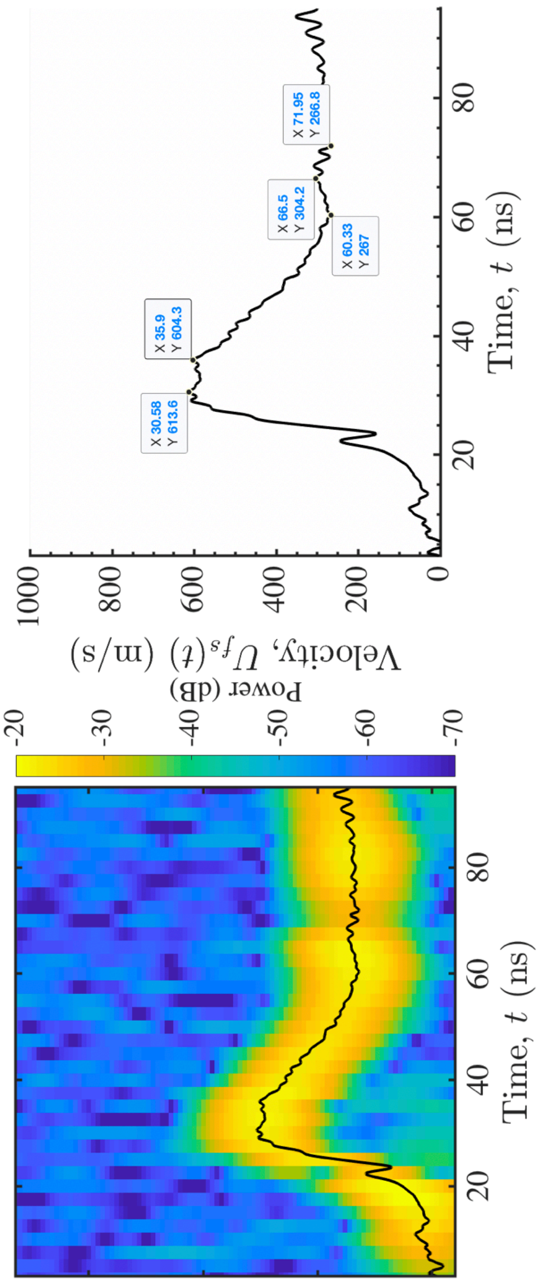

Figure B.45: Data from shot number 2019.02.11.00006

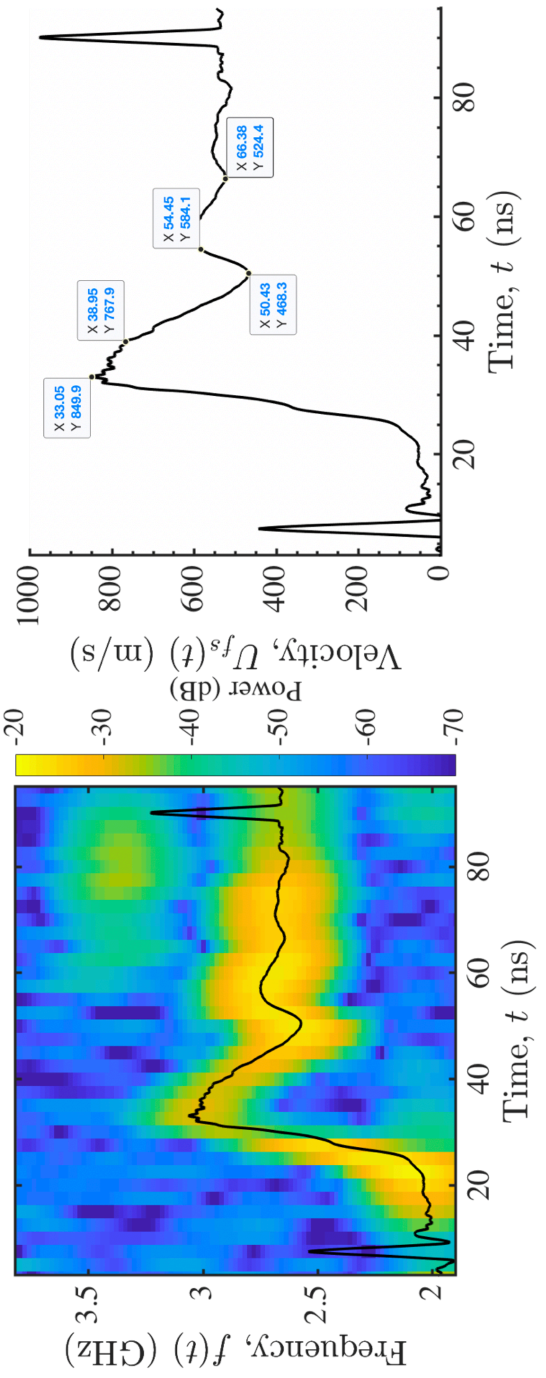

Figure B.46: Data from shot number 2019.02.11.00007

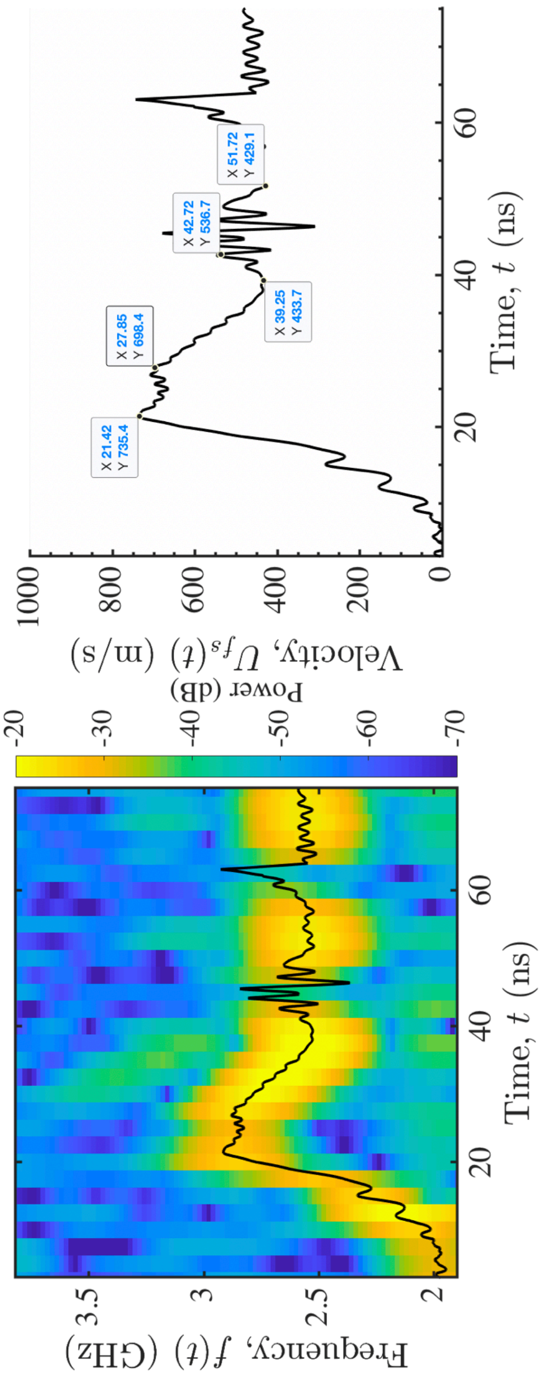

Figure B.47: Data from shot number 2019.02.11.00016

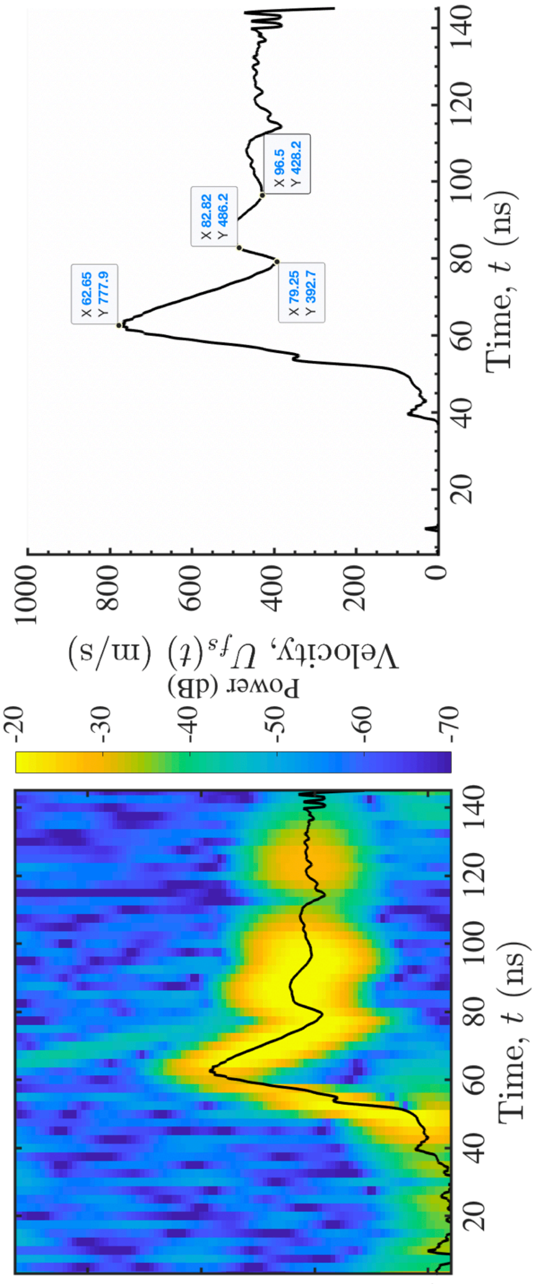

Figure B.48: Data from shot number 2019.02.11.00020

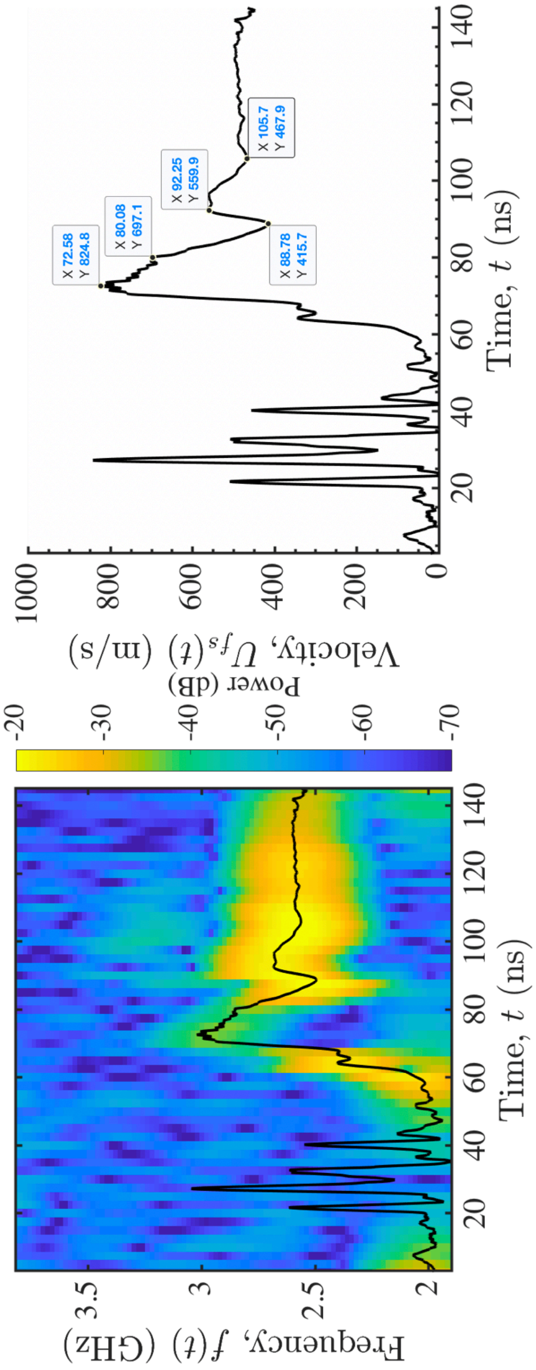

Figure B.49: Data from shot number 2019.02.11.00025

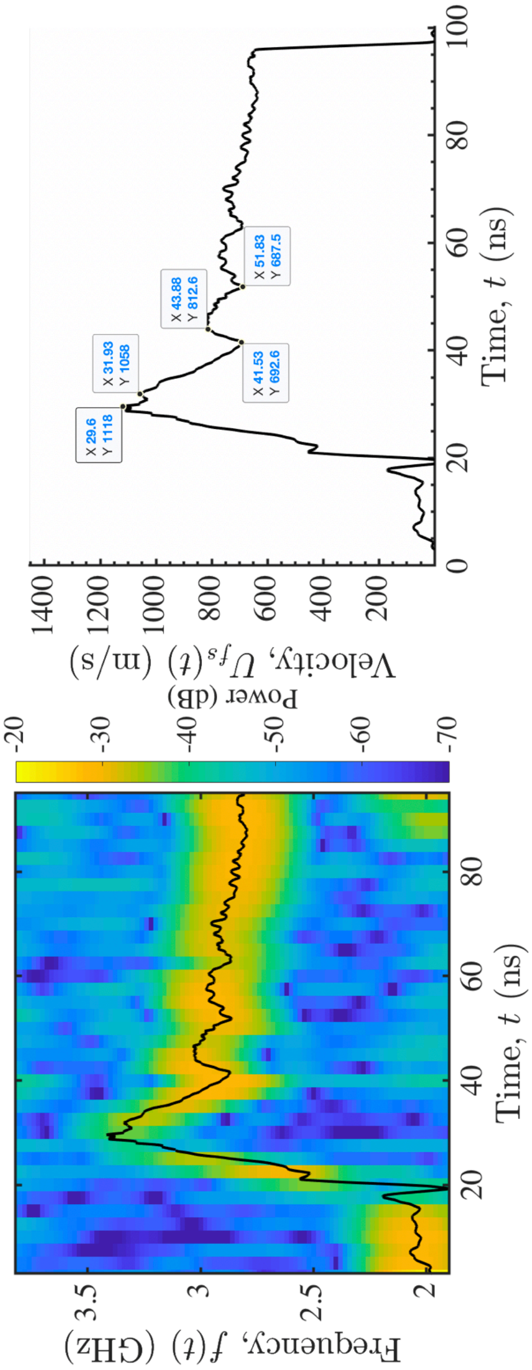

Figure B.50: Data from shot number 2019.02.11.00033

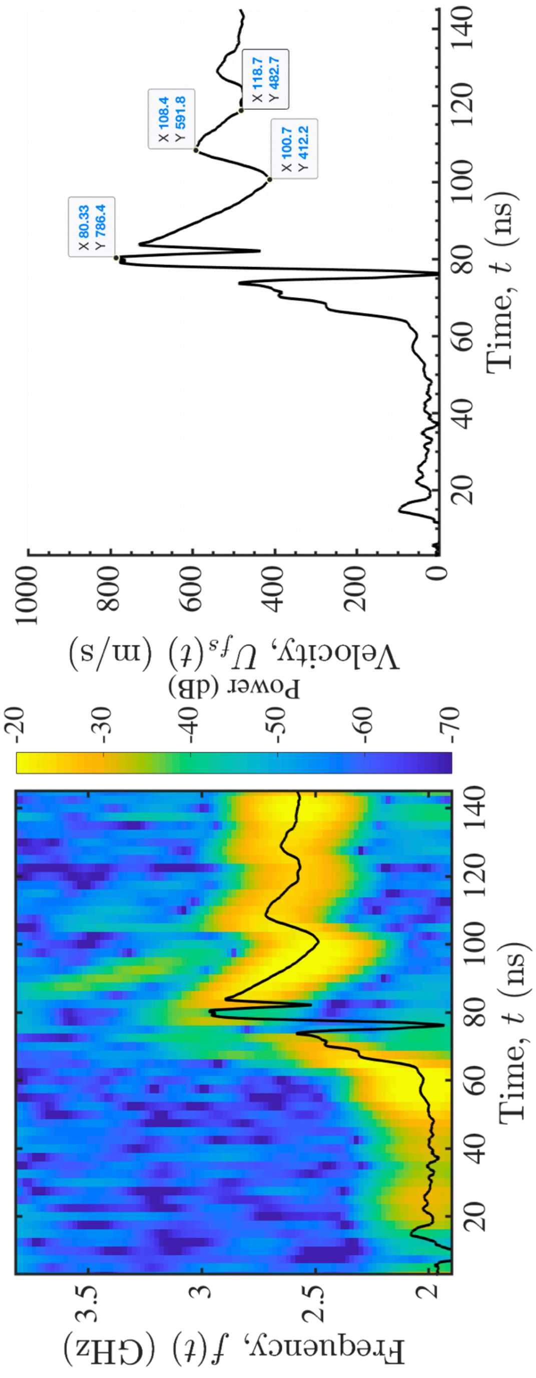

Figure B.51: Data from shot number 2019.02.11.00044

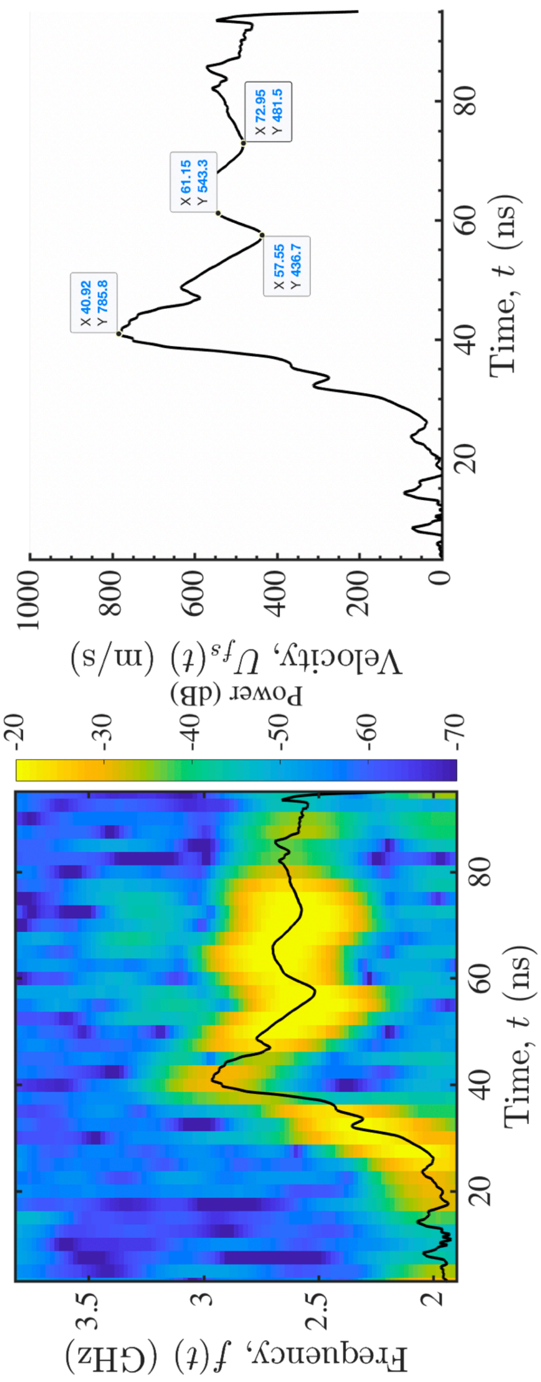

Figure B.52: Data from shot number 2019.02.11.00046

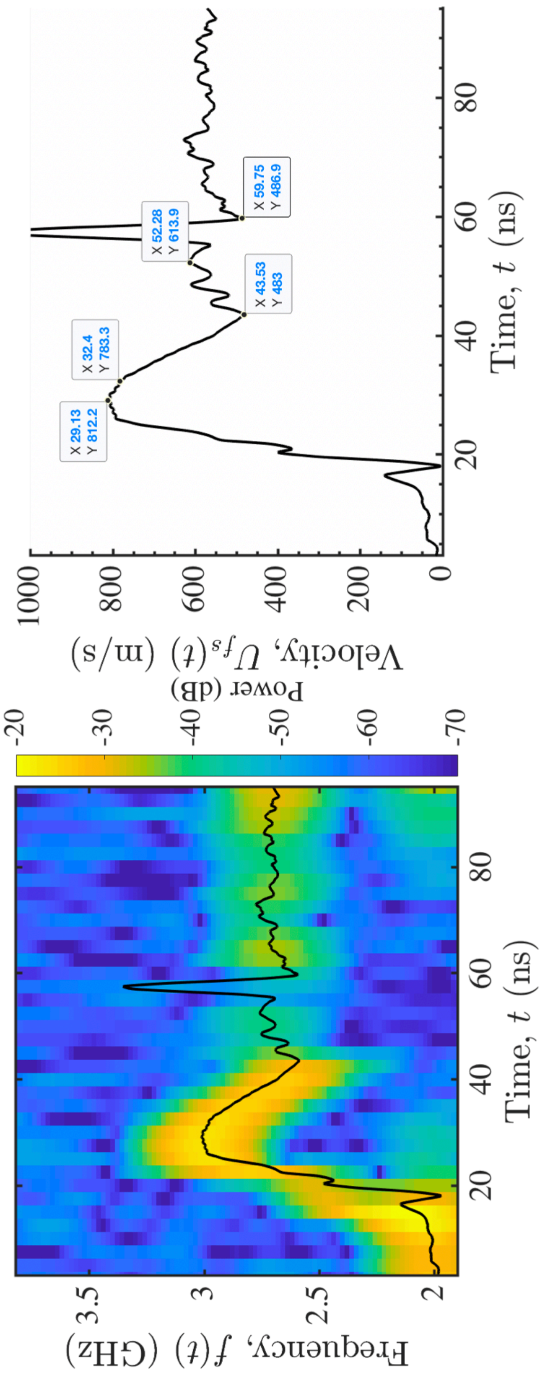

Figure B.53: Data from shot number 2019.02.11.00054

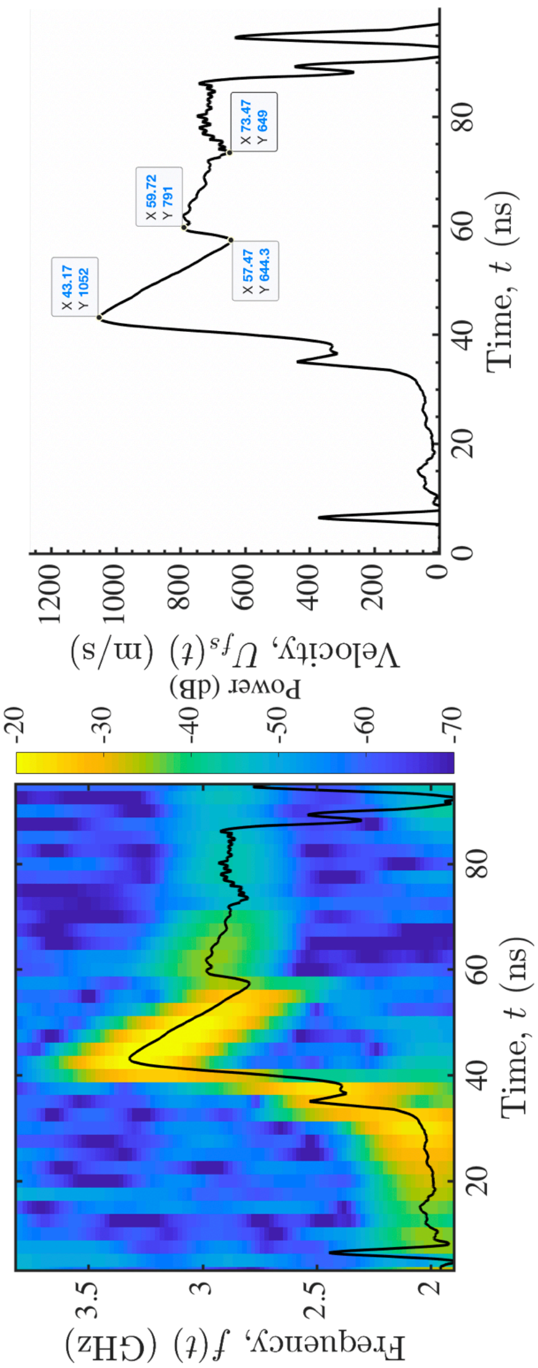

Figure B.54: Data from shot number 2019.02.13.00008

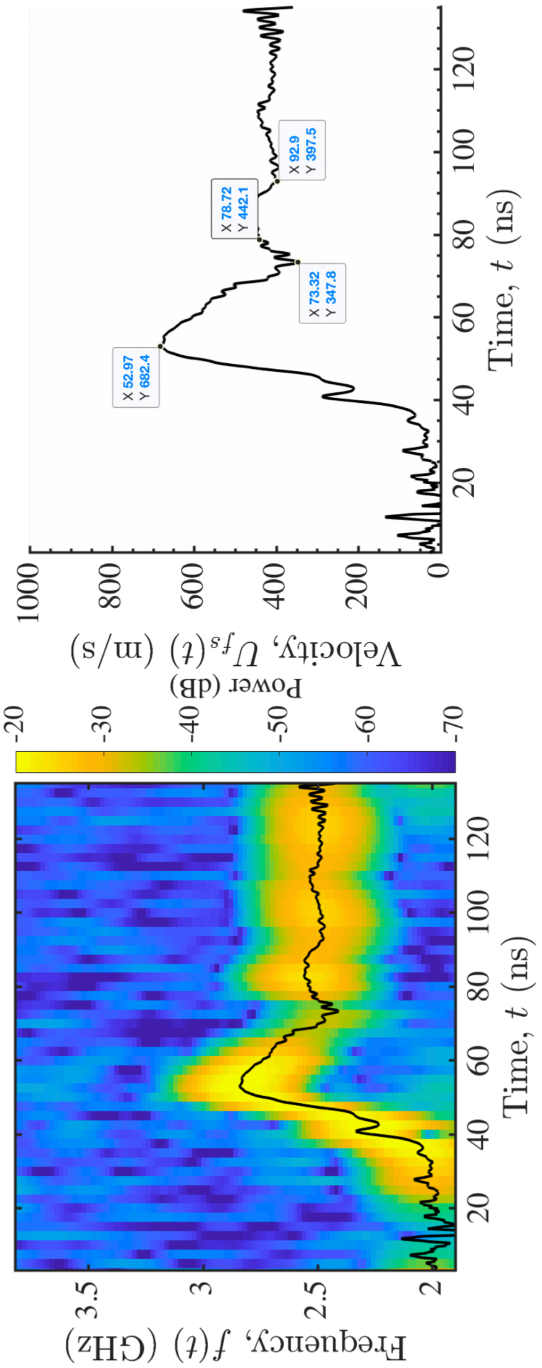

Figure B.55: Data from shot number 2019.02.13.00009

References

[1] J A Vitali et al. *Mobile Nuclear Power Plants for Ground Operations*. Tech. rep. Future Operations and Strategy Washington United States, 2018.

[2] J Bohlen et al. “The texture and anisotropy of magnesium–zinc–rare earth alloy sheets”. In: *Acta Materialia* 55.6 (2007), pp. 2101–2112.

[3] P G Karandikar et al. “A review of ceramics for armor applications”. In: *Advances in Ceramic Armor IV* 29 (2009), pp. 163–175.

[4] B J Ivins et al. “How satisfied are soldiers with their ballistic helmets? A comparison of soldiers’ opinions about the advanced combat helmet and the personal armor system for ground troops helmet”. In: *Military medicine* 172.6 (2007), pp. 586–591.

[5] A Krell and E Strassburger. “Order of influences on the ballistic resistance of armor ceramics and single crystals”. In: *Materials Science and Engineering: A* 597 (2014), pp. 422–430.

[6] G R Fowles et al. “Gas Gun for Impact Studies”. In: *Review of Scientific Instruments* 41.7 (1970), pp. 984–996. DOI: `10.1063/1.1684739`.

[7] T Antoun et al. *Spall fracture*. Springer Science & Business Media, 2003.

[8] J A Fox and D N Barr. “Laser-induced shock effects in Plexiglas and 6061-T6 aluminum”. In: *Applied Physics Letters* 22.11 (1973), pp. 594–596.

[9] B L Mordike and T Ebert. “Magnesium: properties applications potential”. In: *Materials Science and Engineering: A* 302.1 (2001), pp. 37–45.

[10] T L Jones and R D DeLorme. *Development of a Ballistic Specification for Magnesium Alloy AZ31B*. Tech. rep. ARMY RESEARCH LAB ABERDEEN PROVING GROUND MD WEAPONS and MATERIALS RESEARCH, 2008.

[11] G I Taylor. “Plastic strain in metals”. In: *J. Inst. Metals* 62 (1938), pp. 307–324.

[12] V Kannan. “Twinning and the dynamic behavior of magnesium and its alloys”. PhD thesis. PhD thesis. Johns Hopkins University, 2018.

[13] J Zhang and S P Joshi. “Phenomenological crystal plasticity modeling and detailed micromechanical investigations of pure magnesium”. In: *Journal of the Mechanics and Physics of Solids* 60.5 (2012), pp. 945–972.

[14] J W Christian and S Mahajan. “Deformation twinning”. In: *Progress in materials science* 39.1-2 (1995), pp. 1–157.

[15] M T Perez-Prado et al. “Microstructural evolution during large strain hot rolling of an AM60 Mg alloy”. In: *Scripta Materialia* 50.5 (2004), pp. 661–665.

[16] M H Yoo. “Slip, twinning, and fracture in hexagonal close-packed metals”. In: *Metallurgical Transactions A* 12.3 (1981), pp. 409–418.

[17] P D Beggs, W Song, and M Easton. “Failure modes during uniaxial deformation of magnesium alloy AZ31B tubes”. In: *International Journal of Mechanical Sciences* 52.12 (2010), pp. 1634–1645.

[18] C S Meredith, J T Lloyd, and T Sano. “The quasi-static and dynamic response of fine-grained Mg alloy AMX602: An experimental and computational study”. In: *Materials Science and Engineering: A* 673 (2016), pp. 73–82.

[19] J T Lloyd et al. “Dynamic tensile failure of rolled magnesium: Simulations and experiments quantifying the role of texture and second-phase particles”. In: *International Journal of Plasticity* 114 (2019), pp. 174–195.

[20] G I Kanel et al. “Shock response of magnesium single crystals at normal and elevated temperatures”. In: *Journal of Applied Physics* 116.14 (2014), p. 143504.

[21] D J Sandstrom. “ARMOR anti-ARMOR materials by design”. In: *Los Alamos Science* (1989), pp. 36–50.

[22] Y Yu et al. “Influence of initial texture on the shock property and spall behavior of magnesium alloy AZ31B”. In: *Materials Science and Engineering: A* 700 (2017), pp. 259–268.

[23] G V Garkushin et al. “Effect of structural factors on mechanical properties of the magnesium alloy Ma2-1 under quasi-static and high strain rate deformation conditions”. In: *Physics of the Solid State* 57.2 (2015), pp. 337–343.

[24] L Farbaniec et al. “Microstructural effects on the spall properties of ECAE-processed AZ31B magnesium alloy”. In: *International Journal of Impact Engineering* 98 (2016), pp. 34–41.

[25] S J Turneaure et al. “Twinning and Dislocation Evolution during Shock Compression and Release of Single Crystals: Real-Time X-Ray Diffraction”. In: *Physical review letters* 120.26 (2018), p. 265503.

[26] T De Resseguier et al. “Spall fracture and twinning in laser shock loaded single crystal magnesium”. In: *Journal of Applied Physics* 121.16 (2017), p. 165104.

[27] J Kimberley, K T Ramesh, and N P Daphalapurkar. “A scaling law for the dynamic strength of brittle solids”. In: *Acta Materialia* 61.9 (2013), pp. 3509–3521.

[28] V Domnich et al. “Boron carbide: structure, properties, and stability under stress”. In: *Journal of the American Ceramic Society* 94.11 (2011), pp. 3605–3628.

[29] M Chen, J W McCauley, and K J Hemker. “Shock-induced localized amorphization in boron carbide”. In: *Science* 299.5612 (2003), pp. 1563–1566.

[30] Q An, W A Goddard III, and T Cheng. “Atomistic explanation of shear-induced amorphous band formation in boron carbide”. In: *Physical review letters* 113.9 (2014), p. 095501.

[31] L Farbaniec, J D Hogan, and K T Ramesh. “Micromechanisms associated with the dynamic compressive failure of hot-pressed boron carbide”. In: *Scripta Materialia* 106 (2015), pp. 52–56.

[32] J D Hogan et al. “The effects of microstructure and confinement on the compressive fragmentation of an advanced ceramic”. In: *Journal of the American Ceramic Society* 98.3 (2015), pp. 902–912.

[33] J D Hogan et al. “The effects of defects on the uniaxial compressive strength and failure of an advanced ceramic”. In: *Acta Materialia* 102 (2016), pp. 263–272.

[34] D Ghosh et al. "Influence of stress state and strain rate on structural amorphization in boron carbide". In: *Journal of applied physics* 111.6 (2012), p. 063523.

[35] S Zhao et al. "Directional amorphization of boron carbide subjected to laser shock compression". In: *Proceedings of the National Academy of Sciences* 113.43 (2016), pp. 12088–12093.

[36] S Aryal, P Rulis, and W Y Ching. "Mechanism for amorphization of boron carbide B 4 C under uniaxial compression". In: *Physical Review B* 84.18 (2011), p. 184112.

[37] J D Clayton. "Mesoscale modeling of dynamic compression of boron carbide polycrystals". In: *Mechanics Research Communications* 49 (2013), pp. 57–64.

[38] F Thevenot. "Boron carbide a comprehensive review". In: *Journal of the European Ceramic society* 6.4 (1990), pp. 205–225.

[39] X F Li et al. "Dynamic fragmentation of rock material: Characteristic size, fragment distribution and pulverization law". In: *Engineering Fracture Mechanics* 199 (2018), pp. 739–759.

[40] R L Woodward et al. "A study of fragmentation in the ballistic impact of ceramics". In: *International Journal of Impact Engineering* 15.5 (1994), pp. 605–618.

[41] J W McCauley et al. "Experimental observations on dynamic response of selected transparent armor materials". In: *Experimental Mechanics* 53.1 (2013), pp. 3–29.

[42] D L Orphal et al. "Penetration of confined boron carbide targets by tungsten long rods at impact velocities from 1.5 to 5.0 km/s". In: *International journal of impact engineering* 19.1 (1997), pp. 15–29.

[43] J C LaSalvia et al. "Shear localization in a sphere-impacted armor-grade boron carbide". In: *Proceedings of the 23rd International Symposium on Ballistics*. 2007, pp. 16–20.

[44] S Eliezer, I Gilath, and T Bar-Noy. "Laser-induced spall in metals: Experiment and simulation". In: *Journal of applied physics* 67.2 (1990), pp. 715–724.

[45] I Gilath et al. "Brittletoductile transition in laser-induced spall at ultra-high strain rate in 6061 T6 aluminum alloy". In: *Applied physics letters* 52.15 (1988), pp. 1207–1209.

[46] E Moshe et al. “An increase of the spall strength in aluminum, copper, and Metglas at strain rates larger than 10 7 s1”. In: *Journal of Applied Physics* 83.8 (1998), pp. 4004–4011.

[47] F Cottet and M Boustie. “Spallation studies in aluminum targets using shock waves induced by laser irradiation at various pulse durations”. In: *Journal of applied physics* 66.9 (1989), pp. 4067–4073.

[48] N Nissim et al. “Approaching the cold curve in laser-driven shock wave experiment of a matter precompressed by a partially perforated diamond anvil”. In: *Laser and Particle Beams* 31.1 (2013), pp. 73–79.

[49] T DeResseguier et al. “Laser Shock Experiments to Investigate Fragmentation at Extreme Strain Rates”. In: *Dynamic Damage and Fragmentation* (2018), pp. 213–235.

[50] B H Ripin et al. “Laser-Plasma Interaction and Ablative Acceleration of Thin Foils at 1012-1015 W/cm2”. In: *The Physics of Fluids* 23.5 (1980), pp. 1012–1030. DOI: `10.1063/1.863084`.

[51] S P Obenschain et al. “Uniform Ablative Acceleration of Targets by Laser Irradiation at 10 14 W/cm 22”. In: *Physical Review Letters* 50.1 (1983), pp. 44–47. DOI: `https://doi.org/10.1103/PhysRevLett.50.44`.

[52] S A Sheffield, J W Rogers, and J N Castaneda. “Velocity Measurements of Laser-Driven Flyers Backed by High Impedance Windows”. In: *Shock Waves in Condensed Matter* (1986), pp. 541–546. DOI: `https://doi-org./10.1007/978-1-4613-2207-8-78`.

[53] W M Trott and K D Meeks. “High power Nd glass laser transmission through optical fibers and its use in acceleration of thin foil targets”. In: *Journal of Applied Physics* 67.7 (1990), pp. 3296–3301. DOI: `10.1063/1.345364`.

[54] D L Paisley, R H Warnes, and R A Kopp. “Laser driven flat plate Impacts to 100 GPa with sub nanosecond pulse duration and resolution for material property studies”. In: *Proceedings of the APS 1991 Topical Conference on Shock Compression of Condensed Matter,* (1992), pp. 825–828. DOI: `https://doi.org/10.1016/B978-0-444-89732-9.50189-8`.

[55] A M Frank and W M Trott. “Investigation of thin laser-driven flyer plates using streak imaging and stop motion microphotography”. In: *AIP Conference Proceedings- Shock COmpression of Condensed Matter* 370.1 (1996), pp. 1209–1212. DOI: `https://doi.org/10.1063/1.50698`.

[56] H Fujiwara, K E Brown, and D D Dlott. “Laser-Driven Flyer Plates For Reactive Materials Research”. In: *AIP Conference Proceedings- Shock Compression of Condensed Matter* 1195 (2009), pp. 1317–1320. DOI: `10.1063/1.3295050`.

[57] H Fujiwara, K E Brown, and D D Dlott. “High-Energy Flat-top Beams for laser launching using a gaussian mirror”. In: *Applied Optics* 49.19 (2009), pp. 3723–3731. DOI: `https://doi.org/10.1364/AO.49.003723`.

[58] H Fujiwara, K E Brown, and D D Dlott. “A thin-film hugoniot measurement using a laser-driven flyer plate”. In: *AIP Conference Proceedings- Shock COmpression of Condensed Matter* 1426 (2011), pp. 382–385. DOI: `10.1063/1.3686298`.

[59] K E Brown et al. “Simplified laser-driven flyer plates for shock compression science”. In: *Review of Scientific Instruments* 83.103901 (2012), pp. 1–13. DOI: `10.1063/1.4754717`.

[60] A D Curtis et al. “Laser-driven flyer plates for shock compression science: Launch and target impact probed by photon Doppler velocimetry”. In: *Review of Scientific Instruments* 85.043908 (2014), pp. 1–12. DOI: `10.1063/1.4871361`.

[61] A A Banishev et al. “High-Speed Laser-Launched Flyer Impacts Studied with Ultrafast Photography and Velocimetry”. In: *Journal of Dynamic Behavior of Materials* 2 (2016), pp. 194–206. DOI: `10.1007/s40870-016-0058-2`.

[62] J H Lee et al. “Dynamic mechanical behavior of multilayer graphene via supersonic projectile penetration”. In: *Science* 346.6213 (2014), pp. 1092–1096.

[63] J H Lee et al. “High strain rate deformation of layered nanocomposites”. In: *Nature communications* 3 (2012), p. 1164.

[64] D Veysset et al. “Dynamics of supersonic microparticle impact on elastomers revealed by real–time multi–frame imaging”. In: *Scientific reports* 6 (2016), p. 25577.

[65] D L Paisley, R H Warnes, and R A Kopp. “laser-driven flat plate Impacts to 100 GPa with sub nanosecond pulse duration and resolution for material property studies”. In: *Proceedings of the APS 1991 Topical Conference on Shock Compression of Condensed Matter,* (1992), pp. 825–828. DOI: `https://doi.org/10.1016/B978-0-444-89732-9.50189-8`.

[66] T Vogler et al. “Pressure-Shear Experiments on Granular Materials”. In: *Sandia Technical Report SAND2011-6700* (2011), SAND2011–6700.

[67] L Chhabildas, H Sutherland, and J Asay. “A velocity interferometer technique to determine shear wave particle velocity in shock loaded solids”. In: *J. Appl. Phys.* 50.8 (1979), pp. 5196–5201.

[68] M A Meyers. *Dynamic behavior of materials*. John wiley & sons, 1994.

[69] R H Warnes, D L Paisley, and D L Tonks. “Hugoniot and spall data from the laser-driven miniflyer”. In: *AIP Conference Proceedings- Shock COmpression of Condensed Matter,1995* 370.1 (1996), pp. 495–498. DOI: `https://doi.org/10.1063/1.50645`.

[70] D L Robbins et al. “Laser-Driven Miniflyer induced gold spall”. In: *AIP Conference Proceedings- Shock COmpression of Condensed Matter,1999* 505.1 (2000), pp. 1199–1202. DOI: `https://doi.org/10.1063/1.1303676`.

[71] D J Alexander, D L Robbins, and S A Sheffield. “Spall studies in copper foils using the Laser-Driven Miniflyer”. In: *Los Alamos National Lab., NM (US)* LA-UR-00-3288 (2000), pp. 1–8.

[72] D L Paisley et al. “Laser Launched Flyer Plates and Direct Laser Shocks for Dynamic Material Property Measurements”. In: *AIP Conference Proceedings- Shock COmpression of Condensed Matter, 2001* (2002), pp. 1343–1346. DOI: `10.1063/1.1483787`.

[73] D C Swift et al. “Laser launched flyer plates for shock physics experiments”. In: *Review of Scientific Instruments* 76.9 (2005), 093907:1–9. DOI: `10.1063/1.2052593`.

[74] D L Paisley et al. “Laser launched flyer plate and confined laser ablation for shock wave loading: Validation and applications”. In: *Review of Scientific Instruments* 79.2 (2008), 023902:1–8. DOI: `10.1063/1.2839399`.

[75] T deResseguier, H He, and P Berterretche. “Use of laser-accelerated foils for impact study of dynamic material behaviour”. In: *International Journal of Impact Engineering* 31.8 (2005), pp. 945–956. DOI: `https://doi.org/10.1016/j.ijimpeng.2004.07.003`.

[76] P Peralta et al. “Characterization of Incipient Spall Damage in Shocked Copper Multicrystals”. In: *International Journal of Damage Mechanics* 18.4 (2009), pp. 393–413. DOI: `https://doi.org/10.1177/1056789508097550`.

[77] L Wayne et al. “Statistics of weak grain boundaries for spall damage in polycrystalline copper”. In: *Scripta Materialia* 63.12 (2010), pp. 1065–1068. DOI: `doi:10.1016/j.scriptamat.2010.08.003`.

[78] H Wang and Y Wang. “Laser-driven flyer application in thin film dissimilar materials welding and spalling”. In: *Optics and Lasers in Engineering* 97 (2017), pp. 1–8. DOI: `http://dx.doi.org/10.1016/j.optlaseng.2017.04.016`.

[79] D D Mallick et al. “Laser-Driven Flyers and Nanosecond-Resolved Velocimetry for Spall Studies in Thin Films”. In: *Experimental Mechanics* (2019), Sub Judice.

[80] D Mallick et al. “Investigating the velocity envelope of laser-driven micro-flyers for hypervelocity impact experiments”. In: *Procedia engineering* 204 (2017), pp. 215–222.

[81] J Kojima and Q V Nguyen. “Laser pulse-stretching with multiple optical ring cavities”. In: *Applied optics* 41.30 (2002), pp. 6360–6370.

[82] V Reinhard and W Kenneth. “Laser beam homogenizing: limitations and constraints”. In: *Optical Fabrication, Testing, and Metrology III*. Vol. 7102. International Society for Optics and Photonics. 2008, 71020J.

[83] W M Trott et al. “Evaluation of a diffractive microlens-array beam shaper for use in acceleration of laser-driven flyers”. In: *Laser Beam Shaping II*. Vol. 4443. International Society for Optics and Photonics. 2001, pp. 166–178.

[84] J R Lawrence and W M Trott. “Theoretical analysis of a pulsed-laser-driven hypervelocity flyer launcher”. In: *International Journal of Impact Engineering* 14.1-4 (1993), pp. 439–449.

[85] DD Mallick et al. “A Simple Dual-Beam Time-Multiplexed Photon Doppler Velocimeter for Pressure-Shear Plate Impact Experiments”. In: *Experimental Mechanics* 59.1 (2019), pp. 41–49.

[86] R Klopp, R Clifton, and T Shawki. “Pressure-shear impact and the dynamic viscoplastic response of metals”. In: *Mechanics of Materials* 4.3 (1985), pp. 375–385.

[87] R Clifton. “Analysis of the Laser Velocity Interferometer”. In: *Journal of Applied Physics* 41.13 (1970), pp. 5335–5337. DOI: `10.1063/1.1658673`.

[88] K Kim, R Clifton, and P Kumar. “A combined normal- and transverse-displacement interferometer with an application to impact of y-cut quartz”. In: *Journal of Applied Physics* 48.4132 (1977), pp. 4132–4139. DOI: `10.1063/1.323448`.

[89] H Espinosa, M Mello, and Y Xu. "A desensitized displacement interferometer applied to impact recovery experiments". In: *Applied Physics Letters* 69.21 (1996), pp. 3161–3163. DOI: `10.1063/1.116815`.

[90] M Meyers. *Dynamic Behavior of Materials*. John Wiley and Sons, 2007.

[91] O Strand et al. "Compact system for high-speed velocimetry using heterodyne techniques". In: *Rev Sci Instr* 77.08318 (2006), pp. 1–8.

[92] D Dolan. "Accuracy and Precision in photonic Doppler velocimetry". In: *Rev Sci Instr* 81.053905 (2010).

[93] D Holtkamp. "SURVEY OF OPTICAL VELOCIMETRY EXPERIMENTS APPLICATIONS OF PDV, A HETERODYNE VELOCIMETER". In: *2006 International Conference on Megagauss Magnetic Field Generation* (2006).

[94] T Ao and D Dolan. "SIRHEN: a data reduction program for photonic Doppler velocimetry measurements". In: *Sandia Technical Report* (2010), SAND2010–3628.

[95] C Kettenbeil et al. "Heterodyne transverse velocimetry for pressure shear plate impact experiments". In: *Journal of Applied Physics* 123.125902 (2018).

[96] E A Moro, M E Briggs, and L M Hull. "Defining parametric dependencies for the correct interpretation of speckle dynamics in photon Doppler velocimetry". In: *Applied optics* 52.36 (2013), pp. 8661–8669.

[97] J Luo et al. "Axial Strain Calculation Using a Low Pass Digital Differentiator in Ultrasound Elastography". In: *IEEE transactions on ultrasonics, ferroelectrics, and frequency control* 51.9 (2004).

[98] A Cabral and J Rebordao. "Accuracy of frequency sweeping interferometry for absolute distance metrology". In: *Optical Engineering* 46(7).073602 (2007).

[99] J S Rinehart. "Some quantitative data bearing on the scabbing of metals under explosive attack". In: *Journal of Applied Physics* 22.5 (1951), pp. 555–560.

[100] X Y Wu, K T Ramesh, and T W Wright. "The dynamic growth of a single void in a viscoplastic material under transient hydrostatic loading". In: *Journal of the Mechanics and Physics of Solids* 51.1 (2003), pp. 1–26.

[101] A Molinari and T W Wright. “A physical model for nucleation and early growth of voids in ductile materials under dynamic loading”. In: *Journal of the Mechanics and Physics of Solids* 53.7 (2005), pp. 1476–1504.

[102] D S Drumheller. *Introduction to wave propagation in nonlinear fluids and solids*. Cambridge University Press, 1998.

[103] L Davison. *Fundamentals of shock wave propagation in solids*. Springer Science & Business Media, 2008.

[104] D Chen et al. “On the validity of the traditional measurement of spall strength”. In: *International journal of impact engineering* 31.7 (2005), pp. 811–824.

[105] R G Gathers. “Determination of spall strength from surface motion studies”. In: *Journal of applied physics* 67.9 (1990), pp. 4090–4092.

[106] C L Williams et al. “Microstructural effects on the spall properties of ECAE and SWAP magnesium alloys: AZ31B-4E and AMX602”. In: *AIP Conference Proceedings*. Vol. 1793. AIP Publishing. 2017, p. 100011.

[107] D Sagapuram et al. “Controlling texture in magnesium alloy sheet by shear-based deformation processing”. In: *Acta Materialia* 61.18 (2013), pp. 6843–6856.

[108] D Sagapuram et al. “Flow transitions and flow localization in large-strain deformation of magnesium alloy”. In: *Materials Science and Engineering: A* 659 (2016), pp. 295–305. DOI: `https://doi.org/10.1016/j.msea.2016.02.054`.

[109] A Nichols and D Dawson. “Users Manual for ALE3D - an Arbitrary Lagrange/eulerian 2D and 3D Code System”. In: *Livermore Technical Reports* Tech. Rep. LLNL-sm-726137 (2017).

[110] D J Steinberg. *Equation of State and Strength Properties of Selected Materials, 1996, Lawrence Livermore National Laboratory*. Tech. rep. UCRL-MA-106439, 1996.

[111] S P Marsh. *LASL shock Hugoniot data*. Vol. 5. Univ of California Press, 1980.

[112] M Shazly and V Prakash. “Shock response of a gamma titanium aluminide”. In: *Journal of Applied Physics* 104.8 (2008), p. 083513.

[113] D R Ek and J R Asay. “The stress and strain-rate dependence of spall strength in two aluminum alloys”. In: *Shock waves in condensed matter*. Springer, 1986, pp. 413–418.

[114] S J Bless. *Spall criteria for several metals*. Tech. rep. DAYTON UNIV OH RESEARCH INST, 1981.

[115] B Selvarajou, S P Joshi, and A A Benzerga. "Void growth and coalescence in hexagonal close packed crystals". In: *Journal of the Mechanics and Physics of Solids* 125 (2019), pp. 198–224.

[116] T P Remington et al. "Spall strength dependence on grain size and strain rate in tantalum". In: *Acta Materialia* 158 (2018), pp. 313–329.

[117] R Hill. *The mathematical theory of plasticity*. Vol. 11. Oxford university press, 1998.

[118] Y Huang, J W Hutchinson, and V Tvergaard. "Cavitation instabilities in elastic-plastic solids". In: *Journal of the Mechanics and Physics of Solids* 39.2 (1991), pp. 223–241.

[119] J W Wilkerson and K T Ramesh. "Unraveling the anomalous grain size dependence of cavitation". In: *Physical review letters* 117.21 (2016), p. 215503.

[120] C Czarnota et al. "Modelling of dynamic ductile fracture and application to the simulation of plate impact tests on tantalum". In: *Journal of the Mechanics and Physics of Solids* 56.4 (2008), pp. 1624–1650.

[121] Y Wang and H Choo. "Influence of texture on Hall–Petch relationships in an Mg alloy". In: *Acta Materialia* 81 (2014), pp. 83–97.

[122] J W Wilkerson and K T Ramesh. "A dynamic void growth model governed by dislocation kinetics". In: *Journal of the Mechanics and Physics of Solids* 70 (2014), pp. 262–280.

[123] Z Trojanova et al. "High strain rate behaviour of an AZ31 0.5 Ca magnesium alloy". In: *Materials Engineering-Materialove inzinierstvo (MEMI)* 19.1 (2011), pp. 12–17.

[124] G I Kanel. "Distortion of the wave profiles in an elastoplastic body upon spalling". In: *Journal of Applied Mechanics and Technical Physics* 42 (2001), pp. 358–362.

[125] K Callaghan and R Becker. "Examination of ductile spall failure through direct numerical simulation". In: *AIP Conference Proceedings*. Vol. 1979. AIP Publishing. 2018, p. 070010.

[126] J W Wilkerson. "On the micromechanics of void dynamics at extreme rates". In: *International Journal of Plasticity* 95 (2017), pp. 21–42.

[127] S J Turneaure et al. “Twinning and Dislocation Evolution during Shock Compression and Release of Single Crystals: Real-Time X-Ray Diffraction”. In: *Physical review letters* 120.26 (2018), p. 265503.

[128] T de Resseguier et al. “Spall fracture and twinning in laser shock-loaded single-crystal magnesium”. In: *Journal of Applied Physics* 121.16 (2017), p. 165104.

[129] F R Nabarro. “Fifty-year study of the Peierls Nabarro stress”. In: *Materials Science and Engineering: A* 234 (1997), pp. 67–76.

[130] A Akhtar and E Teghtsoonian. “Solid solution strengthening of magnesium single crystals the effect of solute on the ease of prismatic slip”. In: *Acta Metallurgica* 17.11 (1969), pp. 1351–1356.

[131] F F Lavrentev and Y A Pokhil. “Effect of Forest Dislocations the system on hardening in Mg single crystals under basal slip”. In: *physica status solidi (a)* 32.1 (1975), pp. 227–232.

[132] N Ono, R Nowak, and S Miura. “Effect of deformation temperature on Hall Petch relationship registered for polycrystalline magnesium”. In: *Materials Letters* 58.1-2 (2004), pp. 39–43.

[133] J F Nie. “Effects of precipitate shape and orientation on dispersion strengthening in magnesium alloys”. In: *Scripta Materialia* 48.8 (2003), pp. 1009–1015.

[134] N Stanford and M R Barnett. “The origin of ”rare earth” texture development in extruded Mg-based alloys and its effect on tensile ductility”. In: *Materials Science and Engineering: A* 496.1-2 (2008), pp. 399–408.

[135] A K Ray and D S Wilkinson. “The effect of microstructure on damage and fracture in AZ31B and ZEK100 magnesium alloys”. In: *Materials Science and Engineering: A* 658 (2016), pp. 33–41.

[136] E Moshe et al. “An increase of the spall strength in aluminum, copper, and Metglas at strain rates larger than 10 7 s- 1”. In: *Journal of Applied Physics* 83.8 (1998), pp. 4004–4011.

[137] J B Clark. “Age hardening in a Mg-9 wt.% Al alloy”. In: *Acta Metallurgica* 16.2 (1968), pp. 141–152.

[138] S Celotto. “TEM study of continuous precipitation in Mg–9 wt% Al–1 wt% Zn alloy”. In: *Acta materialia* 48.8 (2000), pp. 1775–1787.

[139] D A Porter and J W Edington. “Microanalysis and cell boundary velocity measurements for the cellular reaction in a Mg-9% Al alloy”. In: *Proceedings of the Royal Society of London. A. Mathematical and Physical Sciences* 358.1694 (1978), pp. 335–350.

[140] S W Xu et al. “Effect of Mg17Al12 precipitates on the microstructural changes and mechanical properties of hot compressed AZ91 magnesium alloy”. In: *Materials Science and Engineering: A* 523.1-2 (2009), pp. 47–52.

[141] J D Robson, N Stanford, and M R Barnett. “Effect of precipitate shape on slip and twinning in magnesium alloys”. In: *Acta materialia* 59.5 (2011), pp. 1945–1956.

[142] N Stanford et al. “Effect of plate-shaped particle distributions on the deformation behaviour of magnesium alloy AZ91 in tension and compression”. In: *Acta materialia* 60.1 (2012), pp. 218–228.

[143] S Eswarappa Prameelaa et al. “Dynamic Precipitation and Recrystallization in Mg-9wt%Al During Equal-Channel Angular Extrusion: A Comparative Study to Conventional Aging”. In: Acta Materialia (2019).

[144] L C Chhabildas et al. “Relationship of fragment size to normalized spall strength for materials”. In: *International Journal of Impact Engineering* 10.1-4 (1990), pp. 107–124.

[145] J T Lloyd et al. “Dynamic tensile failure of rolled magnesium: Simulations and experiments quantifying the role of texture and second-phase particles”. In: *International Journal of Plasticity* 114 (2019), pp. 174–195.

[146] GI Kanel et al. “Shock response of magnesium single crystals at normal and elevated temperatures”. In: *Journal of Applied Physics* 116.14 (2014), p. 143504.

[147] M Zhao, V Kannan, and K T Ramesh. “The dynamic plasticity and dynamic failure of a magnesium alloy under multiaxial loading”. In: *Acta Materialia* 154 (2018), pp. 124–136.

[148] S Lavenstein et al. “Effect of temperature on the compression response of solid solution Mg-9wt%Al alloy”. 2019 in preparation.

[149] E W Kelley and W F Hosford Jr. “Plane strain compression of magnesium and magnesium alloy crystals”. In: *Trans Met Soc AIME* 242.1 (1968), pp. 5–13.

[150] J D Hogan et al. “Fragmentation of an advanced ceramic under ballistic impact: mechanisms and microstructure”. In: *International Journal of Impact Engineering* 102 (2017), pp. 47–54.

[151] D D Mallick and K T Ramesh. “Dynamic Fragmentation of Boron Carbide with Laser-Driven Flyers”. In: *Procedia engineering, Hypervelocity Impact Symposium* (2019), pp. 1–8.

[152] D E Grady. “Length scales and size distributions in dynamic fragmentation”. In: *International Journal of Fracture* 163.1-2 (2010), pp. 85–99.

[153] V Paris et al. “Divergent impact study of the compressive failure threshold in SiC and B4C”. In: *International Journal of Impact Engineering* 38.4 (2011), pp. 228–237.

[154] V Paris et al. “The spall strength of silicon carbide and boron carbide ceramics processed by spark plasma sintering”. In: *International Journal of Impact Engineering* 37.11 (2010), pp. 1092–1099.

[155] GI Kanel et al. “Search for conditions of compressive fracture of hard brittle ceramics at impact loading”. In: *International Journal of Plasticity* 25.4 (2009), pp. 649–670.

[156] J Hawreliak et al. “Nanosecond x-ray diffraction from polycrystalline and amorphous materials in a pinhole camera geometry suitable for laser shock compression experiments”. In: *Review of Scientific Instruments* 78.8 (2007), p. 083908.

[157] DH Kalantar et al. “Direct observation of the α- ε transition in shock-compressed iron via nanosecond X-ray diffraction”. In: *Physical review letters* 95.7 (2005), p. 075502.

[158] MD Bowden and SL Knowles. “Optimisation of laser-driven flyer velocity using photonic Doppler velocimetry”. In: *Optical Technologies for Arming, Safing, Fuzing, and Firing V*. Vol. 7434. International Society for Optics and Photonics. 2009, p. 743403.

[159] JM Winey, P Renganathan, and YM Gupta. “Shock wave compression and release of hexagonal-close-packed metal single crystals: Inelastic deformation of c-axis magnesium”. In: *Journal of Applied Physics* 117.10 (2015), p. 105903.

[160] P Renganathan, JM Winey, and YM Gupta. “Shock compression and release of a-axis magnesium single crystals: Anisotropy and time dependent inelastic response”. In: *Journal of Applied Physics* 121.3 (2017), p. 035901.

Debjoy Debasish Mallick

Ph.D Candidate
✉ `dmallick@jhu.edu`
☎ `4437213006`

Education

Sep 2013 – Present	**Ph.D., Johns Hopkins University, MD, USA** in Mechanical Engineering. Advisor: KT Ramesh
May 2005 – May 2009	**B.S., Johns Hopkins University, MD, USA** in Biomedical Engineering.

Employment History

Dec 2012 – Present	**Scientist,** U.S. Army Research Laboratory, Aberdeen Proving Ground, MD.
Aug 2010 – Dec 2012	**Senior Scientist,** Bowhead Science and Technology, Aberdeen Proving Ground, MD.
Jun 2010 – Aug 2010	**Development Intern,** U.S. Army Research Laboratory, Adelphi, MD.
Jun 2009 – Aug 2010	**Electrical Engineer,** Northrop Grumman, Linthicum, MD.

Awards and Achievements

Jun 2019	**APS – SCCM/AIRAPT** Student Travel Award.
Apr 2015 – Jul 2019	**American Soc. for Eng. Ed. D.O.D. SMART Scholarship**
Apr 2019	**Alex Charters Student Scholar Award** Hypervelocity Impact Symposium Conference Award.
Jul 2017	**APS – SCCM/AIRAPT** Student Travel Award.
Apr 2017	**Alex Charters Student Scholar Award** Hypervelocity Impact Symposium Conference Award.
Jan 2017 – Jan 2018	**President of Mechanical Engineering Graduate Association,** Graduate advocacy group for 150+ graduate students, Deparment of Mechanical Engineering.

Research Publications

Journal Articles

① Mallick, D. D., Zhao, M., Bosworth, B. T., Schuster, B. E., Foster, M. A., & Ramesh, K. T. (2019). A simple dual-beam time-multiplexed photon doppler velocimeter for pressure-shear plate impact experiments. *Experimental Mechanics*, *59*(1), 41–49.

② Mallick, D., Zhao, M., Parker, J., Kannan, V., Bosworth, B., Sagapuram, D., … Ramesh, K. (2019). Laser-driven flyers and nanosecond-resolved velocimetry for spall studies in thin metal foils. *Experimental Mechanics*, 1–18.

③ Hogan, J. D., Farbaniec, L., Mallick, D., Domnich, V., Kuwelkar, K., Sano, T., … Ramesh, K. T. (2017). Fragmentation of an advanced ceramic under ballistic impact: mechanisms and microstructure. *International Journal of Impact Engineering*, *102*, 47–54.

Conference Proceedings

① Mallick, D., Shaeffer, M., Dean, S., & Ramesh, K. T. (2017). Investigating the velocity envelope of laser-driven micro-flyers for hypervelocity impact experiments. (Vol. 204, pp. 215–222). Elsevier.

② Hogan, J., Farbaniec, L., Mallick, D., McCauley, J. W., & Ramesh, K. T. (2015a). Dynamic fragmentation of an advanced ceramic during high-speed impact. In *Aps shock compression of condensed matter meeting abstracts*.

③ Hogan, J., Farbaniec, L., Mallick, D., McCauley, J. W., & Ramesh, K. T. (2015b). Impact-induced fragmentation and excavation of boron carbide. In *Sem 2015*.

④ Wingard, Z., Mallick, D., & Bryant, A. (2015). Energy efficient lethality via a cutting mechanism. In *Ndia classified ballistics symposium. monterey*.

Selected Presentations

① Mallick, D., Bosworth, B. T., Eswarappa-Prameela, S., Parker, J., Lloyd, J., Foster, M., … Ramesh, K. T. (2018). *Shock induced failure of mg alloys using laser-driven micro-flyers*. MEDE Fall Meeting, Poster Presentation.

② Mallick, D., Zhao, M., Bosworth, B. T., Schuster, B. E., Foster, M., & Ramesh, K. T. (2018). *Photon doppler velocimetry in plate impact experiments*. The Technical Cooperation Program, US Army Research Lab.

③ Mallick, D. D., Shaeffer, M., Dean, S., & Ramesh, K. T. (2017). *Investigating the velocity envelope of laser-driven micro-flyers for hypervelocity impact experiments*. Hypervelocity Impact Symposium 2017.

④ Mallick, D. D., Shaeffer, M., & Ramesh, K. T. (2017a). *Laser-driven micro-flyer plates for shock compression of protection materials*. APS-Shock Compression of Condensed Matter 2017.

⑤ Mallick, D. D., Shaeffer, M., & Ramesh, K. T. (2017b). *Using laser-driven micro-flyers to study deformation mechanisms*. Mach Conference 2017.

⑥ Mallick, D., Shaeffer, M., & Ramesh, K. T. (2016). *Development of laser shock capabilities for dynamic materials characterization*. MEDE Fall Meeting 2016.

⑦ Mallick, D., Zhao, M., Schuster, B. T., Casem, D., & Ramesh, K. T. (2016). *Photon doppler velocimetry in plate impact experiments*. SES 2016.

⑧ Mallick, D. D., Hogan, J. D., & Ramesh, K. T. (2014). *Dynamic failure of armor ceramics: bridging experimental and modeling efforts*. Mach Conference 2014.

⑨ Mallick, D., Hogan, J., Ayyagari, R., & Ramesh, K. T. (2014). *Microstructure based modeling of the failure and strength of advanced ceramics*. Materials Science and Technology 2014.

Teaching and Mentorship Experience

May 2018 – Sep 2018	**Raymundo Muro Barrios, NSF REU Student.**
Sep 2016 – May 2017	**Montese Hall, Baltimore Polytechnical Institute Research Practicum Student.**
Sep 2017 – May 2018	**Mechanics of Materials Seminar Organizer, 530.809.01 and 530.810.01,** Organized weekly student seminar in solid mechanics group (40+ graduate students), Department of Mechanical Engineering.
Sep 2017 – Dec 2017	**Teaching Assistant, 530.430.01, Applied Finite Element Analysis,** Instructor: Dr. Nitin Daphalapukar, Department of Mechanical Engineering.
Jan 2017 – May 2017	**Teaching Assistant, 530.748.01, Stress Waves, Impacts and Shockwaves,** Instructor: Dr. KT Ramesh, Department of Mechanical Engineering.
Sep 2016 – Dec 2016	**Teaching Assistant, 530.430.01, Applied Finite Element Analysis,** Instructor: Dr. Nitin Daphalapukar, Department of Mechanical Engineering.
Jan 2016 – May 2016	**Teaching Assistant, 530.618.01, Fabricatology- Advanced Materials Processing,** Instructor: Dr. Sung Hoon Kang, Department of Mechanical Engineering.
Sep 2015 – Dec 2015	**Teaching Assistant, 530.630.01, Applied Finite Element Analysis,** Instructor: Dr. Nitin Daphalapukar, Department of Mechanical Engineering.